Università degli Studi di Torino
Doctoral School of the University of Torino
PhD Programme in Innovation for the Circular Economy XXXVII Cycle

Recovery and valorisation of agro-industrial waste through the development of hybrid materials for environmental applications

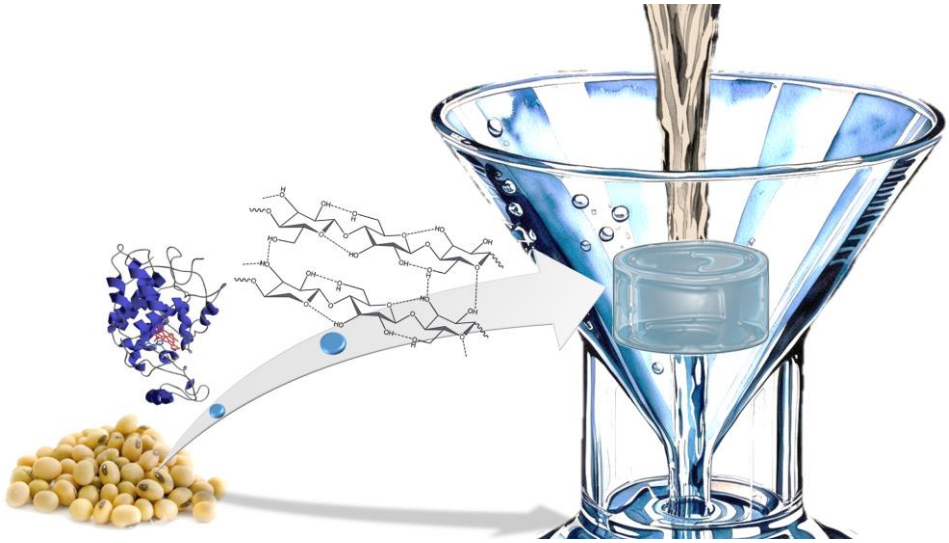

Monica Rigoletto

Università degli Studi di Torino
Doctoral School of the University of Torino
PhD Programme in Innovation for the Circular Economy XXXVII Cycle

Recovery and valorisation of agro-industrial waste through the development of hybrid materials for environmental applications

Candidate: **Monica Rigoletto**

Supervisor: Prof. **Enzo Laurenti**

Jury Members: Prof. **Giuseppina Cerrato**
Università degli Studi di Torino
Dipartimento di Chimica

Prof. **Amaya Arencibia**
Universidad Rey Juan Carlos
Departamento de Tecnología Química, Energética y Mecánica

Dr. **Maria Luisa Testa**
Consiglio Nazionale delle Ricerche (CNR)
Institute for the Study of Nanostructured Materials (ISMN)

Head of the Doctoral School: Prof. **Enzo Medico**
PhD Programme Coordinator: Prof. **Marco Zanetti**

Turin, 2025

Agli incontri inaspettati,
alle amicizie consolidate,
alla famiglia
e un po' anche a me

Summary

1 Introduction

The world we live in is the result of millions of years of evolution and radical changes that have modified its appearance and liveability. Changes that have led to the extinction of some species and the survival of others, like ours, which had the privilege of getting this far. And from simple inhabitants of the Earth, humans become one of the main authors of the changes our planet is going through. Without any awareness of how many of the activities that allowed him to evolve and progress could lead to some of the most significant issues of today, humans continued to exploit the resources available to their advantage, pursuing the objective of infinite growth and development. However, the ability to observe and learn that distinguishes our species eventually revealed the effects of human activities on the environment and ecosystems. The growing awareness and concern of many, unfortunately not all, has materialized in the regulatory framework adopted by many countries, in an attempt to contain the effects of our past ambitions and preserve the world for future generations of future generations. The work of researchers from all over the world fits into this legislative, environmental, social and economic framework and focuses much of their research on proposing sustainable and concrete solutions, as well as tools to the challenges we are called to respond to.

1.1 Contextualization

More than in past, in recent years, it has become increasingly clear how everything is interconnected, not only in nature but also in our socio-economic model. It is not possible to talk about the environment without considering the economic implications of the actions necessary for its protection on companies or individual countries, nor ignoring the social impacts that such actions can have. These aspects are inextricably linked and must be treated as such. For this reason, even if this thesis work focused mainly on more technical aspects, it was deemed necessary to design a clear framework within which the scientific results obtained will be inserted.

1.2 Circular Economy and European framework

Humans have always taken inspiration from nature, however the economic model adopted until now is an exception. In nature, waste from one species often becomes a source of sustenance or resource for another. When plants or animals conclude their life cycle, the nutrients they were composed of are reabsorbed into the soil. All this moved only by the energy of the Sun and with circularity (Ellen MacArthur Fundation, 2021a).

However, the type of economy we have adopted involves a "take-make-dispose" model which is not sustainable in the long term as limited resources are consumed and wastes generated, if not properly treated, can be.

As early as the 1970s-80s (Brundtland, 1987; Meadows et al., 1972) it became evident that an alternative way of managing natural resources had to be found to address continued population growth without exhausting these reserves. This alternative has found its conceptualization in what is today called "*circular economy*". However, it is not at easy to give a univocal meaning of circular economy since hundreds of definitions based on scientific and semi-scientific concepts (Corvellec et al., 2022; Kirchherr et al., 2017) have been developed. Many of them were coined by practitioners as policy makers, businesses, business consultants, business associations, business foundations, and so on (Korhonen et al., 2018). Hence, different definitions of circular economy are typically adopted for different theoretical uses (Kirchherr et al., 2017).

In this complex framework of "final user driven definition" we can still find some central ideas and principles that are well described by the Ellen MacArthur Foundation: (i) eliminate waste and pollution; (ii) circulate products and materials (at their highest value); (iii) regenerate nature.

According to the butterfly diagram they proposed (Figure 1.1), circular economy keeps products, material and components in use at their highest value at all time trying to decouple economic growth and development. It does so distinguishing between two type of cycle: the technical and the biological cycles. In the first one, related to

products that are used rather than consumed, components and materials are kept in circulation in the economy for as long as possible through sharing, reuse, refurbish and recycle strategies. The second one is mainly related to biodegradable materials, such as food or wood-based products, that can be treated to create further value by cascading them for additional application in different value streams.

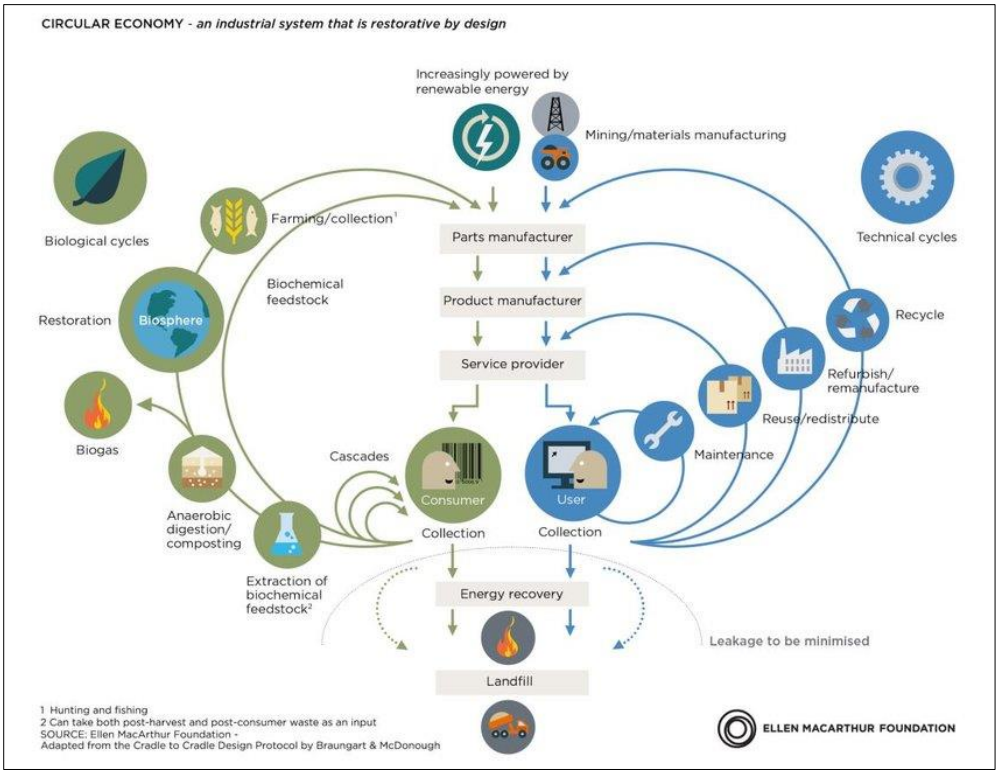

Figure 1.1 - Butterfly Diagram of Circular Economy proposed by Ellen Macarthur Foundation (Ellen MacArthur Fundation, 2021b)

In the last decay this concept has been embraced by European Union which included it in its most recent packages of political initiatives.

The European Parliament (European Parliament, 2023) presents the circular economy as "*a model of production and consumption, which involves sharing, leasing, reusing, repairing, refurbishing and recycling existing materials and products as long as*

possible. […]" and point out several connected benefits in terms of environment protection, reduction of raw materials dependence and creation of jobs.

Its relevance in the current European framework is evidenced by the strategies adopted since 2015: Circular Economy Action Plan (2015), Circular Economy Package (2018) and New Circular Economy Action Plan (2020). The European Commission (European Commission, s.d.) describes the latter as one of the main building blocks of the European Green Deal, a roadmap for becoming a climate-neutral continent by 2050 and to make the climate challenge and the ecological transition an opportunity for a new development model. This model is within the concept of sustainable development, defined as "*development that considers the present without compromising the capacity of future generations to meet their own needs*" (Brundtland, 1987), which is the basis of the *Agenda 2030* and the 17 Sustainable Development Goals (SDGs) promoted by the United Nations (United Nations, 2015).

When circular economy is applied to the agricultural field, it could partially overlap the concept of bioeconomy, defined as converting renewable biological resources into new value-added products, including food, feed, bio-based products and bioenergy (European Commission, 2012), and they have been recently combined in the concept of sustainable circular bioeconomy (European Commission, 2018).

Implementation of circular strategy for food resources production and management is fundamental to reach a sustainable development in all its three dimension (environmental, social and economic) by reducing CO_2 emissions, preventing land degradation, reducing agricultural costs and increasing farmers' profitability (Velasco-Muñoz et al., 2021, 2022).

Transition to a sustainable circular bioeconomy needs a change at a system level with more sustainable behaviours on the part of all actors, new knowledge and development of technologies for sustainable processes and new business model to propose new bio-based products and services corresponding to consumer expectations (de Vries et al., 2021).

However, it is important not to ignore that several authors have highlighted some limits and critical issues related to the circular economy concept. In a recent review (Corvellec et al., 2022). Corvellec and co-workers summarise clearly some of them. Firstly, they point out how the concept of "circularity" can be misleading if it evokes industrial systems modelled according to an understanding of nature as a circular system that is stable, closed, and zero waste. Indeed, modern ecological theory tends to construct the planet as an evolving open system of resilience in dynamic equilibrium or non-equilibrium (Skene, 2018). Furthermore, as stated by Cullen (Cullen, 2017), every circle creates dissipation and entropy, attributed to losses in quantity and quality, leading necessary the introduction of new materials and energy into any circular material loop to overcome these losses. A circular economy future where waste no longer exists is not possible.

Secondly, the authors underline as the circular economy implementation is not clearly delineate in any of the three levels of policies, organizations, and individual consumers. Politic, for example, is very focused on technical and economic aspects and seems less ambitious regarding social justice and environmental protection (Flynn & Hacking, 2019; Kovacic et al., 2019). At organizational level, companies promote circularity but limiting their efforts to certain parts of their activities and often only to improve their reputation while ensuring a long existence and competitiveness with linear business models (Hofmann, 2019; Stål & Corvellec, 2018). Moreover, some circular business models can only work under very specific conditions, for example, the spatial proximity between entities (Winans et al., 2017) and can find several barriers: technical (inappropriate technology, or lack of technical support and training); economic (capital requirements, high initial costs, or uncertain return and profit); institutional or regulatory (lack of a conducive legal system, or a deficient institutional framework) and sociocultural (rigidity of consumer behaviour and businesses routines) (de Jesus & Mendonça, 2018).

From the consumer's point of view, circular consumption places people faced with the choice between the novelty of the moment and regenerated or "green by design" products which are not always able to be attractive (Valenzuela & Böhm, 2017).

Other authors (Korhonen et al., 2018) point out the temporal boundary question underlying how the short-term and long-term environmental impacts remain unknown when designing reuse, remanufacturing, and recycling projects. This, together with the problem of spatial boundaries, makes it essential to evaluate case by case whether circular economy can deliver sustainable value (Manninen et al., 2018). It is therefore important to dispel the myth that circular systems are necessarily more environmentally sustainable than linear systems (Brandão et al., 2020).

1.3 Water pollution and remediation strategies

Nowadays almost every aspect of our lives is characterized by the presence of chemicals. Tens of thousands of industrial chemical substances are produced, distributed and used in Europe continuously and many of these (more than 20,000) are registered under REACH (European Chemicals Agency, s.d.), a regulation that outlines the registration, (eco)-toxicological hazard evaluation, and authorization of industrial chemicals in the European Union. To these must be added also pesticides, herbicides, fertilizers used in agriculture and pharmaceuticals or cosmetics that we use in our everyday life.

As consequence of all the anthropic activities, a lot of chemicals enter in the environment becoming pollutants and affecting soil, air and water quality. The preservation of water quality is a fundamental duty because the socio-economic well-being and livelihood of the human population, as well as the survival of ecosystems and biodiversity, depend on it. The continuous population growth and climate changes contribute to the water crisis, which leads to the death of more than 13,000 people every year due to the lack of water resources availability and water contamination (World Health Organization, 2019).

The increasing of environmental contamination together with the technological innovations enabling us to detect pollutants in even very low concentration, the improved scientific knowledge about the impact of the use of unhealthy water on human health and the precautionary principle have prompted several health bodies

and governments to regulate the water protection and management (Dettori et al., 2022).

Since 1980, Europe has been an active part of political initiatives and strategies for the protection of water resources (European Parliament, 2024). As declared by the European Parliament, the main objective of the EU water policy is to "ensure access to good quality water in sufficient quantities for all Europeans, economic sectors and the environment, and to ensure the good status of all bodies of water across Europe". To reach this purpose and to face the challenges of extreme weather events, the European policy established two main legal framework related to water: The Water Framework Directive (2000/60/EC) and The Marine Strategy Framework Directive (2008/56/EC).

The purpose of the Water Framework Directive (WFD) is to establish a framework for the protection of inland surface waters, transitional waters, coastal waters and groundwater which: (a) prevents further deterioration and protects and enhances the status of aquatic ecosystems […]; (b) promotes sustainable water use based on a long-term protection of available water resources; (c) aims at enhanced protection and improvement of the aquatic environment, *inter alia*, through specific measures for the progressive reduction of discharges, emissions and losses of priority substances and the cessation or phasing-out of discharges, emissions and losses of the priority hazardous substances; (d) ensures the progressive reduction of pollution of groundwater and prevents its further pollution, and (e) contributes to mitigating the effects of floods and droughts.

The WFD is supported by more specific directives that refers to specific water management field: The Groundwater Directive (2006/118/EC), The revised Drinking Water Directive((EU) 2020/2184), The Bathing Water Directive (2006/7/EC), The Environmental Quality Standards Directive (2008/105/EC), The Urban Waste Water Treatment Directive (91/271/EEC), The Nitrates Directive (91/676/EEC), The EU Floods Directive (2007/60/EC) (European Parliament, 2024).

The WFD set the basis for the water bodies classification depending on their ecological and chemical status (Figure 1.2).

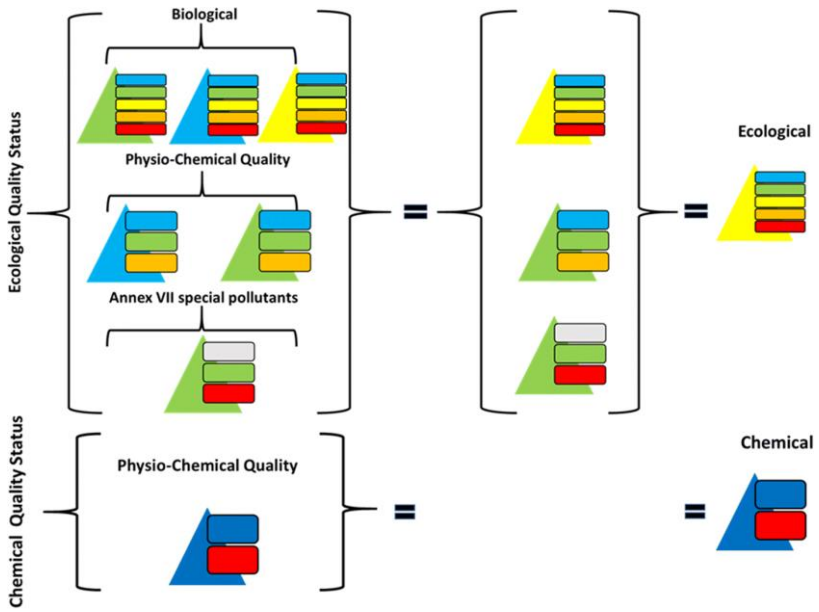

Figure 1.2 - "One out-all out" classification of water bodies according to Directive 2000/60/EC. Colour code: red = "bad" quality status, orange = "poor", yellow = "moderate", green = "good", blue = "high" quality status (Zacharias et al., 2020)

The estimate of the overall ecological quality (EQ) status according to the Annex V of the WFD, it must take into account both biological quality and supporting quality elements, which are: physical-chemicals parameters, presence or absence of special pollutants and hydromorphological characteristics. Special pollutants are indicated in the Annex VIII of the WFD which propose an "indicative list of the main pollutants" including organohalogen, organophosphorous and organotin compounds, substances which have been proved to possess carcinogenic or mutagenic properties, cyanides, metals and their compounds, arsenic and its compounds, biocides, materials which contributes to eutrophication and substances which have an unfavourable influence on the oxygen balance.

On the other hand, for assessing the chemical status of waterbodies the Environmental Quality Standards (EQSs) are used. They have been list in the Directive 2008/105/EC which established the maximum acceptable concentration and/or annual average concentration for 33 priority substances and 8 other pollutants

which, if met, allow(s) the chemical status of the waterbody to be described as *good.* This Directive was updated in 2013 (EC, 2013), extending the number of Priority substances to 45. The list of these substances is also referred to as Annex X substances of the WFD (Technical Guidance for Deriving Environmental Quality Standards - Guidance Document No. 27 Updated version 2018, s.d.). They include compounds of cadmium, nickel, lead and mercury, PAHs, some organic chlorinated substances, dioxins, etc…

As clear from these statements, among all the water contaminants, heavy metals and metalloids or Potentially Toxic Elements (PTEs) represent a well-known problem for ecosystems safety and for human health.

Elements belonging this category of pollutants, as copper (Cu), lead (Pb), cadmium (Cd), nickel (Ni), zinc (Zn), arsenic (As) and mercury (Hg), are ubiquitous and naturally present in the environment. Since they are not biodegradable, PTEs are persistent and may be toxic to biota even at low concentrations. Furthermore, they can bioaccumulate in fishes, causing several pathologies, and biomagnified along the food chain with adverse consequences for end consumers (Strungaru et al., 2018). Some of human health hazards associated with exposure to PTEs are summarized in Figure 1.3.

PTEs water remediation techniques include physical strategies (reverse osmosis, filtration, membrane filtration, flotation, coagulation-flocculation), chemical (precipitation, ion exchange, electrochemical, reduction/oxidation treatments) and biological methods (bioremediation and phytoremediation (Abdullah et al., 2019; Emenike et al., 2022; Farooqi et al., 2022; Kurniawan et al., 2006; Qasem et al., 2021).

However, one of the most widespread strategies to face potentially toxic elements' water pollution, as will be detailed in subsequent chapters, is represented by adsorption. It is a mass transfer process in which a substance is carried from a liquid phase to the surface of a solid and bounds with the solid surface by physical and/or chemical interactions. This strategy is attracting interest also due to the possibility to regenerate adsorbents using suitable desorption processes (Maharana et al., 2021).

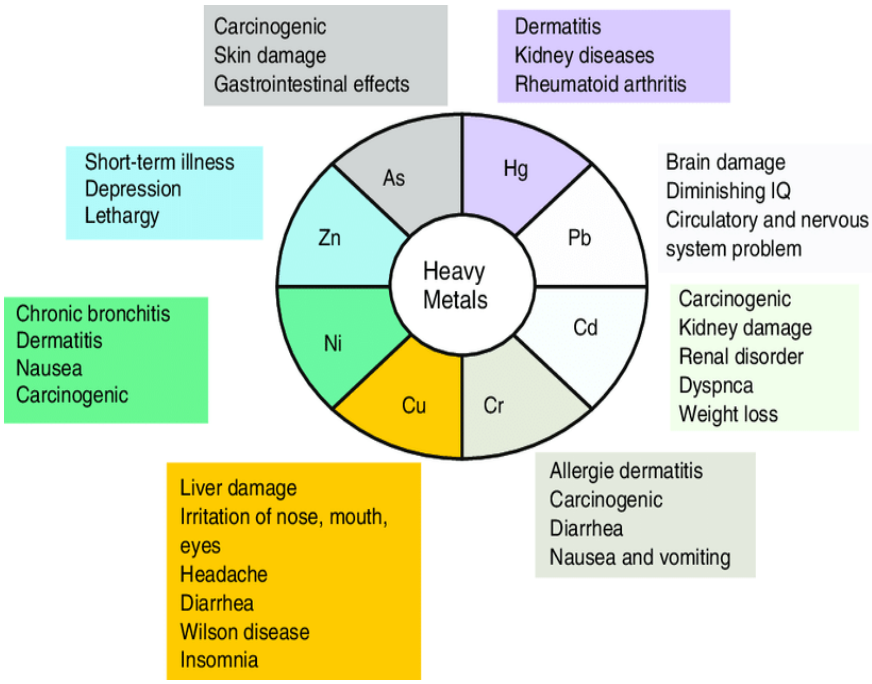

Figure 1.3 - Human health hazards associated with exposure to toxic heavy metals (Maharana et al., 2021)

In parallel with inorganic contaminants, the presence in the environment of several organic compounds that have proven to be persistent and harmful has raised concern. In the last decades pharmaceutically active compounds (PhACs), personal care products (PCPs), endocrine-disrupting chemicals (EDCs), artificial sweeteners (ASWs), etc., have been increasingly detected in the aqueous environment (Parida et al., 2021). These compounds are collectively classified as emerging contaminants (ECs). The list of compounds belonging to this registry of recalcitrant pollutants is constantly evolving and, consequently, most of them are not yet regulated by legislation due to the lack of exhaustive data on toxicity, mode of action, bioaccumulation capacity and reactivity (Deblonde et al., 2011; Gaggero et al., 2023). Given the vastness of the chemical species that fall into the aforementioned categories, it is easy to realize the complexity of the problem and why many scientists are studying new approaches to face this challenge since conventional treatment

process such as coagulation, flocculation and sedimentation are not effective for ECs removal (Parida et al., 2021).

Different techniques have been developed as function of the contaminants' physicochemical properties and nature: adsorption on both inorganic and organic adsorbents (Almeida-Naranjo et al., 2023), Advanced Oxidation Processes (AOPs) involving ozone (Wang et al., 2019) or UV light, electro-oxidation techniques (Rivera-Utrilla et al., 2013), enzymatic reactions (Bilal et al., 2019; Shahid et al., 2021) biological treatments (Garcia-Rodríguez et al., 2014; Shahid et al., 2021), photocatalytic approaches (Ahmaruzzaman, 2021; Antoniadou et al., 2021; Miranda-García et al., 2011).

Furthermore, many integrated strategies, aimed at improving the performance of individual treatments and broadening the target of contaminants, have been developed in recent years. Among them, the so called hybrid materials, are becoming more and more popular. They are the result of the combination of different components whose coupling leads to an improvement of the individual properties (Rigoletto et al., 2022).

Polymers have been widely employed in several of the mentioned techniques and recently also bio-polymers are becoming attractive. This is not only due to their high availability, ease of use and chemical modification, high biodegradability and minimal toxicity (Subash et al., 2023) but also because they can be obtained from exhausted biomass.

1.4 The potential of soybean processing waste: cellulose and SBP

In this research soy was selected as the starting crop and its processing waste, the hulls, as exploitable lignocellulosic materials.

With a global production of around 396 Million Metric Tons in 2023/2024 (United States Department of Agriculture), soy is a globally widespread crop widely used for the production of food, feed, medical products and for several industrial applications (Figure 1.4) (Singh & Krishnaswamy, 2022).

In the 2023 the three main producing countries were Brazil (153 Million Metric Tons), United States (113.34 Million Metric Tons) and Argentina (49.5 Million Metric Tons), while the European Union with a production of 2.98 Million Metric Tons was the twelfth producer in the World. In Europe Italy is one of the countries with the higher soybean production, after Russia and Ukraine (Rotundo et al., 2024, FAOSTAT).

Soybean is considered a highly nutrient crop plant with an abundance of protein (35–45%), lipid (15–25%), carbohydrates (30–35%), dietary fibres (17%), and traces of micronutrient (Hassan, 2013; Sharma et al., 2014; Singh & Krishnaswamy, 2022). Furthermore, other interesting components as isoflavones, saponins, lecithin, phytic acids, glycine, bioactive peptide, vitamins, makes soybeans nutritional profile a well-known beneficial to the health (Qin et al., 2022; Rizzo, 2020; Singh & Krishnaswamy, 2022).

Hence, its application in human food product and animal feed is spread. During the industrial soy processing, various by-products as lecithin, soy meal, soy-whey, hulls, meal, okara and molasses are produced. Most of these by-products could enter in valorisation paths and being recovered as reported in Table 1.1.

In this work we will focus our attention on soybean hulls, that constitute a by-product primarily generated during the extraction of soy oil but that is produced in all the processes that need a de-hulling treatment.

Soybean hulls represents the 8% w/w of the seed and are mainly constituted by cellulose (29–51%), hemicellulose (10–25%), lignin (1–18%), pectin (4–30%), proteins (11–15%) (Alemdar & Sain, 2008; Debiagi et al., 2020; Ferrer et al., 2016; Flauzino Neto et al., 2013; Merci et al., 2015). Due to their composition, soy hulls are widely used in animal feed as source of fibres in replacement of corn. However, they find applications also in human dietary fibres, in medical field or in bio refineries to be converted in fuels/chemicals building blocks (Figure 1.5) (Liu et al., 2017; Singh & Krishnaswamy, 2022). Being a lignocellulosic biomass, soy hulls can be employed as a source of carbon for micro-mesoporous adsorbents but also as source of polysaccharides and cellulose that can be applied in many technological field as

food packaging, food, medicine or bioremediation (Liu et al., 2017; Singh & Krishnaswamy, 2022; Tummino et al., 2020).

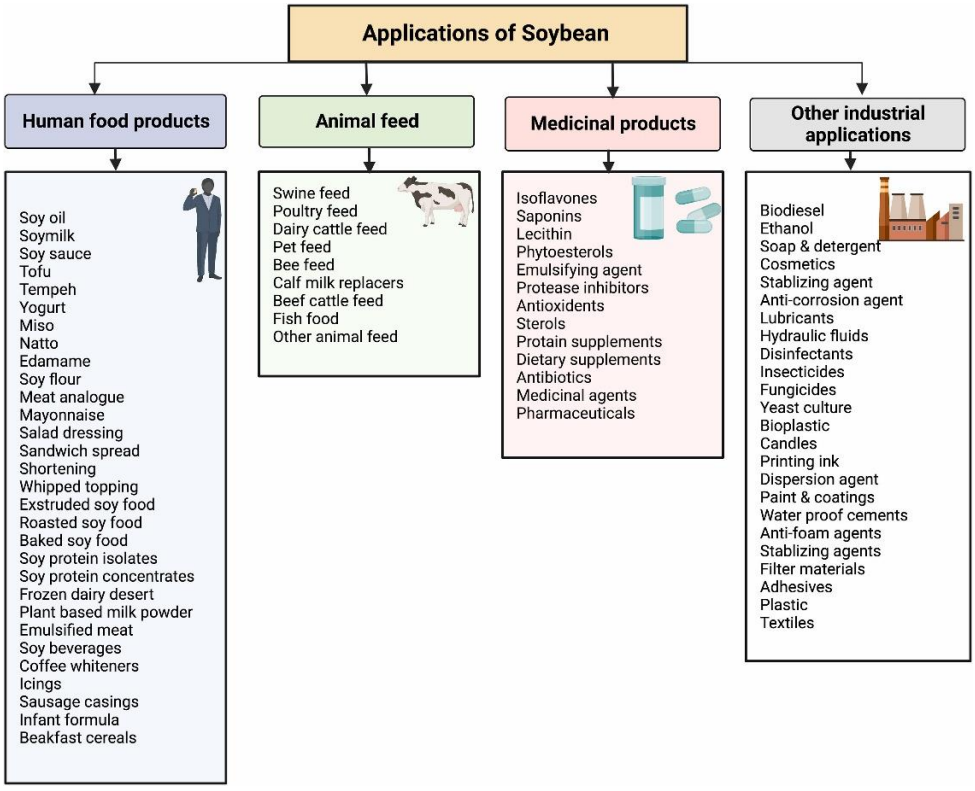

Figure 1.4 - Application of soybean for different human food, animal feed, pharmaceuticals, and other industrial purposes (Singh & Krishnaswamy, 2022)

Moreover, soy hulls have been widely applied as a source of proteins and enzymes, among which of particular interest is soybean peroxidase (SBP), a glycoprotein belonging to class III of the plant peroxidase superfamily.

Its catalytic cycle is activated by the presence of hydrogen peroxide and is able to oxidise many substances, including chlorinated phenolic compounds and different dyes (Calza et al., 2016; Husain, 2010; Katheresan et al., 2018; Marchis et al., 2011).

Table 1.1- soy processing by-products valorisation summary

By-product	Generating process	Main characteristics	Valorisation	Reference
Lecithin	Soy oil processing	emulsifying properties	food and pharmaceutical industries	(Singh & Krishnaswamy, 2022)
Soymeal	Soy oil processing	high amount of protein with an improved profile of amino acid, contains also minerals and vitamins	manufacture of plant-based protein, cookies, bread, meat substitutes, and animal feed	(Singh & Krishnaswamy, 2022)
Soy okara	Soymilk, tofu and soy yogurt processing	rich in protein (25%), dietary fiber (50%), lipid (10%), phenolic components, vitamin, and minerals but low in carbohydrates	animal feed, natural fertilizer and plant-based proteins	(Colletti et al., 2020; Su et al., 2013)
Soy-whey	Soymilk, tofu, and fermented soy product processing	Containing carbohydrates, proteins, fats and minerals	coagulants, prebiotics, citric acid, peptides, soy whey drinks, and alcoholic beverages, emulsifiers, cryoprotectants, adhesives, and gelling agents	(Chua & Liu, 2019)
Soy hulls	Soy oil processing and de-hulling treatments	Rich in cellulose (29-51%), hemicellulose (10-25%), lignin (1-18%), pectin (4-30%), proteins (11-15%)	Animal feed, ethanol production, dietary fibres, polysaccharides and bio polymers extraction, wastewater treatments	(Liu et al., 2017; Singh & Krishnaswamy, 2022; Tummino et al., 2020)

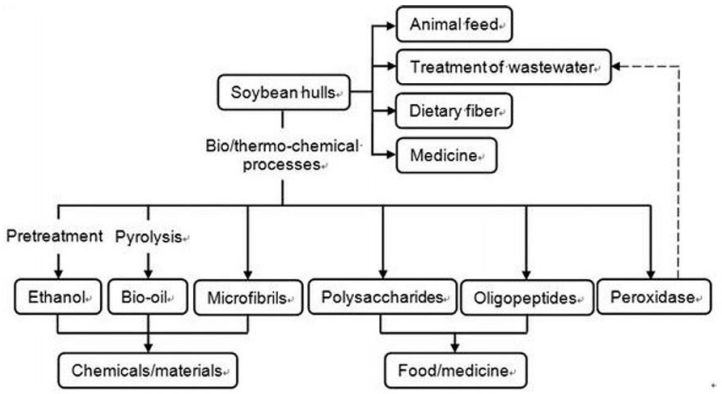

Figure 1.5 - Examples of applications and conversion of soy hulls (Liu et al., 2017)

The active site contains a Fe-heme prosthetic group directly involved in the catalytic cycle. In the resting state, the Fe(III) is coordinated by four nitrogen atoms belonging to heme pyrrolic group and one N-atom of the side chain of an amino acid. The fifth ligand is the nitrogen of the distal histidine while the sixth coordination position is usually free or occupied by a water molecule (Banci, 1997), which is easily substituted by an H_2O_2 molecule. In a typical peroxidase active site, the distal side of the heme is characterized by the presence of one histidine and one arginine residues, which stabilize the coordination with the H_2O_2 molecule and favour the subsequent steps of the catalytic cycle (Faraco et al., 2007; Sugano et al., 1999).

In the presence of organic or inorganic substrates, H_2O_2 oxidizes the Fe(III) to a ferryl (Fe(IV)=O) radical, which can be reduced by inducing two steps of one-electron oxidation of a wide variety of compounds with the production of two molecules of organic or inorganic radicals and water (Battistuzzi et al., 2010) (Figure 1.6).

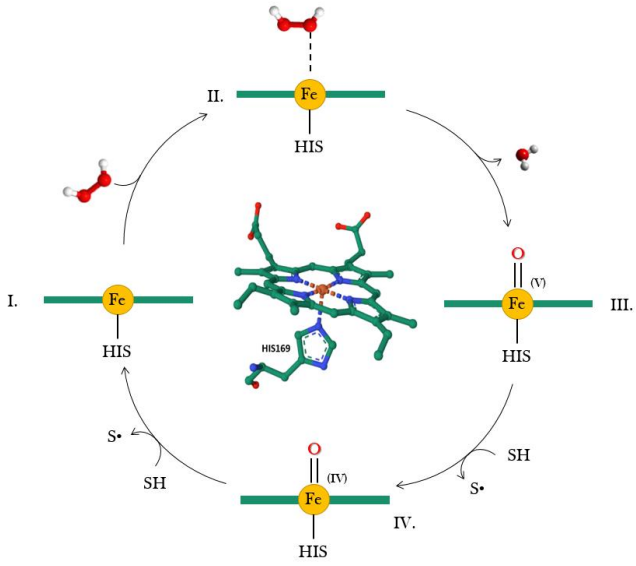

Figure 1.6 - Summary of peroxidase catalytic cycles (HIS = histidine, SH = substrate; S• = radical product) (Rigoletto et al., 2024)

SBP is very interesting not only due to its catalytic potential but also because it maintains its catalytic activity over a wide range of pH and temperature making it exploitable for real water remediation treatments (Rigoletto et al., 2024).

Since hulls cellulose content is considerable, this was also an object of study and valorisation in this thesis work.

Cellulose is an unbranched linear polymer composed of cellobiose repeat units linked by β-(1 → 4)-D-glycosidic bonds. It contains many polar hydroxyl groups, in which the C-6 position is the primary hydroxyl group, and the C-2 and C-3 positions are secondary hydroxyl groups. Through the inter- and intramolecular hydrogen bonds between cellulose molecular chains, the cellulose macromolecular chains in plants are arranged together to form elementary fibrils (Figure 1.7) (Cheng et al., 2023).

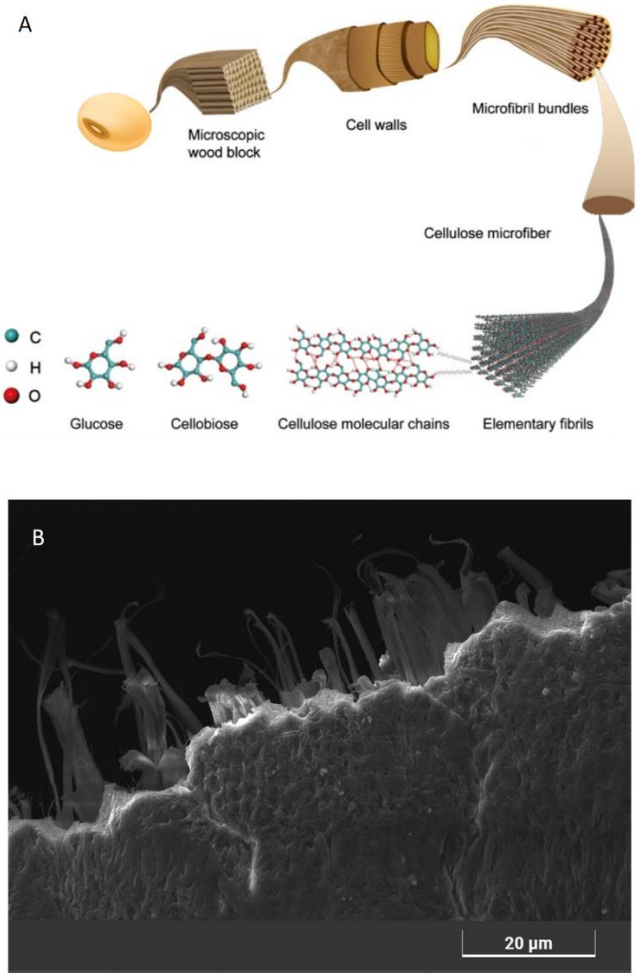

Figure 1.7 – A) Schematic representation of the hierarchical structure of cellulose molecules (modified from (Cheng et al., 2023); B) SEM image of soybean hulls and fibrils (this thesis)

Cellulose has many interesting properties including abundant reserves, degradability and biocompatibility, large specific surface area and thermal stability, adjustable rheological properties, high hydroxyl (–OH) groups content (Cheng et al., 2023).
Due to its large number of active hydroxyl groups, cellulose allows the development of various derivatives with designable properties *via* oxidation, esterification, etherification, grafting, and cross-linking (Credou & Berthelot, 2014; Isogai, 2021; Nemeş et al., 2022).
Its ease of functionalization, as well as affordability and availability, make it an interesting starting point for the development of a wide range of materials which can find applications in different fields, such as food industry, packaging, batteries, drug delivery, cosmetics or water treatments (El Bourakadi et al., 2024).
Moreover, recently the interest in waste-derived cellulose (*i.e.*, derived from agricultural scraps, industrial by-products and even waste textiles) is increasing to lower the environmental impact related to the use of virgin plants (Testa & Tummino, 2021).

1.5 Research-related projects

This research work fell within the framework of "The SusWater Project - Sustainable integrated approach to achieve CECs and PTEs removal from contaminated waters. The aquaculture as case study".
It is a *Research and Innovation Staff Exchange* (RISE) which exploits the complementary skills of participating organizations, as well as other synergies, and enable networking activities, organization of workshops and conferences to facilitate knowledge sharing, the acquisition of new skills and career development for staff members of research and innovation.
It involves a total of nine partners: four European universities (University of Turin - Italy, Politecnico of Turin -Italy, Rey Juan Carlos University - Spain and Aalborg University -Denmark), two non-academic European companies (Società Agricola San Biagio -Italy and Metrohm Hispania - Spain), plus three entities belonging to

third countries including two universities (University of São Paulo - Brazil and Kyushu Institute of Technology - Japan) and a government agency (Department of Science Service - Thailand).

The project aims to face the challenge of safe and clean water availability by applying different levels of actions including the synthesis of green materials for the removal of pollutants, the development of enhanced water treatment technologies, the implementation of effective legal tools against water pollution and the correct management of the present water treatment facilities.

If on the one hand the project focuses on monitoring the water quality of partner aquaculture plants, on the other it aims to develop and test adsorbent materials, photocatalysts and biocatalysts for the removal of emerging contaminants and potentially toxic elements from contaminated water.

1.6 Thesis objectives and development

This research work aims to adopt the circular economy approach in the context of the synthesis and development of cellulose – based materials.

The main goal is to maximise the valorisation of soy processing residue, the hulls, by transforming them into high added value materials exploitable in the environmental remediation sector.

A substantial part of my thesis work focused on the development of strategies for the remediation of water, polluted by emerging contaminants or potentially toxic elements, based on physico-chemical phenomena such as adsorption or enzymatic biocatalysis. Particular attention was paid not only to the initial treatment of the waste, aimed at obtaining the components of greatest interest from the hulls, but also to the synthesis, the reusability and the end of life of the developed materials.

The extraction of SBP and cellulose from soybean hulls has been optimized. Various chemical modifications of cellulose have been carried out to obtaining derivatives which were then characterized and tested for the purification of water contaminated by both organic and inorganic contaminants. Furthermore, part of the work was

dedicated to the study of photocatalysts able to produce hydrogen peroxide under visible light irradiation with the aim of developing self-sustaining systems with the protein.

Finally, regeneration test and biodegradation experiments were also carried out in order to extend the materials' life-time and to close their life cycle by minimizing the impacts.

1.7 References

Abdullah, N., Yusof, N., Lau, W. J., Jaafar, J., & Ismail, A. F. (2019). Recent trends of heavy metal removal from water/wastewater by membrane technologies. *Journal of Industrial and Engineering Chemistry*, *76*, 17–38. https://doi.org/10.1016/j.jiec.2019.03.029

Ahmaruzzaman, Md. (2021). Biochar based nanocomposites for photocatalytic degradation of emerging organic pollutants from water and wastewater. *Materials Research Bulletin*, *140*, 111262. https://doi.org/10.1016/j.materresbull.2021.111262

Alemdar, A., & Sain, M. (2008). Isolation and characterization of nanofibers from agricultural residues – Wheat straw and soy hulls. *Bioresource Technology*, *99*(6), 1664–1671. https://doi.org/10.1016/j.biortech.2007.04.029

Almeida-Naranjo, C. E., Guerrero, V. H., & Villamar-Ayala, C. A. (2023). Emerging Contaminants and Their Removal from Aqueous Media Using Conventional/Non-Conventional Adsorbents: A Glance at the Relationship between Materials, Processes, and Technologies. *Water*, *15*(8), Articolo 8. https://doi.org/10.3390/w15081626

Antoniadou, M., Falara, P. P., & Likodimos, V. (2021). Photocatalytic degradation of pharmaceuticals and organic contaminants of emerging concern using nanotubular structures. *Current Opinion in Green and Sustainable Chemistry*, *29*, 100470. https://doi.org/10.1016/j.cogsc.2021.100470

Banci, L. (1997). Structural properties of peroxidases. *Journal of Biotechnology*, *53*(2), 253–263. https://doi.org/10.1016/S0168-1656(97)01677-5

Battistuzzi, G., Bellei, M., Bortolotti, C. A., & Sola, M. (2010). Redox properties of heme peroxidases. *Archives of Biochemistry and Biophysics*, *500*(1), 21–36. https://doi.org/10.1016/j.abb.2010.03.002

Bilal, M., Adeel, M., Rasheed, T., Zhao, Y., & Iqbal, H. M. N. (2019). Emerging contaminants of high concern and their enzyme-assisted biodegradation – A review.

Environment International, *124*, 336–353. https://doi.org/10.1016/j.envint.2019.01.011

Brandão, M., Lazarevic, D., & Finnveden, G. (2020). *Chapter 38: Prospects for the circular economy and conclusions*. https://www.elgaronline.com/edcollchap/edcoll/9781788972710/9781788972710.00049.xml

Brundtland, G. H. (1987). *Our common future—Report of the World Commission on Environment and Development*. Oxford University Press.

Calza, P., Zacchigna, D., & Laurenti, E. (2016). Degradation of orange dyes and carbamazepine by soybean peroxidase immobilized on silica monoliths and titanium dioxide. *Environmental Science and Pollution Research*, *23*(23), 23742–23749. https://doi.org/10.1007/s11356-016-7399-1

Cheng, W., Zhu, Y., Jiang, G., Cao, K., Zeng, S., Chen, W., Zhao, D., & Yu, H. (2023). Sustainable cellulose and its derivatives for promising biomedical applications. *Progress in Materials Science*, *138*, 101152. https://doi.org/10.1016/j.pmatsci.2023.101152

Chua, J.-Y., & Liu, S.-Q. (2019). Soy whey: More than just wastewater from tofu and soy protein isolate industry. *Trends in Food Science & Technology*, *91*, 24–32. https://doi.org/10.1016/j.tifs.2019.06.016

Colletti, A., Attrovio, A., Boffa, L., Mantegna, S., & Cravotto, G. (2020). Valorisation of By-Products from Soybean (Glycine max (L.) Merr.) Processing. *Molecules*, *25*(9), Articolo 9. https://doi.org/10.3390/molecules25092129

Corvellec, H., Stowell, A. F., & Johansson, N. (2022). Critiques of the circular economy. *Journal of Industrial Ecology*, *26*(2), 421–432. https://doi.org/10.1111/jiec.13187

Credou, J., & Berthelot, T. (2014). Cellulose: From biocompatible to bioactive material. *Journal of Materials Chemistry B*, *2*(30), 4767–4788. https://doi.org/10.1039/C4TB00431K

Cullen, J. M. (2017). Circular Economy: Theoretical Benchmark or Perpetual Motion Machine? *Journal of Industrial Ecology*, *21*(3), 483–486. https://doi.org/10.1111/jiec.12599

de Jesus, A., & Mendonça, S. (2018). Lost in Transition? Drivers and Barriers in the Eco-innovation Road to the Circular Economy. *Ecological Economics*, *145*, 75–89. https://doi.org/10.1016/j.ecolecon.2017.08.001

de Vries, H., Donner, M., & Axelos, M. (2021). A New Conceptual 'Cylinder' Framework for Sustainable Bioeconomy Systems and Their Actors. *Journal of*

Agricultural and Environmental Ethics, *34*(2), 11. https://doi.org/10.1007/s10806-021-09850-7

Debiagi, F., Faria-Tischer, P. C. S., & Mali, S. (2020). Nanofibrillated cellulose obtained from soybean hull using simple and eco-friendly processes based on reactive extrusion. *Cellulose*, *27*(4), 1975–1988. https://doi.org/10.1007/s10570-019-02893-0

Deblonde, T., Cossu-Leguille, C., & Hartemann, P. (2011). Emerging pollutants in wastewater: A review of the literature. *International Journal of Hygiene and Environmental Health*, *214*(6), 442–448. https://doi.org/10.1016/j.ijheh.2011.08.002

Dettori, M., Arghittu, A., Deiana, G., Castiglia, P., & Azara, A. (2022). The revised European Directive 2020/2184 on the quality of water intended for human consumption. A step forward in risk assessment, consumer safety and informative communication. *Environmental Research*, *209*, 112773. https://doi.org/10.1016/j.envres.2022.112773

El Bourakadi, K., Semlali, F.-Z., Hammi, M., & El Achaby, M. (2024). A review on natural cellulose fiber applications: Empowering industry with sustainable solutions. *International Journal of Biological Macromolecules*, *281*, 135773. https://doi.org/10.1016/j.ijbiomac.2024.135773

Ellen MacArthur Fundation. (2021a, febbraio 12). *Explaining the circular economy: Re-thinking progress*. Ellen MacArthur Fundation. https://www.ellenmacarthurfoundation.org/videos/explaining-the-circular-economy-rethink-progress

Ellen MacArthur Fundation. (2021b, febbraio 12). *The butterfly diagram: Visualising the circular economy*. https://www.ellenmacarthurfoundation.org/circular-economy-diagram

Emenike, E. C., Iwuozor, K. O., & Anidiobi, S. U. (2022). Heavy Metal Pollution in Aquaculture: Sources, Impacts and Mitigation Techniques. *Biological Trace Element Research*, *200*(10), 4476–4492. https://doi.org/10.1007/s12011-021-03037-x

European Chemicals Agency. (s.d.). *Registered substances—ECHA*. Recuperato 6 dicembre 2024, da https://echa.europa.eu/it/information-on-chemicals/registered-substances

European Commission. (s.d.). *New Circular Economy Action Plan* [Text]. European Commission - European Commission. Recuperato 5 dicembre 2024, da https://ec.europa.eu/commission/presscorner/detail/en/ip_20_420

European Commission. (2012). *Innovating for sustainable growth :a bioeconomy for Europe*. Publications Office of the European Union. https://data.europa.eu/doi/10.2777/6462

European Commission (A c. Di). (2018). *A sustainable bioeconomy for Europe: Strengthening the connection between economy, society and the environment: updated bioeconomy strategy*. Publications Office. https://doi.org/10.2777/478385

European Parliament. (2023, maggio 24). *Circular economy: Definition, importance and benefits*. Topics | European Parliament. https://www.europarl.europa.eu/topics/en/article/20151201STO05603/circular-economy-definition-importance-and-benefits

European Parliament. (2024, marzo 31). *Water protection and management | Fact Sheets on the European Union | European Parliament*. https://www.europarl.europa.eu/factsheets/en/sheet/74/water-protection-and-management

Faraco, V., Piscitelli, A., Sannia, G., & Giardina, P. (2007). Identification of a new member of the dye-decolorizing peroxidase family from Pleurotus ostreatus. *World Journal of Microbiology and Biotechnology*, *23*(6), 889–893. https://doi.org/10.1007/s11274-006-9303-5

Farooqi, Z. U. R., Hussain, M. M., Ayub, M. A., Qadir, A. A., & Ilic, P. (2022). Chapter 2 - Potentially toxic elements and phytoremediation: Opportunities and challenges. In R. A. Bhat, F. M. P. Tonelli, G. H. Dar, & K. Hakeem (A c. Di), *Phytoremediation* (pp. 19–36). Academic Press. https://doi.org/10.1016/B978-0-323-89874-4.00020-0

Ferrer, A., Salas, C., & Rojas, O. J. (2016). Physical, thermal, chemical and rheological characterization of cellulosic microfibrils and microparticles produced from soybean hulls. *Industrial Crops and Products*, *84*, 337–343. https://doi.org/10.1016/j.indcrop.2016.02.014

Flauzino Neto, W. P., Silvério, H. A., Dantas, N. O., & Pasquini, D. (2013). Extraction and characterization of cellulose nanocrystals from agro-industrial residue – Soy hulls. *Industrial Crops and Products*, *42*, 480–488. https://doi.org/10.1016/j.indcrop.2012.06.041

Flynn, A., & Hacking, N. (2019). Setting standards for a circular economy: A challenge too far for neoliberal environmental governance? *Journal of Cleaner Production*, *212*, 1256–1267. https://doi.org/10.1016/j.jclepro.2018.11.257

Gaggero, E., López-Muñoz, M. J., Paganini, M. C., Arencibia, A., Bertinetti, S., Fernández De Paz, N., & Calza, P. (2023). Mercury and Organic Pollutants Removal from Aqueous Solutions by Heterogeneous Photocatalysis with ZnO-

Based Materials. *Molecules*, *28*(6), 2650. https://doi.org/10.3390/molecules28062650

Garcia-Rodríguez, A., Matamoros, V., Fontàs, C., & Salvadó, V. (2014). The ability of biologically based wastewater treatment systems to remove emerging organic contaminants—A review. *Environmental Science and Pollution Research*, *21*(20), 11708–11728. https://doi.org/10.1007/s11356-013-2448-5

Hassan, S. M. (2013). Soybean, Nutrition and Health. In *Soybean—Bio-Active Compounds*. IntechOpen. https://doi.org/10.5772/54545

Hofmann, F. (2019). Circular business models: Business approach as driver or obstructer of sustainability transitions? *Journal of Cleaner Production*, *224*, 361–374. https://doi.org/10.1016/j.jclepro.2019.03.115

Husain, Q. (2010). Peroxidase mediated decolorization and remediation of wastewater containing industrial dyes: A review. *Reviews in Environmental Science and Bio/Technology*, *9*(2), 117–140. https://doi.org/10.1007/s11157-009-9184-9

Isogai, A. (2021). Emerging Nanocellulose Technologies: Recent Developments. *Advanced Materials*, *33*(28), 2000630. https://doi.org/10.1002/adma.202000630

Katheresan, V., Kansedo, J., & Lau, S. Y. (2018). Efficiency of various recent wastewater dye removal methods: A review. *Journal of Environmental Chemical Engineering*, *6*(4), 4676–4697. https://doi.org/10.1016/j.jece.2018.06.060

Kirchherr, J., Reike, D., & Hekkert, M. (2017). Conceptualizing the circular economy: An analysis of 114 definitions. *Resources, Conservation and Recycling*, *127*, 221–232. https://doi.org/10.1016/j.resconrec.2017.09.005

Korhonen, J., Honkasalo, A., & Seppälä, J. (2018). Circular Economy: The Concept and its Limitations. *Ecological Economics*, *143*, 37–46. https://doi.org/10.1016/j.ecolecon.2017.06.041

Kovacic, Z., Strand, R., & Völker, T. (2019). *The Circular Economy in Europe: Critical Perspectives on Policies and Imaginaries*. Routledge. https://doi.org/10.4324/9780429061028

Kurniawan, T. A., Chan, G. Y. S., Lo, W.-H., & Babel, S. (2006). Physico–chemical treatment techniques for wastewater laden with heavy metals. *Chemical Engineering Journal*, *118*(1), 83–98. https://doi.org/10.1016/j.cej.2006.01.015

Liu, H.-M., Li, H.-Y., Liu, H.-M., & Li, H.-Y. (2017). Application and Conversion of Soybean Hulls. In *Soybean—The Basis of Yield, Biomass and Productivity*. IntechOpen. https://doi.org/10.5772/66744

Maharana, M., Manna, M., Sardar, M., & Sen, S. (2021). Heavy Metal Removal by Low-Cost Adsorbents. In Inamuddin, M. I. Ahamed, E. Lichtfouse, & A. M. Asiri

(A c. Di), *Green Adsorbents to Remove Metals, Dyes and Boron from Polluted Water* (pp. 245–272). Springer International Publishing. https://doi.org/10.1007/978-3-030-47400-3_10

Manninen, K., Koskela, S., Antikainen, R., Bocken, N., Dahlbo, H., & Aminoff, A. (2018). Do circular economy business models capture intended environmental value propositions? *Journal of Cleaner Production*, *171*, 413–422. https://doi.org/10.1016/j.jclepro.2017.10.003

Marchis, T., Avetta, P., Bianco-Prevot, A., Fabbri, D., Viscardi, G., & Laurenti, E. (2011). Oxidative degradation of Remazol Turquoise Blue G 133 by soybean peroxidase. *Journal of Inorganic Biochemistry*, *105*(2), 321–327. https://doi.org/10.1016/j.jinorgbio.2010.11.009

Meadows, D. H., Meadows, D. L., Randers, J., & Behrens, W. W. (1972). *The Limits to Growth. A Report for the Club of Rome's Project on the Predicament of Mankind*. Universe Books.

Merci, A., Urbano, A., Grossmann, M. V. E., Tischer, C. A., & Mali, S. (2015). Properties of microcrystalline cellulose extracted from soybean hulls by reactive extrusion. *Food Research International*, *73*, 38–43. https://doi.org/10.1016/j.foodres.2015.03.020

Miranda-García, N., Suárez, S., Sánchez, B., Coronado, J. M., Malato, S., & Maldonado, M. I. (2011). Photocatalytic degradation of emerging contaminants in municipal wastewater treatment plant effluents using immobilized TiO2 in a solar pilot plant. *Applied Catalysis B: Environmental*, *103*(3), 294–301. https://doi.org/10.1016/j.apcatb.2011.01.030

Nemeş, N. S., Ardean, C., Davidescu, C. M., Negrea, A., Ciopec, M., Duţeanu, N., Negrea, P., Paul, C., Duda-Seiman, D., & Muntean, D. (2022). Antimicrobial Activity of Cellulose Based Materials. *Polymers*, *14*(4), 735. https://doi.org/10.3390/polym14040735

Parida, V. K., Saidulu, D., Majumder, A., Srivastava, A., Gupta, B., & Gupta, A. K. (2021). Emerging contaminants in wastewater: A critical review on occurrence, existing legislations, risk assessment, and sustainable treatment alternatives. *Journal of Environmental Chemical Engineering*, *9*(5), 105966. https://doi.org/10.1016/j.jece.2021.105966

Qasem, N. A. A., Mohammed, R. H., & Lawal, D. U. (2021). Removal of heavy metal ions from wastewater: A comprehensive and critical review. *Npj Clean Water*, *4*(1), 1–15. https://doi.org/10.1038/s41545-021-00127-0

Qin, P., Wang, T., & Luo, Y. (2022). A review on plant-based proteins from soybean: Health benefits and soy product development. *Journal of Agriculture and Food Research*, *7*, 100265. https://doi.org/10.1016/j.jafr.2021.100265

Rigoletto, M., Calza, P., Gaggero, E., & Laurenti, E. (2022). Hybrid materials for the removal of emerging pollutants in water: Classification, synthesis, and properties. *Chemical Engineering Journal Advances*, *10*, 100252. https://doi.org/10.1016/j.ceja.2022.100252

Rigoletto, M., Laurenti, E., & Tummino, M. L. (2024). An Overview of Environmental Catalysis Mediated by Hydrogen Peroxide. *Catalysts*, *14*(4), 267. https://doi.org/10.3390/catal14040267

Rivera-Utrilla, J., Sánchez-Polo, M., Ferro-García, M. Á., Prados-Joya, G., & Ocampo-Pérez, R. (2013). Pharmaceuticals as emerging contaminants and their removal from water. A review. *Chemosphere*, *93*(7), 1268–1287. https://doi.org/10.1016/j.chemosphere.2013.07.059

Rizzo, G. (2020). The Antioxidant Role of Soy and Soy Foods in Human Health. *Antioxidants*, *9*(7), Articolo 7. https://doi.org/10.3390/antiox9070635

Rotundo, J. L., Marshall, R., McCormick, R., Truong, S. K., Styles, D., Gerde, J. A., Gonzalez-Escobar, E., Carmo-Silva, E., Janes-Bassett, V., Logue, J., Annicchiarico, P., de Visser, C., Dind, A., Dodd, I. C., Dye, L., Long, S. P., Lopes, M. S., Pannecoucque, J., Reckling, M., … Rufino, M. C. (2024). European soybean to benefit people and the environment. *Scientific Reports*, *14*(1), 7612. https://doi.org/10.1038/s41598-024-57522-z

Shahid, M. K., Kashif, A., Fuwad, A., & Choi, Y. (2021). Current advances in treatment technologies for removal of emerging contaminants from water – A critical review. *Coordination Chemistry Reviews*, *442*, 213993. https://doi.org/10.1016/j.ccr.2021.213993

Sharma, S., Kaur, M., Goyal, R., & Gill, B. S. (2014). Physical characteristics and nutritional composition of some new soybean (Glycine max (L.) Merrill) genotypes. *Journal of Food Science and Technology*, *51*(3), 551–557. https://doi.org/10.1007/s13197-011-0517-7

Singh, P., & Krishnaswamy, K. (2022). Sustainable zero-waste processing system for soybeans and soy by-product valorization. *Trends in Food Science & Technology*, *128*, 331–344. https://doi.org/10.1016/j.tifs.2022.08.015

Skene, K. R. (2018). Circles, spirals, pyramids and cubes: Why the circular economy cannot work. *Sustainability Science*, *13*(2), 479–492. https://doi.org/10.1007/s11625-017-0443-3

Stål, H. I., & Corvellec, H. (2018). A decoupling perspective on circular business model implementation: Illustrations from Swedish apparel. *Journal of Cleaner Production*, *171*, 630–643. https://doi.org/10.1016/j.jclepro.2017.09.249

Strungaru, S.-A., Nicoara, M., Teodosiu, C., Baltag, E., Ciobanu, C., & Plavan, G. (2018). Patterns of toxic metals bioaccumulation in a cross-border freshwater

reservoir. *Chemosphere*, *207*, 192–202. https://doi.org/10.1016/j.chemosphere.2018.05.079

Su, S. I. T., Yoshida, C. M. P., Contreras-Castillo, C. J., Quiñones, E. M., & Venturini, A. C. (2013). Okara, a soymilk industry by-product, as a non-meat protein source in reduced fat beef burgers. *Food Science and Technology*, *33*, 52–56. https://doi.org/10.1590/S0101-20612013000500009

Subash, A., Naebe, M., Wang, X., & Kandasubramanian, B. (2023). Biopolymer – A sustainable and efficacious material system for effluent removal. *Journal of Hazardous Materials*, *443*, 130168. https://doi.org/10.1016/j.jhazmat.2022.130168

Sugano, Y., Sasaki, K., & Shoda, M. (1999). cDNA cloning and genetic analysis of a novel decolorizing enzyme, peroxidase gene *dyp* from *Geotrichum candidum* Dec 1. *Journal of Bioscience and Bioengineering*, *87*(4), 411–417. https://doi.org/10.1016/S1389-1723(99)80087-5

Technical Guidance for Deriving Environmental Quality Standards—Guidance Document No. 27 Updated version 2018. (s.d.).

Testa, M. L., & Tummino, M. L. (2021). Lignocellulose Biomass as a Multifunctional Tool for Sustainable Catalysis and Chemicals: An Overview. *Catalysts*, *11*(1), 125. https://doi.org/10.3390/catal11010125

Tummino, M. L., Tolardo, V., Malandrino, M., Sadraei, R., Magnacca, G., & Laurenti, E. (2020). A Way to Close the Loop: Physicochemical and Adsorbing Properties of Soybean Hulls Recovered After Soybean Peroxidase Extraction. *Frontiers in Chemistry*, *8*, 763. https://doi.org/10.3389/fchem.2020.00763

United Nations. (2015). *Transforming our world: The 2030 Agenda for Sustainable Development | Department of Economic and Social Affairs*. https://sdgs.un.org/2030agenda

Valenzuela, F., & Böhm, S. (2017). *Against wasted politics: A critique of the circular economy*.

Velasco-Muñoz, J. F., Aznar-Sánchez, J. A., López-Felices, B., & Román-Sánchez, I. M. (2022). Circular economy in agriculture. An analysis of the state of research based on the life cycle. *Sustainable Production and Consumption*, *34*, 257–270. https://doi.org/10.1016/j.spc.2022.09.017

Velasco-Muñoz, J. F., Mendoza, J. M. F., Aznar-Sánchez, J. A., & Gallego-Schmid, A. (2021). Circular economy implementation in the agricultural sector: Definition, strategies and indicators. *Resources, Conservation and Recycling*, *170*, 105618. https://doi.org/10.1016/j.resconrec.2021.105618

Wang, B., Zhang, H., Wang, F., Xiong, X., Tian, K., Sun, Y., & Yu, T. (2019). Application of Heterogeneous Catalytic Ozonation for Refractory Organics in Wastewater. *Catalysts*, *9*(3), Articolo 3. https://doi.org/10.3390/catal9030241

Winans, K., Kendall, A., & Deng, H. (2017). The history and current applications of the circular economy concept. *Renewable and Sustainable Energy Reviews*, *68*, 825–833. https://doi.org/10.1016/j.rser.2016.09.123

World Health Organization. (2019). *Progress on household drinking water, sanitation and hygiene 2000–2017: Special focus on inequalities*. https://www.who.int/publications/i/item/9789241516235

Zacharias, I., Liakou, P., & Biliani, I. (2020). A Review of the Status of Surface European Waters Twenty Years after WFD Introduction. *Environmental Processes*, *7*(4), 1023–1039. https://doi.org/10.1007/s40710-020-00458-z

2 Valorisation of soybean hulls

As mentioned in the introductory section, part of the research dealing with the challenge of resolving the contamination of water bodies has turned its attention to materials of natural origin. Furthermore, if possible, the use of virgin raw materials is avoided, preferring to recover waste and by-products from other industrial processes. This is not only due to the great availability of waste, especially in some sectors such as the agro-industrial one, but also because the circular economy approach is becoming increasingly widespread, also driven by the mentioned above policies promoted by the European Union.

Mitigating the impact of decontamination strategies is one of the challenges we are trying to respond to, not only by switching some materials from waste to resources but also by developing new materials from waste, capable of being used multiple times while maintaining high efficiency.

As explained previously, in this research work we focused on maximizing the valorisation of soybean hulls, a residue from soybean industrial processing, aiming at two of the components of main interest: soybean peroxidase (SBP) and cellulose.

SBP is well known for its ability to oxidise many substances, including chlorinated phenolic compounds and different dyes (Calza et al., 2016; Husain, 2010; Katheresan et al., 2018; Marchis et al., 2011) and, for this reason, it has been used in several studies on water remediation. However, despite the very high added value of this enzyme, it must be considered that SBP represents only a negligible percentage of hulls mass, which are mainly composed of other biopolymers: cellulose, hemicellulose and lignin (Alemdar & Sain, 2008).

In particular, since cellulose is a significant component of the hulls (29-51% w/w), its isolation after the SBP extraction can be considered an efficient way of waste biomass valorisation. Indeed, this biopolymer can find a high number of applications given its availability and ease of chemical modifications. Cellulose derivatives are studied for the development of innovative materials to be used in the environmental field and, among the other, the possibility to insert new functionalities into its structure making cellulose efficient for the removal of specific contaminants from

water (D. Wang, 2019) or suitable as support for enzyme immobilization(Y. Liu & Chen, 2016; Sulaiman et al., 2015; F. Zhang et al., 2022).
In the further section SBP extraction and purification and cellulose isolation and characterization will be deeply discussed.

2.1 Isolation of soybean peroxidase (SBP)

2.1.1 Materials and methods

All chemical reagents are in analytical grade and used without purification. Fresh yellow soybean (*Glycine max*) seeds were purchased by Del Prete s.r.l. (Fondi, LT, Italy) and stored vacuum-packed at room temperature before use.

Soybean extraction and purification

Soybean peroxidase (SBP) was extracted from fresh soybean hulls and successively purified following a previously optimized method (Calza et al., 2016), which can be summarised in 5 steps:

i) SBP extractions in phosphate buffer: hulls were manually separated by seeds, added to a proper volume of buffer (500-700 mL, 0.025 M, pH 7) and subjected to a subsequent three-hours extractions under stirring. The extraction in buffer was repeated three times to complete the procedure.

ii) SBP concentration and precipitation: all the enzyme containing solutions were combined and concentrated by a Vivaflow 50 tangential filter (Sartorius, 30000 MWCO). Then, SBP was precipitated by addition of ammonium sulphate (53 g/100 mL), and the mixture was left under stirring for one night at 4 °C. This step is necessary to facilitate the separation of non-protein components, avoid enzyme denaturation and to guarantee its conservation until successive purification steps.

iii) SBP recover and dialysis: the precipitate was centrifuged for 20 min at 4000 rpm and dissolved in a proper amount of phosphate buffer (0.025 M, pH 7). The resulting solution was then dialyzed for 24 h at 4 °C against the same buffer.

iv) SBP purification: the SBP was purified from the other proteins and peptides by ionic exchange chromatography using a DEAE-Sepharose CL-6B resin as stationary phase and a KCl gradient (0–0.5 M in phosphate buffer 0.025 M, pH 7) as elution phase. The collected fractions were analysed with a Thermospectronic UNICAM UV-300 dual-beam spectrophotometer and the absorbance values at 280 and 403 nm were used to select the fractions containing SBP.

v) SBP concentration and storage: the selected fractions were pooled and concentrated by ultrafiltration on Vivaspin 20 (Sartorius, 10000 MWCO) until their concentration was approximately 0.1 mM. The final SBP sample was then stored frozen at −12 °C until use.

Before storage, each enzyme batch was characterized by UV-Vis spectroscopy for the evaluation of concentration, purity level and activity.

The SBP final concentration was calculated through the Lambert Beer law selecting the absorbance value at 403 nm wavelength and by using 94600 $M^{-1}cm^{-1}$ as value of molar extinction coefficient (Kamal & Behere, 2002). The purity level was obtained by the same data and expressed through the Reinheitszahl index (Rz, equation 2.1):

$$R_z = \frac{A_{403}}{A_{280}} \qquad (2.1)$$

where A_{403} and A_{280} are the absorbance values at 403 and 280 nm respectively. According to literature on peroxidases (Dunford, 1999), an Rz higher than 2 suggest a good enzyme purity level.

The enzymatic activity was evaluated through a kinetic test based on the formation of a purple adduct between 4-(dimethylamino)benzoic acid (DMAB) and 3-methyl-2-benzothiazolinonehydrazone (MBTH) catalysed by SBP in the presence of H_2O_2 (Ngo & Lenhoff, 1980). The activity is expressed as the variation of the absorbance at 590 nm as a function of time (Tolardo et al., 2019).

2.1.2 Results and discussion

SBP extraction and purification procedure has been previously optimized (Calza et al., 2016). During my PhD, this procedure was used to obtain several samples of SBP to be used in all the studies described in this elaborate. Hence, the most important characterization results obtained on SBP samples will be summarized taking into account also the previous studies.

Three main parameters can be evaluated to understand the efficiency of the process: *i)* SBP concentration; *ii)* SBP purity and *iii)* SBP activity.

Employing the described optimized procedure, an average enzyme's concentration of $5\pm2\times10^{-5}$ M can be obtained with Rz values around 0.5. Although it shows a limited purity, its activity is still such as to guarantee a high efficiency in environmental applications already studied (Costa et al., 2020; Lavagna et al., 2021; Sarro et al., 2018; Tolardo et al., 2019). Indeed, the average activity value for the extracted SBP was found to be around the 70% of that of the commercial sample used as reference. Furthermore, as known from the literature, the extracted enzyme has a maximum activity at pH 5 although it is still active between pH 3.5 and 8.5. Therefore, since the typical values of natural waters fall within this pH range, SBP is considered an excellent candidate for the remediation of aquatic systems.

2.2 Multi-hydrolysis cellulose isolation from residual soybean hulls

After SBP extraction, the hulls were recovered, dried at 60 °C and grinded before being treated for cellulose isolation. As known from the literature, the fractionation of lignocellulosic biomass can be achieved through both alkaline and acid hydrolysis of existing bonds binding cellulose, hemicellulose and lignin (Figure 2.1).

In alkaline enviroment the fibers swell beacause of the break-up of the hydrogen bonds between the cellulose chains, furthermore the cleavage of the bonds within hemicellulose and lignin occurs. On the other hand, acid treatments ensure, among other things, hemicellulose solubilisation and depolymerization. The combination of

all these effects leads to the release of the cellulosic components (Alemdar & Sain, 2008).

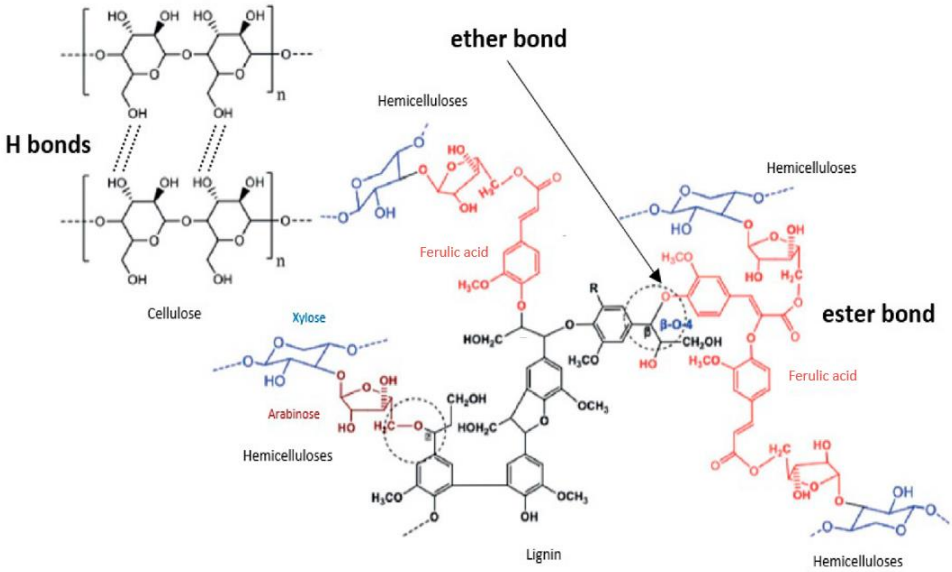

Figure 2.1 – Links between lignocellulosic components (Oriez et al., 2020)

2.2.1 Materials and methods

The biomass resulting from extraction of SBP was treated with a 2% w/v sodium hydroxide solution (solid-liquid ratio 1:10) for 2 h at 80 °C, then washed with distilled water up to reach a neutral pH value and dried at 60 °C. Successively, the pre-treated pulp was subjected to acid hydrolysis by reaction with 1 M HCl (solid-liquid ratio 1:10) at 80 °C for 2 h. At the end of the reaction, the solid was washed with distilled water up to a neutral pH and dried at 60 °C. Finally, the pulp was treated once again with 2% w/v NaOH solution (solid-liquid ratio 1:10), washed and dried again to obtain the final product (Dodero et al., 2019; Tolardo et al., 2019).

The sample morphology was investigated with a FESEM Tescan S9000G instrument with a Schottky emission source, while attenuated total reflectance Fourier transform infrared (ATR-FTIR) spectrum was recorded using a Spectrum Two UATR (PerkinElmer) instrument in the range 4000-600 cm^{-1}.

The dried sample was fractionated into its constituents by using different solvent according to the NREL methodology (Calcio Gaudino et al., 2022; Genevini et al., 1997).

The isolated cellulose thermal behaviour was investigated by thermogravimetric analysis (TGA) and differential scanning calorimetry (DSC). For TGA analyses (TGA 1 Star System of Mettler Toledo, Schwerzenbach, Switzerland), about 10 mg of sample was heated from room temperature to 100 °C, left at this temperature for 30 min and then heated to 1000 °C at a rate of 10 °C min^{-1} in 30 mL min^{-1} of nitrogen flux. Derivative thermogravimetry (DTG) was used to identify the temperature of maximum mass-loss rates. Differential scanning calorimetry (DSC) was carried out with a DSC calorimeter (Mettler Toledo 821e, Schwerzenbach, Switzerland) calibrated by an indium standard. The calorimeter cell was flushed with 100 ml min^{-1} nitrogen. The run was performed from 30 to 500 °C, at the heating rate of 10 °C min^{-1} and the mass sample was about 5 mg. The data processing was conducted with the STARe Software.

2.2.2 Results and Discussion

Cellulose was isolated by following a conventional chemical method already proven efficient on soybean hulls. The combination of acid and alkali treatments has been successfully employed in the removal of hemicellulose, lignin and minor components from this lignocellulosic biomass (Alemdar & Sain, 2008; Ferrer et al., 2016; Iglesias et al., 2021; Sinclair et al., 2018).

The isolated cellulose was in form of powder with a light brown colour indicating the presence of a small portion of chromophore-rich compounds due to the lack of a bleaching phase, considered unnecessary for the purposes of this research.

Cellulose sample morphology (Figure 2.2-A1 and 2.2-A2) was investigated through electron microscopy. SEM images highlighted its fibrous nature, but regions of well-separated fibres alternate with areas in which clusters of fibres appear to be cemented, probably due to some residues of lignin or hemicellulose (the same ones responsible

for the brownish colour to the powder). As a representative dimensional parameter, the distribution of fibre lengths, fitted by a Gaussian function, displayed a narrower range of lengths for soy-derived cellulose that were shorter than those of the commercial one (Fig 2.2-B1 and 2.2-B2).

Actually, the distribution values are centred at 56 ± 3 μm for commercial cellulose-derived samples and 35 ± 1 μm for soy-derived ones (Tummino et al., 2023).

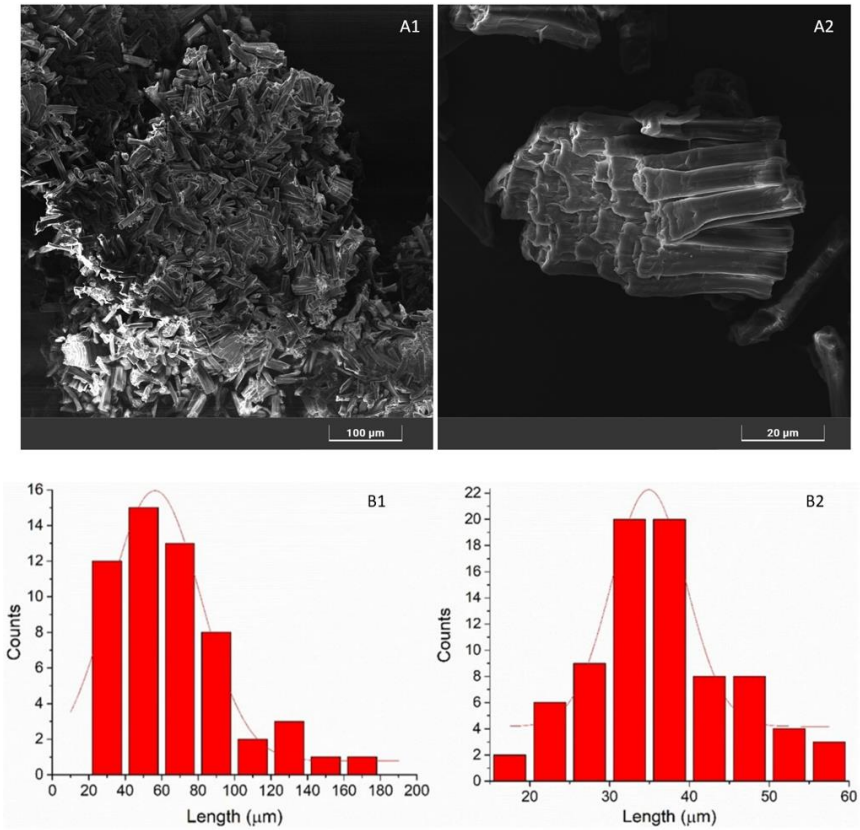

Figure 2.2 – A) soy-derived cellulose SEM images at different magnifications; B) Fibers length distribution: B1) commercial cellulose and B2) soy-derived cellulose (Tummino et al., 2023)

ATR-FTIR measurements mainly showed the typical signals of cellulose (Figure 2.3-A). The signals between 3400 and 3200 cm^{-1} are related to the stretching vibration of OH groups (Tummino et al., 2020), whereas the asymmetric and symmetric stretching vibrations of C-H are visible between 3000 and 2800 cm^{-1}; the absorption band assigned to the bending vibration of adsorbed water could be found at 1640 cm^{-}

[1] while the characteristic signals between 1430-1314 cm^{-1} are attributable to the symmetric bending of CH_2, and the bending vibration of C-O and C-H in the polysaccharide ring. The 1160-1030 cm^{-1} signals are related to the C-O stretching and the C-H rocking vibrations of the pyranose ring skeleton, while the β-glycosidic linkage signal appears at 896 cm^{-1} (Hospodarova et al., 2018; Y. Liu & Kim, 2017; Yang et al., 2017).

Figure 2.3-B shows the percentage composition of the cellulose isolated by the acid-alkaline treatments, confirming what already suggested by the brownish colour of the powder and the morphological analysis. The 88% w/w of the sample is represented by cellulose while the remaining 12% is made up of three components: hemicellulose, proteins, sugars and fulvic acids (5%), lignin (4%) and lipids (3%).

The presence of these impurities is also evident in the results of thermal analyses. Indeed, despite having the same trend, soy-derived cellulose presents a higher residue at 1000°C (12%) in the TGA thermogram (Figure 2.4-A) compared to the commercial cellulose sample (8%) (Tummino et al., 2023). Also in DSC curves (Figure 2.4-B), soy cellulose shows a thermal degradation trend similar to that of commercial cellulose. However, in the 250-300 °C range the curve is not flat showing a first degradation event that can be related to the residual hemicellulose components (Garcia-Maraver et al., 2013; J. Wang et al., 2020).

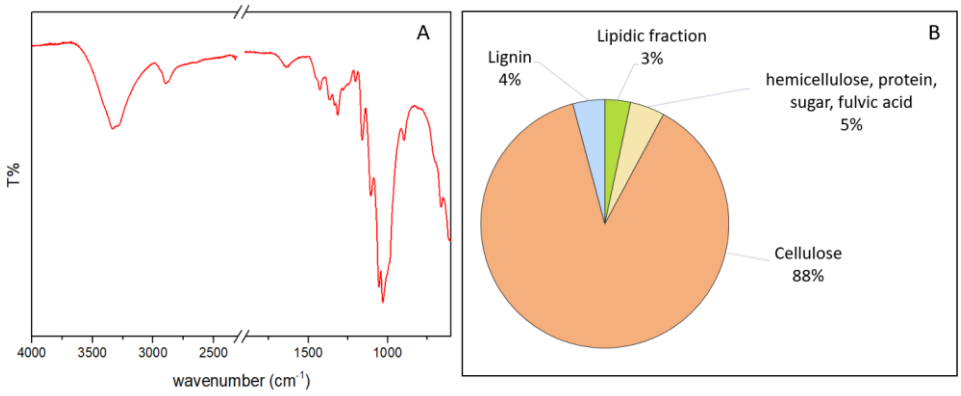

Figure 2.3 – A) ATR-FTIR spectrum of soy-derived cellulose; B) soy-derived cellulose compositions from NREL analysis

Furthermore, also the shift of the principal endothermic peak at higher temperature could be a consequence of the presence of residues of lignin or other compounds rich in aromatic rings. Several studies suggest that this kind of compounds could improve cellulose thermal stability (Garcia-Maraver et al., 2013; Jiang et al., 2019; N. Zhang et al., 2019).

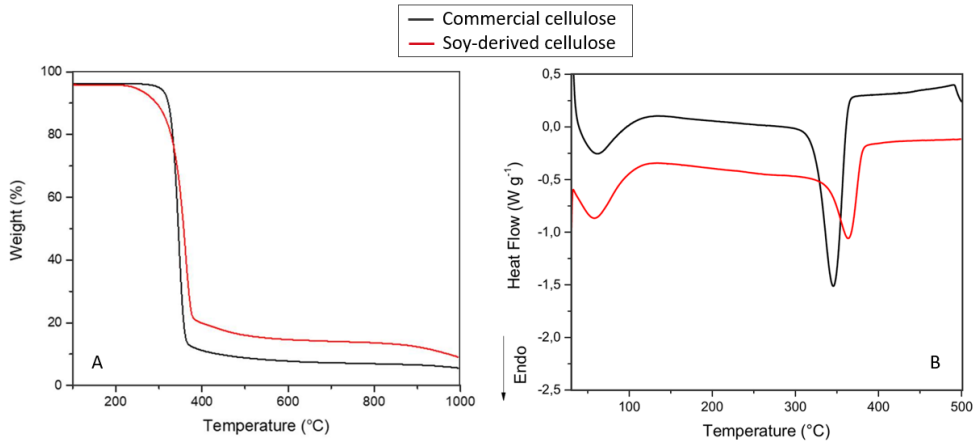

Figure 2.4 – comparison between commercial cellulose (black) and soy-derived cellulose (red): A) TGA thermograms; B) DSC curves.

2.3 Microwave-assisted cellulose isolation from residual soybean hulls

The fractionation of biomass through alkaline and acid hydrolysis has proven effective and the cellulose obtained is of good quality. However, there are critical aspects that need to be reviewed based on the context outlined in the previous chapter. It has been clear for decades that the development of new laboratory or industrial processes and the adaptation of old ones cannot fail to adapt to the growing awareness of the need to reduce environmental and economic impacts. The publication of the twelve principles of Green Chemistry (P. Anastas & Warner, 2000) and the twelve principles of Green Engineering (P. Anastas & Zimmerman, 2003) defined the good practices to be adopted to reach these purposes. What emerges is the attempt to optimize the use of mass, energy, space and time, moving to processes safer for

humans and environment which minimize the production of wastes by using reusable materials and energy from renewable sources.

The safety of reagents and solvents is a central challenge, and more and more often, we try, where possible, to make the choice to fall on water.

Indeed, water is the most environmentally friendly solvent as it is non-flammable, non-toxic and readily available. However, its dielectric properties limit its solvent power to polar molecules only. These properties can be modified in particular temperature and pressure conditions below the critical point (373.946 °C, 22.064 MPa) called subcritical conditions, in which it can be maintained in liquid form even if above the normal boiling point (Freitas et al., 2024).

In general, in the temperature range between 100°C and 374°C, as the temperature rises, the dielectric constant of water ($\varepsilon' = 80$ at 25°C) decreases, reaching values near those of organic solvents and increasing its solvent capacity of low and medium polarity compounds (Freitas et al., 2024; Gallina et al., 2022; J. Zhang et al., 2020).

Increasing the temperature, water viscosity and surface tension decrease steadily, but its diffusivity is improved as well as mass transfer (J. Zhang et al., 2020).

Furthermore, subcritical water has a slightly acid nature thanks to the self-ionization that provides more hydronium ions (H_3O^+) that facilitate acid-catalysed reactions (Okolie et al., 2020; Pattnaik et al., 2022; R.-Y. Zhang et al., 2021).

The interest in subcritical water is growing particularly in the field of biomass valorisation in a bio-refinery concept, in which natural resources and by-products are more comprehensively considered, developing new products and reducing waste disposal (Costa et al., 2023). According to the literature, many studies employed this technique to extract bioactive compounds (Majeed et al., 2024), pectin (Basak & Annapure, 2022), proteins, lipids (Álvarez-Viñas et al., 2021), sugars (Mohd Thani et al., 2020), nutraceuticals and antioxidants from food and herbaceous plants (Costa et al., 2023).

However, there is a limited numer of studies using subcritical water in processes to obtain cellulose from biomass (Gomez-Contreras et al., 2024; Kurian et al., 2015).

The mildly acidic nature of subcritical water selectively hydrolyses hemicelluloses without degrading the cellulosic moieties (Pattnaik et al., 2022). As reported in the literature, during the hydrothermal process, hemicellulose deacetylation occurs, leading to the acetic acid release with a consequent decrease in pH, which can, in turn, catalyse the hydrolysis of hemicelluloses to shorter oligomers and, consequently, decrease their molar mass (Alonso-Riaño et al., 2023; Cocero et al., 2018; Yedro et al., 2017). At the same time, the breaking of ether and ester bonds that bind hemicellulose and lignin takes place, also leading to the release of lignin fraction (Nguyen Thi et al., 2017; Pińkowska et al., 2012). These processes are the same as those that occur during classical acid hydrolysis. As reported in several studies, the acid treatment breaks the disordered and amorphous parts of the cellulose, hydrolyses the hemicelluloses and pectin by breaking down the polysaccharides to simple sugars and hence releasing cellulose fibres (Alemdar & Sain, 2008; Flauzino Neto et al., 2013).

Subcritical conditions can be obtained through a hybrid technique involving rapid microwave (MW) heating under controlled temperature and pressure-sealed vessels in which water is heated above its normal boiling point (Cravotto et al., 2022; Matusiewicz & Ślachciński, 2014). Microwave processing has attracted attention as a green technique since it avoids solvent use, has fast heat transfer because it is produced directly inside the material and reduces reaction time (Aguilar-Reynosa et al., 2017).

Microwaves are electromagnetic energy waves with wavelengths and frequencies ranging from 1 m to 1 mm and 0.3 GHz–300 GHz, respectively (Bayat et al., 2023). Constant changes in electrical fields cause dipoles in polar liquids to undergo continuous alignment and realignment (Bundhoo, 2018). The continuous changes in dipoles generate friction within the material which is heated depending both on the ability of the materials to be polarized by an electric field absorbing and storing energy (*i.e.*, the dielectric constant ε') and the potential to disperse this internal energy as heat (*i.e.*, the dielectric loss ε'') (Qin et al., 2022). The relationship between these

two parameters is called dissipation factor (or dielectric loss tangent) (equation 2.2) and it is usually used to describe the material capacity to be heated by microwaves.

$$\tan d = \frac{\varepsilon''}{\varepsilon'} \quad (2.2)$$

According to *tan d* values, materials may be conductive (*tan d* < 0), non-conductive (0.1 < *tan d* < 0.5) or dielectric (*tan d* > 0.5). Conductive materials cannot be penetrated by MW because they reflect the incident microwave beam, whereas non-conductive materials are microwave-transparent and dielectric materials adsorb well MW and are ideal for MW-based treatments (Fia & Amorim, 2023).

Usually, lignocellulosic biomasses have low *tan d*, meaning that they cannot be efficiently heated through microwave irradiation (Fia & Amorim, 2023). Indeed, according to several studies, they are characterized by low-loss dielectric properties resulting in poor MW absorption (Domínguez et al., 2007; Salema et al., 2013, 2017; Wan et al., 2009).

However, even in the dry form, biomass cells can still contain very small amounts of water that acts as a target for microwaves heating as MW selectively heat more polar components creating hotsposts which can results in local expansion or "explosion" (Aguilar-Reynosa et al., 2017; Hu & Wen, 2008; Palav & Seetharaman, 2007).

To enhance biomasses MW absorption capacity and the treatment outcomes, the addition of a microwaves absorbing solution (solvent solutions) is needed (Ethaib, 2024). Solvents with high dielectric constant and dielectric loss, like water, are the most suitable.

Subcritical water treatments are generally used as biomass pre-treatments capable of altering or modifying the lignocellulosic matrix in such a way as to provide easier access to chemical reagents or enzymes for subsequent hydrolysis (Ethaib, 2024; Sarker et al., 2021). Among the treatments that can be coupled with extraction in subcritical water, the alkaline ones are widely employed. Indeed, at high pH, lignocellulosic biomasses swell due to the breakdown of intermolecular hydrogen bonds between cellulose and hemicellulose chains. At the same time, alkali-labile linkages between lignin monomers or lignin and hemicellulose, as esters, are broken (Oriez et al., 2020; Singh et al., 2017). The breaking of these bonds leads to the

fractionation of lignocellulosic biomass in its main components which can therefore be recovered and valorised.

In further paragraphs, the isolation of cellulose from soybean hulls previously deprived of the soybean peroxidase was optimized. Different conditions of microwave-assisted subcritical water hulls fractionation were studied. The obtained solid residues have been characterized and the need to add an alkaline treatment for further purification was evaluated.

2.3.1 Materials and methods

All the reagents were used without purification.

Fresh yellow soybean (*Glycine max*) seeds were purchased by Del Prete s.r.l. (Fondi, LT, Italy). Sodium hydroxide (NaOH), gallic acid, sodium carbonate (Na_2CO_3) and Folin–Ciocalteu reagent were purchased by Sigma Aldrich.

Microwave-assisted subcritical water extraction (MW-SWE) experiments

Soybean hulls employed for cellulose isolation were previously subjected to SBP extraction, dried and grinded.

Then, the hulls were mixed with distilled water at a 1:10 solid-liquid ratio in a Teflon vessel, left to moisturize for 5 minutes and introduced in a MW multimodal reactor (SynthWAVE, Milestone, Bergamo, Italy) able to exploit an external inert gas feeding (N_2). For each test, an appropriate purging with N_2 was performed three times to remove oxygen traces from the system, reducing oxidative stress on the biomass. The reaction chamber was then pressurized with the necessary amount of N_2 to avoid water ebullition (20 bars). The samples were heated at different temperatures (150, 180 and 200 °C) with a maximum irradiation power of 1500 W. The temperature was increased through a 10-minute ramp and maintained constant for a further time of 10 minutes under stirring.

The resulting solutions were filtered under vacuum, while thoroughly washing the biomass with distilled water. Both the liquid and the washed biomass were freeze-

dried (LyoQuest-85, Telstar, Madrid, Spain), weighed, and stored at 4 °C for further analyses.

The extraction results (Biomass%, Extract% and Loss%) are calculated through equations 2.3, 2.4, and 2.5 respectively.

$$Biomass\ \% = \frac{biomass\ after\ MW{-}SWE\ (g)}{biomass\ before\ MW{-}SWE\ (g)} \times 100 \quad (2.3)$$

$$Extract\ \% = \frac{freeze{-}dried\ extract\ (g)}{biomass\ before\ MW{-}SWE\ (g)} \times 100 \quad (2.4)$$

$$Loss\ \% = \frac{(Theoretical\ recovery\ (g)) - (biomass\ after\ MW{-}SWE\ (g))}{Theoretical\ recovery\ (g)} \times 100 \quad (2.5)$$

The theoretical recovery could be calculated by the difference between the total mass of the sample before MW-SWE treatment and the mass of the freeze-dried MW-SWE extract.

Microwave-assisted alkaline (MW-NaOH) treatment

The freeze-dried biomasses were also subjected to a microwave-assisted alkaline treatment to remove any residues of hemicellulose and lignin.

A proper amount of biomass was mixed with a NaOH solution (10% w/w) at a 1:20 solid-liquid ratio in a Teflon vessel and then introduced in the MW multimodal reactor. For this treatment, the samples were heated at 120 °C with a maximum irradiation power of 1500 W. The temperature was increased through a 10 minutes' ramp and maintained constant for 120 minutes under stirring.

The resulting solutions were filtered under a vacuum, neutralized and freeze-dried. The biomass was washed, as well, and neutralized before freeze-drying and storage.

Biomass characterization

Morphological investigations were performed using an EVO 10 Scanning Electron Microscope (SEM, Carl Zeiss AG, Oberkochen, Germany) with an acceleration voltage of 20 kV. The samples were sputter-coated with a 20 nm-thick gold layer in

rarefied argon, using a Quorum Q150R ES Plus Sputter Coater. Attenuated total reflectance Fourier transform infrared (ATR-FTIR) spectrum was recorded using a Spectrum Two UATR (PerkinElmer) instrument in the range 4000-600 cm^{-1}.

The dried samples were fractionated into their constituents by using different solvents according to the NREL methodology (Appendix I).

The isolated biomasses' thermal behaviour was investigated by thermogravimetric analysis (TGA) and differential scanning calorimetry (DSC). For TGA analyses (TGA 1 Star System of Mettler Toledo, Schwerzenbach, Switzerland), about 10 mg of sample was heated from room temperature to 100 °C, left at this temperature for 30 min and then heated to 1000 °C at a rate of 10 °C/min in 30 mL/min of nitrogen flux. Differential scanning calorimetry (DSC) was carried out with a DSC calorimeter (Mettler Toledo 821e, Schwerzenbach, Switzerland) calibrated by an indium standard. The calorimeter cell was flushed with 100 mL/min nitrogen. The run was performed from 30 to 500 °C, at the heating rate of 10 °C/min and the mass sample was about 5 mg. Data processing was conducted using STARe Software.

Total Phenolic Content (TPC)–Folin-Ciocalteu Assay

The TPC of freeze-dried liquid fraction deriving from the MW-SWE treatment was determined using the Folin–Ciocalteu assay, as described by Cravotto and co-workers (Cravotto et al., 2022). In brief, polyphenol quantification was performed by applying a calibration curve of gallic acid as a reference compound (with dilutions between 5 and 250 µg/mL) in aqueous solutions. Dried extracts were dissolved in deionized water at concentrations of 4–6 mg/mL. Both gallic acid and sample solutions (250 µL) were dispensed into borosilicate test tubes. The following solutions were added sequentially for each test: 500 mL of Na_2CO_3 solution (10% w/v), 4 mL of distilled water, and 250 µL of Folin–Ciocalteu reagent (diluted 1:1 with distilled H_2O). The resulting mixtures were vigorously shaken and kept at room temperature for 25 min before the analysis. A Cary 60 UV-Vis spectrophotometer (Agilent Technologies, Santa Clara, CA, USA) was used to read the absorption at 740 nm in a quartz cuvette (1 cm). The TPC was expressed as mg/g of gallic acid equivalents (GAE) over the

dried extract (selectivity) and over the dried matrix (yield). The measurements were performed in triplicate.

2.3.2 Results and discussion

Microwave-assisted subcritical water extraction: samples characterization

After MW-SWE treatments, three samples of dried biomasses have been obtained depending on the extraction temperature: MW-SWE-150, MW-SWE-180 and MW-SWE-200. As emerges from Figure 2.5, increasing the extraction temperature from 150 to 200°C led to a reduction in the percentage of biomass recovered and an increase in the amount of extract. The increase in biomass loss could be related to a higher formation of low molecular weight and volatile thermal degradation products of biomass during the extraction.

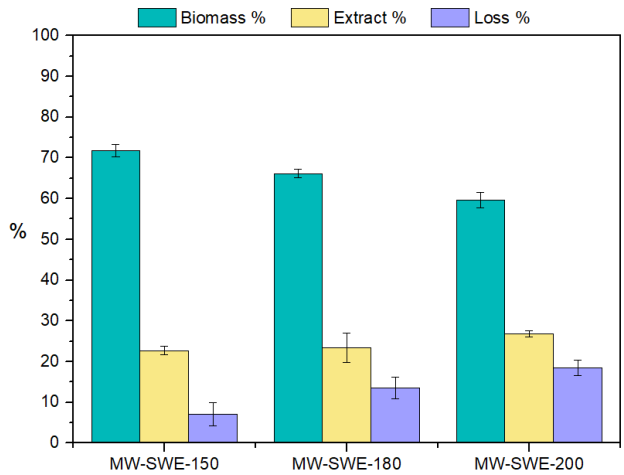

Figure 2.5 – Biomasses and extracts percentage recover after MW-SWE extraction

Each sample of biomass has been subjected to the NREL protocol (Appendix I) to investigate the change in percentage composition induced by subcritical water extraction. To have a complete overview of the samples, also the pristine soybean hulls and the hulls resulting after SBP extraction have been analysed (Figure 2.6).

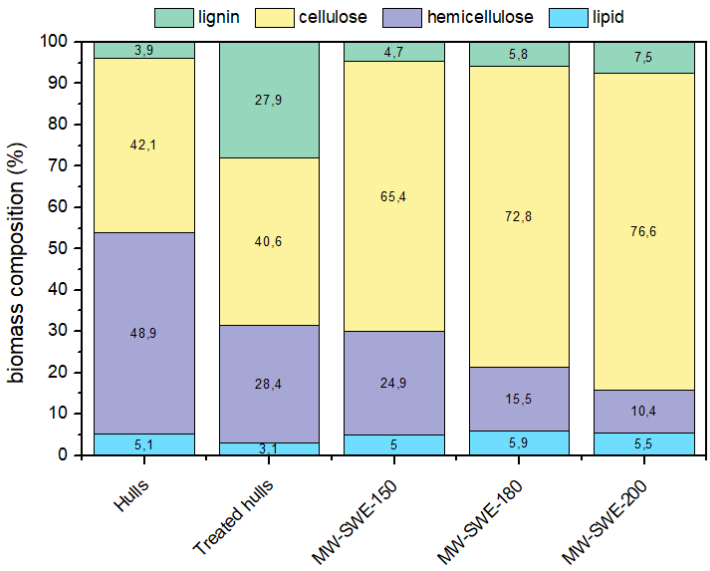

Figure 2.6 – Outcomes of biomasses compositional analysis (NREL) of original soybean hulls and treated soybean hulls before and after MW-SWE treatment normalized for 1 g of biomass

The enzyme's removal treatment reduces the percentage of hemicellulose in the treated hulls with respect to the original biomass without, however, changing the quantity of cellulose that remains around 41% in weight.

The MW-SWE extraction leads to an increase of these percentages in all samples with a growing trend depending on the temperature: 65.4, 72.8 and 76.6% for MW-SWE-150, MW-SWE-180 and MW-SWE-200, respectively. These increases are accompanied by a loss in lignin, which seems comparable in the three treatments, and a loss in hemicellulose, which increases as the extraction temperature increases. This trend has already been observed in the literature (Gil-Guillén et al., 2024; Hanim et al., 2012). According to Yedro and co-workers (Yedro et al., 2017), the extraction kinetics of hemicellulose is strongly dependent on temperature. However, as this parameter and extraction times increase, not only does the carbohydrate solubilisation increase, but also its deacetylation and degradation into oligomers and molecules with lower molecular weight. Hemicellulose deacetylation leads to acetic acid release, which reduces the pH of the solution and catalyses biomass acid hydrolysis (Alonso-

Riaño et al., 2023; Cocero et al., 2018). As described above, this causes the breaking of ether and ester bonds that bind hemicellulose and lignin, leading to the latter fraction release (Nguyen Thi et al., 2017; Pińkowska et al., 2012).

ATR-FTIR and morphological analysis were carried out to investigate the quality of the biomasses. As evidenced in Figure 2.7, the MW-SWE extraction is not sufficient to ensure the complete removal of non-cellulosic components of the pristine biomass. Indeed, in all sample spectra, there are signals not ascribable to cellulose.

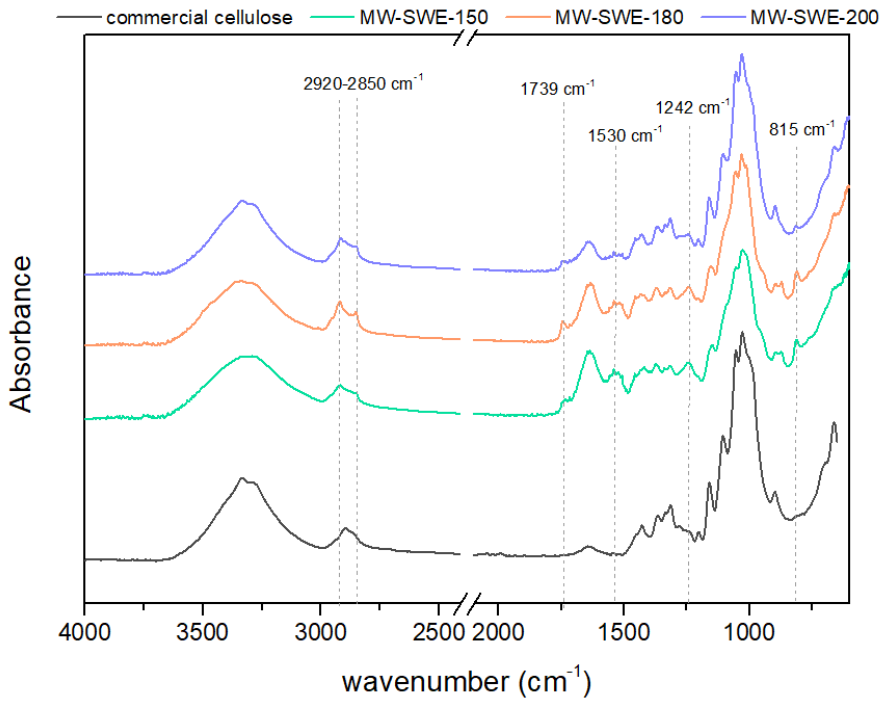

Figure 2.7 – Comparison between ATR-FTIR spectrum of commercial cellulose and spectra of MW-SWE treatments derived biomasses

The presence of bands at 2920-2850 cm^{-1} is one of the main differences. In the literature, there is no single attribution for these signals. According to some authors, they would be ascribable to the asymmetric and symmetric stretching of the methyl and methylene groups that can be found in both lignin (Guo et al., 2008; Li et al., 2017; Md Salim et al., 2021; Meraj et al., 2024) and hemicellulose (Taşar & Özer,

2022). However, some studies also suggest their possible attribution to the extractives' content in the biomass matrix, like methyl esters and phenolic acid methyl esters, which contain methyl and methylene groups (Md Salim et al., 2021; Poletto et al., 2012).

Furthermore, the peaks at 1739 and 1242 cm^{-1} are other evidence of hemicellulose residues. According to the literature, the first is the stretching of C=O present in acetyl and carboxyl hemicellulose functionalities, while the second could be related to the C-O stretching in carboxylic groups (Horikawa et al., 2019; Lionetto et al., 2012; Toscano et al., 2022). On the other hand, the 815 cm^{-1} signal can be ascribable to the out-of-plane vibration of the lignin guaiacyl unit (Boeriu et al., 2004; Horikawa et al., 2019).

The presence of non-cellulosic residues is also evidenced in the SEM images (Figure 2.8). Indeed, in MW-SWE-150 and MW-SWE-180 samples (Fig 2.8-A and C) the fibres are well organized and held together by a coating that is probably made up of hemicellulose and lignin. At the same time, even if there are separate fibres in the MW-SWE-200 sample (Fig. 2.8-E), it is still possible to see more aggregated areas which confirm what was already highlighted by the ATR-FTIR spectra. Figure 2.8-B and D show some fibres that appear "exploded." As previously noted, this could be due to the formation of hot spots and the rapid increase in pressure in preferential points within the biomass during the microwave treatment (Aguilar-Reynosa et al., 2017; Hu & Wen, 2008; Palav & Seetharaman, 2007).

Hemicellulose and lignin residues lead to thermal behaviour different from that of commercial cellulose (Figure 2.9). As shown in Figure 2.9-A, MW-SWE-150 and MW-SWE-180 samples present the onset of thermal degradation at 220°C and 240°C respectively, a lower temperature than pure cellulose (~300°C).

According to the literature, this could be related to the hemicellulose component. Indeed, it begins to decompose earlier than the other components at a temperature of around 160 °C, and weight loss mainly occurs in the temperature range of 200–300 °C (Faleeva et al., 2024).

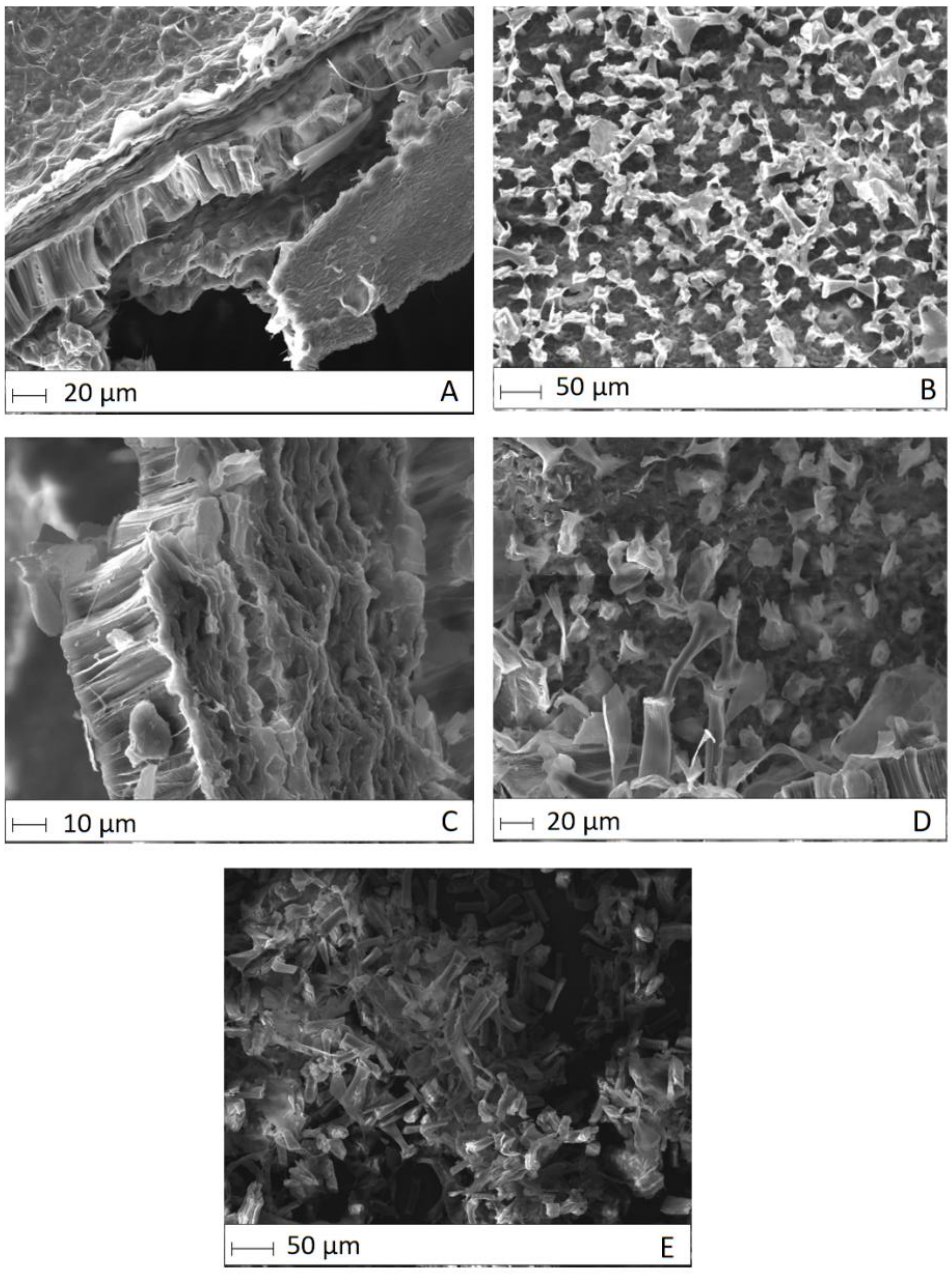

Figure 2.8 - SEM images of MW-SWE-150 (A and B), MW-SWE-180 (C and D) and MW-SWE-200 (E)

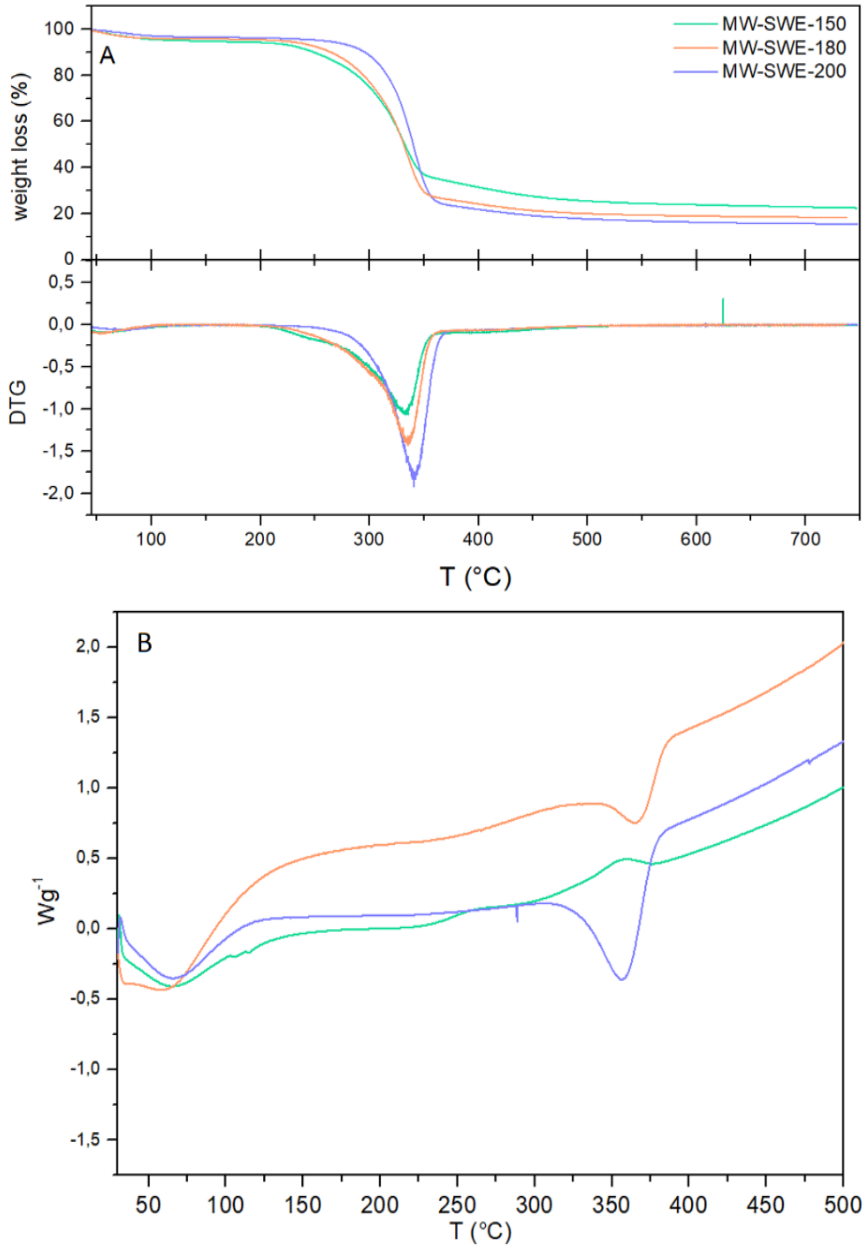

Figure 2.9 – Thermal behaviour of MW-SWE derived biomass: A) TGA and DTG; B) DSC

Two weight loss peaks relating to the thermal decomposition of hemicellulose have been reported in the literature. The first, at 250°C, is due to the cleavage of glycosidic bonds and the decomposition of side chains, while the second, at 290°C, is due to

depolymerization reactions (Collard & Blin, 2014; Faleeva et al., 2024; McCaffrey et al., 2021; Peng & Wu, 2010). In DTG curves (Fig. 2.9-A) of MW-SWE-150 and MW-SWE-180, the main peak presents two shoulders in correspondence to these thermal decomposition temperatures, indicating the presence of hemicellulose residues in the samples.

At the same time, decreasing the subcritical water extraction treatment temperature from 200°C to 150°C, the amount of char at the end of thermo-gravimetric analysis increases (15.6% for MW-SWE-200, 18.3% for MW-SWE-180 and 22.7% for MW-SWE-150). This trend is opposite to the amount of cellulose calculated through NREL analysis, which is higher as treatment temperatures increase. This means that higher TGA final % correspond to higher hemicellulose and lignin content, since these components tend to form more charred residues. Indeed, cellulose thermal degradation occurs mainly through depolymerisation and subsequent degradation reactions that are very fast and have volatile compounds as main products, which are mostly condensable organic compounds (Collard & Blin, 2014). Conversely, even if hemicellulose pyrolysis goes through depolymerisation, it leads to the formation of a greater quantity of char that some authors attribute to the presence of minerals such as potassium (Couhert et al., 2009; Jensen et al., 1998). However, also studies on demineralised hemicellulose show that two or three times more char is formed during its pyrolysis respect to cellulose (Hosoya et al., 2007). This has been attributed to the difference in thermal stability of the monomer units and the linkages between the monomers or in the different crystallinity of the constituents (Alén et al., 1996).

Lignin also significantly influences the amount of char. Indeed, during the thermal degradation, it does not undergo depolymerisation, but still release volatile compounds, which are mainly incondensable gases. This seems to be due to the instability of the propyl chains, of some linkages between monomer units and of the methoxy substituents of the aromatic rings. The final lignin charring process consists of the rearrangement of the carbon-based skeleton in a polycyclic aromatic structure (Cao et al., 2013; Collard & Blin, 2014; Liu et al., 2008).

All our samples show TGA residue percentages higher than commercial cellulose (8%) and soy-derived cellulose obtained following the multi-hydrolysis method described above (12%).

Regarding the DSC curves (Fig. 2.9-B), only MW-SWE-200 shows a pattern comparable to that of commercial cellulose (Fig. 2.4-B) with the endothermic peak at the decomposition temperature of 356°C. MW-SWE-150 does not present any endothermic peak, while MW-SWE-180 shows an intermediate behaviour.

All these findings led to the need to add the alkaline treatment to remove the non-cellulosic components and obtain final samples with a greater enrichment in cellulose.

Microwave-assisted alkaline treatment: samples characterization

After the MW-SWE extraction, all samples were subjected to a microwave-assisted alkaline treatment (MW-NaOH) to complete the removal of non-cellulosic components.

As shown in Figure 2.10, which compares the percentage composition of samples before and after MW-NaOH, the enrichment in cellulose induced by the alkaline treatment is effective, with better results for MW-SWE-180-A (91.5%).

The enrichment in cellulose is mainly due to a reduction in the hemicellulose content. Indeed, in alkaline mediums, cellulose swells and the hydrogen bonds with hemicellulose are destroyed. At the same time, alkali-labile ester bonds between lignin monomers or lignin and hemicellulose, are broken. Both of these mechanisms enhance the dissolution of hemicellulose (Lu et al., 2021; Oriez et al., 2020).

The quality of the cellulose-enriched biomasses has been investigated through ATR-FTIR and morphological analysis.

As shown in Figure 2.11, the ATR-FTIR pattern of all the samples is comparable to that of commercial cellulose, confirming that this component is the main one.

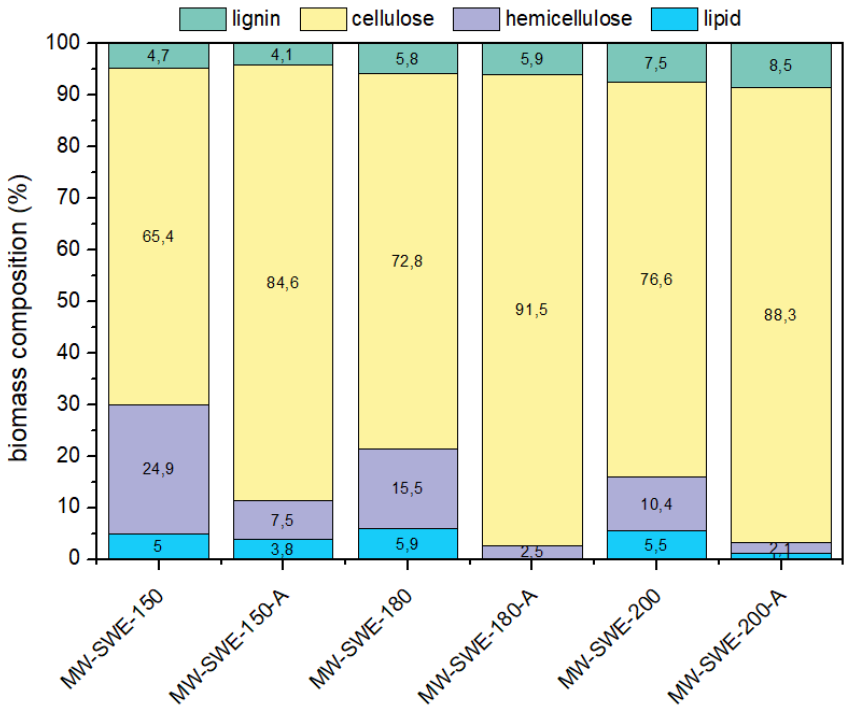

Figure 2.10 – Comparison between outcomes of compositional analysis of MW-SWE biomasses before and after the MW-NaOH treatment

Despite this, the morphological analysis highlighted that for the MW-SWE-150-A sample, even the alkaline treatment was not sufficient to completely separate the fibres (Figure 2.12-A1). On the other hand, MW-SWE-180-A (Fig. 2.12-B1) and MW-SWE-200-A (Fig. 2.12-C1) present a comparable morphology to both the commercial and the cellulose derived from the multi-hydrolysis process described above (Fig. 2.2-A).

Regarding the fibres' dimension (Fig. 2.12-A2, B2 and C2), the final biomasses show an average length between 35 and 40 µm, which is shorter than commercial cellulose (60 µm) fibres but comparable with that of cellulose derived from the multi-hydrolysis process (Fig. 2.2-B2).

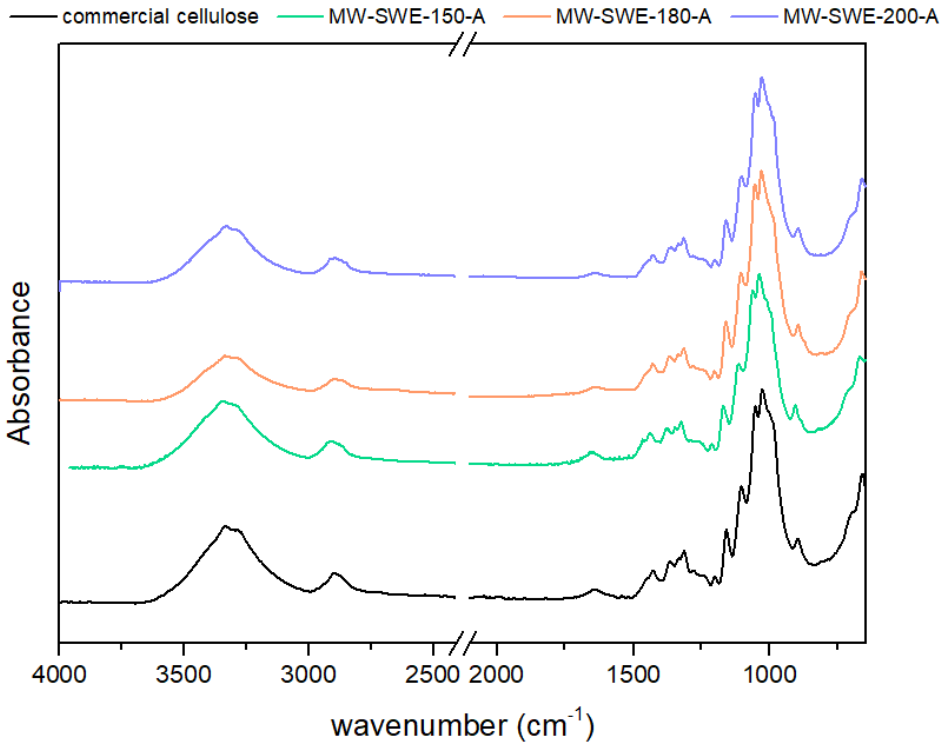

Figure 2.11 – ATR-FTIR of commercial cellulose and post-MW-NaOH treatment biomasses

Figure 2.13 summarizes the final biomasses' thermal behaviour. TGA curves of MW-SWE-150-A (Fig. 2.13-A) show an onset of thermal degradation at 280°C, slightly lower than the other two samples and commercial cellulose.

The lowering of degradation temperature, together with the shoulder of the peak of the main thermal event at 290°C in DTG graph, suggests that limited residues of hemicellulose are still present in the biomass. This is in agreement with both the sample morphology and NREL results. On the other hand, MW-SWE-180-A and MW-SWE-200-A curves are more comparable to that of commercial cellulose, confirming the effectiveness of alkaline treatment.

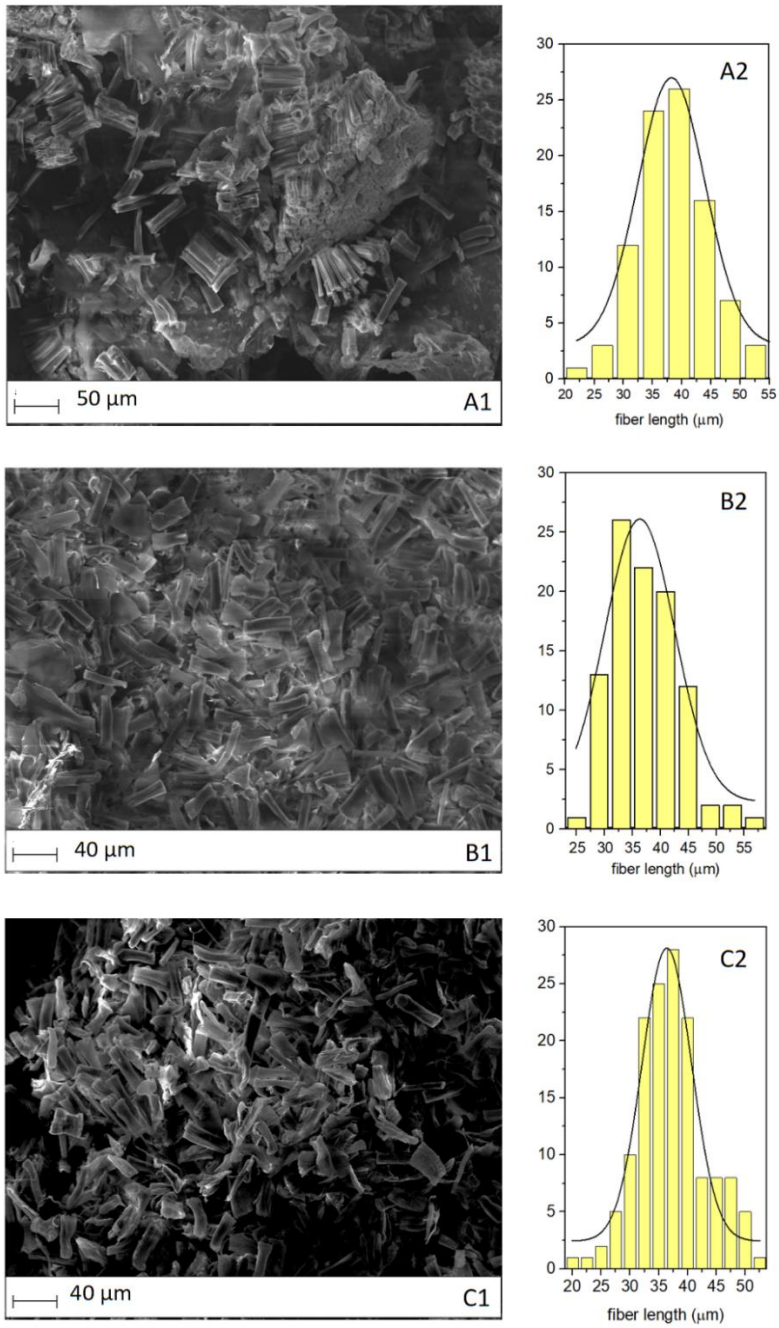

Figure 2.12 – SEM images and fibre length distribution of A) MW-SWE-150-A, B) MW-SWE-180-A and C) MW-SWE-200-A

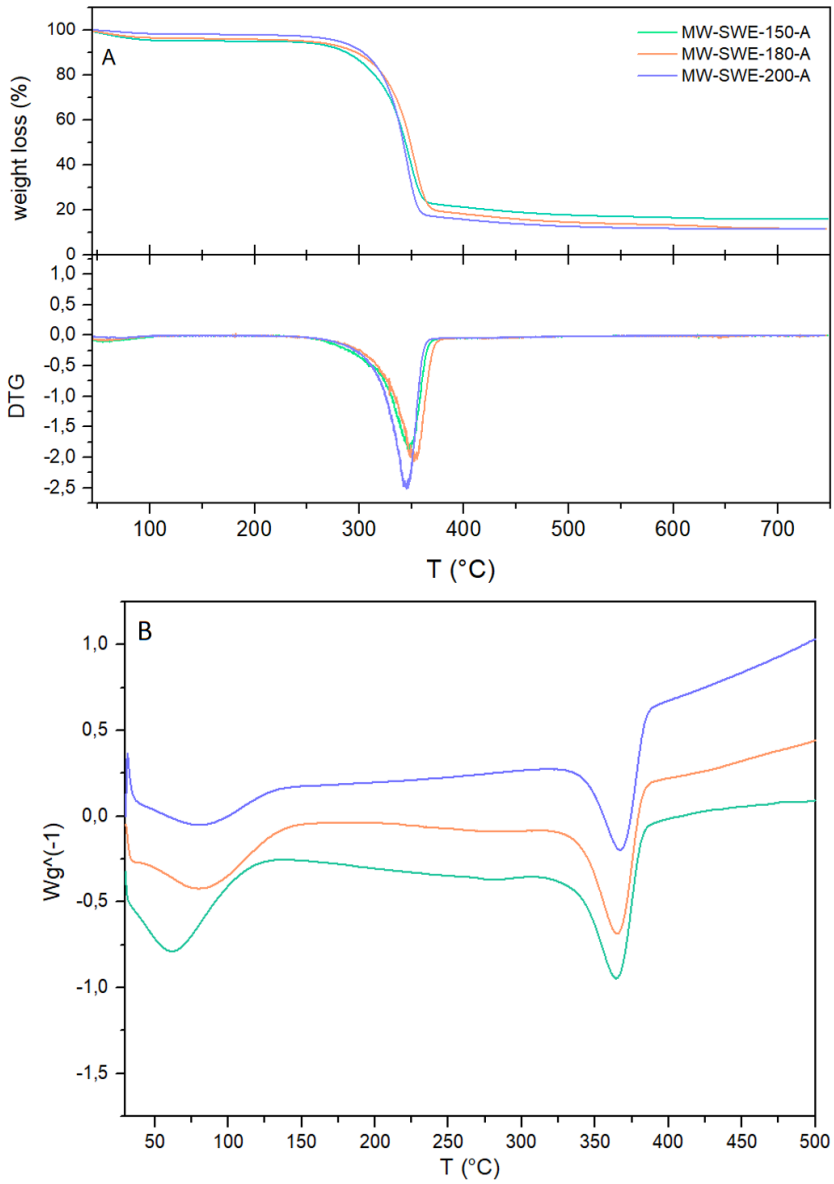

Figure 2.13 - Thermal behaviour of MW-SWE derived biomass after alkaline treatment: A) TGA and DTG; B) DSC

2.4 Soy-derived cellulose functionalization strategies

The great availability of cellulose both from virgin sources and from waste materials, its non-toxicity, low cost and stable structure made this biopolymer extremely interesting in various sectors. However, cellulose as such does not meet all the requirements necessary to be used in all the fields in which it is actually employed since, for example, it is moisture sensitive, insoluble in water and most common solvent, poor in surface functionalities and low resistant to microbial activity (Seddiqi et al., 2021).

Hence, cellulose can be chemically modified introducing functionalizing moieties to obtain materials with multiple and specific activities.

According to the molecular structure of cellulose (Figure 2.14), hydroxyl groups in glucose units are responsible for its chemical activity. Their accessibility and reactivity depend on the degree of involvement in the hydrogen bond network which characterize cellulose three-dimensional structure. The hydrogen of the C3-hydroxyl group binds strongly to the ring oxygen on adjacent anhydroglucose unit (AGU) and so it is not available to react (Credou & Berthelot, 2014). On the other hand, C2 and C6-hydroxyl groups, having multiple and variable hydrogen bonding options, are statistically less involved in the hydrogen bond network with a resulting higher reactivity (Credou & Berthelot, 2014).

Among the three hydroxyl groups in each AGU, the C6-OH group (primary alcohol) is described as the most reactive site, far more than hydroxyl groups at C2- and C3-positions (secondary alcohols) (Roy et al., 2009). Hence, the relative reactivity of the hydroxyl groups can be summarized as C6-OH >> C2-OH > C3-OH.

The accessibility of hydroxyl groups also depends on the crystallinity of cellulose, since chemical reagents can penetrate only the amorphous region and not the crystalline one. For this reason, often activation treatments are needed to allow functionalization reactions (Credou & Berthelot, 2014).

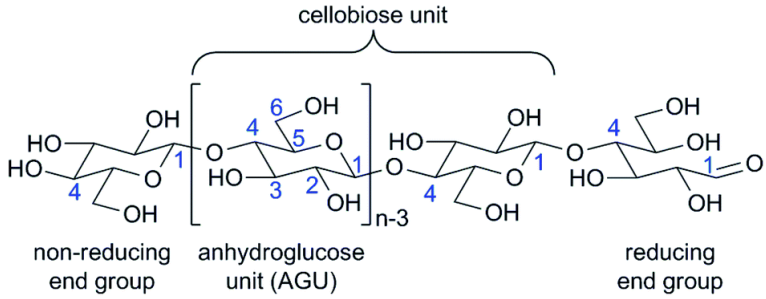

Figure 2.14 - Cellulose molecular structure (n = degree of polymerization) (Credou & Berthelot, 2014)

Typical functionalization reactions exploited in literature are oxidation, amination, esterification, etherification, activation or condensation (Aziz et al., 2022; Credou & Berthelot, 2014; Oberlintner et al., 2021).

A widespread method used to introduce functional groups in cellulose structure is the employment of alkoxysilane reagents (Figure 2.15).

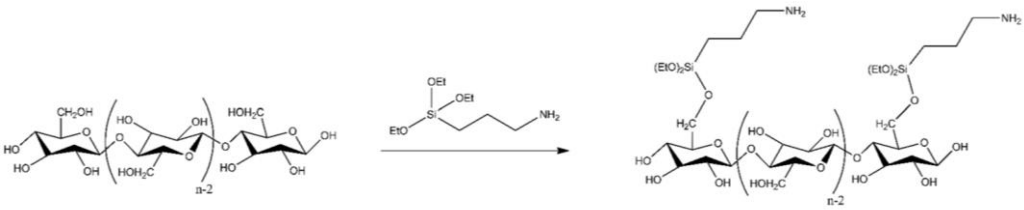

Figure 2.15 – Example of silanization reaction of cellulose with 3-aminopropyltriethoxysilane (Tummino et al., 2023)

For these kind of functionalization low polarity solvent as usually employed as toluene, dimethylformamide (DMF) and tetrahydrofuran (THF) (Habibi, 2014) to prevent the oligomerization of silane derivatives that usually occurs in water-based systems.

Recently, some authors proposed ethanol as good reaction medium for silanization reactions since it avoid oligomerization being at the same time more eco-compatible (Testa, 2021; Testa & La Parola, 2021; Tummino et al., 2023). Nevertheless, there is no shortage of studies in the literature reporting functionalizations in water with promising results (Beaumont et al., 2018; Khanjanzadeh et al., 2018; Ludovici et al., 2023; Z. Zhang et al., 2015).

Cellulose-derivatives obtained through these strategies are insoluble in common solvents, however for several applications soluble biopolymers are needed.

Among them, carboxymethylcellulose (CMC) represents a widely employed choice. It is an ether prepared from the replacement of a hydroxyl group with a carboxymethyl one at positions O-2, O-3, or O-6 of the glucose unit of a previously alkali swelled cellulose (Figure 2.16). It is soluble in hot or cold water and is usually find in anionic form as sodic salt, a characteristic that allows CMC to interact with several organic and inorganic cations. Through these interactions it can easily form hydrogels through cross-linking reaction (W. Zhang et al., 2022) and find applications in several field as textile, food, pharmaceutical, biomedical, materials engineering and water remediation (Rahman et al., 2021).

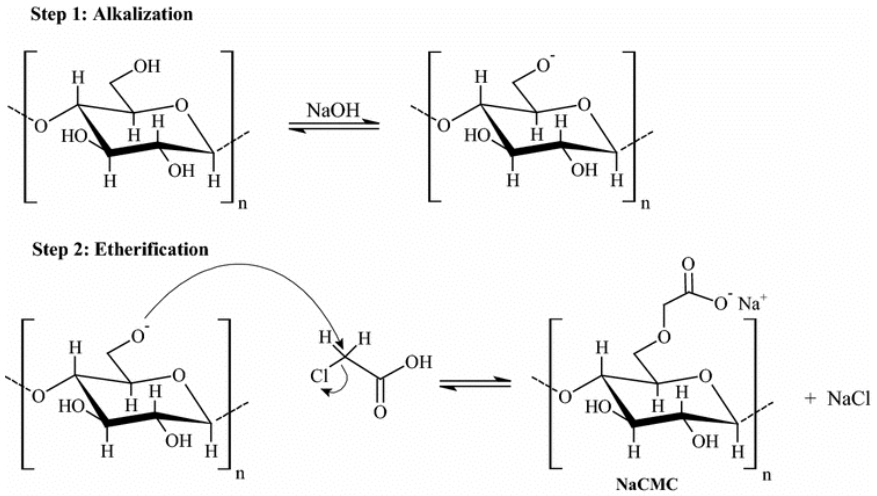

Figure 2.16 – Cellulose carboxymethylation reaction (Yáñez-S et al., 2018)

In this work cellulose isolated from soybean hulls through acid-base hydrolytic process has been functionalized introducing primary amino groups, thiols and carboxymethyl functionalities. All these cellulose-derivatives have been characterized and employed to prepare cellulose-based sorbents for water remediation as described in detail in Chapter 3.

2.4.1 Materials and methods

All chemical reagents were in analytical grade and used without further purification. (3-aminopropyl)triethoxysilane (APTES); (3-mercaptopropyl)trimethoxysilane (MPTMS), chloroacetic acid (CA), isopropyl alcohol, ethanol, and acetone were purchased by Merck, hydrochloric acid (HCl) was purchased by Carlo Erba.

Synthesis of primary amino groups containing cellulose (Cell-NH_2)

For Cell-NH_2 synthesis, an APTES-functionalization method proposed by Tummino et al. (Tummino et al., 2023) was employed with minor modifications. In brief, 1 g of cellulose was dispersed in 20 mL of ethanol and 3 mL of APTES were added. The mixture was then refluxed at room temperature for 24 h under stirring, filtered, washed with distilled water, and dried at 100°C.

Synthesis oh thiols containing cellulose (Cell-SH)

For Cell-SH preparation, the MPTMS-functionalization procedure proposed by Beaumont et al. (Beaumont et al., 2018) was used: 1 g of cellulose was dispersed in 100 mL of distilled water, then 2 mL of HCl 0.5 M and 3.2 mL of MPTMS were added. The mixture was left under stirring for 30 min and then 4 mL of NaOH 0.5 M were added. After stirring 150 min at room temperature, the sample was filtered and washed with acetone and distilled water to remove the unreacted MPTMS, and finally dried.

Synthesis of carboxymethyl cellulose

Carboxymethylcellulose (CMC) was synthesised through the acetylation of cellulose following the method proposed by Robles Barros et al. (Robles Barros et al., 2020) with minor modifications.

This procedure consists of two steps: alkalinisation and etherification. For the first stage, 3 g of cellulose was homogenised in 80 mL of isopropyl alcohol under stirring

for 30 minutes, followed by the addition of 10 mL of 50% NaOH. After 30 minutes of stirring the suspension was heated up to 63°C and 6.3 g of chloroacetic acid were added for the etherification stage. At the end of the reaction (190 min), the modified cellulose was recovered by filtration and washed with 70% ethanol. Finally, CMC was left under stirring in ethanol for 30 minutes, washed again with methanol and dried in an oven at 50°C. The degree of substitution (DS) was evaluated according to the methodology described by Aguir and M'Henni (Aguir & M'Henni, 2006). In brief, 1 g of CMC was mineralized at 600°C for 4h and the obtained ash was cooled to room temperature and dissolved in 25 mL of hot distilled water (80°C). The resulting solution was titrated with 0.1N (0.05M) H_2SO_4 in presence of methyl orange. The reddish solution was heated to remove dissolved CO_2 until it turned yellow. A second titration was performed with H_2SO_4. The DS could be calculated using the equation (2.6)

$$DS = \frac{0.162 \times B}{0.08 \times B} \; ; B \; = 0.1 \times \frac{V}{m} \quad (2.6)$$

where 0.162 is the molar mass of the anhydroglucose unit (AGU) expressed in kg/mol, 0.08 is the molar mass of $-CH_2COO^-Na^+$ group substituted in the cellulose (kg/mol); 0.1 is the normality of sulphuric acid solution; m is the mass (g) of the CMC samples mineralized and V is the total volume (mL) of H_2SO_4 used for the titration.

Cellulose-derivatives characterization

All cellulose-derivatives have been characterized both morphologically and physico-chemically.

The morphology was investigated through electron microscopy analysis. For Cell-NH_2 and Cell-SH a FESEM Tescan S9000G instrument with a Schottky emission source and equipped with the Ultim Max detector (Oxford, UK) for microanalysis was employed; while for CMC sample an EVO10 Scanning Electron Microscope

(SEM, Carl Zeiss Microscopy GmbH) with an acceleration voltage of 20 kV was used. The samples were sputter-coated with a 20 nm-thick gold layer in rarefied argon, using a Quorum SC7620 Sputter Coater.

Attenuated total reflectance Fourier transform infrared (ATR-FTIR) spectra were recorded using a Spectrum Two UATR (PerkinElmer) instrument in the range 4000-600 cm^{-1}.

Elemental analysis (C, N, S, H) was performed on Cell-NH_2 and Cell-SH with a FLASH 2000 instrument equipped with a thermal conductivity detector.

The thermal behaviour of the samples was investigated by thermogravimetric analysis (TGA) and differential scanning calorimetry (DSC). For TGA analyses (Mettler Toledo TGA-DSC 1, Schwerzenbach, Switzerland), the sample (10 mg) was heated from room temperature to 100 °C, left at this temperature for 30 min and then heated to 1000 °C at a rate of 10 °C/min under 30 mL/min of nitrogen flux.

Derivative thermogravimetry (DTG) was used to identify the temperature of maximum mass-loss rates. Differential scanning calorimetry (DSC) was carried out with a DSC equipment (Mettler Toledo 821e, Schwerzenbach, Switzerland) calibrated by an indium standard. The calorimeter cell was flushed with 100 mL/min nitrogen. The run was performed from 30 to 500 °C, at the heating rate of 10 °C/min and the mass sample was about 5 mg. Data processing was conducted using the STARe Software.

The Zeta potential of the Cell-NH_2 and Cell-SH samples was determined using a NanoPlus DLS Zeta Potential from Micromeritics. Aqueous suspensions were prepared with a mass-to-volume ratio of 0.5 mg/mL at pH values in the range of 2-9 by adjusting the pH with HCl 0.1 M and NaOH 0.1 M solutions.

2.4.2 Results and discussion

<u>Comparison between outcomes of silanization reactions</u>

Amino-containing cellulose synthesis has been recently optimized and Cell-NH_2 composition, morphology, crystallinity and thermal behaviour have been investigated

and published (Tummino et al., 2023). In this section, results from this study will be summarized to be compared with those of pristine cellulose and prepared Cell-SH samples.

Cellulose-derivatives elemental composition (C, H, N, S), expressed in mass weight percentage and in mmol/g, is shown in Table 2.1. The results confirm the success of both functionalization processes despite their different outcomes: 15.5% w/w of sulphur and 0.48% w/w of nitrogen were introduced in Cell-SH and Cell-NH_2, respectively. Consequently, the estimated amount of grafted silane is 4.83 mmol/g for Cell-SH and 0.346 mmol/g for Cell-NH_2.

Nitrogen and sulphur insertion in the functionalized materials was also confirmed by the ATR-FTIR spectra, as shown in Figure 2.17.

Table 2.1 - Elemental composition of pristine waste-derived cellulose and functionalized samples

	Cellulose	**Cell-SH**	**Cell-NH_2**
C % w/w	41.9 ± 0.09	42.3 ± 1.1	30.4 ± 0.4
C mmol/g	34.9 ± 0.08	35.2 ± 0.3	25.8 ± 0.9
H % w/w	5.90 ± 0.07	6.07 ± 0.07	5.42 ± 0.09
H mmol/g	58.4 ± 0.7	60.2 ± 0.9	53.7 ± 0.7
N % w/w	-	-	0.48 ± 0.04
N mmol/g	-	-	0.346 ± 0.026
S % w/w	-	155 ± 2.3	-
S mmol/g	-	4.8 ± 0.7	-

All the samples present the characteristic pattern of cellulose-based materials. The signals between 3400 and 3200 cm^{-1} are related to the stretching vibration of –OH groups (Tummino et al., 2023), whereas the asymmetric and symmetric stretching vibrations of C-H contained both in the cellulose structure and in the side chains of APTES and MPTMS are visible between 3000 and 2800 cm^{-1}; the absorption band assigned to the bending vibration of adsorbed water could be found at 1640 cm^{-1}, while the characteristic signals between 1430-1314 cm^{-1} are attributable to the symmetric bending of CH_2, and the bending vibration of C-O and C-H in the polysaccharide ring. The 1160-1030 cm^{-1} signals are related to the C-O stretching and the C-H rocking vibrations of the pyranose ring skeleton, while the β-glycosidic linkage signal appears at 896 cm^{-1} (Hospodarova et al., 2018; Y. Liu & Kim, 2017; Yang et al., 2017).

In both ATR-FTIR spectra of Cell-NH_2 and Cell-SH, a signal appears at about 800 cm^{-1}, which can be correlated to the Si-O-Si bending due to the introduction and polymerization of silanizing agents (*i.e.* APTES and MPTMS) (Beaumont et al., 2018; Testa et al., 2023).

Furthermore, as an additional evidence of the functionalization, the Cell-NH_2 spectrum shows a band at 1556 cm^{-1} that can be ascribed to the N-H bending vibration in primary amines (Kawalerczyk et al., 2022; Khanjanzadeh et al., 2018).

On the other hand, in the Cell-SH spectrum, further signals related to the introduction of the silanizing reagent are present.

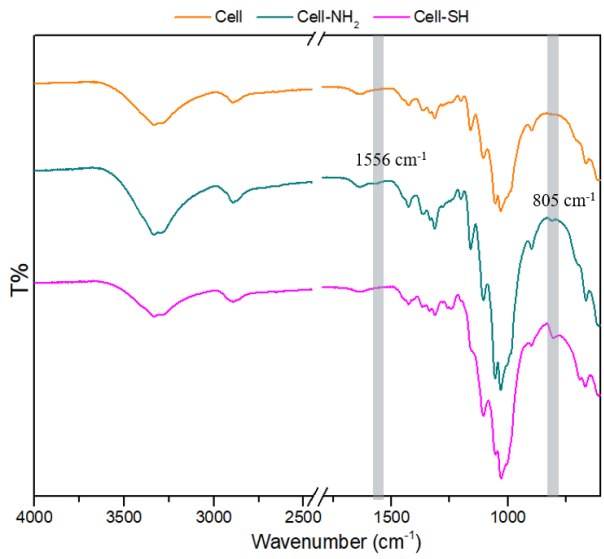

Figure 2.17 - ATR-FTIR spectra of pristine hulls-derived cellulose; Cell-NH_2 sample and Cell-SH sample

Indeed, according to the literature, the weak bands at 1260-1240 cm^{-1} could be assigned to silicon-carbon vibration modes (Launer & Arkles, 2013; S. Liu et al., 2018; Loof et al., 2016).

The morphological properties of both primary amine and thiol containing cellulose samples were analysed by electron microscopy.

According to Tummino et al. (Tummino et al., 2023), soybean hulls derived-cellulose shows a fibrous morphology characterized by a fibre length of around 35 µm and the sporadic presence of cemented regions related to impurities or residues of hemicellulose and lignin. As shown in Figures 2.18-A1 and B1, no significant morphological changes were induced on cellulose fibres by MPTMS and APTES functionalization, although the presence of aggregates is evident in Cell-SH.

The surface distribution of sulphur and nitrogen in the cellulosic matrix was investigated by FESEM analysis. As shown in Figures 2.18-A3, S-atoms seem to form aggregates on the Cell-SH fibres and a similar distribution is also confirmed for Si-atoms (Fig. 2.18-A2), which are present in ratio 1:1 with S since both elements were simultaneously introduced in the material through MPTMS-functionalization. As previously reported, the aggregation of MPTMS derivative could be related to a homopolycondensation of alkoxysilanes leading to the formation of a polysiloxane layer (Loof et al., 2016).

On the other hand, in the Cell-NH_2 sample, the N-atom distribution is not visible, probably due to the lower amount introduced in the matrix compared to sulphur. However, the distribution map of Si in this sample (Fig. 2.18-B2) suggests a good dispersion of APTES-derived functional groups on the Cell-NH_2 fibres, leading to the assumption of similar behaviour for nitrogen distribution.

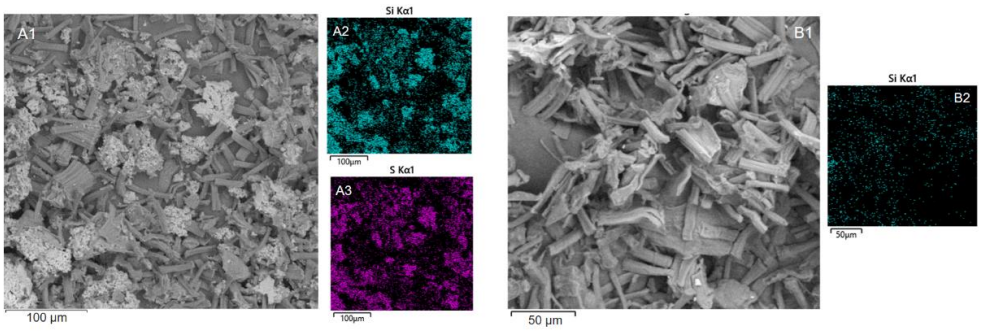

Figure 2.18 - FE-SEM images. (A1) Cell-SH image; (A2) surface distribution of Si in Cell-SH sample; (A3) surface distribution of S in Cell-SH sample; (B1) Cell-NH_2 image; (B2) surface distribution of Si in Cell-NH_2 sample.

Figure 2.19 shows Cell-SH outcomes of TGA, DTG and DSC analysis. As evidenced by the TGA thermogram, at 900 °C the remaining residue is 47% which is higher than the amounts previously found both for cellulose (12%) and Cell-NH_2 (21%) (Tummino et al., 2023). The charred residue, which is related to the formation of both pyrolyzed cellulose and silicon oxycarbide, can be correlated to the higher grafted silane amount (Thimmiah & Nallathambi, 2021).

Indeed, the highest residual weight (%) of the Cell-SH is in agreement with the data obtained from the FESEM-EDS and the elemental analysis, which highlight a greater content of MPTMS-deriving functionalities. Similar results have been obtained by Thimmiah and co-workers, who observed a TGA residue of around 40% for cellulose extracted from *Aloe Vera* and functionalized with MPTMS, with respect to 14% found in the raw fibres (Ram Thimmiah & Nallathambi, 2023).

Furthermore, DTG and DSC curves suggest a different pyrolytic pathway for the sulphur-containing sample with respect to those observed for nitrogen-containing and pristine celluloses. Indeed, the maximum weight loss percentage can be identified in the DTG graph at two temperatures (300 and 355 °C), which correspond to the endothermic peaks in DSC measurements, and an additional smaller peak at 500 °C is also present. On the other hand, Cell and Cell-NH_2 DSC curves showed only the cellulose characteristic endothermic peak centred at 350-360 °C (Tummino et al., 2023) due to a one-step decomposition. The different decomposition stages experienced by Cell-SH could be related to the presence of a surface layer of condensed polysiloxanes, which result in a two-step decomposition at 350-450°C and 450-550°C respectively (Loof et al., 2016).

The point of zero charge (PZC) was determined for all the cellulose-based samples in water suspension and Figure 2.20 displays the Z-potential values as a function of pH. The low PZC of cellulose and Cell-SH is related to the presence of –OH and –SH surface groups that lead to a negative surface charge for most of the pH range studied. Increasing the acidity of the suspension decreases the magnitude of zeta potential due to the repression of the deprotonation of the functional groups. At pH values lower than the PZC, the zeta potential becomes positive as a result of

functional groups protonation (Lee et al., 2011). Both cellulose and Cell-SH show a linear dependence of zeta potential on increasing pH, reaching -32 mV and -43 mV at pH 9, respectively, meaning that the suspensions become more stable by decreasing the acidity of the medium.

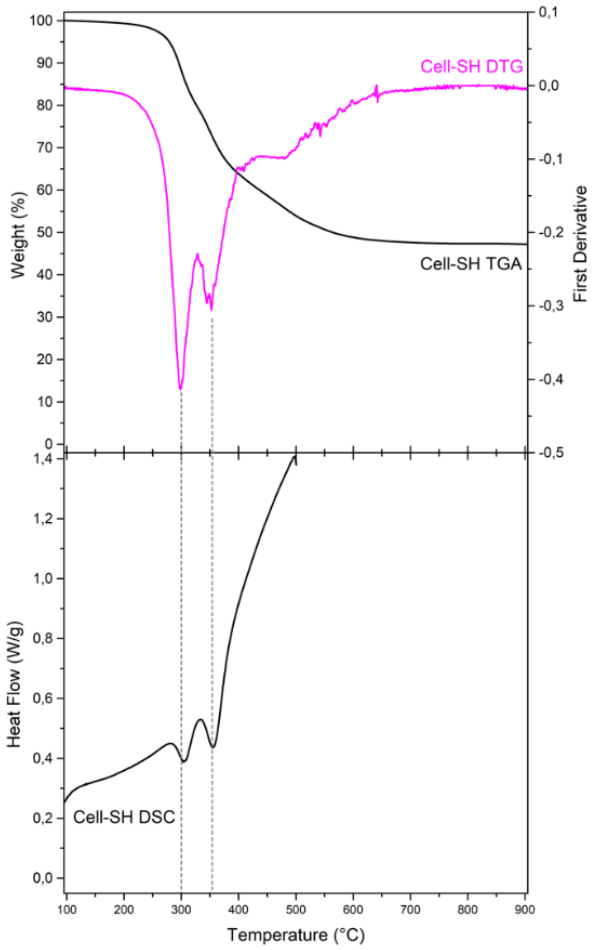

Figure 2.19 - Cell-SH thermal analysis. Top: TGA and DTG curves. Bottom: DSC curve

Indeed, Z-potential is also considered a measure of electrostatic stability of a suspension: for absolute values above 30 mV, the repulsive forces prevail and no aggregation phenomena occur (Ramírez-García et al., 2018).

Non-functionalized cellulose shows a PZC slightly lower than that reported in the literature (3.7) (Blaker et al., 2009; Lee et al., 2011) and a greater slope of the curve describing the trend of the Z-potential as a function of pH. This could be probably due to some residual acidic functionalities deriving from the procedure used for cellulose isolation.

The Cell-SH Z-potential trend is also in agreement with different studies that reported similar results in terms of absolute values in the whole pH range (Coelho Braga de Carvalho et al., 2021; Geng et al., 2017).

On the other hand, according to the literature (Hokkanen et al., 2014), the introduction of primary amines shifts the isoelectric point of the Cell-NH_2 sample toward a more alkaline pH (5.0). In this case, the suspension does not reach stability conditions, maintaining some aggregation tendency in all the pH range since the maximum absolute value of Z potential is only -8 mV (Ramírez-García et al., 2018).

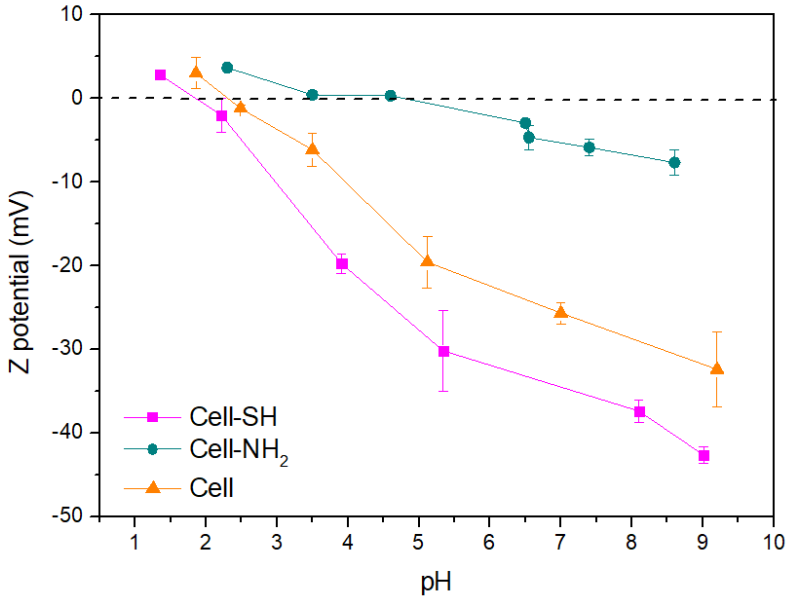

Figure 2.20 - Z-potential of prepared samples in aqueous suspensions as a function of pH

CMC characterization

Carboxymethylcellulose has been obtained with a degree of substitution (DS) of 1.2. The acetylation of cellulose was confirmed by infrared analysis of the sample. ATR-FTIR spectrum of CMC (Figure 2.21) shows a broad band around 3400 cm^{-1} followed by a peak at 2990 cm^{-1} attributable to the –OH and C-H stretching vibrations respectively. Moreover, the intense bands at 1587 and 1413 cm^{-1} seems to be ascribable to the asymmetric and symmetric stretching of carboxylate groups introduced in the cellulose structure (Melilli et al., 2020; Song et al., 2019). However, not all the studies in the literature agree on the allocation of the second signal, indeed some authors ascribe this band to the $–CH_2$ scissoring mode (Biswal & Singh, 2004; Haleem et al., 2014; Rajeh et al., 2019; Rozali et al., 2015). Perhaps, the high intensity of this signal is the result of the combination of both vibration modes. Finally, the peak at 1322 cm^{-1} is related to C-O bending vibration (Song et al., 2019).

Unlike soy-derived cellulose and its derivatives Cell-NH_2 and Cell-SH, which show a fibrous morphology, CMC is characterized by the presence of aggregates with contoured surfaces (Figure 2.22). Similar results have been obtained by Robles Barros and co-workers (Ascheri et al., 2024; Robles Barros et al., 2020) who attribute this morphological variation to the breaking of the fibres occurring during the functionalization process. Actually, the use of NaOH in the carboxymethylation reaction, which penetrates the amorphous regions of the cellulose, causes a partial disruption of the structure resulting in a final smoothed and defective morphology (Çelikçi et al., 2022). This loss of the fibrous structure and the appearance of spherical shaped objects which tend to merge in some points are evidenced in Figure 2.22, where SEM images of CMC at different magnifications are shown.

Regarding the CMC thermal behaviour, TGA and DSC outcomes are reported in Figure 2.23. As evidenced by the TGA thermogram (Fig 2.23-A), the thermal degradation of carboxymethyl cellulose is constituted by two main steps. The first one between 30 and 200°C is related to the weight loss ascribed to moisture evaporation (23%).

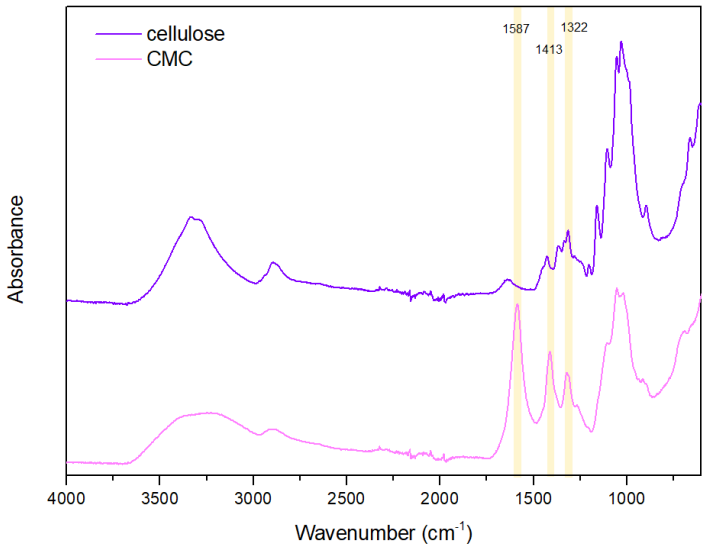

Figure 2.21 - ATR-FTIR spectra of pristine soy-derived cellulose and CMC

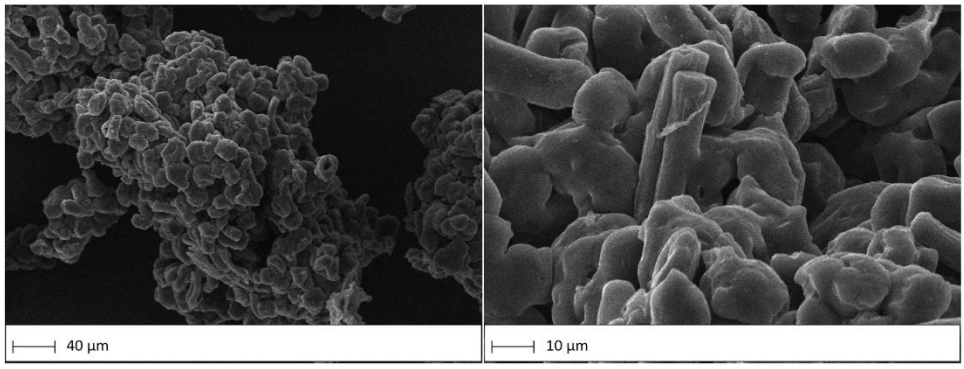

Figure 2.22 - Soy-derived CMC SEM images at different magnifications

The second and fastest thermal degradation step occurs between 250 and 315°C. In this case, the weight loss is equal to approximately 50% and is attributed to the decomposition of the main polymeric chain, where cleavage of the glycosidic bonds and breaking of the bonds of the carboxymethyl groups occur, leading to the decarboxylation of CMC with a CO_2 releasing (Robles Barros et al., 2020). Furthermore, some authors reported that in this temperature range also the loss of

oxygen molecules can happen due to the splitting off of various side groups (Akram et al., 2016; Biswal & Singh, 2004; Han et al., 2013).

A further degradation takes also place at a temperature higher than 320 °C, with a weight loss of about 15% as a result of the progression of the pyrolytic processes (Obele et al., 2021). At the end of the process, CMC presents a final 32% of residue. Robles Barros and co-workers (Robles Barros et al., 2020) suggest that, beyond the char component, part of this residue can contain ashes that could be formed by sodium oxide since CMC has been synthesised as sodium salt.

The DSC curve is reported in Figure 2.23-B, which displays a broad endothermic peak around 85 °C (attributable to adsorbed water) followed by two overlapping exothermic peaks at 292 °C and 308 °C. This double phenomenon finds correspondence in the steep thermal degradation observed in TGA (250-315 °C).

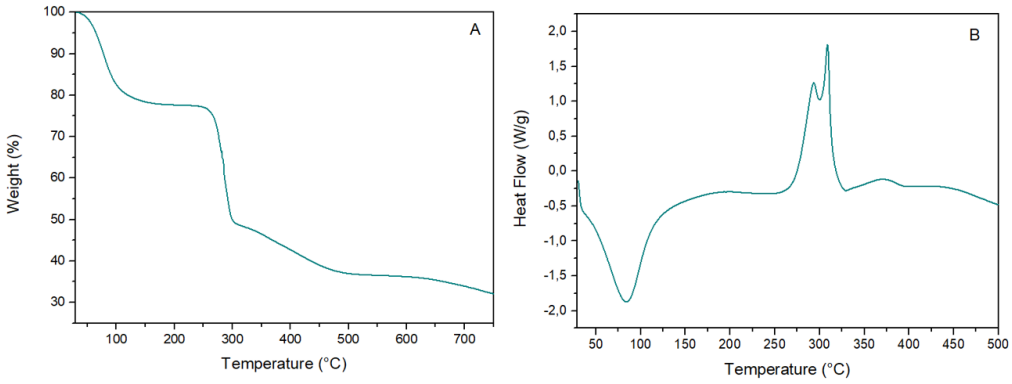

Figure 2.23 – CMC thermal analysis outcomes: A) TGA thermogram and B) DSC curve

According to the literature (Biswal & Singh, 2004), the first DSC peak coincides with melting of the sample, while the second appears as a result of the breaking down of the CMC backbone (depolymerisation with cleavage of glycosidic bonds). Moreover, both in TGA, as a slope change, and in DSC, as a sort of shoulder (exothermic), at about 380 °C, another thermal event can be seen and represent the further decomposition of CMC degradation products.

2.5 Final remarks

With a view to valorising soybean hulls, two of the most interesting components constituting the biomass have been successfully isolated. SBP was obtained with a satisfactory level of purity and enzymatic activity to guarantee its subsequent use in the context of the treatment of aqueous matrices contaminated by organic contaminants. On the other hand, two different cellulose isolation strategies have been tested: a three-steps acid-base hydrolysis process and a two-steps microwave assisted method. The analysis on isolated cellulose from both the developed strategies confirms the good quality of the final biomass, which was obtained in a powder form, made up by micrometric fibres composed by 88-91% w/w of pure cellulose.

However, the microwave-assisted hulls fractionation method shows several advantages, such as the reduction from three to only two treatment steps, the complete elimination of hydrochloric acid as reagent and an 80% reduction in the amount of sodium hydroxide used for the alkaline treatment. Despite these evidence, to really compare the two cellulose isolation processes it will be necessary to do a Life Cycle Assessment to taking into account also the energy consumption and to evaluate more comprensively all the impacts.

Furthermore, a first biomass fractionation step avoiding strongly acidic or alkaline reagents allows other exploitable components, such as polyphenols, to be isolated from the extraction solution. The TPC analysis on the first step extract of the optimized process revealed a total concentration of polyphenols of 114 mg of gallic acid equivalents per gram of extract. With the perspective of a complete valorization of the treated biomass, not only aimed at the recovery of cellulose, it will be necessary to characterize the extracts and quantify the dissolved compounds (hemicellulose or related oligomers and monomers; sugars such as glucose, xylose or arabinose; furfural, 5- hydroxymethylfurfural, *etc*) to optimize also their further recovery and uses.

As for the acid-alkaline hydrolysis, the microwave assisted cellulose isolation method is actually only applied in lab scale. As well known, a critical aspect in processes development is the scalability and the difficult scalability of processes that exploit

microwaves at a semi-industrial or industrial level could be a limit. However, the temperature and pressure conditions necessary to obtain subcritical water can be achieved in also pressurized reactors as reported by Cravotto et al. (Cravotto et al., 2022) and Aimone et al. (Aimone et al., 2023) making these treatments an interesting option also for real applications.

Cellulose isolated through the multi-hydrolysis treatment successfully underwent to different chemical modification to make it suitable for further applications and three soybean cellulose derivatives were effectively obtained. The silanization and carboxymethylation reactions were verified through different characterization techniques as well as the main properties of the synthesised materials.

The outcomes of silanization reactions revealed that Cell-NH_2 and Cell-SH reached different degrees of functionalization, probably due both to the different reagents involved (APTES and MPTMS) and the operating conditions. In particular, thiol groups were introduced in a higher amount. Therefore, from the chemical-physical point of view, diverse characteristics emerged when analysing the two materials because of both the type and the extent of grafted moieties. The main discrepancies were detected in terms of surface zeta potential values and thermal behaviour: Cell-SH showed a more negative surface with a higher Z potential and a more complex thermic degradation probably related to the presence of a layer of condensed polysiloxanes. As will be described in the further chapter, these differences will be responsible for the different behaviours in the contexts in which these materials will be tested. However, both Cell-NH_2 and Cell-SH have been effectively applied in this thesis work obtaining good results.

Regarding the CMC sample, the effectiveness of the carboxymethylation reaction has been proven by various characterization techniques as well as by preliminary tests of solubility in water, a fundamental property for subsequent applications. Indeed, its solubility in water makes it an extremely interesting and versatile cellulose derivative, especially for the development of materials without use of dangerous organic solvents.

2.6 References

Aguilar-Reynosa, A., Romaní, A., Ma. Rodríguez-Jasso, R., Aguilar, C. N., Garrote, G., & Ruiz, H. A. (2017). Microwave heating processing as alternative of pretreatment in second-generation biorefinery: An overview. Energy Conversion and Management, 136, 50–65. https://doi.org/10.1016/j.enconman.2017.01.004

Aguir, C., & M'Henni, M. F. (2006). Experimental study on carboxymethylation of cellulose extracted from Posidonia oceanica. Journal of Applied Polymer Science, 99(4), 1808–1816. https://doi.org/10.1002/app.22713

Aimone, C., Grillo, G., Boffa, L., Giovando, S., & Cravotto, G. (2023). Tannin Extraction from Chestnut Wood Waste: From Lab Scale to Semi-Industrial Plant. Applied Sciences, 13(4), 2494. https://doi.org/10.3390/app13042494

Akram, M., Taha, I., & Ghobashy, M. M. (2016). Low temperature pyrolysis of carboxymethylcellulose. Cellulose, 23(3), 1713–1724. https://doi.org/10.1007/s10570-016-0950-x

Alemdar, A., & Sain, M. (2008). Isolation and characterization of nanofibers from agricultural residues – Wheat straw and soy hulls. Bioresource Technology, 99(6), 1664–1671. https://doi.org/10.1016/j.biortech.2007.04.029

Alén, R., Kuoppala, E., & Oesch, P. (1996). Formation of the main degradation compound groups from wood and its components during pyrolysis. Journal of Analytical and Applied Pyrolysis, 36(2), 137–148. https://doi.org/10.1016/0165-2370(96)00932-1

Alonso-Riaño, P., Ramos, C., Trigueros, E., Beltrán, S., & Sanz, M. T. (2023). Study of subcritical water scale-up from laboratory to pilot system for brewer's spent grain valorization. Industrial Crops and Products, 191, 115927. https://doi.org/10.1016/j.indcrop.2022.115927

Álvarez-Viñas, M., Rodríguez-Seoane, P., Flórez-Fernández, N., Torres, M. D., Díaz-Reinoso, B., Moure, A., & Domínguez, H. (2021). Subcritical Water for the Extraction and Hydrolysis of Protein and Other Fractions in Biorefineries from Agro-food Wastes and Algae: A Review. Food and Bioprocess Technology, 14(3), 373–387. https://doi.org/10.1007/s11947-020-02536-4

Anastas, P. T., & Zimmerman, J. B. (2003). Design Through the 12 Principles of Green Engineering. Environmental Science & Technology, 37(5), 94A-101A. https://doi.org/10.1021/es032373g

Anastas, P., & Warner, J. (2000). Green Chemistry: Theory and Practice. Oxford University Press.

Ascheri, D. P. R., Barros, P. J. R., Ascheri, J. L. R., & Signini, R. (2024). Potential use of cellulose soybean hulls as a source of carboxymethyl cellulose for coating bean seeds. Ciência e Agrotecnologia, 48, e003924. https://doi.org/10.1590/1413-7054202448003924

Aziz, T., Farid, A., Haq, F., Kiran, M., Ullah, A., Zhang, K., Li, C., Ghazanfar, S., Sun, H., Ullah, R., Ali, A., Muzammal, M., Shah, M., Akhtar, N., Selim, S., Hagagy, N., Samy, M., & Al Jaouni, S. K. (2022). A Review on the Modification of Cellulose and Its Applications. Polymers, 14(15), 3206. https://doi.org/10.3390/polym14153206

Basak, S., & Annapure, U. S. (2022). The potential of subcritical water as a “green” method for the extraction and modification of pectin: A critical review. Food Research International, 161, 111849. https://doi.org/10.1016/j.foodres.2022.111849

Bayat, M., Karimi, N., Karami, M., Haghighi, A. B., Bayat, K., Akbari, S., & Haghani, M. (2023). Chronic exposure to 2.45 GHz microwave radiation improves cognition and synaptic plasticity impairment in vascular dementia model. International Journal of Neuroscience, 133(2), 111–122. https://doi.org/10.1080/00207454.2021.1896502

Beaumont, M., Bacher, M., Opietnik, M., Gindl-Altmutter, W., Potthast, A., & Rosenau, T. (2018). A General Aqueous Silanization Protocol to Introduce Vinyl, Mercapto or Azido Functionalities onto Cellulose Fibers and Nanocelluloses. Molecules, 23(6), Articolo 6. https://doi.org/10.3390/molecules23061427

Biswal, D. R., & Singh, R. P. (2004). Characterisation of carboxymethyl cellulose and polyacrylamide graft copolymer. Carbohydrate Polymers, 57(4), 379–387. https://doi.org/10.1016/j.carbpol.2004.04.020

Blaker, J. J., Lee, K.-Y., Li, X., Menner, A., & Bismarck, A. (2009). Renewable nanocomposite polymer foams synthesized from Pickering emulsion templates. Green Chemistry, 11(9), 1321–1326. https://doi.org/10.1039/B913740H

Boeriu, C. G., Bravo, D., Gosselink, R. J. A., & van Dam, J. E. G. (2004). Characterisation of structure-dependent functional properties of lignin with infrared spectroscopy. Industrial Crops and Products, 20(2), 205–218. https://doi.org/10.1016/j.indcrop.2004.04.022

Bundhoo, Z. M. A. (2018). Microwave-assisted conversion of biomass and waste materials to biofuels. Renewable and Sustainable Energy Reviews, 82, 1149–1177. https://doi.org/10.1016/j.rser.2017.09.066

Calcio Gaudino, E., Grillo, G., Manzoli, M., Tabasso, S., Maccagnan, S., & Cravotto, G. (2022). Mechanochemical Applications of Reactive Extrusion from Organic Synthesis to Catalytic and Active Materials. Molecules, 27(2), Articolo 2. https://doi.org/10.3390/molecules27020449

Calza, P., Zacchigna, D., & Laurenti, E. (2016). Degradation of orange dyes and carbamazepine by soybean peroxidase immobilized on silica monoliths and titanium dioxide. Environmental Science and Pollution Research, 23(23), 23742–23749. https://doi.org/10.1007/s11356-016-7399-1

Cao, J., Xiao, G., Xu, X., Shen, D., & Jin, B. (2013). Study on carbonization of lignin by TG-FTIR and high-temperature carbonization reactor. Fuel Processing Technology, 106, 41–47. https://doi.org/10.1016/j.fuproc.2012.06.016

Çelikçi, N., Department of Chemical Technologies, Afsin Vocational School, Kahramanmaras Sutcu Imam University, Kahramanmaras, Turkey, Dolaz, M., & Department of Environmental Engineering, Faculty of Engineering and Architecture, Kahramanmaras Sutcu Imam University, Kahramanmaras, Turkey. (2022). SYNTHESIS AND CHARACTERIZATION OF CARBOXYMETHYL CELLULOSE (CMC) FROM DIFFERENT WASTE SOURCES CONTAINING CELLULOSE AND INVESTIGATION OF ITS USE IN THE CONSTRUCTION INDUSTRY. Cellulose Chemistry and Technology, 56(1–2), 55–68. https://doi.org/10.35812/CelluloseChemTechnol.2022.56.05

Cocero, M. J., Cabeza, Á., Abad, N., Adamovic, T., Vaquerizo, L., Martínez, C. M., & Pazo-Cepeda, M. V. (2018). Understanding biomass fractionation in subcritical & supercritical water. The Journal of Supercritical Fluids, 133, 550–565. https://doi.org/10.1016/j.supflu.2017.08.012

Coelho Braga de Carvalho, A. L., Ludovici, F., Goldmann, D., Silva, A. C., & Liimatainen, H. (2021). Silylated Thiol-Containing Cellulose Nanofibers as a Bio-Based Flocculation Agent for Ultrafine Mineral Particles of Chalcopyrite and

Pyrite. Journal of Sustainable Metallurgy, 7(4), 1506–1522. https://doi.org/10.1007/s40831-021-00439-y

Collard, F.-X., & Blin, J. (2014). A review on pyrolysis of biomass constituents: Mechanisms and composition of the products obtained from the conversion of cellulose, hemicelluloses and lignin. Renewable and Sustainable Energy Reviews, 38, 594–608. https://doi.org/10.1016/j.rser.2014.06.013

Costa, J. M., Strieder, M. M., Saldaña, M. D. A., Rostagno, M. A., & Forster-Carneiro, T. (2023). Recent Advances in the Processing of Agri-food By-products by Subcritical Water. Food and Bioprocess Technology, 16(12), 2705–2724. https://doi.org/10.1007/s11947-023-03071-8

Costa, R. A., Cunha, A. S., Peres, J. C. G., Azzoni, A. R., Laurenti, E., & Vianna, A. S. (2020). Enzymatic Degradation of 2,4,6-Trichlorophenol in a Microreactor using Soybean Peroxidase. Symmetry 2020, Vol. 12, Page 1129, 12(7), 1129. https://doi.org/10.3390/sym12071129

Couhert, C., Commandre, J.-M., & Salvador, S. (2009). Is it possible to predict gas yields of any biomass after rapid pyrolysis at high temperature from its composition in cellulose, hemicellulose and lignin? Fuel, 88(3), 408–417. https://doi.org/10.1016/j.fuel.2008.09.019

Cravotto, C., Grillo, G., Binello, A., Gallina, L., Olivares-Vicente, M., Herranz-López, M., Micol, V., Barrajón-Catalán, E., & Cravotto, G. (2022). Bioactive Antioxidant Compounds from Chestnut Peels through Semi-Industrial Subcritical Water Extraction. Antioxidants, 11(5), Articolo 5. https://doi.org/10.3390/antiox11050988

Credou, J., & Berthelot, T. (2014). Cellulose: From biocompatible to bioactive material. Journal of Materials Chemistry B, 2(30), 4767–4788. https://doi.org/10.1039/C4TB00431K

Dodero, A., Pianella, L., Vicini, S., Alloisio, M., Ottonelli, M., & Castellano, M. (2019). Alginate-based hydrogels prepared via ionic gelation: An experimental design approach to predict the crosslinking degree. European Polymer Journal, 118, 586–594. https://doi.org/10.1016/j.eurpolymj.2019.06.028

Domínguez, A., Fernández, Y., Fidalgo, B., Pis, J. J., & Menéndez, J. A. (2007). Biogas to Syngas by Microwave-Assisted Dry Reforming in the Presence of Char. Energy & Fuels, 21(4), 2066–2071. https://doi.org/10.1021/ef070101j

Dunford, H. B. (1999). Heme Peroxidases (1st Edition, 1st Printing). Vch Verlagsgesellschaft Mbh.

Ethaib, S. (2024). Microwave-assisted pretreatment for lignocellulosic biomass energy conversion path. Bioresource Technology Reports, 28, 102006. https://doi.org/10.1016/j.biteb.2024.102006

Faleeva, Y. M., Lavrenov, V. A., & Zaichenko, V. M. (2024). Investigation of plant biomass two-stage pyrolysis based on three major components: Cellulose, hemicellulose, and lignin. Biomass Conversion and Biorefinery, 14(13), 14519–14529. https://doi.org/10.1007/s13399-022-03385-1

Ferrer, A., Salas, C., & Rojas, O. J. (2016). Physical, thermal, chemical and rheological characterization of cellulosic microfibrils and microparticles produced from soybean hulls. Industrial Crops and Products, 84, 337–343. https://doi.org/10.1016/j.indcrop.2016.02.014

Fia, A. Z., & Amorim, J. (2023). Microwave pretreatment of biomass for conversion of lignocellulosic materials into renewable biofuels. Journal of the Energy Institute, 106, 101146. https://doi.org/10.1016/j.joei.2022.11.006

Flauzino Neto, W. P., Silvério, H. A., Dantas, N. O., & Pasquini, D. (2013). Extraction and characterization of cellulose nanocrystals from agro-industrial residue – Soy hulls. Industrial Crops and Products, 42, 480–488. https://doi.org/10.1016/j.indcrop.2012.06.041

Freitas, P. A. V., Santana, L. G., González-Martínez, C., & Chiralt, A. (2024). Combining subcritical water extraction and bleaching with hydrogen peroxide to obtain cellulose fibres from rice straw. Carbohydrate Polymer Technologies and Applications, 7, 100491. https://doi.org/10.1016/j.carpta.2024.100491

Gallina, L., Cravotto, C., Capaldi, G., Grillo, G., & Cravotto, G. (2022). Plant Extraction in Water: Towards Highly Efficient Industrial Applications. Processes, 10(11), 2233. https://doi.org/10.3390/pr10112233

Garcia-Maraver, A., Salvachúa, D., Martínez, M. J., Diaz, L. F., & Zamorano, M. (2013). Analysis of the relation between the cellulose, hemicellulose and lignin content and the thermal behavior of residual biomass from olive trees. Waste Management, 33(11), 2245–2249. https://doi.org/10.1016/j.wasman.2013.07.010

Genevini, P., Adani, F., & Villa, C. (1997). Rice hull degradation by co-composting with dairy cattle slurry. Soil Science and Plant Nutrition, 43(1), 135–147. https://doi.org/10.1080/00380768.1997.10414722

Geng, B., Wang, H., Wu, S., Ru, J., Tong, C., Chen, Y., Liu, H., Wu, S., & Liu, X. (2017). Surface-Tailored Nanocellulose Aerogels with Thiol-Functional Moieties for Highly Efficient and Selective Removal of Hg(II) Ions from Water. ACS Sustainable Chemistry & Engineering, 5(12), 11715–11726. https://doi.org/10.1021/acssuschemeng.7b03188

Gil-Guillén, I., Freitas, P. A. V., González-Martínez, C., & Chiralt, A. (2024). Obtaining Cellulose Fibers from Almond Shell by Combining Subcritical Water Extraction and Bleaching with Hydrogen Peroxide. Molecules, 29(14), Articolo 14. https://doi.org/10.3390/molecules29143284

Gomez-Contreras, P. A., Obando, C., Freitas, P. A. V. de, Martin-Perez, L., Chiralt, A., & Gonzalez-Martinez, C. (2024). Applying Subcritical Water Extraction to Obtain Bioactive Compounds and Cellulose Fibers from Brewer Spent Grains. Molecules, 29(20), Articolo 20. https://doi.org/10.3390/molecules29204897

Guo, X., Zhang, S., & Shan, X. (2008). Adsorption of metal ions on lignin. Journal of Hazardous Materials, 151(1), 134–142. https://doi.org/10.1016/j.jhazmat.2007.05.065

Habibi, Y. (2014). Key advances in the chemical modification of nanocelluloses. Chemical Society Reviews, 43(5), 1519–1542. https://doi.org/10.1039/C3CS60204D

Haleem, N., Arshad, M., Shahid, M., & Tahir, M. A. (2014). Synthesis of carboxymethyl cellulose from waste of cotton ginning industry. Carbohydrate Polymers, 113, 249–255. https://doi.org/10.1016/j.carbpol.2014.07.023

Han, F., Xiong, D., Wang, Q., Shao, B., & Chen, M. (2013). Thermal Properties of Carboxymethylcellulose and Methyl Methacrylate Graft Copolymers. Journal of Macromolecular Science, Part B, 52(9), 1242–1249. https://doi.org/10.1080/00222348.2013.763568

Hanim, S. S., Norsyabilah, R., Suhaila, M. H. N., Noraishah, A., & Kartina, A. K. S. (2012). Effects of Temperature, Time and Pressure on the Hemicelluloses Yield Extracted Using Subcritical Water Extraction. Procedia Engineering, 42, 562–565. https://doi.org/10.1016/j.proeng.2012.07.448

Hokkanen, S., Repo, E., Suopajärvi, T., Liimatainen, H., Niinimaa, J., & Sillanpää, M. (2014). Adsorption of Ni(II), Cu(II) and Cd(II) from aqueous solutions by amino modified nanostructured microfibrillated cellulose. Cellulose, 21(3), 1471–1487. https://doi.org/10.1007/s10570-014-0240-4

Horikawa, Y., Hirano, S., Mihashi, A., Kobayashi, Y., Zhai, S., & Sugiyama, J. (2019). Prediction of Lignin Contents from Infrared Spectroscopy: Chemical Digestion and Lignin/Biomass Ratios of Cryptomeria japonica. Applied Biochemistry and Biotechnology, 188(4), 1066–1076. https://doi.org/10.1007/s12010-019-02965-8

Hosoya, T., Kawamoto, H., & Saka, S. (2007). Pyrolysis behaviors of wood and its constituent polymers at gasification temperature. Journal of Analytical and Applied Pyrolysis, 78(2), 328–336. https://doi.org/10.1016/j.jaap.2006.08.008

Hospodarova, V., Singovszka, E., & Stevulova, N. (2018). Characterization of Cellulosic Fibers by FTIR Spectroscopy for Their Further Implementation to Building Materials. American Journal of Analytical Chemistry, 9(6), Articolo 6. https://doi.org/10.4236/ajac.2018.96023

Hu, Z., & Wen, Z. (2008). Enhancing enzymatic digestibility of switchgrass by microwave-assisted alkali pretreatment. Biochemical Engineering Journal, 38(3), 369–378. https://doi.org/10.1016/j.bej.2007.08.001

Husain, Q. (2010). Peroxidase mediated decolorization and remediation of wastewater containing industrial dyes: A review. Reviews in Environmental Science and Bio/Technology, 9(2), 117–140. https://doi.org/10.1007/s11157-009-9184-9

Iglesias, M. C., Hamade, F., Aksoy, B., Jiang, Z., Davis, V. A., & Peresin, M. S. (2021). Correlations between rheological behavior and intrinsic properties of nanofibrillated cellulose from wood and soybean hulls with varying lignin content. BioResources, 16(3), 4831–4845. https://doi.org/10.15376/biores.16.3.4831-4845

Jensen, A., Dam-Johansen, K., Wójtowicz, M. A., & Serio, M. A. (1998). TG-FTIR Study of the Influence of Potassium Chloride on Wheat Straw Pyrolysis. Energy & Fuels, 12(5), 929–938. https://doi.org/10.1021/ef980008i

Jiang, Y., Liu, X., Yang, Q., Song, X., Qin, C., Wang, S., & Li, K. (2019). Effects of residual lignin on composition, structure and properties of mechanically defibrillated cellulose fibrils and films. Cellulose, 26(3), 1577–1593. https://doi.org/10.1007/s10570-018-02229-4

Kamal, J. K. A., & Behere, D. V. (2002). Thermal and conformational stability of seed coat soybean peroxidase. Biochemistry, 41(29), 9034–9042. https://doi.org/10.1021/bi025621e

Katheresan, V., Kansedo, J., & Lau, S. Y. (2018). Efficiency of various recent wastewater dye removal methods: A review. Journal of Environmental Chemical Engineering, 6(4), 4676–4697. https://doi.org/10.1016/j.jece.2018.06.060

Kawalerczyk, J., Walkiewicz, J., Dziurka, D., Mirski, R., & Brózdowski, J. (2022). APTES-Modified Nanocellulose as the Formaldehyde Scavenger for UF Adhesive-Bonded Particleboard and Strawboard. Polymers, 14(22), Articolo 22. https://doi.org/10.3390/polym14225037

Khanjanzadeh, H., Behrooz, R., Bahramifar, N., Gindl-Altmutter, W., Bacher, M., Edler, M., & Griesser, T. (2018). Surface chemical functionalization of cellulose nanocrystals by 3-aminopropyltriethoxysilane. International Journal of Biological Macromolecules, 106, 1288–1296. https://doi.org/10.1016/j.ijbiomac.2017.08.136

Kurian, J. K., Gariepy, Y., Orsat, V., & Raghavan, G. S. V. (2015). Comparison of steam-assisted versus microwave-assisted treatments for the fractionation of sweet sorghum bagasse. Bioresources and Bioprocessing, 2(1), 30. https://doi.org/10.1186/s40643-015-0059-3

Launer, P., & Arkles, B. (2013). Infrared Analysis of Organosilicon Compounds (pp. 175–178).

Lavagna, L., Tummino, M. L., Magnacca, G., Corazzari, I., & Laurenti, E. (2021). Immobilized bi-enzymatic system for the determination of biogenic amines in solution. Biochemical Engineering Journal, 169, 107960. https://doi.org/10.1016/j.bej.2021.107960

Lee, K.-Y., Quero, F., Blaker, J. J., Hill, C. A. S., Eichhorn, S. J., & Bismarck, A. (2011). Surface only modification of bacterial cellulose nanofibres with organic acids. Cellulose, 18(3), 595–605. https://doi.org/10.1007/s10570-011-9525-z

Li, J., Wang, B., Chen, K., Tian, X., Zeng, J., Xu, J., & Gao, W. (2017). The Use of Lignin as Cross-linker for Polyurethane Foam for Potential Application in Adsorbing Materials.

Lionetto, F., Del Sole, R., Cannoletta, D., Vasapollo, G., & Maffezzoli, A. (2012). Monitoring Wood Degradation during Weathering by Cellulose Crystallinity. Materials, 5(10), 1910–1922. https://doi.org/10.3390/ma5101910

Liu, Q., Wang, S., Zheng, Y., Luo, Z., & Cen, K. (2008). Mechanism study of wood lignin pyrolysis by using TG–FTIR analysis. Journal of Analytical and Applied Pyrolysis, 82(1), 170–177. https://doi.org/10.1016/j.jaap.2008.03.007

Liu, S., Zhou, Q., Peng, Z., Song, N., & Ni, L. (2018). Silicon alkyne hybrid polymers containing Si–H and Si–CH3: Synthesis, characterization, and thermal and oxidative properties. High Performance Polymers, 30(3), 259–266. https://doi.org/10.1177/0954008317698546

Liu, Y., & Chen, J. Y. (2016). Enzyme immobilization on cellulose matrixes. Journal of Bioactive and Compatible Polymers, 31(6), 553–567. https://doi.org/10.1177/0883911516637377

Liu, Y., & Kim, H.-J. (2017). Fourier Transform Infrared Spectroscopy (FT-IR) and Simple Algorithm Analysis for Rapid and Non-Destructive Assessment of Developmental Cotton Fibers. Sensors, 17(7), Articolo 7. https://doi.org/10.3390/s17071469

Loof, D., Hiller, M., Oschkinat, H., & Koschek, K. (2016). Quantitative and Qualitative Analysis of Surface Modified Cellulose Utilizing TGA-MS. Materials, 9(6), Articolo 6. https://doi.org/10.3390/ma9060415

Lu, Y., He, Q., Fan, G., Cheng, Q., & Song, G. (2021). Extraction and modification of hemicellulose from lignocellulosic biomass: A review. Green Processing and Synthesis, 10(1), 779–804. https://doi.org/10.1515/gps-2021-0065

Ludovici, F., Hartmann, R., & Liimatainen, H. (2023). Aqueous bifunctionalization of cellulose nanocrystals through amino and alkyl silylation: Functionalization, characterization, and performance of nanocrystals in quartz microflotation. Cellulose, 30(2), 775–787. https://doi.org/10.1007/s10570-022-04961-4

Majeed, T., Shabir, I., Srivastava, S., Maqbool, N., Dar, A. H., Jan, K., Pandey, V. K., Shams, R., Bashir, I., Dash, K. K., Hanan, E., & Wani, N. R. (2024). Valorization of food wastes by implementation of subcritical water extraction: A comprehensive review. Trends in Food Science & Technology, 143, 104316. https://doi.org/10.1016/j.tifs.2023.104316

Marchis, T., Avetta, P., Bianco-Prevot, A., Fabbri, D., Viscardi, G., & Laurenti, E. (2011). Oxidative degradation of Remazol Turquoise Blue G 133 by soybean peroxidase. Journal of Inorganic Biochemistry, 105(2), 321–327. https://doi.org/10.1016/j.jinorgbio.2010.11.009

Matusiewicz, H., & Ślachciński, M. (2014). Development of a one-step microwave-assisted subcritical water extraction for simultaneous determination of inorganic elements (Ba, Ca, Cu, Fe, Mg, Mn, Na, Pb, Sr, Zn) in reference materials by microwave induced plasma spectrometry. Microchemical Journal, 115, 6–10. https://doi.org/10.1016/j.microc.2014.02.002

McCaffrey, Z., Torres, L., Chiou, B.-S., Ferreira, S. R., Silva, L. E., Wood, D. F., & Orts, W. J. (2021). Torrefaction of Almond and Walnut Byproducts. Frontiers in Energy Research, 9. https://doi.org/10.3389/fenrg.2021.643306

Md Salim, R., Asik, J., & Sarjadi, M. S. (2021). Chemical functional groups of extractives, cellulose and lignin extracted from native Leucaena leucocephala bark. Wood Science and Technology, 55(2), 295–313. https://doi.org/10.1007/s00226-020-01258-2

Melilli, G., Carmagnola, I., Tonda-Turo, C., Pirri, F., Ciardelli, G., Sangermano, M., Hakkarainen, M., & Chiappone, A. (2020). DLP 3D Printing Meets Lignocellulosic Biopolymers: Carboxymethyl Cellulose Inks for 3D Biocompatible Hydrogels. Polymers, 12(8), Articolo 8. https://doi.org/10.3390/polym12081655

Meraj, A., Jawaid, M., Singh, S. P., Nasef, M. M., Ariffin, H., Fouad, H., & Abu-Jdayil, B. (2024). Isolation and characterisation of lignin using natural deep eutectic solvents pretreated kenaf fibre biomass. Scientific Reports, 14(1), 8672. https://doi.org/10.1038/s41598-024-59200-6

Mohd Thani, N., Mustapa Kamal, S. M., Sulaiman, A., Taip, F. S., Omar, R., & Izhar, S. (2020). Sugar Recovery from Food Waste via Sub-critical Water Treatment. Food Reviews International, 36(3), 241–257. https://doi.org/10.1080/87559129.2019.1636815

Ngo, T. T., & Lenhoff, H. M. (1980). A sensitive and versatile chromogenic assay for peroxidase and peroxidase-coupled reactions. Analytical Biochemistry, 105(1), 389–397. https://doi.org/10.1016/0003-2697(80)90475-3

Nguyen Thi, B. T., Ong, L. K., Nguyen Thi, D. T., & Ju, Y.-H. (2017). Effect of subcritical water pretreatment on cellulose recovery of water hyacinth (Eichhornia crassipe). Journal of the Taiwan Institute of Chemical Engineers, 71, 55–61. https://doi.org/10.1016/j.jtice.2016.12.028

Obele, C. M., Ibenta, M. E., Chukwuneke, J. L., & Nwanonenyi, S. C. (2021). Carboxymethyl cellulose and cellulose nanocrystals from cassava stem as

thickeners in reactive printing of cotton. Cellulose, 28(4), 2615–2633. https://doi.org/10.1007/s10570-021-03694-0

Oberlintner, A., Likozar, B., & Novak, U. (2021). Hydrophobic functionalization reactions of structured cellulose nanomaterials: Mechanisms, kinetics and in silico multi-scale models. Carbohydrate Polymers, 259, 117742. https://doi.org/10.1016/j.carbpol.2021.117742

Okolie, J. A., Nanda, S., Dalai, A. K., & Kozinski, J. A. (2020). Optimization and modeling of process parameters during hydrothermal gasification of biomass model compounds to generate hydrogen-rich gas products. International Journal of Hydrogen Energy, 45(36), 18275–18288. https://doi.org/10.1016/j.ijhydene.2019.05.132

Oriez, V., Peydecastaing, J., & Pontalier, P.-Y. (2020). Lignocellulosic Biomass Mild Alkaline Fractionation and Resulting Extract Purification Processes: Conditions, Yields, and Purities. Clean Technologies, 2(1), Articolo 1. https://doi.org/10.3390/cleantechnol2010007

Palav, T., & Seetharaman, K. (2007). Impact of microwave heating on the physico-chemical properties of a starch–water model system. Carbohydrate Polymers, 67(4), 596–604. https://doi.org/10.1016/j.carbpol.2006.07.006

Pattnaik, F., Nanda, S., Kumar, V., Naik, S., & Dalai, A. K. (2022). Isolation of cellulose fibers from wetland reed grass through an integrated subcritical water hydrolysis-pulping-bleaching process. Fuel, 311, 122618. https://doi.org/10.1016/j.fuel.2021.122618

Peng, Y., & Wu, S. (2010). The structural and thermal characteristics of wheat straw hemicellulose. Journal of Analytical and Applied Pyrolysis, 88(2), 134–139. https://doi.org/10.1016/j.jaap.2010.03.006

Pińkowska, H., Wolak, P., & Złocińska, A. (2012). Hydrothermal decomposition of alkali lignin in sub- and supercritical water. Chemical Engineering Journal, 187, 410–414. https://doi.org/10.1016/j.cej.2012.01.092

Poletto, M., Zattera, A. J., & Santana, R. M. C. (2012). Structural differences between wood species: Evidence from chemical composition, FTIR spectroscopy, and thermogravimetric analysis. Journal of Applied Polymer Science, 126(S1), E337–E344. https://doi.org/10.1002/app.36991

Qin, M., Zhang, L., & Wu, H. (2022). Dielectric Loss Mechanism in Electromagnetic Wave Absorbing Materials. Advanced Science, 9(10), 2105553. https://doi.org/10.1002/advs.202105553

Rahman, Md. S., Hasan, Md. S., Nitai, A. S., Nam, S., Karmakar, A. K., Ahsan, Md. S., Shiddiky, M. J. A., & Ahmed, M. B. (2021). Recent Developments of Carboxymethyl Cellulose. Polymers, 13(8), 1345. https://doi.org/10.3390/polym13081345

Rajeh, A., Morsi, M. A., & Elashmawi, I. S. (2019). Enhancement of spectroscopic, thermal, electrical and morphological properties of polyethylene oxide/carboxymethyl cellulose blends: Combined FT-IR/DFT. Vacuum, 159, 430–440. https://doi.org/10.1016/j.vacuum.2018.10.066

Ram Thimmiah, B., & Nallathambi, G. (2023). Thiol Functionalized Aloe Vera Fibre Filter: A Simple Portable Water Filter For Heavy Metal Ion Removal. ChemistrySelect, 8(3), e202203747. https://doi.org/10.1002/slct.202203747

Ramírez-García, G., Trapiella-Alfonso, L., d'Orlyé, F., & Varenne, A. (2018). Chapter 17—Electrophoretic Methods for Characterizing Nanoparticles and Evaluating Their Bio-interactions for Their Further Use as Diagnostic, Imaging, or Therapeutic Tools. In C. F. Poole (A c. Di), Capillary Electromigration Separation Methods (pp. 397–421). Elsevier. https://doi.org/10.1016/B978-0-12-809375-7.00019-8

Robles Barros, P. J., Ramirez Ascheri, D. P., Siqueira Santos, M. L., Morais, C. C., Ramirez Ascheri, J. L., Signini, R., dos Santos, D. M., de Campos, A. J., & Alessandro Devilla, I. (2020). Soybean hulls: Optimization of the pulping and bleaching processes and carboxymethyl cellulose synthesis. International Journal of Biological Macromolecules, 144, 208–218. https://doi.org/10.1016/j.ijbiomac.2019.12.074

Roy, D., Semsarilar, M., Guthrie, J. T., & Perrier, S. (2009). Cellulose modification by polymer grafting: A review. Chemical Society Reviews, 38(7), 2046–2064. https://doi.org/10.1039/B808639G

Rozali, M. L. H., Ahmad, Z., & Isa, M. I. N. (2015). Interaction between Carboxy Methylcellulose and Salicylic Acid Solid Biopolymer Electrolytes. Advanced Materials Research, 1107, 223–229. https://doi.org/10.4028/www.scientific.net/AMR.1107.223

Salema, A. A., Ani, F. N., Mouris, J., & Hutcheon, R. (2017). Microwave dielectric properties of Malaysian palm oil and agricultural industrial biomass and biochar during pyrolysis process. Fuel Processing Technology, 166, 164–173. https://doi.org/10.1016/j.fuproc.2017.06.006

Salema, A. A., Yeow, Y. K., Ishaque, K., Ani, F. N., Afzal, M. T., & Hassan, A. (2013). Dielectric properties and microwave heating of oil palm biomass and biochar. Industrial Crops and Products, 50, 366–374. https://doi.org/10.1016/j.indcrop.2013.08.007

Sarker, T. R., Pattnaik, F., Nanda, S., Dalai, A. K., Meda, V., & Naik, S. (2021). Hydrothermal pretreatment technologies for lignocellulosic biomass: A review of steam explosion and subcritical water hydrolysis. Chemosphere, 284, 131372. https://doi.org/10.1016/j.chemosphere.2021.131372

Sarro, M., Gule, N. P., Laurenti, E., Gamberini, R., Paganini, M. C., Mallon, P. E., & Calza, P. (2018). ZnO-based materials and enzymes hybrid systems as highly efficient catalysts for recalcitrant pollutants abatement. Chemical Engineering Journal, 334, 2530–2538. https://doi.org/10.1016/j.cej.2017.11.146

Seddiqi, H., Oliaei, E., Honarkar, H., Jin, J., Geonzon, L. C., Bacabac, R. G., & Klein-Nulend, J. (2021). Cellulose and its derivatives: Towards biomedical applications. Cellulose, 28(4), 1893–1931. https://doi.org/10.1007/s10570-020-03674-w

Sinclair, A., Jiang, L., Bajwa, D., Bajwa, S., Tangpong, S., & Wang, X. (2018). Cellulose nanofibers produced from various agricultural residues and their reinforcement effects in polymer nanocomposites. Journal of Applied Polymer Science, 135(21), 46304. https://doi.org/10.1002/app.46304

Singh, R. D., Bhuyan, K., Banerjee, J., Muir, J., & Arora, A. (2017). Hydrothermal and microwave assisted alkali pretreatment for fractionation of arecanut husk. Industrial Crops and Products, 102, 65–74. https://doi.org/10.1016/j.indcrop.2017.03.017

Song, L., Liu, F., Zhu, C., & Li, A. (2019). Facile one-step fabrication of carboxymethyl cellulose based hydrogel for highly efficient removal of Cr(VI) under mild acidic condition. Chemical Engineering Journal, 369, 641–651. https://doi.org/10.1016/j.cej.2019.03.126

Sulaiman, S., Mokhtar, M. N., Naim, M. N., Baharuddin, A. S., & Sulaiman, A. (2015). A Review: Potential Usage of Cellulose Nanofibers (CNF) for Enzyme

Immobilization via Covalent Interactions. Applied Biochemistry and Biotechnology, 175(4), 1817–1842. https://doi.org/10.1007/s12010-014-1417-x

Taşar, Ş., & Özer, A. (2022). A comparative study of hemicellulose isolation with hot water, alkaline, and delignification methods from tea leaf brewing waste. Biomass Conversion and Biorefinery, 12(7), 2501–2514. https://doi.org/10.1007/s13399-020-00978-6

Testa, M. L. (2021). Functionalized nanomaterials for biomass conversion. Materials Today: Proceedings, 35, 156–163. https://doi.org/10.1016/j.matpr.2020.04.064

Testa, M. L., & La Parola, V. (2021). Sulfonic Acid-Functionalized Inorganic Materials as Efficient Catalysts in Various Applications: A Minireview. Catalysts, 11(10), Articolo 10. https://doi.org/10.3390/catal11101143

Testa, M. L., Tummino, M. L., Venezia, A. M., & Russo, M. (2023). Interesterification of Glyceryl Trioctanoate Catalyzed by Sulfonic Silica-Based Materials: Insight into the Role of Catalysts on the Reaction Mechanism. Materials, 16(14), Articolo 14. https://doi.org/10.3390/ma16145121

Thimmiah, B. R., & Nallathambi, G. (2021). Response surface methodology approach to optimize the functionalization process on Agave americana fibre. Cellulose, 28(15), 10065–10075. https://doi.org/10.1007/s10570-021-04142-9

Tolardo, V., García-Ballesteros, S., Santos-Juanes, L., Vercher, R., Amat, A. M., Arques, A., & Laurenti, E. (2019). Pentachlorophenol Removal from Water by Soybean Peroxidase and Iron(II) Salts Concerted Action. Water, Air, & Soil Pollution, 230(6), 140. https://doi.org/10.1007/s11270-019-4189-7

Toscano, G., Maceratesi, V., Leoni, E., Stipa, P., Laudadio, E., & Sabbatini, S. (2022). FTIR spectroscopy for determination of the raw materials used in wood pellet production. Fuel, 313, 123017. https://doi.org/10.1016/j.fuel.2021.123017

Tummino, M. L., Laurenti, E., Bracco, P., Cecone, C., Parola, V. L., Vineis, C., & Testa, M. L. (2023). Antibacterial properties of functionalized cellulose extracted from deproteinized soybean hulls. Cellulose, 30(12), 7805–7824. https://doi.org/10.1007/s10570-023-05339-w

Tummino, M. L., Tolardo, V., Malandrino, M., Sadraei, R., Magnacca, G., & Laurenti, E. (2020). A Way to Close the Loop: Physicochemical and Adsorbing

Properties of Soybean Hulls Recovered After Soybean Peroxidase Extraction. Frontiers in Chemistry, 8, 763. https://doi.org/10.3389/fchem.2020.00763

Wan, Y., Chen, P., Zhang, B., Yang, C., Liu, Y., Lin, X., & Ruan, R. (2009). Microwave-assisted pyrolysis of biomass: Catalysts to improve product selectivity. Journal of Analytical and Applied Pyrolysis, 86(1), 161–167. https://doi.org/10.1016/j.jaap.2009.05.006

Wang, D. (2019). A critical review of cellulose-based nanomaterials for water purification in industrial processes. Cellulose, 26(2), 687–701. https://doi.org/10.1007/s10570-018-2143-2

Wang, J., Minami, E., & Kawamoto, H. (2020). Thermal reactivity of hemicellulose and cellulose in cedar and beech wood cell walls. Journal of Wood Science, 66(1), 41. https://doi.org/10.1186/s10086-020-01888-x

Yáñez-S, M., Matsuhiro, B., Maldonado, S., González, R., Luengo, J., Uyarte, O., Serafine, D., Moya, S., Romero, J., Torres, R., & Kogan, M. J. (2018). Carboxymethylcellulose from bleached organosolv fibers of Eucalyptus nitens: Synthesis and physicochemical characterization. Cellulose, 25(5), 2901–2914. https://doi.org/10.1007/s10570-018-1766-7

Yang, Y. P., Zhang, Y., Lang, Y. X., & Yu, M. H. (2017). Structural ATR-IR analysis of cellulose fibers prepared from a NaOH complex aqueous solution. IOP Conference Series: Materials Science and Engineering, 213(1), 012039. https://doi.org/10.1088/1757-899X/213/1/012039

Yedro, F. M., Grénman, H., Rissanen, J. V., Salmi, T., García-Serna, J., & Cocero, M. J. (2017). Chemical composition and extraction kinetics of Holm oak (Quercus ilex) hemicelluloses using subcritical water. The Journal of Supercritical Fluids, 129, 56–62. https://doi.org/10.1016/j.supflu.2017.01.016

Zhang, F., Lian, M., Alhadhrami, A., Huang, M., Li, B., Mersal, G. A. M., Ibrahim, M. M., & Xu, M. (2022). Laccase immobilized on functionalized cellulose nanofiber/alginate composite hydrogel for efficient bisphenol A degradation from polluted water. Advanced Composites and Hybrid Materials, 5(3), 1852–1864. https://doi.org/10.1007/s42114-022-00476-5

Zhang, J., Wen, C., Zhang, H., Duan, Y., & Ma, H. (2020). Recent advances in the extraction of bioactive compounds with subcritical water: A review. Trends in Food Science & Technology, 95, 183–195. https://doi.org/10.1016/j.tifs.2019.11.018

Zhang, N., Tao, P., Lu, Y., & Nie, S. (2019). Effect of lignin on the thermal stability of cellulose nanofibrils produced from bagasse pulp. Cellulose, 26(13), 7823–7835. https://doi.org/10.1007/s10570-019-02657-w

Zhang, R.-Y., Liu, H.-M., Hou, J., Yao, Y.-G., Ma, Y.-X., & Wang, X.-D. (2021). Cellulose fibers extracted from sesame hull using subcritical water as a pretreatment. Arabian Journal of Chemistry, 14(6), 103178. https://doi.org/10.1016/j.arabjc.2021.103178

Zhang, W., Liu, Y., Xuan, Y., & Zhang, S. (2022). Synthesis and Applications of Carboxymethyl Cellulose Hydrogels. Gels, 8(9), Articolo 9. https://doi.org/10.3390/gels8090529

Zhang, Z., Tingaut, P., Rentsch, D., Zimmermann, T., & Sèbe, G. (2015). Controlled Silylation of Nanofibrillated Cellulose in Water: Reinforcement of a Model Polydimethylsiloxane Network. ChemSusChem, 8(16), 2681–2690. https://doi.org/10.1002/cssc.201500525

3 Materials for aquaculture water remediation

Water bodies decontamination is one of the greatest challenges facing scientists today not only because water is essential for the life and well-being of humans and ecosystems but also because it represents a source of food sustenance.

Indeed, in the last seven decades' total fisheries and aquaculture production has significantly expanded with an average growth rate of 3.3% per year. Aquaculture is one of the few sectors which maintained its growth trend also even during the global spread of the COVID-19 pandemic, highlighting its importance since it contributes to fighting poverty, hunger and malnutrition. Indeed, over half of aquatic food is currently farmed (FAO, 2022).

According to the report "The State of World Fisheries and Aquaculture 2022", in 2020, Asian countries were the main producers, accounting for 70% of the total fisheries and aquaculture production of aquatic animals, followed by countries in the Americas (12%), Europe (10%), Africa (7%) and Oceania (1%) (FAO, 2022).

According to the Council Directive 2006/88/EC, aquaculture is defined as the rearing or cultivation of aquatic organisms using techniques designed to increase the production of those organisms beyond the natural capacity of the environment (Council of the European Union, 2006). Among these techniques, the use of chemicals is consistent to ensure successful and profitable aquaculture production. These chemicals include antibiotics, hormones, antifoulants, disinfectants, anaesthetics and fertilizers (A. Ahmad et al., 2022; A. L. Ahmad et al., 2022). Therefore, aquaculture can not only be affected by the pollution of surface water bodies but can itself become a source of contaminants of emerging concern (CECs) released into the environment through wastewater and farmed fish. This is known as cross-contamination (Lai et al., 2018). CECs change natural resource quality, interfere with biochemical processes, exert adverse effects on mutagenesis, disrupt endocrine function, and cause congenital disorders and carcinogenesis in aquatic species (A. Ahmad et al., 2022; Ramírez-Malule et al., 2020).

In addition to organic contaminants, potentially toxic elements also represent a hazard in aquaculture. Along with the well-known routes through which potentially toxic

elements (PTEs) enter water bodies (agricultural activities, industrial activities, etc.) in fish farming these pollutants can also be introduced through antifoulants, feed, algaecides, herbicides and plastic objects (Emenike et al., 2022; Mohsen et al., 2022). Some of PTEs such as Zinc, Iron, Copper, Nickel, Manganese and Cobalt are essential micronutrients for fish growth, however they become toxic above a certain amount. Hence their concentrations in water and aquatic food, together with those of non-essential elements (Lead, Cadmium, Mercury, Arsenic and Chromium), are strictly regulated (*COMMISSION REGULATION (EU) 2023/915*, s.d.; COM(2021)236, 2021; D. Lgs 31/2001, s.d.; Emenike et al., 2022) and several techniques have been developed to not exceed the law limits.

As mentioned in the introductory section, aquaculture water, contaminated surface water and waste water can be treated exploiting several techniques including physical processes (reverse osmosis, filtration, membrane technique, flotation, coagulation-flocculation), chemical (precipitation, ion exchange, electrochemical, reduction/oxidation treatments) and biological methods (Emenike et al., 2022). Among these, adsorption represents an effective strategy for the removal of PTEs and the development of adsorbent materials has become an increasingly important area of research (Noè et al., 2022).

The adsorption phenomenon is based on physicochemical interaction between adsorbent's functional groups and PTEs' species present in solution. The most common mechanism of adsorption occurs through electrostatic interactions as well as other mechanisms, including ion exchange, complexation, chelation, coordination and hydrogen bonding. Consequently, the PTEs removal efficiency is affected by experimental conditions as pH, temperature and pollutants concentration (Ugwu et al., 2020). Therefore, properly designing materials and setting up tests are fundamental.

Biopolymers-based materials, as already stated in the previous chapter, have been reported as an interesting alternative to classic adsorbents not only due to their low cost, high availability, ease of use and chemical modification, high biodegradability

and minimal toxicity (Subash et al., 2023) but also because they can be obtained from exhausted biomass deriving from the agro-industrial sector.

Although biopolymers such as cellulose, alginate, chitosan and gelatine naturally contain chemical groups capable of interacting with PTEs, it is often necessary to introduce new functionalities into the polymer matrix to improve the affinity with the species in solution. Furthermore, functionalization reactions are fundamental for the preparation of smart materials easily handleable, regenerable and reusable that can be used more efficiently than the pristine powdered bio-polymers. Among them, hydrogels represent a class of material increasingly studied in the recent literature (Kanmani et al., 2017; Medeiros Borsagli et al., 2015; Noè et al., 2021; Zanon et al., 2022).

Hydrogels are three-dimensional networks with high swelling properties in water thanks to the presence of the hydrophilic groups present in the polymeric structure such as hydroxyl, amino or carboxyl ones. They could be cross-linked *via* chemical bonds or other cohesive forces such as hydrogen bonds or hydrophobic interactions (Rana et al., 2024).

Depending on the kind of network, hydrogels could be classified as reversible or permanent. Reversible hydrogels are physically cross-linked, they can be easily formed thanks to weak interaction between the polymer chains, often obtained by the introduction of gelling ions. An example is the case of alginate in which mannuronic (M) and glucuronic blocks can be cross-linked through ionic interactions using Ca^{2+} as gelling ion (Figure 3.1) (K. Y. Lee & Mooney, 2012). This hydrogel network could be destroyed in presence of non-gelling cations as Na^{+}. Therefore, physically cross-linked natural hydrogels could possess lower stability and poorer mechanical properties in respect to other materials.

On the other hand, permanent hydrogels could be obtained forming covalent bonds between the polymer's chains exploiting several strategies (Mehta et al., 2023). A widely applied method is based on the use of selective functional groups through Schiff base formation, disulphide bonding, Michael addition or using several linkers

(small mono- or bi-functional molecules as formaldehyde, glutaraldehyde, genipin, diethyl squarate, *etc.*).

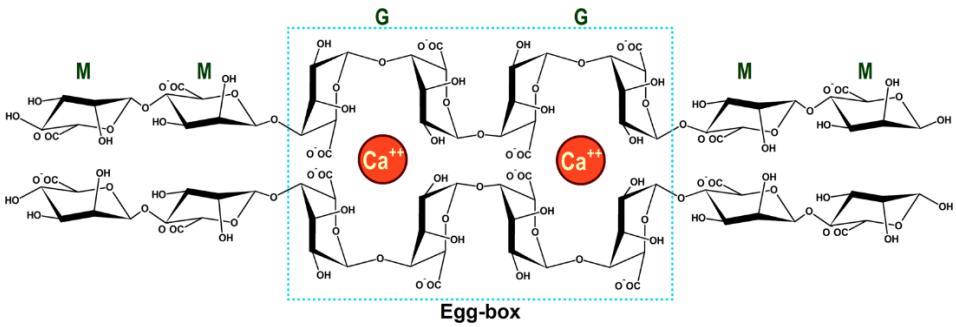

Figure 3.1 - Schematic of "Egg-box" structure in alginate hydrogel cross-linked with calcium ions (H.-R. Lee et al., 2019)

Cross-linking of free radicals is also reported in literature. It is started by an initiator and can be used to graft synthetic monomers over natural polysaccharides to improve their intrinsic properties (Bashir et al., 2020). An interesting strategy to obtain chemical cross-linked hydrogels is the UV-curing. This eco-friendly polymerization technique involves neither the use of solvents nor the production of waste and is very fast, thus saving energy (Pezzana et al., 2023; Sangermano et al., 2014; Sesia et al., 2024). An appropriate functionalization of the natural polymer allows the formation of covalent bonds between polymer chains under UV-light irradiation following the addition of a photoinitiator (Noè et al., 2021).

If potentially toxic elements can be efficiently removed exploiting appropriately developed adsorbent materials, for organic contaminants other techniques as advanced oxidation process, photocatalysis, electrochemistry or biological processes may be preferable.

Many integrated strategies, aimed at improving the performance of individual treatments and broadening the target of contaminants, have been developed in recent years. Among them, the so-called *hybrid materials*, are becoming more and more popular. They are the result of the combination of different components whose coupling leads to an improvement of the individual properties (Rigoletto et al., 2022).

The introduction of enzymes in these materials' structures is widely studied. Indeed, enzymes are increasingly used for environmental applications since they offer high catalytic capacity with milder reaction conditions, production of nontoxic compounds, absence of byproducts and environmental friendliness. Enzymes in free form have a very high activity, but they are not usually stable in solution and can be easily inactivated; in addition, they are often characterized by high costs (Calza et al., 2016). Hence, several immobilization techniques have been developed to improve their stability, facilitate their reuse and reduce the costs (Bornscheuer & Buchholz, 2005; Sheldon & Pelt, 2013; W. Zhou et al., 2021).

However, it must be taken into consideration that immobilization can on the one hand stabilize the enzymes and allow the exploitation of their catalytic capacities for multiple processing cycles, but it can also often involves a reduction in their activity (Marchis et al., 2012; Sheldon & Pelt, 2013).

Among the different enzyme immobilization strategies (Figure 3.2), covalent binding possesses many advantages, such as producing durable enzymes, increasing the enzyme stability and reducing probability of enzyme leakage (Maghraby et al., 2023) The covalent binding basically takes place by activation of the support *via* adding reactive molecules (Besharati Vineh et al., 2018). In the literature the coupling of enzymes with several inorganic materials is reported. The most studied systems involve the preparation of silica monoliths (Magnacca et al., 2012), titanium nanoparticles (Calza et al., 2016; Morsi et al., 2021), glass beads (Gomez et al., 2006; Marchis et al., 2012), and magnetic nanoparticles (Donadelli et al., 2018; Tavares et al., 2018). Furthermore, both synthetic and natural organic supports are also considered (Bracco et al., 2017; Chagas et al., 2015; Magri et al., 2005; Prokopijevic et al., 2014, 2017).

The use of hydrophilic polysaccharides is widespread. In this case the interaction with the enzymes occurs between functional groups present in amino acids (carboxylic group of aspartic acid, hydroxyl group of threonine, amino group of arginine, or sulfhydryl group of thiol) and those present in the polymers' structure (Sizemore et al., 2013).

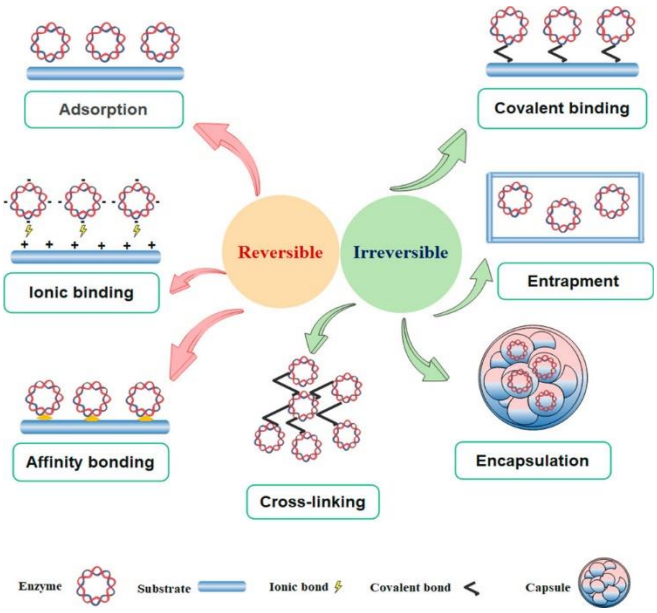

Figure 3.2 - Diagram illustrating major enzyme immobilization methods (Maghraby et al., 2023)

As in the case previously discussed of specific interaction with the PTEs, also for the enzyme immobilization it may be necessary to modify the biopolymers by introducing specific functionalities that guarantee the formation of stable bonds with the protein component (D.-M. Liu et al., 2018; Y. Liu & Chen, 2016; Maghraby et al., 2023).

In the following sections, the employment of biopolymers, both in powder and in hydrogel form, for the removal of PTEs from water matrices will be presented. Furthermore, the application of the same materials coupled with enzymatic catalysis for the treatment of water contaminated by organic compounds will be discussed.

3.1 Adsorption of mercury in aqueous solutions by functionalized soy derived

Among the PTEs, mercury (Hg) has received special attention due to its high toxicity for living organisms (Basu et al., 2023). It is released into the environment from different anthropogenic sources, including iron, steel, cement, and gold industries,

non-ferrous metal smelting, chloro-alkali industry, and direct mercury production industries (Pavithra et al., 2023).

Mercury and its compounds, both organic and inorganic, have neurotoxic, genotoxic, teratogenic, carcinogenic, and bioaccumulative effects (Algieri et al., 2024; Balali-Mood et al., 2021). Therefore, the Hg concentration limit in drinking water is set at very low values by different institutions. According to the World Health Organization (World Health Organization, 2021), U.S. Environmental Protection Agency (US EPA, 2015) and the European Directive (EU) 2020/2184, the Hg concentration limit in drinking water is 1 µg/L. Other restrictions are, in turn, oriented to minimize the mercury content in food, especially within fishery products, as reported in the EU Commission Regulation 2023/915 of 25 April 2023.

In recent years, different remediation techniques have been developed to avoid exceeding the threshold of mercury concentration in water and, among them, adsorption is considered one of the most effective methods for the purification of heavy metal-polluted water (Noè et al., 2022).

It is well known that mercury shows a high affinity for functional groups containing sulphur and nitrogen atoms in agreement with the hard-soft acid-base theory (Awad et al., 2021; Chowdhury et al., 2021; Du et al., 2021). Indeed, Lewis acids like Hg(II), could coordinate with lone pairs of Lewis bases (like N and S atoms), forming stable coordination complexes (Awad et al., 2021).

Considering this framework, in this research work, we tested the previous synthesised soy-deriving cellulose samples containing primary amino groups and thiols to treat both ultrapure and real water spiked with increasing concentration of mercury.

3.1.1 Materials and Methods

All chemical reagents were in analytical grade and used without further purification. The cellulose derivatives employed (Cell-SH and Cell-NH_2) have been synthesised and characterised as described in Chapter 1. Soy-derived cellulose (Cell) has been used as control material.

The real water sample has been collected in the farm *Società Agricola San Biagio Delia Revelli* located in the north of Italy (12084 Mondovì, Cuneo).

Real water sampling and characterization

Water was sampled in amber glass bottles, filtered with 70 mm glass microfibers filters (VWR) and stored at 4 °C. The sampled water was analysed to determine the main anionic species (by Ionic Chromatography, IC Metrohm Eco 925), metals (by Inductively Coupled Plasma Atomic Emission Spectrometry using an Agilent 5800 ICP-OES) and total organic carbon content (TOC) (obtained with Shimadzu TOC-5000 analyser).

Mercury adsorption tests

Mercury adsorption experiments were performed to evaluate the effect of Hg(II) initial concentration, solutions pH, and the role of the water matrix on the adsorption behaviour of the synthesized materials.

All the experiments were carried out using an adsorbent dose of 1 mg/mL and a contact time of 18 h, on the basis of preliminary adsorption tests (data not shown), which confirmed to be a sufficient period to reach equilibrium conditions.

Mercury stock solutions were prepared starting from mercuric chloride ($HgCl_2$). The concentration of Hg(II) in the aqueous solutions was determined by Cold Vapour Atomic Fluorescence Spectroscopy (CV-AFS) using a PSA Analytical Millennium Merlin instrument. The analyses were performed following the EN 13506 standard procedure.

The amount of mercury adsorbed at equilibrium, q_e (mg/g), was calculated according to the equation 3.1:

$$q_e = \frac{(C_0 - C_e) \cdot V}{W} \qquad (3.1)$$

where C_0 (mg/L) is the initial concentration of Hg(II), C_e (mg/L) is the equilibrium concentration after the adsorption experiment, V (mL) is the volume of the solution and W (g) is the mass of the adsorbent.

The equilibrium isotherms were mainly described using the Langmuir and Freundlich models. The first one considers the adsorption as chemisorption with the formation of a monolayer of adsorbate (Langmuir, 1918) and it is described by equation 3.2

$$q_e = \frac{q_m \cdot K_L \cdot C_e}{1 + K_L \cdot C_e} \quad (3.2)$$

where q_m (mg/L) is the maximum adsorption capacity and K_L (L/mg) is the Langmuir constant, which is related to the energy of the adsorption process.

The isotherm parameters were calculated using the linearized equation 3.3:

$$\frac{C_e}{q_e} = \frac{1}{q_m} \cdot C_e + \frac{1}{K_L \cdot q_m} \quad (3.3)$$

The separation factor R_L was also calculated using equation 3.4, as an index of the reversibility or irreversibility of the adsorption process:

$$R_L = \frac{1}{1 + K_L \cdot q_m} \quad (3.4)$$

When $R_L = 0$, it means that the isotherm is irreversible, and when $R_L = 1$, it indicates a linear isotherm. Moreover, if $0 < R_L < 1$, the isotherm is favourable, whereas $R_L > 1$ indicates an unfavourable isotherm (Gul et al., 2022).

On the other hand, the Freundlich model (Freundlich, 1932) considers the possible formation of multilayers of adsorbate or different surface energies for the monolayer in heterogeneous materials. This model is described by equation 3.5:

$$q_e = K_F \cdot C_e^{1/n} \quad (3.5)$$

where C_e (mg/L) is the Hg(II) equilibrium concentration, and K_F and *n* are the Freundlich constant and the heterogeneity factor, respectively. The value of the *1/n* factor indicates if the isotherm is favourable ($0 < 1/n < 1$), unfavourable ($1/n > 1$) or irreversible ($1/n = 0$) (Kaur & Jindal, 2019).
Isotherm parameters were calculated using the linearized equation 3.6:

$$ln(q_e) = ln(K_F) + \frac{1}{n} ln(C_e) \quad (3.6)$$

Finally, additional adsorption runs were carried out in real water from aquaculture production spiked with Hg(II) (1 mg/L).

3.1.2 Results and discussion

Characterization of real water sample

Before using aquaculture water as the matrix for the Hg(II) adsorption tests, the sample was analysed using different techniques. As summarized in Table 3.1, it was characterized by a pH of 7.3, a hardness value of 102.74 mg/L of $CaCO_3$ and 28.54 mg/L of total organic carbon.
The heavy metals and semimetals content (As, Cd, Cu, Pb and Hg) was below the detection limit (LOD) and anions' concentrations were near the value indicated in the Directive (EU) 2020/2184, meaning that the selected matrix was not polluted. Therefore, for the Hg(II) adsorption tests, the stock solution was prepared without any concentration correction.

Mercury adsorption tests in ultrapure water

Mercury adsorption tests were first carried out in ultra-pure water by analysing the final concentrations at equilibrium, *i.e*. after 18 hours of contact between mercury-containing solutions and the adsorbent materials (in accordance with the preliminary

kinetic tests). The adsorption isotherms were obtained from single experimental runs at 20 °C and natural pH (ca 5.0) with the initial mercury concentration ranging from 1 to 200 mg/L.

Table 3.1 - Real water sample characterization and comparison with the limit concentration values set by European Directive

Parameter	Unit	Value	Limits for human usage*	Limits for protection of salmonids**
pH		7.3	6.5-9.5[a]	6-9
Hardness	mg/L $CaCO_3$	102.74	-	-
TOC	mg/L	28.54	-	-
Ca	mg/L	24.5	-	-
K	mg/L	1.91	-	-
Mg	mg/L	10.6	-	-
Na	mg/L	5.06	200[a]	-
Si	mg/L	4.54	-	-
As	µg/L	< LOD	10[b]	50
Cd	µg/L	< LOD	5[b]	2.5
Cu	mg/L	< LOD	2[b]	0.04
Pb	µg/L	< LOD	5[b]	10
Hg	µg/L	< LOD	1[b]	0.5
F^-	mg/L	1.44	1.5[b]	6
Cl^-	mg/L	24.7	250[a]	-
NO_3^-	mg/L	52.5	50[b]	-
SO_4^{2-}	mg/L	51.04	250[a]	-
NO_2^-	mg/L	0.634	0.5[b]	0.01

*Directive (EU) 2020/2184 of the European Parliament and of the Council of 16 December 2020 on the quality of water intended for human consumption, Annex I, a) Indicator parameters, b) Chemical parameters

**(i) Directive (EU) 2006/44/EC of the European Parliament and of the Council of 6 September 2006 on quality of fresh waters needing protection or improvement to support fish life, Annex I; (ii) Italian Legislative Decree n. 152/2006 [Annex 2 and 5 part III], Section B: Criteri generali e metodologie per il rilevamento delle caratteristiche qualitative, per la classificazione ed il calcolo della conformità delle acque dolci superficiali idonee alla vita dei pesci salmonicoli e ciprinicoli.

Figure 3.3-A shows the amount of mercury adsorbed q_e (mg/g) plotted as a function of the equilibrium Hg(II) concentration C_e (mg/L). The isotherms can be classified as L2-type according to the Giles classification (Giles et al., 1974), with a significant slope at low mercury concentrations and a saturation value when the concentration of mercury in the solution increases.

The linear Langmuir and Freundlich plots are presented in Figures 3.3-B and C, while the estimated adsorption parameters are summarized in Table 3.2. For all the tested adsorbents, the best fitting of experimental data was obtained with the Langmuir model, suggesting that the adsorption of Hg(II) is mainly attributable to a chemisorption characterized by the formation of a monolayer of the adsorbate on the cellulose surface. The separation factor R_L is less than one for all the materials, indicating that mercury adsorption is a favourable process.

As evidenced by the maximum adsorption capacity at pH~5, which is 9.23, 32.26 and 43.86 mg(Hg)/g for Cellulose, Cell-NH_2 and Cell-SH, respectively, the introduction of thiols in the cellulose matrix ensures a greater removal of mercury from water solution. This is also highlighted by the K_L value, which expresses the affinity between adsorbate and adsorbent surface, which is significantly higher for the Cell-SH sample (1.1 L/mg).

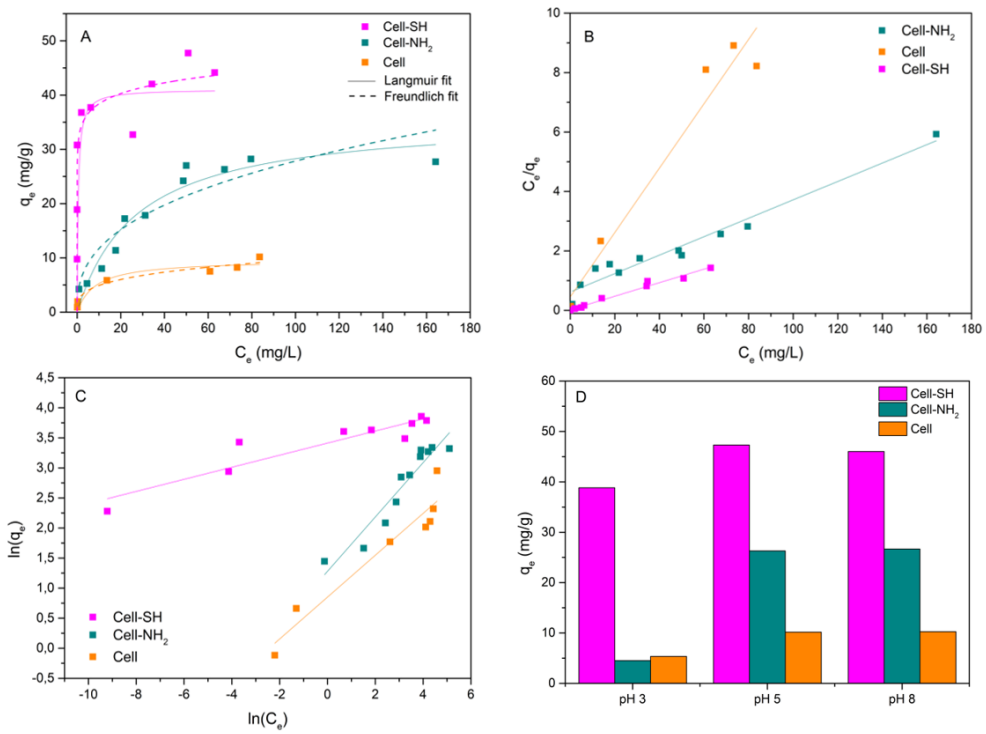

Figure 3.3 - A) Experimental data for mercury adsorption at pH 5, and Langmuir and Freundlich fit; B) Linear Langmuir model; C) Linear Freundlich model; D) qe values obtained for a 100 mg/L mercury solution at different pH.

Table 3.2 - Adsorption isotherms parameters for Hg(II) adsorption on cellulose based materials at pH 5

Langmuir parameters				
Material	**K_L (L/mg)**	**q_m (mg/g)**	**R^2**	**R_L**
Cell	0.24	9.23	0.961	0.31
Cell-SH	1.1	43.86	0.982	0.02
Cell-NH_2	0.05	32.26	0.963	0.38
Freundlich parameters				
Material	**K_F (L/mg)**	**n**	**R^2**	**1/n**
Cell	2.34	2.87	0.924	0.348
Cell-SH	30.3	9.96	0.863	0.100
Cell-NH_2	3.59	2.21	0.909	0.452

Indeed, the related isotherm shows a marked initial slope indicating that Cell-SH has very high effectiveness at low levels of initial mercury concentrations: a value of q_e = 0.99 mg/g was estimated for Cell-SH at the initial Hg(II) concentration of 1 mg/L and equilibrium concentration near zero.

This behaviour can be attributed to the strong affinity of sulphur toward mercury according to the principle of hard/soft acids and bases of Pearson (Pearson, 1988).

The effect of pH on the adsorption capacity of Cell-SH, Cell-NH_2 and Cellulose was investigated as well. The q_e values obtained for a 100 mg/L Hg(II) solution at pH 3, 5 and 8, are shown in Figure 3.3-D. As observed, increasing the pH from 5 to 8 did not lead to a significant difference in the adsorption capacities of the materials. However, by decreasing the pH at 3, a reduction in the amount of Hg(II) adsorbed by 18%, 83% and 48% was observed for Cell-SH, Cell-NH_2 and Cellulose, respectively. This behaviour could be ascribed to two different factors: (i) the Z-potential and surface charge of the three adsorbent materials as a function of pH, as discussed in Chapter 2 (Figure 2.20), and (ii) the speciation of $HgCl_2$. Indeed, at pH 3, $HgCl_2$ is the dominant species in solution, whereas by increasing the pH value up to 5, a contribution of HgClOH has to be also considered. Moreover, at pH 8, the two species HgClOH and $Hg(OH)_2$ coexist in the solution, becoming mercury hydroxide predominant at higher pH values (López-Muñoz et al., 2011).

The variation in the maximum adsorption capacity as a function of pH could also be an evidence of the different affinities between the functionalized cellulose surfaces and the characteristic mercury species at each pH value. According to these results, Cell-NH_2 and pristine cellulose show a low affinity for $HgCl_2$, but a high affinity for

$HgClO$ and $Hg(OH)_2$. By contrast, Cell-SH seems to be able to strongly interact with all the mercury species existing in the aqueous solution at different pH values.
Finally, it is reported in the literature that at low pH, metal adsorption could also be affected by the competition with protons for the occupation of the surface adsorption sites (Choi et al., 2020). This aspect could facilitate the removal of metal species adsorbed on the surface and allow the reuse of the material in subsequent adsorption-desorption cycles.

Mercury adsorption tests in real spiked water

Mercury adsorption tests were also carried out using the sampled aquaculture water as the aqueous matrix and Cell-SH as the adsorbent. Since the natural content of Hg in the aquaculture water was under the detection limit (Table 3.1), the mercury stock solution was prepared as described in the previous paragraph without any concentration correction. The adsorption isotherm of mercury was obtained at 20 °C from many single experimental runs with the initial Hg(II) concentration ranging from 1 to 200 mg/L.
The behaviour of Cell-SH was then compared with that of Cell and Cell-NH_2 at low (15 mg/L) and high (100 mg/L) Hg(II) initial concentrations.
Results are shown in Figure 3.4-A, where the amount of mercury adsorbed at equilibrium, q_e, is plotted as a function of the resulting aqueous Hg(II) concentration, C_e (mg/L). As already observed in the previous experiments in ultra-pure water, also these isotherms can be classified as L2-type according to the Giles classification.
The linear Langmuir and Freundlich plots are presented in Figures 3.4-B and C, while the estimated adsorption parameters are summarized in Table 3.3. Similarly, to the experiment in ultra-pure water, the best fitting of experimental data was obtained with the Langmuir model, suggesting that the adsorption of Hg(II) is mainly attributable to a chemisorption characterized by the formation of a monolayer of the adsorbate on the cellulose surface. The separation factor $R_L < 1$ indicates that mercury adsorption is a favourable process.

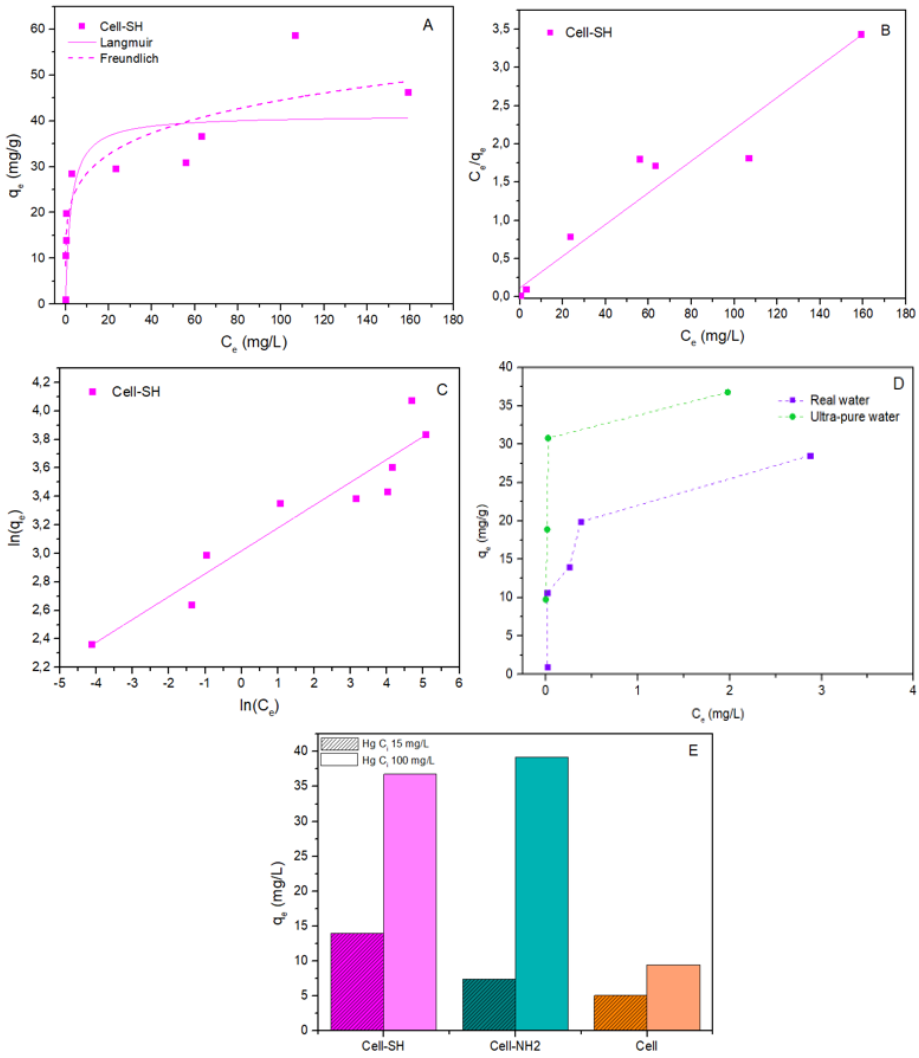

Figure 3.4 - A) Experimental data for mercury adsorption in real water, and Langmuir and Freundlich fit; B) Linear Langmuir model; C) Linear Freundlich model; D) comparison between q_e of Cell-SH in ultra-pure water and real water at low Hg(II) concentration; E) q_e values obtained for a 15 mg/L and 100 mg/L mercury solution in real water matrix using Cellulose, Cell-NH_2 and Cell-SH

Table 3.3 - Adsorption isotherms parameters for Hg(II) adsorption in the spiked real water matrix

Langmuir parameters				
Material	**K_L (L/mg)**	**q_m (mg/g)**	**R^2**	**R_L**
Cell-SH	0.17	48.3	0.936	0.1186
Freundlich parameters				
Material	**K_F (L/mg)**	**n**	**R^2**	**1/n**
Cell-SH	20.45	6.23	0.887	0.1604

Looking at the estimated maximum adsorption capacity q_m, Cell-SH shows a comparable performance in real water (48.3 mg/g) and in ultra-pure water (43.86 mg/g), while the matrix effect is noticeable in the first part of the isotherm. Indeed, as shown in Figure 3.4-D, for low Hg(II) initial concentration, the affinity of the Cell-SH surface seems to be affected by the other substances present in aquaculture water. One of the factors affecting the results in real matrices could be represented by the dissolved organic matter since it shows complexing capabilities toward metals due to the presence of different functional groups. The complexation of mercury could hinder the reaching of the Cell-SH surface, affecting the adsorption process (C. Chen et al., 2020; Johs et al., 2019; D. Li et al., 2024).

However, the relatively low TOC value (28.54 mg/L) justifies a competitive effect at low Hg(II) concentration but without affecting the maximum adsorption capacity, resulting in a q_m comparable to that obtained in ultra-pure water.

Moreover, the presence of anions or cations could also influence the adsorbent capabilities of Cell-SH. According to recent studies on similar materials (Algieri et al., 2024; D. Li et al., 2024), the presence of anions such as NO_3^- has no influence on mercury adsorption and SO_4^{2-} shows only a limited effect, while Cl^- has a greater influence on mercury removal due to its complexation capabilities that increase Hg(II) distribution in water (Z. Li et al., 2013; D. Zhang et al., 2017). The newly formed species $HgCl_3^-$ and $HgCl_4^{2-}$, which are negatively charged, could hardly interact with the surface of adsorbents such as Cell-SH with a strongly negative Z-potential at the working pH (Figure 2.20, Chapter 2) (P. H. Chen et al., 2014).

The stronger interaction of mercury with sulphur in the presence of competing cations was also observed (Ruan et al., 2022; Tran et al., 2015; M. Wang et al., 2022). Similar findings were reported by Wang et al. for amino-functionalized materials, who tested the effect of typical wastewater background ions (Na^+, Mg^{2+}, Ca^{2+}, K^+) and other heavy metals (Co^{2+}, Cu^{2+}, Pb^{2+}, Zn^{2+}, Ni^{2+}), confirming the anti-interference ability of Hg(II) adsorption process (Z. Wang et al., 2024).

As shown in Figure 3.4-E, at low Hg(II) initial concentrations (15 mg/L) the adsorbent capacities of Cell-NH_2 remain unchanged compared to the results obtained

in ultra-pure water. Nevertheless, the improvement of the Cell-NH_2 performance and, thus, the flattening of the differences in adsorption efficiency between Cell-NH_2 and Cell-SH in aquaculture water at 100 mg/L may be somehow attributed to the matrix effect (Cui et al., 2013; M. Wang et al., 2022; G. Zhang et al., 2009; J. Zhu et al., 2009). One possible hypothesis is based on the fact that when ions are adsorbed *via* inner-sphere association (namely through specific adsorption, such as ligand exchange), they are less susceptible to the effect of the ionic strength, being able to even respond to it with greater adsorption (Lv et al., 2012; Sarkar et al., 2000). However, the explanation that seems more reasonable, according to what has already been highlighted in ultra-pure water experiments, is that Cell-NH_2 is more sensitive to mercury speciation and the species like $HgCl_3^-$ and $HgCl_4^{2-}$ can interact with amino groups, although the surface charge is overall slightly negative (Nabais et al., 2007). Finally, additional tests were carried out with a 1 mg/L Hg(II) solution prepared in real water with different amounts of Cell-SH as adsorbent in order to reach a mercury concentration below the EU allowed limit for drinking water (1 μg/L). The final concentrations of Hg(II) remaining in the solution obtained using 1, 2 and 3 mg/mL of Cell-SH were 18, 11 and 0.8 μg/L, respectively, indicating that the developed materials could be considered effective in the treatment of real mercury-contaminated waters.

Overall, the Hg removal results obtained in this work fall within average values found in the literature for biomass-derived adsorbents, except for activated carbons/biochars (Jeong et al., 2024), in which a generally favourable textural and porosity features play a major role (Aleku et al., 2024; Giwa et al., 2022). A very recent review, indeed, summarizes the efficiencies of different mercury adsorbents, confirming our statement (Georgin et al., 2024). Moreover, what comes to light from a broader examination of the studies focused on Hg decontamination is that many strategies rely on the presence of metal-based compounds, often in the form of nanoparticles (I. Ahmad et al., 2024; Chizitere Emenike et al., 2023) that, although able to bring about high efficiencies, might be associated with secondary environmental side effects (Bahadar et al., 2016; Kumah et al., 2023). In the specific field of aquaculture, the

presence of iron, aluminium and zinc, not considered among the most dangerous metals and widely used in Hg adsorption (Tonu et al., 2024), poses risks for the welfare of fish, potentially resulting in the reduction of oxygen transfer if precipitate as salts (EU Platform on Animal Welfare Own Initiative Group on Fish, 2022).

3.2 Cellulose-based hydrogels for PTEs from aquaculture water and comparison with other bio-based hydrogels

Not only mercury but also the presence of other potentially toxic elements such as Pb, Cu, Cd, Zn, Ni and As in water represent a well-known problem for ecosystems safety and for human health. Furthermore, the transition from controlled laboratory conditions to those of a system that comes close to the real one implies the consideration of several aspects.

The study of the adsorption phenomenon becomes much more complex when the variables considered increase. Factors such as working pH, contaminants concentration and matrix effect significantly influence sorbents' behaviour.

Indeed, the acidity of the system determines on the one hand the surface charge of the adsorbent materials and on the other the speciation of the PTEs. This must be considered together with the intrinsic properties of each element such as electronegativity, ionic radius and charge density as well as the metal-ligand complexation constants that determines the strength of the specific interaction with the sorbent functional groups. All these aspects influence in a more or less significant way the competition of PTEs for the surface adsorption sites and, consequently, the efficiency of the water remediation treatment. Furthermore, real water samples may contain non-negligible levels of organic matter and inorganic ions which can inhibit adsorption efficiency by complexing contaminants or themselves acting as competitors for the surface sites of adsorbents.

In the next paragraphs the role of these factors on the adsorbent capacities of three different sorbents will be discussed in depth. The properties of soy-derived cellulose

based hydrogels has been studied and compared with that of gelatine and chitosan based hydrogels synthesised in collaboration with the Politecnico of Turin.
All hydrogels have been characterized and tested for the removal of a mixture of seven PTEs (copper, lead, cadmium, nickel, zinc, arsenic and mercury) in both ultra-pure and aquaculture spiked water. The influence of pH and pollutants' initial concentration have been evaluated as well as the matrix effect. Furthermore, we optimized hydrogels regeneration treatment and investigated the reusability of our materials for several subsequent adsorption-regeneration cycles.

3.2.1 Materials and methods

Materials

Medium molecular weight chitosan (CHI, Mw = 190–310 KDa, 75–85% N-deacetylation degree), gelatine from cold-water fish skin (GEL), methacrylic anhydride (MA, 94%), acetic acid (96%), the photoinitiator Irgacure 2959, alginic acid sodium salt (99%), calcium chloride $CaCl_2$ (>93%), disodium ethylenediaminetetraacetate Na_2EDTA (99%), hydrochloric acid HCl (37%) and sodium hydroxide NaOH (>98%) were purchased from Sigma-Aldrich (Milano, Italy).
Carboxymethyl cellulose (CMC) was synthesised as described in Chapter 2.
Multi-elements standard solutions were prepared from concentrated (1000 and 10,000 mg/L) stock solutions (Sigma-Aldrich TraceCERT St. Louis, MO, USA) and diluted to the selected concentrations with high pure water (HPW), i.e., water purified in a Milli-Q system and having a resistivity of 18.2 MΩ·cm, and used for ICP-OES measurements.

Synthesis of carboxymethylcellulose-alginate hydrogels

CMC-alginate hydrogels (HY-ACMC) were prepared through gelation in calcium chloride solution using a CMC-alginate ratio of 1:3. In brief, 0.225 g of sodium alginate and 0.18 g of CMC were dissolved in 12 mL of distilled water and left under

stirring until complete homogenization. Successively, the viscous solution was dripped in 0.2 M $CaCl_2$ solution with a plastic syringe in order to obtain beads (Rigoletto et al., 2023). Spherical hydrogels were left in the gelling solution for 3 days, then washed with distilled water and dried at 105°C overnight.

Synthesis of chitosan hydrogels

To synthesise chitosan-based hydrogel, an initial methacrylation reaction is required. The methacrylation reaction of chitosan (CHI) was carried out as previously mentioned (Sesia et al., 2022). CHI was solubilized in 2% wt acetic acid aqueous solution with a concentration of 1.5% wt. Then, methacrylic anhydride (MA) was added dropwise with a 1:20 molar ratio between aminoglucose moieties of CHI and MA. The solution was stirred for 4 h at 50°C, then transferred into a dialysis tubing cellulose membrane and dialyzed against distilled water for 4 days to remove the excess of MA and the resulting by-products from the methacrylation reaction. Successively, the product was freeze-dried to remove water and obtain the methacrylated chitosan (MCHI).

In order to obtain a three-dimensional polymeric network, the chitosan-based hydrogels (HY-MCHI) were produced by means of radical photopolymerization (Sesia et al., 2022). A total of 1.5% wt of MCHI was dissolved in 2% wt acetic acid solution, then 2 phr (per hundred resin) of Irgacure 2959 was added. Once the mixture was homogenous, the formulation was poured into a cylinder-shape silicone mold (1 cm in diameter, 1 cm in the height) and irradiated for 5 min with UV light (90 mW/cm^2) using a Hamamatsu LC8 lamp with 8 mm light guide and spectral distribution range of 240-400 nm. Finally, the produced hydrogels were air-dried and store at room temperature.

Synthesis of gelatine hydrogels

As for CHI, gelatine from fish skin (GEL) was also methacrylated following a previously reported procedure (Noè et al., 2022; Vigata et al., 2020). Firstly, 30% wt of GEL was solubilized in distilled water at 50°C. Then, after the complete

homogeneity was achieved, 0.6 g of MA for 1 g of GEL was added dropwise. The reaction was conducted for 4 h at 50°C under stirring condition and at pH 8 by the addition of 3 M NaOH solution. The resulting solution was dialyzed against distilled water for 3 days and then freeze-dried. As well as HY-MCHI, also the gelatine-based hydrogels (HY-MGEL) were obtained through radical UV-curing (Noè et al., 2022). MGEL (30% wt) was dissolved in distilled water before adding 1 phr of Irgacure 2959. Subsequently, the liquid solution was transferred in rectangular silicone mold with thickness equal to 1 mm. The samples were irradiated for 1 min with UV light (90 mW/cm^2) by means of the same Hamamatsu lamp mentioned above, finally the hydrogels were air-dried.

Characterization techniques

CMC characterization is completely reported in Chapter 2.

The successful methacrylation reactions of CHI and GEL were confirmed by attenuated total reflectance-infrared spectroscopy (ATR-FTIR). Thermo Scientific Nicolet iS50 FTIR spectrometer (Thermo Fisher Scientific, Milano, Italy) equipped with a diamond crystal ATR accessory and a resolution of 4 cm^{-1} in the range of 4000–600 cm^{-1} was used.

The surface charge of HY-ACMC hydrogels was investigated through the Z-potential measurement. About 500 mg of swelled samples were introduced into a cylindrical cell. The ζ potential was evaluated as a function of pH in 0.001 M KCl electrolyte solution. 0.05 M HCl and 0.05 M NaOH solutions were added to change the pH for titration in the acid and alkaline range, respectively. Four ramps were carried out for each point collected. An electrokinetic analyzer (SurPASS, Anton Paar) equipped with an automatic titration unit was used.

The swelling capability of the hydrogels was investigated using a gravimetric method. Dried hydrogels were placed in distilled water at room temperature and the weight increase was monitored by removing gels from the water and weighing them after a quick removal of water from the surface with filter paper. The swelling ratio (S_w) was calculated with the equation 3.7 where ws and wd are the weight of the swollen and dry samples, respectively.

$$S_w = \frac{W_s - W_d}{W_d} \quad (3.7)$$

PTEs adsorption test in high pure water

As previously mentioned, the adsorption behaviour of the different hydrogels was tested evaluating the removal from water of seven PTEs: copper (Cu), lead (Pb), cadmium (Cd), nickel (Ni), zinc (Zn), arsenic (As) and mercury (Hg).

To evaluate the influence of PTEs initial concentration and pH on the adsorption capacity, adsorption experiments were carried out in multi-element solution at specific concentration and maintaining a fixed pH value. PTEs solutions have been prepared in high pure water and treated using 1 g/L of adsorbents.

PTEs removal percentage (R%) and adsorbent capacities (q_e), expressed in mg of PTEs adsorbed for g of adsorbent have been calculated using the following equations:

$$R\% = 100 - \left(\frac{C}{C_0} \times 100\right) \quad (3.8)$$

$$q_e = \frac{(C_0 - C) \times V}{W_{HY}} \quad (3.9)$$

where C_0 is the PTE's initial molar concentration, C is the PTE's molar concentration at each contact time, V is the volume (L) of PTEs multi-element solution and w_{HY} is the weight (g) of adsorbent use for adsorption experiments.

Influence of PTEs initial concentration

The influence of PTEs initial concentration was investigated by using multi-element stock solutions prepared at the concentration of 10^{-6}, 10^{-5} and 10^{-4} M (for each element). Adsorption experiments were carried out at pH 5 with an adsorbent concentration of 1 g/L and PTEs' concentration have been determined at different contact times (in the range 0-24 hours) by Inductively Coupled Plasma Atomic Emission Spectrometry (ICP-AES, PerkinElmer Optima 7000 DV spectrometer) or

by Inductively Coupled Plasma Mass Spectrometry (ICP-MS, Agilent 7500ce) as function of initial concentration.

Influence of solution pH

The influence of pH on adsorbents' behaviour was evaluated by performing adsorption tests in a 10^{-5} M multi-element solution, using an adsorbent concentration of 1 g/L at pH 3.5, 5 and 7.

PTEs' concentrations were determined at different contact times by ICP-AES and their speciation was studied. For this purpose, a modelling technique was employed, assuming that only hydrolysis equilibria occur as expected on the basis of the composition of solutions used during the test. Speciation diagrams for each metal cation were obtained by PyES software (Castellino et al., 2023) taking into consideration: (i) thermodynamic formation constants (infinite dilution condition) (*Academic Software. Sourby Old Farm, Timble, Otley, Yorks, LS21 2PW. In SC-Database. The IUPAC Stability Constant Database,Version 5.84*, s.d.); (ii) temperature of 25°C; (iii) metal concentration 10-5 M; (iv) pH range between 3 and 8.

PTEs adsorption tests in real water samples

Two different water samples from aquaculture farms have been employed as matrix to study adsorption capacity in real conditions: Italian koi carps' aquaculture water from the Agrozootechnics Centre "Tetto Frati" (Carmagnola – Turin, Italy) and Danish aquaculture water from Ultraaqua (Aalborg, Denmark). After the sampling, the water samples were stored at – 18°C until their use.

Water samples were thawed and filtered with 0.45 µm cellulose acetate filters, their pH and hardness were measured. Successively, water samples were acidified with HNO_3 (0.1%) and their original PTEs' content determined by ICP-MS spectrometry. For the employment in adsorption experiments, water samples thawed, not-filtered and not-acidified were used as matrices for PTEs solutions. Adsorption tests were carried out in multi-element solutions in which each element was present around its

Italian legal limit concentration (50 µg/L As; 22 or 40 µg/L Cu; 10 or 20 µg/L Pb; 50 or 75 µg/L Ni and 200 or 300 µg/L Zn as reported in Table AII-2 Appendix II) as function of water hardness (Italian Legislative Decree n°152/2006, Annex 2, Part III, Section B). Instead, Cd and Hg were introduced with a concentration of 5 µg/L which is higher than the legal limit (2.5 and 0.5 µg/L respectively). PTEs solutions were prepared using real waters as matrix and treated with 1 g/L of each adsorbent. PTEs' concentrations were determined at different contact times by ICP-AES. The experiments were carried out between 0 and 180 minutes of contact with the hydrogels, which is the appropriate time to reach the equilibrium of PTEs removals, as previously verified.

Hydrogels regeneration and reuse

Different regeneration methods were investigated in order to evaluate the possibility to use the hydrogels for multiple successive adsorption-desorption cycles. For this purpose, preliminary tests with HY-ACMC have been done using HCl 0.01 M; HCl 0.1M and Na_2EDTA 0.01 M as PTEs desorption mediums (Charpentier et al., 2016; Fan et al., 2019; Z.-H. Hu et al., 2018).

At the end of each adsorption test, HY-ACMC hydrogels were washed with 10 mL of ultrapure water and put in contact with 20 mL of desorption solution. Released PTEs' concentrations in the washing water and in the regeneration solutions were determined at different times (0-240 min) by ICP-AES spectrometry.

In a second phase, multiple desorption methods were studied. At the end of the adsorption test HY-ACMC hydrogels were added to 20 mL of each desorption solution for 30 minutes, then filtered and added to 20 mL of fresh desorption solution. The treatment was repeated two more times and the four volumes of regeneration medium were analysed by ICP-AES spectrometry to evaluate the released amount of PTEs.

To evaluate the possibility to reuse the hydrogels for several cycles of adsorption-desorption, 0.01 M Na_2EDTA was selected as the best regeneration solution.

Classic adsorption experiments of 10^{-5} M multi-element solution at pH 5 were carried out using 1g/L of adsorbent and PTEs concentrations were monitored at fixed adsorption time (0, 60, 120 and 180 min) by ICP-AES spectrometry. At the end of the experiments, hydrogels were washed with 10 mL of ultrapure water and then subjected to 3 subsequent regeneration treatments, each one lasting about 30 min, with 20 mL of Na_2EDTA 0.01 M. PTEs concentrations released during each treatment were monitored by ICP-AES spectrometry.

After the regeneration process, the hydrogels have been used for two other adsorption cycles interspersed with 3 regeneration cycles.

The desorption (Des), expressed in mg/g, and desorption percentages (Des%) were calculated using the following equations:

$$Des = \frac{C \times V_{reg}}{W_{HY}} \quad (3.10)$$

$$Des\% = \frac{W_{PTE\ des}}{W_{PTE\ ads}} \times 100 \quad (3.11)$$

Where V_{reg} (L) is the volume of regeneration solution (HCl 0.01 M; HCl 0.1 M or Na_2EDTA 0.01 M), W_{HY} (g) is the dried weight of adsorbent, C is the PTEs molar concentration at each regeneration treatment time, $W_{PTE\ ads}$ is the weight (mg) of each PTE adsorbed at the end of the adsorption experiment, $W_{PTE\ des}$ is the weight (mg) of each PTE desorbed at each regeneration treatment time.

3.2.2 Results and discussion

Characterization of synthesised hydrogels

Attenuated total reflectance-infrared spectroscopy (ATR-FTIR) was used to confirm the functionalization reactions of chitosan and gelatine. Figure 3.5 shows ATR-FTIR spectra of all the pristine and chemically modified materials employed for the hydrogel synthesis.

For HY-MGEL and HY-MCHI preparation the incorporation of methacrylic groups is crucial to UV-cure gelatine and chitosan.

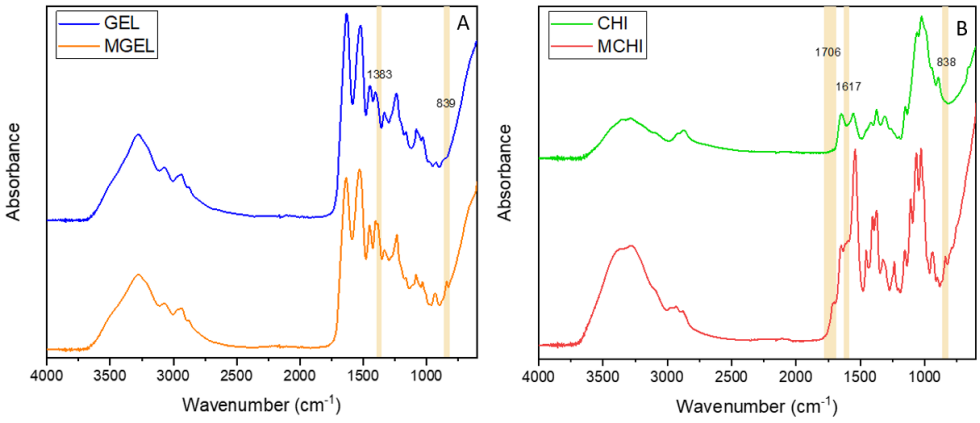

Figure 3.5 - ATR-FTIR spectra of pristine and functionalized materials (, spectral zones showing the functionalization are highlighted in light brown): (A) comparison between gelatine and methacrylated gelatine; (B) comparison between chitosan and methacrylated chitosan

In Figure 3.5-A the FTIR spectra of GEL before and after the functionalization are reported. As can be noted in the MGEL spectrum, two new peaks appeared at 1383 and 839 cm^{-1}, that can be assigned to the C-O stretching and C=C bending vibrations, respectively (Noè et al., 2022). In Figure 3.5-B the spectra of CHI and MCHI are compared. Also in this case, the appearance of new signals in the MCHI spectrum suggested the achievement of the methacrylation reaction. In particular, the introduction of the methacrylic groups was confirmed in the MCHI spectrum by the presence of the signal at 1706 cm^{-1}, attributed to the C=O stretching, and the signals at 1617 and 838 cm^{-1}, assigned to the C=C stretching and bending vibrations, respectively (Sesia et al., 2022).

After functionalization either physical or chemical cross-linked hydrogels were prepared. The swelling capabilities of the different hydrogels were assessed by a gravimetric measure. Figure 3.6 shows the increase in weight as a function of the contact time with ultrapure water for HY-ACMC and HY-MGEL, while the Sw values at the equilibrium state for all the adsorbent materials are reported in Table 3.4. According to Noè et al, HY-MCHI shows a superior swelling capability with a

Sw_{eq} of 6.16 achieved in less than an hour of immersion in water (Noè et al., 2022), while HY-MGEL and HY-ACMC present similar behaviour with Sw_{eq} values of 2.2 and 2.1 respectively, reaching the equilibrium in 4 and 5 hours.

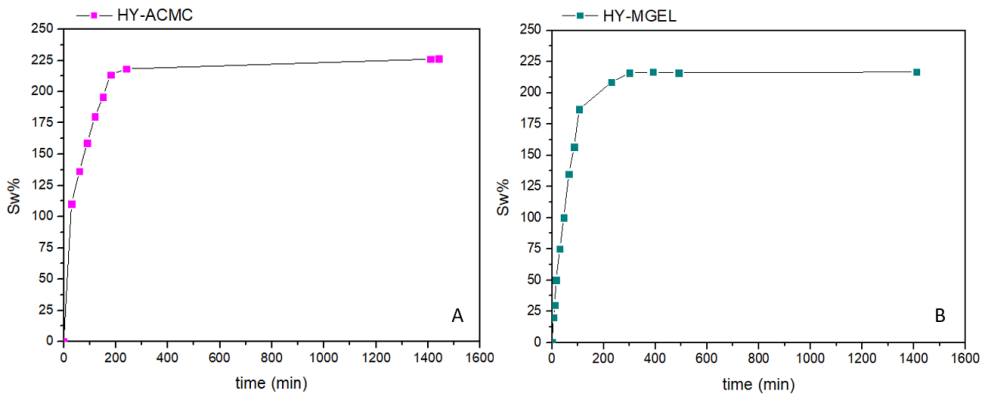

Figure 3.6 - Swelling tests results on HY-ACMC and HY-MGEL

Table 3.4 - Swelling and point of zero charge (PZC) values for synthesised hydrogels

	S_{Weq}	PZC
HY-ACMC	2.2 (This work)	< 3 (This work)
HY-MGEL	2.1 (This work)	4.4 (Goudie et al., 2023; Noè et al., 2022)
HY-MCHI	6.16 (Noè et al., 2022)	6.3-7.4 (Sesia et al., 2022)

Another important aspect is the ionic state of the hydrogels' surface that plays a crucial role in the interactions with metal ions, as it depends on pH. The surface charge as a function of pH values was investigated by means of the Z-potential measurement.

As shown in Table 3.4, the HY-MGEL's surface charge was proved to be strongly affected by pH with a point of zero charge (PZC) at pH around 4.4 (Benbettaïeb et al., 2020; Goudie et al., 2023; Noè et al., 2022; Shih et al., 2018; Song et al., 2019). Noè et al. (Noè et al., 2022) performed Z-potential analysis on methacrylated gelatine and demonstrated that under acidic conditions HY-MGEL possesses a positively charged surface due to the protonation of its amino groups. Instead, at pH values

above 4.4, the HY-MGEL's surface charge is negative as a result of the functional group deprotonation (Noè et al., 2022; Song et al., 2019). The same trend of Z-potential was also found for HY-MCHI with a PZC at a pH of about 6.3-7.4, as suggested by chitosan pKa of 6.5. Therefore, at acidic pH the HY-MCHI amino groups are protonated causing a positive charge of the surface, while the HY-MCHI exhibits negative zeta potentials as pH increased due to the deprotonation of hydroxyl groups (N. Li & Bai, 2005; Noè et al., 2022; Sesia et al., 2022; Y. Zhu et al., 2018). Furthermore, the protonated amino groups cause an electrostatic repulsion among the HY-MCHI's polymeric chains, making the hydrogel chemically and mechanically unstable (Sesia et al., 2022). As suggested by the measurement of the Z-potential, both HY-MGEL and HY-MCHI exhibit an amphoteric nature (Borges-Vilches et al., 2020; Dong et al., 2014; Peng et al., 2021; Shih et al., 2018; B. Wang et al., 2020; Zhao et al., 2012; F. Zhu et al., 2022).

The Z-potential analysis of HY-ACMC hydrogels (data not shown) evidenced a negative surface charge of the material throughout the pH range studied (3-7) with a tendency to increase as acidity increases, suggesting a PZC at pH<3 (Table 3.4). This trend is in agreement with several studies (Bastos et al., 2018; Chung et al., 2022; C. Liu et al., 2019) that reported similar results for both sodium alginate and carboxymethyl cellulose. Both these biopolymers contain carboxylate and show pKa value between 3.5 and 3.7 (T. Cai et al., 2013; Chung et al., 2022). Therefore, since the pH range studied is above the pKa, the functional groups are deprotonated, resulting in a negative surface charge of HY-ACMC hydrogels.

The Z-potential values of these adsorbents at different pH together with the PTEs chemical speciation are crucial factors to understand the adsorption process (Lam et al., 2018).

PTEs adsorption test in ultra-pure water

HY-ACMC, HY-MGEL and HY-MCHI have been tested for PTEs' removal from aqueous matrix. To elucidate adsorption behaviour of each material, experiments at different initial PTEs concentration and at diverse pH values were carried out.

The influence of initial PTEs concentration was studied through adsorption tests carried out at pH 5 in 10^{-6}, 10^{-5} and 10^{-4} M multi-element solutions (complete removal curves as function of contact time are reported in Appendix II, Figure AII-1). As reported in Figure 3.7, both HY-ACMC and HY-MGEL show good removal percentages for most of the tested elements after 24 hours of treatment. In particular, HY-ACMC hydrogel leads to a removal percentage > 95% for Pb and ≥ 75% for Cu and Cd for all the PTEs' initial concentrations considered.

Gelatine based hydrogel adsorption capacity is more affected by elements' concentration. Indeed, HY-MGEL shows decreasing R% of Zn (96%; 54% and 6%) going from 10^{-6} M to 10^{-4} M and a similar behaviour can be noted also for Cd and Ni. However, for all investigated concentrations, a removal percentage higher than 40% for most contaminants is ensured.

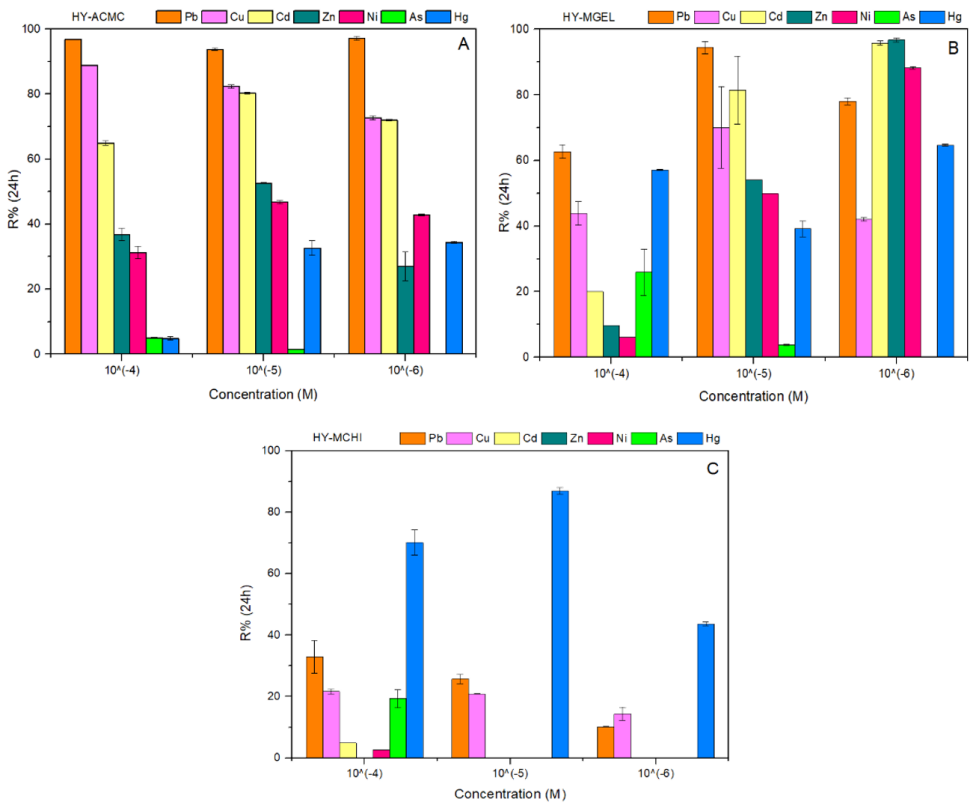

Figure 3.7 - Removal percentages after 24 h of contact with 1g/L of adsorbent as function of PTEs concentration:(A) HY-ACMC; (B) HY-MGEL; (C) HY-MCHI

On the other hand, HY-MCHI shows a high specificity for Hg which is removed between 45 and 90% as a function of initial concentration.

To evaluate the possible use of hydrogels in aqueous matrix with different acidity levels and monitor the PTEs' removal efficiency as the pH varies, adsorption tests were carried out at different pH values (3.5, 5 and 7) maintaining an initial PTEs concentration of 10^{-5} M. The solution pH affects not only the surface charge of the materials, as demonstrated by Z-potential measurements, but also PTEs speciation (Appendix II, Figure AII-3). Therefore, both these factors influence the adsorption phenomenon since they determine the interaction between adsorbate and adsorbent (Lam et al., 2018).

Figure 3.8 summarizes the removal percentages obtained after 24 hours of contact for HY-ACMC (Fig 3.8-A), HY-MGEL (Fig 3.8-B) and HY-MCHI (Fig 3.8-C), while the complete adsorption curves as a function of contact time are reported in Appendix II, Figure AII-2.

HY-ACMC shows similar adsorption capacities throughout the studied pH range after 24 hours of contact. This behaviour agrees with Z-potential, which is negative for all the pH considered with decreasing values as the alkalinity of the solution increases (Table 3.4). The negative surface allows HY-ACMC to establish an electrostatic interaction with metals in cationic form or as positively charged hydrolytic species. Indeed, the highest removal percentages for HY-ACMC were found for Pb, Cu and Cd, which are predominantly present as Pb^{2+} or $Pb(OH)^{+}$, Cu^{2+} and Cd^{2+}, respectively (Appendix II, Fig. AII-3), in the pH range 3-7. Although Figure 3.8-A shows a selectivity of Pb, Cu and Cd removal by HY-ACMC in the multi-element solution, the removal percentages for Zn and Ni are not negligible (about 30-50%) since they are present as divalent cations, as well as Cd, and can be adsorbed through electrostatic interactions.

The removal trend (Pb > Cu > Cd >> Zn ≥ Ni) is the result of a competition for the surface adsorption sites of the adsorbent and depends on metallic ions properties as electronegativity, ionic radius and charge density. Considering Pb, Cu, Cd and Zn, the removal affinity of HY-ACMC matches with Pauling's electronegativity order

(Pb 2.33; Cu 1.9; Cd 1.69 and Zn 1.65) and with the reverse order of hydrated ionic radius (Pb 4.01 Å; Cu 4.19 Å; Cd 4.26 Å and Zn 4.3 Å), and consequently of the charge density. These trends are in agreement with those reported in similar studies about metal ions competitive removal (Zhan et al., 2018; L. Zhang et al., 2016; M. Zhang et al., 2020).

Furthermore, to explain competitive adsorption another crucial factor is the stability constants of the metal-ligand complexes, that in HY-ACMC hydrogels are represented by metal – acetate complexes:

$$M^{n+} + \text{-}COO^{-} \leftrightarrow M(COO)^{n-}$$

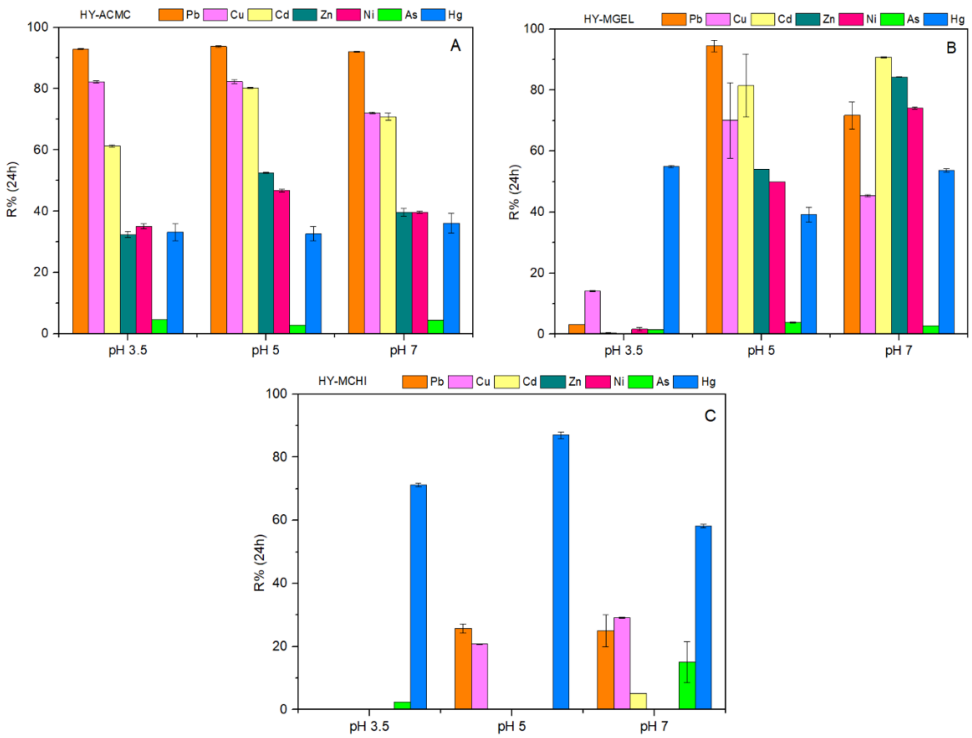

Figure 3.8 - Removal percentages after 24 h of contact with 1g/L of adsorbent as function pH: (A) HY-ACMC; (B) HY-MGEL; (C) HY-MCHI

As reported in Appendix II, Table AII-1, the logK values for Pb, Cu, Cd, Zn, and Ni are 2.58, 2.21, 1.92, 1.57 and 1.44, respectively (NIST SDR 96 Database (t = 25 °C, I = 0), which perfectly reflect the removal order found experimentally.

However, it was found out that in neutral condition a longer time was required by HY-ACMC to reach the equilibrium state (Appendix II, Fig AII-2) from around 4 hours at pH 3.5 and 5 to 5 hours at pH 7. Pb and Cu are removed with similar kinetics at pH 3.5 and 5 since they are present as aquaions. Instead, at pH 7, the species $Pb(OH)^+$, $Cu(OH)^+$ and $Cu(OH)_{2(s)}$ are present (Appendix II, Fig. AII-3) reducing the amount of aquaions species and leading to a slightly lower removal percentage after 24 hours of contact.

Unlike HY-ACMC, HY-MGEL shows very low or no effectiveness in removing the majority of the PTEs studied at pH 3.5 (Fig 3.8-B). As can be detectable from the Z-potential measurements, the gelatine-based material has a positive surface charge at pH 3.5 (PZC = 4.4, Table 3.4). Therefore, the protonation of HY-MGEL's amino groups causes electrostatic repulsion towards metal cations, making their adsorption difficult. On the other hand, as alkalinity increases the HY-MGEL surface becomes negatively charged due to the deprotonation of hydroxyl groups, hence more available to establish attractive electrostatic interactions with metallic cations. Indeed, at pH 5 Cu^{2+} and Pb^{2+} are predominant in the aqueous solution (Appendix II, Fig. AII-3) and can be adsorbed by HY-MGEL through electrostatic bonds. However, Pb and Cu R% values slightly decrease at pH 7 (Fig 3.8-B) since also $Pb(OH)^+$, $Cu(OH)^+$ and $Cu(OH)_{2(s)}$ species are present (Appendix II, Fig. AII-3), highlighting a HY-MGEL's selectivity toward divalent metallic cations. As noted before for HY-ACMC, the outcome of competitive adsorption is also dependent from the ionic radius and the relative charge density since ions with less charge and larger size lead to less stable complexes (Sun et al., 2022). Therefore, the reduced removal of Pb and Cu compared to pH 5 is also justified because the species $Pb(OH)^+$ and $Cu(OH)^+$ are characterized by a greater ionic radius and a lower charge than Pb^{2+} and Cu^{2+}.

Furthermore, as shown in the Figure 3.8-B, a linear trend of R% for Cd, Zn and Ni as a function of pH is noteworthy: Cd > Zn > Ni. Since they are present as Cd^{2+}, Zn^{2+} and Ni^{2+} in all the pH range investigated, the removal sequence could be related to a sum of factor including their electronegativity, charge density and affinity for surface functional groups (amino and hydroxyl groups, and amide functionalities). Moreover,

the same trend has been reported in different studies carried out employing materials containing the same functionalities (Ma et al., 2018; Singh et al., 2019; G. Zhou et al., 2016).

As well as HY-MGEL, also HY-MCHI is not effective in removing the PTEs investigated at pH 3.5, while at pH 5 and 7 it allows a removal between 20 and 30% for Cu and 25% for Pb after a contact time of 24 hours. Cd, Zn and Ni are not removed by the material throughout the pH range examined (Fig. 3.8-C). The minor adsorption capacity of HY-MCHI can be explained by its positive surface charge at pH values below its PZC (Table 3.4), which produces electrostatic repulsion toward metals in cationic form or positively charged aqua ion species. However, as can be noted in Figure 3.8-C, HY-MCHI has a remarkably high removal efficiency for Hg present in the multi-element solution. Indeed, the removal percentage for this element reaches approximately 90% at pH 5 and maintains values higher than 60% at pH 3.5 and 7. Similar observation has also been reported by Dubey et al. (Dubey et al., 2016) and Monier et al. (Monier & Abdel-Latif, 2013): as the solution's pH increases, the Hg ions adsorption also increases with an optimum at pH 5, condition close to HY-MCHI's PZC. Dubey et al. (Dubey et al., 2016) explained this behaviour as a consequence of the lone pair of electrons on chitosan's nitrogen atoms, which is available for the complex formation with the metal ions. At strong acidic pH values, the abundant presence of H^+ and H_3O^+ ions could compete with Hg adsorption (Badsha et al., 2021; Dubey et al., 2016; Monier & Abdel-Latif, 2013). However, at pH>5 HY-MCHI adsorbs more than other PTEs and the predominant mercury species in solution is the hydroxide $Hg(OH)_2$ (Appendix II, Fig. AII-3). Hence, the Hg ions retention decreases (Badsha et al., 2021).

Finally, in order to analyse the effectiveness of arsenic removal by HY-ACMC, HY-MGEL and HY-MCHI, the speciation of arsenic in solution needs to be considered. According to the equilibrium dissociation constants, the arsenate species are negative at pH>2.2 (Alakhras et al., 2005; Noè et al., 2022). Therefore, as mentioned above, HY-ACMC removed As with R%<10% due to its negatively charged surface, which causes an electrostatic repulsion toward the arsenic species (Fig. 3.8-A). Although

HY-MGEL shows a positive Z-potential at pH<4.4, the As removal is insignificant at pH 3.5 (Fig. 3.8-B), since the HY-MGEL's carboxylic groups can interact with amino groups of the structure (Cassone et al., 2018; Y. Hu et al., 2002; Noè et al., 2022). As well as HY-ACMC, also the HY-MGEL's negative surface hindered the As adsorption at pH higher than its PZC (Fig. 3.8-B). By contrast, HY-MCHI proved to be the better in As removal, especially at neutral pH (Fig. 3.8-C), where $H_2AsO_3^-$ is the predominant species (Alakhras et al., 2005). At this pH, HY-MCHI still shows a partially positive surface (Table 3.4) and a balance between the surface amino groups' charge and the distance between the polymeric chains (Noè et al., 2022). These factors allowed the chitosan-based hydrogel to remove arsenic with a R% at about 15% (Fig. 3.8-C).

PTEs adsorption test in real aquaculture water

To study the behaviour of the synthesised hydrogels in real conditions, two water samples from aquaculture farms were employed as a matrix for the preparation of a multi-element solution for further adsorption tests.

Before usage, these water samples were characterized by analysing natural PTEs content, hardness and acidity. Table AII-2 (Appendix II) reports the results of characterization and summarizes the Italian legal limits concentration for all the studied elements. For Italian koi-carps' aquaculture water the hardness, expressed in mg/L of $CaCO_3$, was 98.06 and it presented a pH value of 8.03. Whereas Danish water was characterized by a hardness of 194.71 and a pH of 7.76. Both samples displayed very low concentration of PTEs so spikes of each element were necessary to perform adsorption experiments. These experiments have been carried out at concentration close to the Italian legal limit (50 µg/L As; 22 or 40 µg/L Cu; 10 or 20 µg/L Pb; 50 or 75 µg/L Ni and 200 or 300 µg/L Zn, as reported in Table AII-2 (Appendix II) as a function of water hardness (Italian Legislative Decree n°152/2006, Annex 2, Part III, Section B). Instead, Cd and Hg were introduced with a concentration of 5 µg/L which is higher than their legal limit (2.5 and 0.5 µg/L, respectively).

Figure 3.9 summarizes R% values obtained with HY-ACMC, HY-MGEL and HY-MCHI after 180 min of contact with PTEs multi-element solution prepared in the two aquaculture water samples. Complete adsorption curves are reported in Appendix II, Figure AII-4.

Regarding the koi-carps' spiked water, HY-ACMC hydrogels ensure a sufficient R% to bring all the pollutants concentration studied below the legal limits with the exception of copper and arsenic.

As evidenced in Figure 3.7-A, HY-ACMC PTEs removal behaviour is not significantly affected by the pollutant initial concentrations. This suggests that the inhibition of Cu removal could be ascribable to its speciation. Indeed, at pH 8 the main species in solution is $Cu(OH)_{2(s)}$, which is neutral, while the concentration of the aquaion form is negligible.

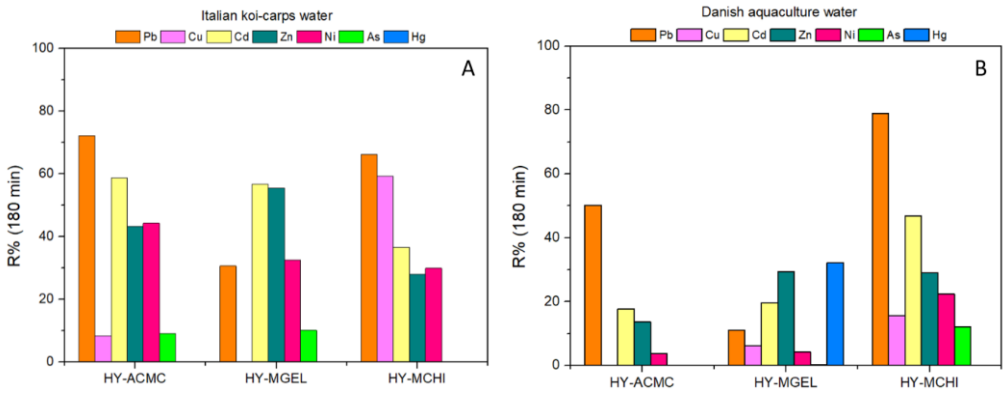

Figure 3.9 - Removal percentages after 180 minutes of contact with 1g/L of adsorbent in (A) Italian koi-carps spiked water and (B) Danish aquaculture spiked water

Furthermore, Cu can be strongly complexed by dissolved organic matter, in particular by humic acids (HA), forming soluble complexes, which reduce its availability for adsorption. Esfandiar et al. (Esfandiar et al., 2022) studied the influence of humic acid on different metal speciation and reported as, at high organic matter concentration (20 mg/L), the metal-HA complexes represented the main species in solution for Cu and Pb. On the other hand, Zn, Ni and Cd's speciation is less affected by the presence of HA. This is consistent for koi-carps' water as the organic carbon

content was 150 mg/L, as previously evaluated by a non-purgeable organic carbon (NPOC) analysis (Rigoletto et al., 2023).

On the other hand, since As is in an anionic form and the surface of the HY-ACMC is negative in aquaculture water pH (7.7-8.1), the repulsion between the charges justifies the limited removal of this contaminant. As in ultra-pure water experiments, the most removed PTEs are Pb and Cd with R% values of 72% and 59%, respectively. HY-MGEL is effective in reducing concentration below the legal limits for most of the elements studied, with removal percentages between 30 and 56%. Conversely, As (R% <10%) and Cu (R% = 0%) are not sufficiently removed to return within legal limits. As for HY-ACMC, also in this case the speciation of copper and arsenic, the HA-metal complexes formation and the surface charge of the material can explain the poor R% obtained for these two PTEs.

Finally, although in general HY-MCHI removal capacity is inversely proportional to the contaminant initial concentration (Fig. 3.7-C), it shows a good removal capacity for most of the PTEs investigated, except for As and Zn, leading to a sufficient removal percentage to bring them below the concentration legal limits. Indeed, Pb and Cu are removed more than 60%; Cd around 40% and Ni 35%. Despite the low PTEs concentration (10^{-7} M) these R% values are probably related to the water pH, which is around 8. At pH higher than HY-MCHI PZC the material surface is negatively charged ensuring a better removal capacity.

As shown in Figure 3.9-B, in Danish aquaculture water HY-ACMC and HY-MGEL show lower removal capabilities in respect to those obtained in the previous aquaculture water sample. It is important to consider that in this case there was a higher content of salts since the hardness is 194.71 mg/L. Cations as K^+, Na^+, Ca^{2+} and Mg^{2+} could compete with other aquaions for material surface active sites affecting their R%. Several studies (Esfandiar et al., 2022; W.-B. Wang et al., 2013; G. Zhou et al., 2016) concerning the influence of environmental factors on PTEs competitive adsorption reported that natural divalent cations show a higher inhibition effect on metal ions removal compared to the monovalent ones according to the rank $Mg^{2+} > Ca^{2+} > K^+$. Indeed, in the treatment with HY-ACMC the higher removal

percentages reductions are those of Cd (from 60 to 17%), Zn (from 43 to 13%) and Ni (from 45 to 4%). All of them at a pH of 7.76 (Danish water pH value) are mainly present in solution as bi-charged cations (Appendix II, Fig. AII-3). On the other hand, in these conditions Pb is in the form of aquaions and of mono-charged cation ($Pb(OH)^+$), hence its R% undergoes a smaller reduction effect.

A similar behaviour is evidenced for HY-MGEL, which shows a lower removal capacity for all the PTEs studied except mercury. Indeed, Cd and Pb show removal percentage at about 35% of those in koi-carps' water, Zn around 50% and Ni 13%.

As for the koi-carps sample, also in this case HY-MCHI shows a better efficiency in removing contaminants compared to pure water, similar to those obtained in the previous real sample.

Hydrogel regeneration and reuse

Preliminary regeneration tests have been done on HY-ACMC hydrogels. According to existing literature, three different regeneration solutions have been tested: HCl 0.01 and 0.1 M (Z.-H. Hu et al., 2018; Sesia et al., 2022) and Na_2EDTA 0.01 M (Fan et al., 2019). Figure 3.10-A displays the desorption percentages at the equilibrium state of HY-ACMC in the three different regeneration solutions. HCl 0.01 M solution leads to a release of less than 50% for all elements studied and is ineffective for Pb desorption, while increasing its concentration to 0.1 M the percentage rises between 70 and 80%. The best regeneration solution is Na_2EDTA 0.01 M as it ensures a complete desorption for all the PTEs except for Ni which is however released for 65%. This effectiveness is related to the Na_2EDTA high complexing capacity toward PTEs as evidenced by the complexation constants reported in Appendix II, Table AII-3.

Figure 3.10-B and 3.10-C summarize the desorption percentages obtained using HCl 0.1 M and Na_2EDTA 0.01 M for subsequent regeneration cycles each lasting 30 min. In the first two desorption cycles with HCl 0.1M PTEs release is between 50 and 60% and it is not significant in the third and fourth cycles. Pb is released in all regeneration cycles with a percentage of still 1,5% in the fourth one. Regeneration treatment with

HCl 0.1 M ensures a total release around 70% for Cd, Cu and Pb, 65% for Zn and 55% for Ni.

Employing Na_2EDTA 0.01 M as a regeneration solution, a desorption percentage higher than 85% is achieved for all PTEs in the first cycle, between 10 and 20% in the second one and it decreases under 10% and then near 0% in the last two cycles. This regeneration treatment ensures a complete release for all investigated elements. The higher percentages of PTEs desorption, the lower concentration of the solution and the not excessive acidity led to the selection of Na_2EDTA 0.01M as the most promising regeneration treatment.

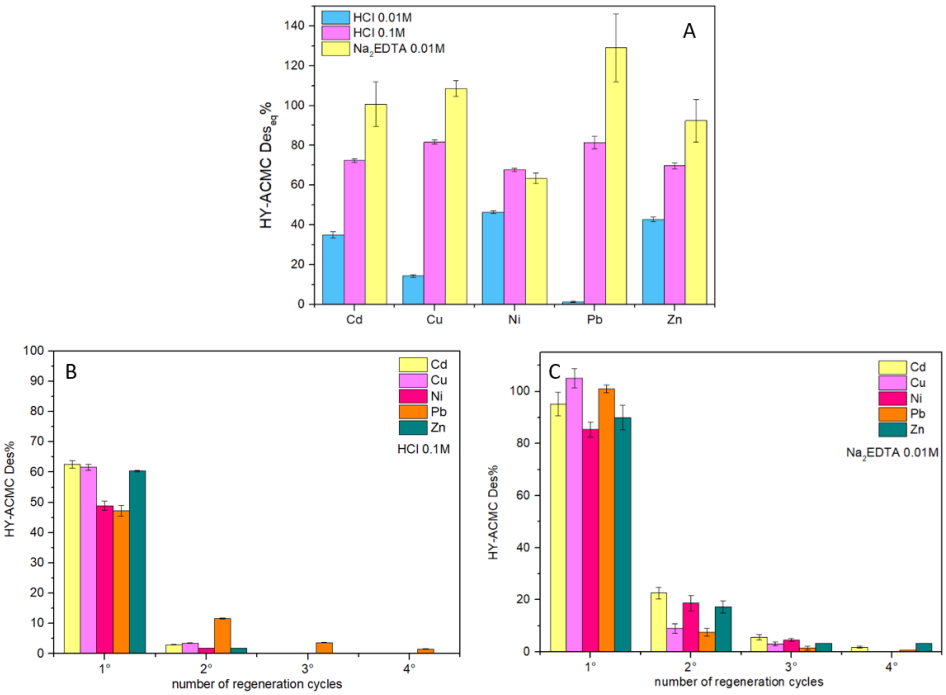

Figure 3.10 - Percentages of PTEs desorption from HY-ACMC hydrogels (A) with different regeneration solutions; (B) with subsequent cycles of regeneration with HCl 0.1 M; (C) with subsequent cycles of regeneration with Na_2EDTA 0.01 M

Then, HY-ACMC, HY-MGEL and HY-MCHI were reused for different subsequent PTEs adsorption tests interspersed with 0.01M Na_2EDTA regeneration treatments.

Each regeneration treatment included only 3 desorption cycles as the releases of the fourth one was found to be not significant.

Figure 3.11 and Table 3.5 summarize the results of PTEs adsorption-desorption cycles obtained with the three hydrogels.

Desorption values include the total releases obtained with all three 30-minutes' cycles that make up each regeneration treatment. Between each adsorption and desorption process, hydrogels have been washed with ultrapure water. PTEs concentrations in washing water were also evaluated and resulted not significant in all the regeneration treatments except for HY-ACMC, probably due to the breakdown of its network. Indeed, Figure 3.11-A reported the results of only two adsorption-desorption cycles with HY-ACMC which proves to be less resistant than other materials.

Its PTEs removal efficiency is reduced more than 65% after the first regeneration treatment. Moreover, the desorption percentages obtained in the second regeneration treatment are very low due to the damage of the hydrogel polymeric network, making subsequent uses very difficult.

As shown in Table 3.5, HY-MGEL shows a good PTEs removal capacity in the first adsorption cycle which decreases in the second and in the third ones for Zn, Cd and Ni. Pb and Cu removals are reduced in the second cycle while they increase again in the third one. Hg adsorption efficiency remains almost constant in the first two cycles and decreases only in the third one. Regarding the regeneration process, desorption is not complete in all cycles for most of the studied PTEs (< 65%) and first decreases from the first to the second cycle and then rises again in the third one. Only for Ni and Zn in the last regeneration treatment full release is achieved.

HY-MCHI increases its adsorption capacities going from the first to the second cycle of PTEs removal and the efficiency is maintained also in the third cycle. It is noteworthy that the first regeneration treatment allows the adsorption of elements firstly not removed like Cd, Cu Ni and Zn by HY-MCHI. It can be assumed that during the desorption treatment, the excess of Na_2EDTA not involved in metal ions complexation could enter in the HY-MCHI polymeric structure and interact electrostatically with chitosan.

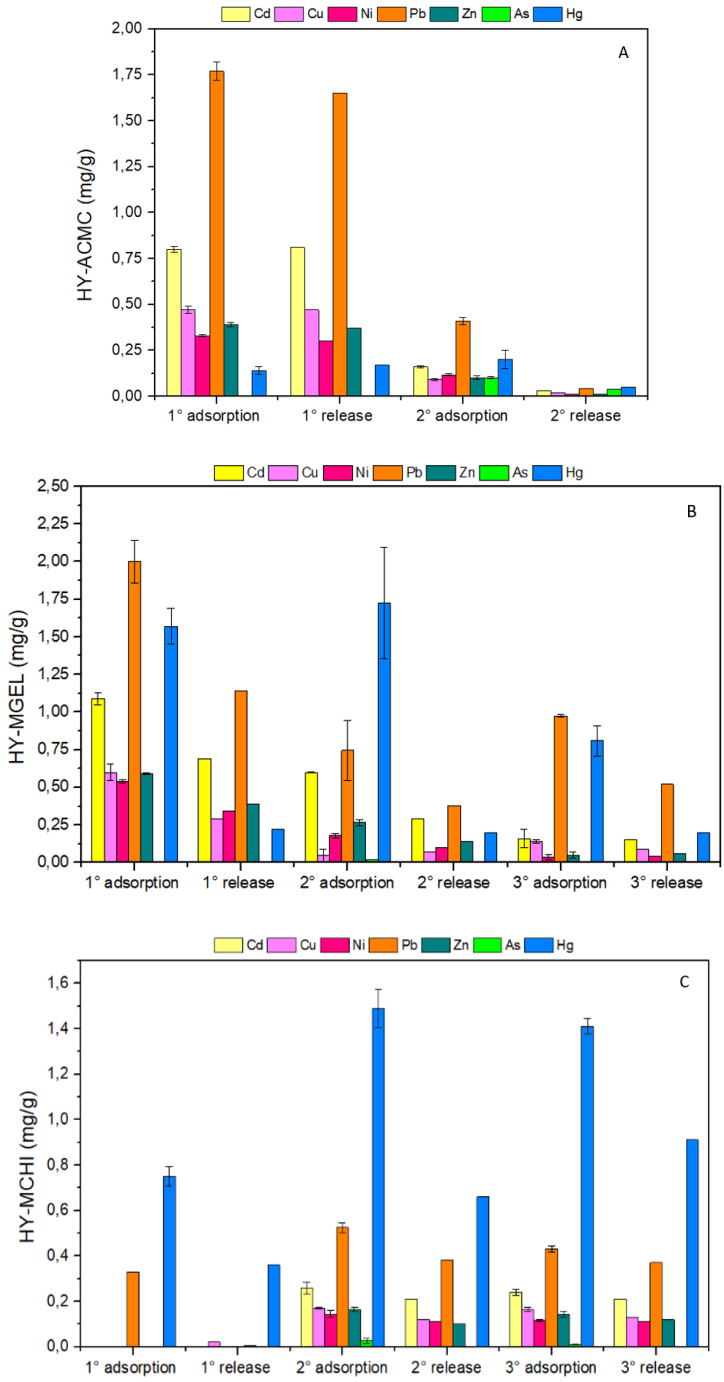

Figure 3.11 - PTEs adsorptions (after 180 min of contact with adsorbent materials) and releases obtained with Na_2EDTA 0.01 M, expressed in mg/g, in subsequent cycle of reuse. (A) HY-ACMC; (B) HY-MGEL; (C) HY-MCHI

Table 3.5 - Subsequent adsorption-desorption cycles results of PTEs adsorption (mg/g, %) and desorption (mg/g and %)

HY-ACMC												
	First adsorption-desorption cycle				Second adsorption-desorption cycle				Third adsorption-desorption cycle			
	Ads (mg/g)	Ads %	Des (mg/g)	Des %	Ads (mg/g)	Ads %	Des (mg/g)	Des %	Ads (mg/g)	Ads%	Des (mg/g)	Des %
As	-	-	-	-	0.1	13.39	0.04	40	-	-	-	-
Cd	0.8	72.83	0.81	101.25	0.16	14.11	0.03	18.75	-	-	-	-
Cu	0.47	78.84	0.47	100	0.09	13.81	0.02	22.22	-	-	-	-
Ni	0.33	56.02	0.3	90.9	0.116	19.03	0.01	8.62	-	-	-	-
Hg	0.14	5.02	0.17	121.43	0.2	9.78	0.05	25	-	-	-	-
Pb	1.77	90.44	1.65	93.22	0.41	19.88	0.04	9.76	-	-	-	-
Zn	0.39	61	0.37	94.87	0.1	16.33	0.01	10	-	-	-	-
HY-MGEL												
	First adsorption-desorption cycle				Second adsorption-desorption cycle				Third adsorption-desorption cycle			
	Ads (mg/g)	Ads %	Des (mg/g)	Des%	Ads (mg/g)	Ads%	Des (mg/g)	Des %	Ads (mg/g)	Ads%	Des (mg/g)	Des%
As	-	-	-	-	-	-	-	-	-	-	-	-
Cd	1.09	88.05	0.69	63.3	0.6	51.3	0.29	48.33	0.16	15.15	0.15	93.75
Cu	0.6	77.68	0.29	48.33	0.05	0.89	0.07	140	0.14	20.51	0.09	64.29
Ni	0.54	81.04	0.34	62.96	0.18	29.35	0.1	55.56	0.037	6.07	0.04	108.1
Hg	1.57	54.98	0.22	14.01	1.725	59	0.2	11.59	0.81	35.51	0.2	24.7
Pb	2	94.06	1.14	57	0.745	39.4	0.38	51.01	0.975	46.89	0.52	53.33
Zn	0.59	82.97	0.39	66.01	0.265	38.53	0.14	52.83	0.05	6.33	0.06	120
HY-MCHI												
	First adsorption-desorption cycle				Second adsorption-desorption cycle				Third adsorption-desorption cycle			
	Ads (mg/g)	Ads%	Des (mg/g)	Des%	Ads (mg/g)	Ads%	Des (mg/g)	Des %	Ads (mg/g)	Ads %	Des (mg/g)	Des %
As	-	-	-	-	0.027	3.8	-	0	0.01	1.44	-	0
Cd	-	-	-	-	0.26	24.39	0.21	80.77	0.24	23.45	0.21	87.5
Cu	0.001	0.16	0.02	-	0.17	27.92	0.12	70.59	0.165	27.11	0.13	78.79
Ni	-	-	-	-	0.145	25.14	0.11	75.86	0.116	20.77	0.11	94.82
Hg	0.75	28.45	0.36	48	1.49	73.06	0.66	44.30	1.41	74.05	0.91	64.54
Pb	0.33	1.46	-	-	0.525	27.78	0.38	72.38	0.43	23.92	0.37	86.05
Zn	-	-	-	-	0.165	26.57	0.1	60.60	0.14	24.06	0.12	85.71

Indeed, at the regeneration solution pH, which was 4.6, the surface amino-groups of HY-MCHI are protonated and positively charged while Na_2EDTA shows two carboxylate groups negatively charged (pKa 2.0, 2.7, 6.2, 10.3 (H. Wang et al.,

2020)). This electrostatic interaction remains also in the subsequent PTEs adsorption phases since they were carried out at pH 5.

Regeneration treatments of HY-MCHI are effective for all PTEs adsorbed with released between 60 and 85% except for Hg which interacts strongly with hydrogel's surface, and which is desorbed around 50%.

It is complex to make a meaningful comparison with other materials described in recent studies due to the exploitation of different concentrations of contaminants and adsorbent materials. Moreover, the influence of diverse environmental factors has to be considered. However, in Table AII-4 (Appendix II) a summary of the existing literature concerning the materials' reusability and a comparison with our results is reported.

The number of cycles carried out with the hydrogels developed in this work is in line with the studies in the literature about the removal of mixtures of PTEs, although in some cases a lower loss in efficiency was reported. It is worth emphasizing that in most existing papers the materials' adsorptions capabilities are evaluated in bi- or tri-elements mixture. On the contrary, in this study we considered solutions containing 7 PTEs, which imply more competition mechanisms for the surface sites. This lead to an increase in the complexity of the adsorption-desorption processes that can results in a reduction of efficiency.

3.3 Soybean peroxidase immobilised on cellulose-alginate hydrogels for removal of recalcitrant organic pollutants in water

Water contamination by organic compounds is an extremely complex problem to address given the great variety of existing classes of pollutants, both well-known and emerging.

As previously introduced, the use of enzymatic catalysis for water remediation has proven to be of great scientific interest and several studies have been dedicated to this topic. However, like many existing strategies, it presents some limitations including that of the specificity of the enzymes for limited substrates' categories.

Among them (chlorinated-)phenolic compounds, aryl- amines and sulfonated azo-dyes can be efficiently oxidised by soybean peroxidase.

For our studies we selected three target contaminants within these categories, namely 2,4,6-trichlorophenol, Triclosan and Bisphenol-A (Figure 3.12).

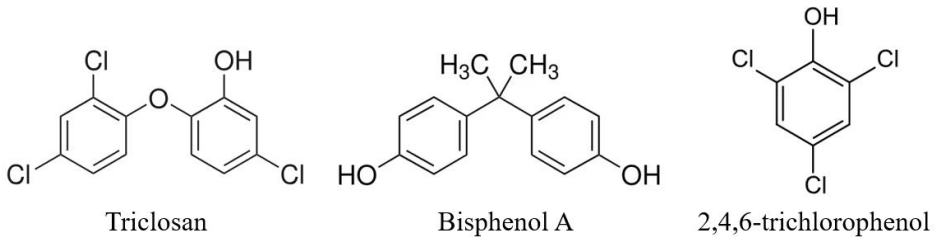

Figure 3.12 – structure of Triclosan, Bisphenol A and 2,4,6-trichlorophenol

The first two belong to the class of halogenated organic compounds, most of which are considered persistent organic pollutants due to their high lipophilicity, long lifetime in the environmnet, and high tendency to accumulate in fatty tissues. Since they possess a strong resistance to chemical and biological degradation, these molecules tend to be accumulated in aquatic and terrestrial organisms, leading to adverse biological effects as a consequence of their biomagnification in the food chain (Sharma et al., 2022).

2,4,6-Trichlorophenol (TCP) is widely used as an antiseptic, glue, leather and wood preservative, anti-mildew, fungicides and bactericides agent, water chlorinator, organic solvent and in the synthesis of various agricultural chemicals (Benbachir et al., 2017; Olaniran & Igbinosa, 2011). Trichlorophenols tend to accumulate in the lipid tissues of several organisms, they are mutagenic or co-mutagenic, and have been linked to cancer in animals, producing lymphomas and leukemia after eating contaminated water or food (Díaz-Báez & Valderrama-Rincon, 2017). In chronic toxicity studies on fishes, chlorophenols have been reported to cause a wide range of negative impacts such as oxidative stress, carcinogenesis and reproductive toxicity, alterations in plasma steroids, liver size, sexual maturity, growth and survival and

various condition indices (e.g. condition factor, hepatosomatic and gonadosomatic index) (Mukherjee et al., 2022).

Triclosan (TCS, 5-chloro-2-(2,4-dichlorophenoxy) phenol) is a synthetic, multi-purpose antimicrobial agent which could be found as an ingredient in mouthwashes, toothpastes, soaps, disinfectants, deodorants, clothing textiles, furniture and other materials (Dhillon et al., 2015). In contrast to many pharmaceuticals that are ingested orally and therefore excreted mainly as metabolites, TCS, due to its exclusive external use, is released into the environment unmetabolized. In 2015, the European Chemicals Agency (ECHA) decided to restrict the use of TCS for biocide type 1 products (*i.e.* human hygienic products). However, TCS is still used in many cosmetic products in concentrations of up to 0.3% in toothpastes, soaps, deodorants, or shower gels and up to 0.2% in mouthwashes, as stated by the European Commission in the *Fitness check on endocrine disruptors* (SWD(2020) 251 final). This leads to a continuous release of TCS into waters bodies with possible adverse consequences on the health of aquatic organisms and humans (Contardo-Jara et al., 2021). Indeed, studies on fishes shows that TCS is metabolized but at the same time tends to accumulate in muscle, liver and brain causing pathologies and constituting an hazards when consumed as food (S. Kumar et al., 2021; Maulvault et al., 2019).

Unfortunately, to date, little is known about chronic ecosystem level effects of TCS. However, toxicology data suggest its acute toxicity to aquatic organisms and potential human carcinogenicity, mild genotoxicity, endocrine disruption and induction of antimicrobial resistance (C.-L. Huang et al., 2014; L. Li, 2021).

Bisphenol A (BPA) is a suspected endocrine disrupting chemical widely used in the production of polycarbonate plastics, epoxy resins and thermal papers (Cerkvenik-Flajs et al., 2018; Tarafdar et al., 2022). The toxicological effects of BPA are still controversial, despite the wealth of studies conducted to date. Among the adverse effects on human health, it seems that BPA can disrupt the production, function and activity of endogenous hormones, can has an immune-suppression activity and cause metabolic disorders (Tarafdar et al., 2022).

Studies on fishes suggested that BPA can act as an androgen receptor antagonist, impacting the proper functioning of the hypothalamus-pituitary-gonadal altering the sex hormones balance and inducing transgenerational effects on brain probably affecting sexual behaviour. BPA can also alter the development of gonads and gamete, negatively impacting the development of the fish embryo and growth both at the larval and juvenile stage, and can interfere with thyroid hormone signaling pathways, thereby disrupting energy metabolism and muscle function (Faheem & Bhandari, 2021; Wu & Seebacher, 2020). On this basis, BPA is currently classified as reproductive toxicant category 1B under the EU CLP Regulation (Regulation 2016/1179) and is restricted in numerous consumer products for babies and children (Bousoumah et al., 2021).

In 2015 EFSA re-examined BPA exposure and toxicity issues, reducing the BPA Total Daily Intake, previously set at 50 μg kg^{-1} body weight (bw) day^{-1} to 4 μg kg^{-1} bw day^{-1} (EFSA Scientific Opinion, 2015) (Russo et al., 2019).

Given their phenolic structure, all these contaminants easily enter as substrates in the catalytic cycle of peroxidases. For this reason, they were selected as target molecules for evaluating the efficiency of the peroxidases containing hydrogels not only in ultrapure spiked water but also using a real pond water to evaluate the matrix effect.

3.3.1 Materials and methods

Materials

All chemical reagents are in analytical grade and used without purification.

Triclosan (TCS, >99%) was purchased from Alfa-Aesar, while 2,4,6-trichlorophenol (TCP, >99%), bisphenol A (BPA, >99%), glutaraldehyde (25% in H_2O), sodium alginate (99%), calcium chloride ($CaCl_2$, >93%), 3-(dimethylamino)benzoic acid (DMAB, 99%), 3-methyl2-benzothiazolinonehydrazone (MBTH, 97%), H_2O_2 30% (w/w) and sodium dihydrogen phosphate (NaH_2PO_4, > 99%) were purchased by Merck.

The pond water was taken from goldfish and carp aquaculture basins in the *Tetto Frati Agrozootechnology Centre, Department of Agricultural and Forestry Sciences, University of Torino* (Carmagnola, Northern Italy).
SBP extracted from soybean hulls and soy-derived cellulose functionalized with primary amino groups (Cell-NH_2) were obtained as described in Chapter 2.

Immobilization of SBP on cellulose

For the SBP immobilization on Cell-NH_2, a further functionalization with glutaraldehyde was necessary in order to introduce functional groups suitable for the enzyme grafting through a Schiff base formation.
0.5 g of Cell-NH_2 were suspended in 0.05 L of glutaraldehyde 2.5% (v/v) in 0.1 M phosphate buffer solution at pH 7.0 and left under stirring in the dark for 1 h at room temperature. The resulting suspension was then filtered, and the solid powder was washed and added to 0.015 L of SBP 0.13 mg/mL solution in 0.1 M phosphate buffer at pH 7.5 and left to react at 4 °C overnight under gentle stirring. The amount of the immobilised enzyme was evaluated through UV-visible analysis carried out in a Thermospectronic UNICAM UV-300 dual-beam spectrophotometer. The enzyme concentrations before and after immobilisation were calculated following an established method on the basis of the absorbance at 403 nm, typical of SBP Fe(III)-heme group, by using 94 600 M^{-1} cm^{-1} as molar extinction coefficient (Kamal & Behere, 2002).

Hydrogels preparation

Three different kinds of hydrogels containing alginate were prepared, namely HY-A (alginate hydrogels), HY-AC (alginate hydrogels with dispersed cellulose), HY-AC-SBP (alginate hydrogels with dispersed cellulose functionalised with SBP). To synthesise HY-A, 75 mg of alginate were dissolved in 3 ml of distilled water under stirring and then dripped in a $CaCl_2$ solution (0.2 M) (Alemzadeh & Nejati, 2009; Farias et al., 2017; Fei et al., 2016). The obtained spherical hydrogels were left in the gelling solution for around 30 min and then filtered and washed.

To synthesise the other types of hydrogels, 75 mg of alginate were dissolved into 3 ml of distilled water, and then 200 mg of cellulose (with or without loaded enzyme) were dispersed in the viscous solution by sonication. These viscous suspensions were dripped in a $CaCl_2$ solution (0.2 M). The obtained hydrogels were left in the gelling solution for around 30 min and then filtered and washed. All the hydrogels were then stored at 4 °C until use.

The morphology of hydrogels was examined using an EVO10 Scanning Electron Microscope (SEM, Carl Zeiss Microscopy GmbH) with an acceleration voltage of 20 kV. The samples were sputter-coated with a 20 nm-thick gold layer in rarefied argon, using a Quorum SC7620 Sputter Coater.

The swelling behaviour of the hydrogels, due to water uptake, was investigated using a gravimetric method. Oven-dried hydrogels were placed in deionised water at room temperature and the weight increase was monitored by removing gels from the water and weighing them after a quick removal of water from the surface with filter paper. The swelling ratio percentage (Sw%) was calculated with the equation 3.7 (paragraph 3.2).

Enzyme activity test

The activity of both free and immobilised SBP was evaluated by the H_2O_2/DMAB-MBTH system: in a solution containing 5×10^{-4}M of DMAB, 2×10^{-5} M of MBTH, and 1×10^{-4}M of H_2O_2 in acetate buffer (0.1 M pH 5.5), one hydrogel, or 5 mg of functionalised cellulose or 5 μL of SBP solution were added in order to introduce similar amount of SBP (0.018 ± 0.002 mg) (Tolardo et al., 2019). The enzyme activity was calculated with the initial rate method following the increase in absorbance at 590 nm of the reaction product (Ngo & Lenhoff, 1980).

Real water sampling and pre-treatment

A real pond water sample was collected in March 2022. Sampled water was collected in amber glass bottles, filtered with 70 mm glass microfibers filters (VWR) and stored at 4 °C. Hardness, pH and non-purgeable organic carbon (NPOC) of real aqueous

samples were measured. The water had a pH of 8 and a hardness of 100, expressed in mg/L of $CaCO_3$. The organic matter content, assessed by a NPOC analysis with a TOC-VCSH analyser, was 150 mg/L. Before spiking with the three organic contaminants, the water was analysed by HPLC-UV under the same chromatographic conditions described in the further paragraph and no signal were detected at the retention time of the pollutants.

Test on pollutant removal

Hydrogels efficiency in the removal of organic pollutants in water was evaluated by using 2,4,6-trichlorophenol (TCP), bisphenol-A (BPA) and triclosan (TCS) in single solutions at a concentration of 5 mg/L and in mixture at a concentration of 1.67 mg/L (total concentration 5 mg/L) as substrates. All the tests were performed both in ultrapure and real pond water. The removal of contaminants was evaluated by HPLC-UV analysi susing a Merck-Hitachi HPLC equipped with a LiChrospher RP-C18 reverse phase column (5µm, 4mm i.d.×125 mm long, Merck) and a Hitachi L-4200 UV-visible detector. Elution was carried out with acetonitrile and phosphate buffer (1×10^{-2}M) at pH 2.8 (70%:30% v/v) at a flow rate of 1 mL/min. The analytical detector wavelength was set at 275 nm for BPA and 242 nm for TCP, and TCS. In the case of the analysis of the pollutants' mixture, a two-step gradient starting from 45% v/v to 70% v/v of acetonitrile in 3 min followed by 5 min of isocratic elution was carried out. In each experiment, 4 HY-AC-SBP hydrogels were added to a 5 mL of solution containing a single contaminant or the whole mixture. The removal of each pollutant was followed for 5 hours in the presence of an initial H_2O_2 concentration of 1×10^{-4}M. For comparison, similar measurements were carried out with SBP in solution at almost the same concentration introduced into the hydrogels. In addition, to evaluate the extent of compounds' adsorption, other experiments were performed only in the presence of hydrogels. Moreover, to determine the possible non-enzymatic oxidation of the substrates, preliminary tests were performed in the presence of H_2O_2 but without hydrogels. The possible reuse of hydrogels was also investigated: after the first contaminants removal experiment, hydrogels were washed

with distilled water, the excess surface water was removed with filter paper, and they were used again for another reaction cycle. A total of 8 subsequent cycles of treatment were performed. Finally, the toxicity of the reaction products was evaluated following the evolution of bioluminescence of *Vibrio fischeri* bacteria in a Microtox Model 500 Toxicity Analyzer (SDI Europa) and analysed with the APAT-IRSA 8030 method.23

3.3.2 Results and discussion

Alginate-based hydrogels containing dispersed cellulose functionalised with SBP (HY-AC-SBP) were prepared, characterised, and tested in the abatement of the selected organic pollutants. As reference materials, simple alginate hydrogels (HY-A) and alginate hydrogels with dispersed cellulose (HY-AC) were also synthesised.

Hydrogel preparation and characterization

The whole HY-AC-SBP preparation procedure is reported in Figure 3.13.

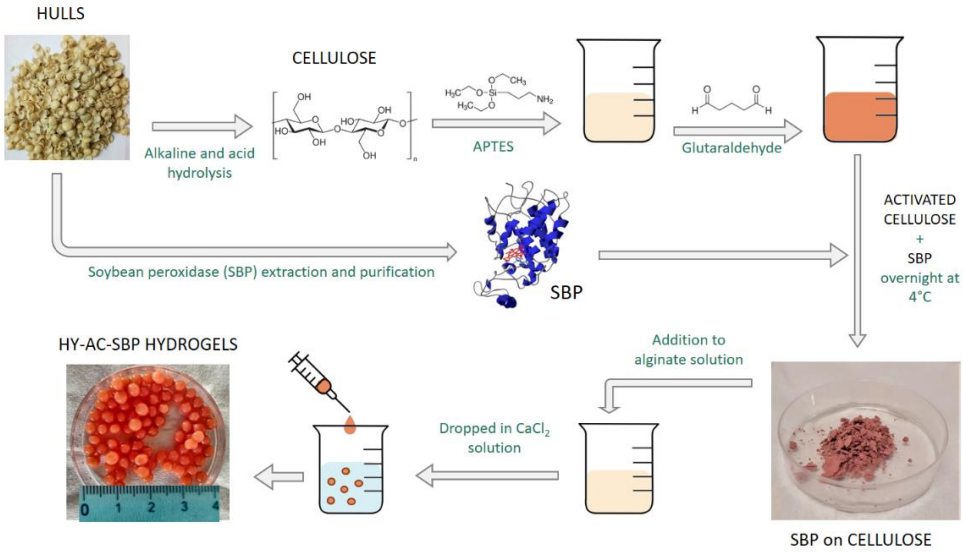

Figure 3.13 – HY-AC-SBP hydrogel preparation scheme

The total amount of soybean peroxidase loaded on cellulose was 3.3 mg/g. HY-AC-SBP hydrogels were formed by dripping a suspension containing alginate and functionalised cellulose in a calcium chloride solution. The so obtained beads are characterised by a diameter of 4–5 mm and an average weight of 35–45 mg. Each bead contains 6.5 ± 0.5 mg of functionalised cellulose (corresponding to 0.023 ± 0.002 mg of SBP).

The morphology of the bead bulk of HY-AC and HY-AC-SBP hydrogels was investigated by SEM analysis. In Figure 3.14, both hydrogel morphologies evidence the prevalence of cellulose fibres, which are well dispersed in the whole gel matrix and whose shape is in good agreement with the literature (Alemdar & Sain, 2008; Merci et al., 2015). No significant differences were detected due to the chemical modification related to SBP loading on the biopolymer. From the detail in Fig. 3.14-B, it is also possible to note bundles of fibres that are not completely separated, probably due to the residual lignin and hemicellulose not totally removed during the extraction process.

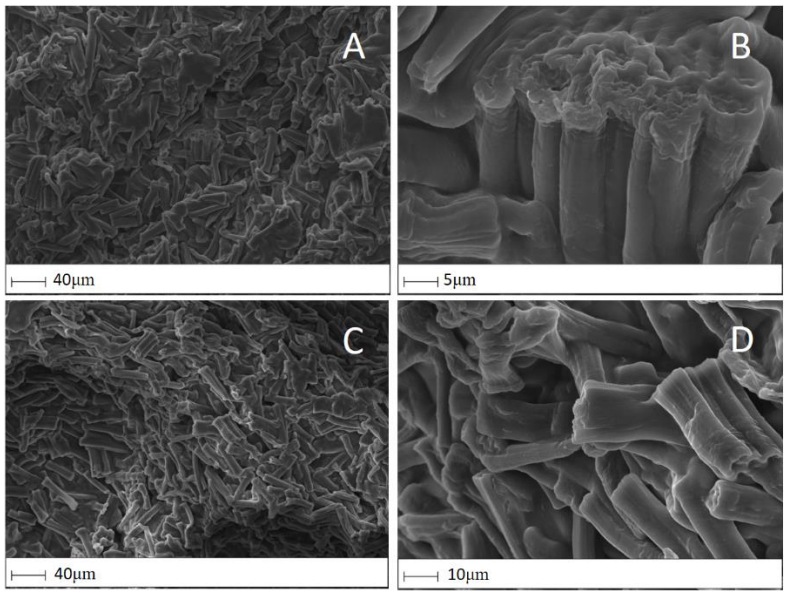

Figure 3.14 - SEM images of hydrogels. (A) HY-AC (hydrogel containing cellulose fibres); (B) HY-AC detail of fibres not completely separated; (C) HY-AC-SBP (hydrogel containing cellulose fibres with enzymes); (D) detail of HY-AC-SBP.

The hydrogel swelling behaviour was investigated as well and results are reported in Figure 3.15. Experimental data evidence that all the hydrogels reach an equilibrium condition after 4 hours, with swelling ratio values higher than 100%. The presence of cellulose appears to increase the swelling capacity of the material; as already observed in other studies. This behaviour could be ascribed to the hydrophilic characteristics of cellulose (R. Cai et al., 2022; Y. Li et al., 2022). On the other hand, soybean peroxidase is a water-soluble globular protein able to form electrostatic interactions with the surrounding environment (Henriksen et al., 2001). Indeed, the highest swelling percentage occurs with the introduction of chemically modified cellulose and SBP in HY-AC-SBP (about 178%). Moreover, electrostatic interactions between cellulose and other molecules modify the gelly structure increasing the mesh size of the network (Fernández et al., 2005; Horn et al., 2021). Therefore, a high swelling ratio can also promote better contact between aqueous contaminants and hydrogel active phase.

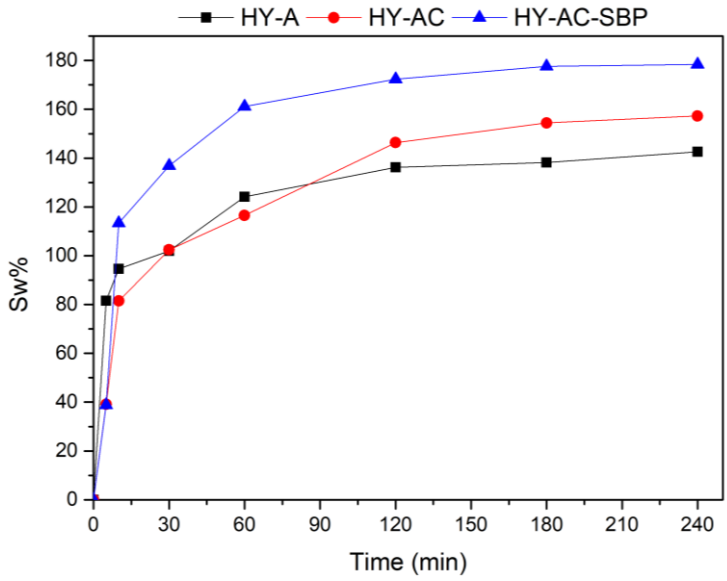

Figure 3.15 – Swelling behaviour of different hydrogels

In order to evaluate the residual activity of SBP immobilised in HY-AC-SBP, a comparison between the activity of SBP in solution, loaded on cellulose and incorporated in one hydrogel was made by using the DMAB/MBTH method.

Results confirm that the SBP grafting on Cell-NH_2-glutharaldeyde leads to a significant reduction of enzymatic activity. Indeed, it shows a DMAB/MBTH reaction kinetic an order of magnitude lower than the free protein (Table 3.6). Furthermore, the encapsulation in alginate beads further reduces activity by halving it. However, as reported in Figure 3.16, this system is stable and maintains its activity for almost 10 cycles.

Table 3.6 – results of enzymatic activity test (DMAB/MBTH/H_2O_2) expressed in variation of absorbance at 590 nm per second (ΔA590/s) and in micromoles of purple product formed per minutes (µmol/min)

	ΔA_{590}/s	**µmol/min**
Free SBP	1.8×10^{-2}	22.7
SBP on cellulose	4×10^{-4}	0.504
HY-AC-SBP	$2{,}07\times10^{-4}$	0.261

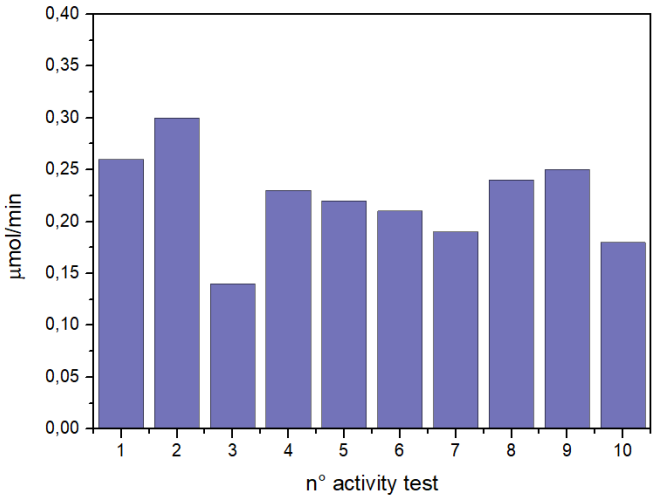

Figure 3.16 - Results of 10 consecutives activity tests of one HY-AC-SBP with DMAB/MBTH/H_2O_2 colorimetric method expressed in µmol/min of formed purple product

Pollutants removal

As introduced above, HY-AC-SBP hydrogels were used to remove three organic pollutants, 2,4,6-trichlorophenol (TCP), bisphenol-A (BPA) and triclosan (TCS), both in ultra-pure and pond water (Figure 3.17). The experiments were carried out both in a single contaminant solution and in a mixture of the three compounds in order to mimic possible interactions between them in a more complex system. Preliminary tests were carried out to evaluate the contribution of the adsorption of pollutants on HY-AC-SBP hydrogels. Moreover, their possible oxidation by H_2O_2 only was also tested before studying the removal by the final HY-AC-SBP/H_2O_2 system. The results obtained after 5 hours of treatment in ultra-pure water are summarised in Table 3.7.

Experimental data show as the oxidation by hydrogen peroxide in the absence of SBP is negligible for BPA and limited for TCS and TCP when they are alone. Still, a slightly higher effect is observed when they are in the mixture, with a removal of 10–16% after 5 hours of reaction (Appendix III, Figure AIII-1). The contribution of adsorption to pollutants removal by HY-AC-SBP is more consistent and shows a similar trend (BPA < TCP < TCS) both in single solutions and in the mixture (Appendix III, Figure AIII-2). This behaviour agrees with the increasing lipophilicity of the three compounds, in terms of their *logP* values (3.32, 3.69, 4.76 respectively (Hazardous Substances Data Bank).

More interesting results were obtained with HY-AC-SBP hydrogels in the presence of H_2O_2, when SBP catalytic cycle occurs, since the experimental data show the complete removal of all the contaminants in 5 hours, both in a single-component solution and in the mixture (Fig. 3.17-A and B).

Pollutants abatement can be assimilable to a pseudo-first-order decay and the different reaction rates can be due to distinct affinities of substrates for the enzyme. The corresponding kinetic constants (k_{obs}), together with the calculated half-life times ($t_{1/2}$), are reported in Table 3.7.

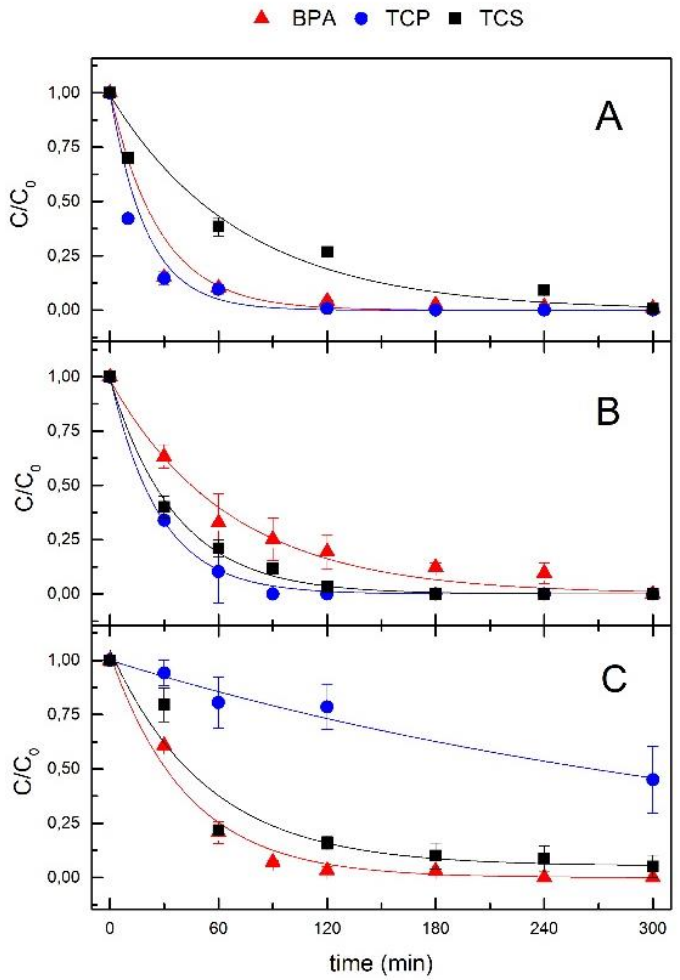

Figure 3.17 - Removal of BPA, TCP and TCS with HY-AC-SBP. (A) Enzymatic removal of single contaminant solutions in ultrapure water; (B) enzymatic removal of contaminants mixture in ultrapure water; (C) enzymatic removal of contaminants mixture in real water (pond water).

TCP shows the shortest half-life time, with similar values both in single and in the mixture (15 and 19 min, respectively), while BPA and TCS reaction rates are significantly influenced by the presence of the other contaminants.

Indeed, BPA half-time life increases from 18 to 46 min, whereas that of TCS decreases from 50 to 26 min (results for single solution and mixture, respectively). These effects can be related to differences in the reaction mechanism. Indeed, according to the literature, peroxidases induce the formation of phenoxy radicals

which subsequently leave the active site of the enzyme and undergo different fates depending on their structure (Appendix III, Figure AIII-3). In the case of TCP, the intermediate is stabilised by the substitution of one chlorine atom with an oxygen and the formation of the stable product 2,6-dichloro-1,4-benzoquinone (Ferrari et al., 1999; Hammel & Tardone, 1988).

On the contrary, in the case of BPA and TCS, the first radical intermediate generates a mixture of substances at higher molecular weight deriving from the coupling with parent molecules or secondary radicals (Q. Huang & Weber, 2005; J. Li et al., 2016). In the latter case, interferences due to the contemporary presence of these species generated by TCS and BPA could explain the differences in reaction rates observed in the experiments with the mixture of pollutants.

Table 3.7 - Removal percentage due to different processes after 5 hours of treatment in ultra-pure and pond water

		Abatement % (H_2O_2 only)	**Adsorption% (HY-AC-SBP)**	**Removal % (HY-AC-SBP + H_2O_2)**	**Time of complete removal (min)**	**Observed kinetic constant k_{obs} (min^{-1})**	**Half-life time (min)**
Single contaminants	BPA	0.7	20	100	200	0.037±0.003	18.0±1.6
	TCP	2.4	42	100	120	0.049±0.010	14.0±2.8
	TCS	10	62	100	300	0.014±0.001	50.0±5.0
Mix in ultrapure water	BPA	10	28	100	300	0.015±0.001	46.0±4.0
	TCP	13	38	100	120	0.037±0.001	19.0±0.3
	TCS	16	43	100	180	0.027±0.001	26.0±1.2
Mix in real pond water	BPA	-	36	100	240	0.0230±0.002	30.0±2.3
	TCP	-	35	55	-	0.0026±0.0002	-
	TCS	-	64	96	~300	0.018±0.002	39.0±5.0

The removal rate trend (TCP > BPA ≫ TCS) in the single solution is also in agreement with analogous test carried out with free SBP, in which calculated half-life times are 5.7, 6.4 and 79 min, respectively (Appendix III, Figure AIII-4).

In order to investigate the possibility of using HY-AC-SBP hydrogels to treat actual water, spiked pond water from aquaculture was also used. The complexity of the real matrix does not influence the physical removal of contaminants. Indeed, adsorption values follow a similar trend to those measured in ultrapure water (Table 3.7): physical removal is higher for TCS, while for TCP and BPA, it is similar.

In contrast, removal due to enzymatic catalysis in the real matrix is slower and undergoes significant changes, as shown in Fig. 3.17-C and Table 3.7. Nevertheless,

BPA and TCS are completely removed after 5 hours with similar trends (half-life times are 30 and 40 minutes, respectively), whereas TCP is only reduced to 55%. To better understand the reason for the uncompleted TCP removal, we carried out additional measurements with different concentrations of H_2O_2 and at different pH values in ultra-pure water (Appendix III, Figure AIII-5). Both factors appear not to significantly affect the removal of TCP, so implying that the reduced abatement could be attributable to the inorganic and organic matter present in pond water (J. Li et al., 2017; Yang et al., 2018) and the possible inhibition of SBP, as already observed in previous studies concerning the degradation of pentachlorophenol in tap water (Tolardo et al., 2019).

Hydrogel reuse

The possible reuse of HY-AC-SBP for further contaminants removal experiments was tested by undergoing hydrogels to 8 reaction cycles in ultrapure water. Although a slight decrease in the removal rate of contaminants can be observed after 120 min of treatment, the compounds are completely abated after 300 min of treatment also in the eighth reaction cycle, indicating that the system maintains a high efficiency and stability even after repeated use (Figure 3.18).

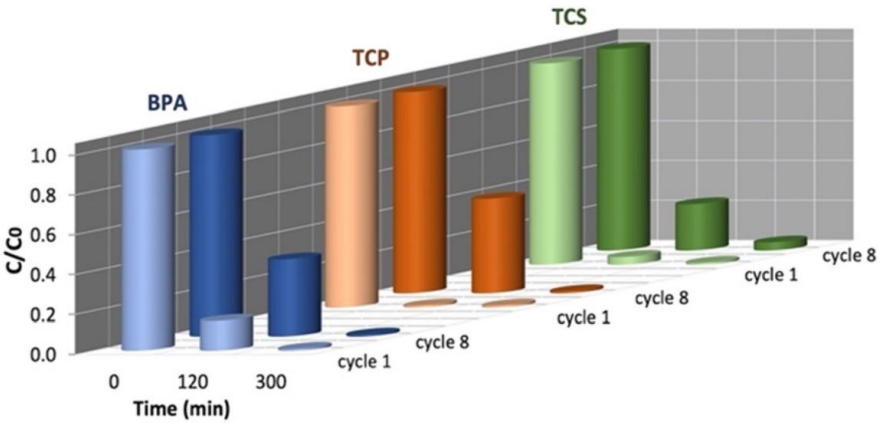

Figure 3.18 - Different results in BPA, TCP and TCS removal at 120 and 300 min. Comparison between the first and eighth cycle of HY-AC-SBP treatment

This fact also emerges when comparing the kinetic parameters calculated for the first and eighth cycles (Table 3.8). The k_{obs} values decrease whereas half-life times increase, but this effect does not significantly influence the possibility to obtain the complete removal of the pollutants at the end of the treatments.

Table 3.8 - k_{obs} and half-time life values for the first and eighth reaction cycles with HY-AC-SBP

Contaminant	First cycle		Eighth cycle	
	k_{obs} (min^{-1})	$t_{1/2}$ (min)	k_{obs} (min^{-1})	$t_{1/2}$ (min)
BPA	0.015±0.001	46±4.0	$0.009±4.15\times10^{-4}$	76±3.5
TCP	0.037±0.001	19±0.3	$0.0082±8\times10^{-4}$	84.4±8.00
TCS	0.027±0.001	26±1.2	$0.0138±9.2\times10^{-4}$	50.2±3.35

Toxicity test

Acute toxicity of contaminants mixture as a function of reaction time, was evaluated in ultrapure water by following the bioluminescence produced by *Vibrio fischeri* bacteria (Figure 3.19). The parent compounds exhibit a high toxicity, as assessed by the very high percentage of inhibition effect (close to 100%) detectable in the initial conditions at 0 min.

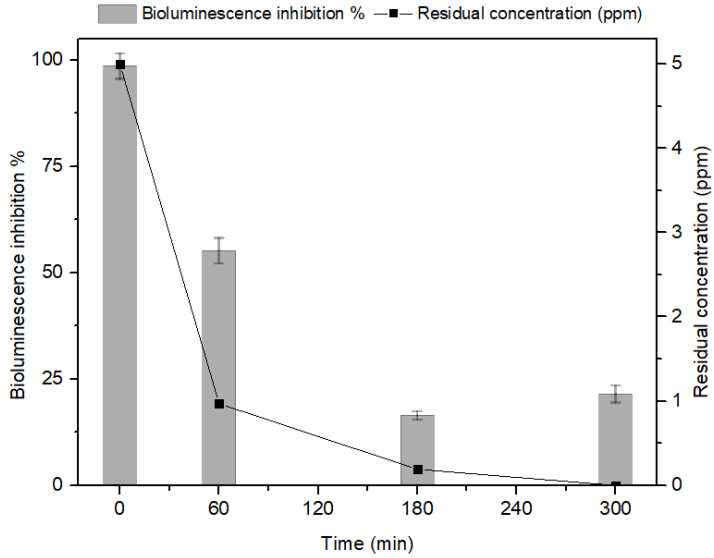

Figure 3.19 - Comparison between the residual total concentration of BPA, TCP and TCS and bioluminescence inhibition percentage as function of reaction time with the HY-AC-SBP/H_2O_2 system.

The progressive decrease in the pollutants concentration during the reaction with HY-AC-SBP is associated with a consistent decrease in toxicity, as the luminescence inhibition percentage is reduced to about 21% after 300 min. These results suggest that the removal of the initial pollutants proceeded through the formation of less hazardous compounds, in agreement with literature data showing the lower toxicity of the reaction products with respect to the parent molecules (Hautphenne et al., 2016; Karci, 2014; J. Li et al., 2016; Melo & Dezotti, 2013).

3.4 Biodegradation of bio-based hydrogels

The end of life of developed materials is an aspect that must be considered from the perspective of a process that is as circular and sustainable as possible. The choice of biopolymers as raw materials is functional for this purpose since many of them are biodegradable.

According to IUPAC definition, biodegradation is "the breakdown of a substance catalysed by enzymes in vitro or in vivo" (McNaught & Wilkinson, 1997). It is a natural process by which organic chemicals in the environment are converted to simpler compounds, mineralized and redistributed through elemental cycles such as the carbon, nitrogen and sulphur cycles. Biodegradation can only occur within the biosphere as microorganisms play a central role in the biodegradation process (Chandra & Rustgi, 1998).

According to several authors (Awasthi et al., 2022; Harrison et al., 2018; Lucas et al., 2008; Silva et al., 2023), biodegradation could be divided in four stages: (bio)deterioration, (bio)fragmentation, assimilation, and mineralization. The first occurs after the adherence of microorganisms on the polymer surface and its colonization and leads to a superficial degradation in which macro-materials are reduced in smaller fractions. In the second stage a reduction of the polymer molecular weight occurs as a consequence of secretion of extracellular enzymes. Oligomers, dimers or monomers formed in this phase are used in the third stage in the microbial metabolism for energy, biomass and metabolites production. Finally, the

mineralization stage occurs concurrently with assimilation, during which organic material is converted into H_2O, CO_2, N_2 or CH_4 which are released into the environment (Adjuik et al., 2023; Oliveira et al., 2020; Tokiwa et al., 2009).

Biodegradation is governed by several factors as physicochemical characteristics of the polymers and biotic and abiotic environmental factors (humidity, O_2, temperature, sunlight, weathering, and pH) (Nikolaivits et al., 2021). Temperature and humidity facilitate the abiotic hydrolysis of the polymer while oxygen availability regulates the biological reactions (Awasthi et al., 2022). The process could stop at any of the described stages and involves several kinds of microorganisms.

A widely employed biodegradation experiment is the polymer's soil burial. Obviously, given the high number of existing soil types, biodegradation will depend on the internal characteristics of the soil, first of all the microbial community, together with soil composition (N/C ratio), pH and humidity (Awasthi et al., 2022).

This methodology allows to obtain both qualitative (macro- and microscopic change in morphology, colour or shape changes, chemical structure modification) and quantitative (weight loss or produced CO_2) information on sample biodegradability.

In the next section, the results obtained from the biodegradation tests by burial in compost of the hydrogels previously tested for the enzymatic removal of organic contaminants and the adsorption of PTEs from aqueous matrices will be discussed. In this second case, particular attention has been paid not only to the biodegradation of the material but also to the evaluation of the possible environmental impact that this type of *end of life* could have on the used compost.

3.4.1 Materials and methods

Materials

Compost Florawiva® was provided by ACEA Pinerolese (Pinerolo, TO, Italy) (composition reported in Appendix IV, Table AIV-1 and AIV-2). All the tested materials (HY-AC-SBP, HY-ACMC, HY-MGEL and HY-MCHI) were prepared and employed for water remediation as described in previous sections.

Burial test of HY-AC-SBP

A plastic box (15 × 20 × 10 cm) was filled with Florawiva® compost and hydrogels were buried at a depth of 4 cm from the soil surface to ensure aerobic degradation conditions. The box was stored at room temperature (23 ± 2 °C) and the soil humidity was maintained at 30% by spraying water regularly on the surface. Fluctuations in soil moisture were followed gravimetrically using the standard method of oven drying (ASTM D2216). Comparative tests were also carried out in sterilised soil by burying the hydrogels in compost previously heat-treated at 105 °C for almost 24 hours (Dalev et al., 2014; Deepa et al., 2016; Doh et al., 2020; Martucci & Ruseckaite, 2009). The morphology of hydrogels was examined before and after biodegradation tests using an EVO10 Scanning Electron Microscope (SEM, Carl Zeiss Microscopy GmbH) with an acceleration voltage of 20 kV. The samples were sputter-coated with a 20 nm-thick gold layer in rarefied argon, using a Quorum SC7620 Sputter Coater. The biodegradation experiments have been followed for 20 days.

Burial test of HY-ACMC, HY-MGEL and HY-MCHI

The hydrogels were subjected to compost burial tests after being used for the removal of the seven PTEs (Pb, Cd, Cu, Ni, Zn, Hg and As) and regenerated with a 0.01M Na_2EDTA solution as described in section 3.2.

Cylindrical plastic containers (5.5 cm diameter and 3 cm height) were filled with 10 g of humidified compost and a perforated plastic support, covered with a nylon mesh previously conditioned in nitric acid, was inserted on the top. The swelled hydrogels (0.5 g HY-MCHI, 0.7 g HY-MGEL and 3.6 g HY-ACMC) were deposited on this support and subsequently covered with a layer of compost of 2 cm (8 g). A perforated plastic lid has been added to each container to maintain humidity but at the same time allow air to enter to maintain aerobic conditions.

As for HY-AC-SBP, the plastic containers were stored at room temperature (23 ± 2 °C) and the soil humidity was maintained at 40% by spraying water regularly on the surface. Fluctuations in soil moisture were followed gravimetrically using the standard method of oven drying (ASTM D2216). Comparative tests were also carried

out in sterilised soil by burying the hydrogels in compost previously heat-treated at 105 °C for almost 24 hours.

The compost was analysed before and after the biodegradation experiments to evaluate the possible increase in the background values of the main PTEs studied. The compost was previously air dried, pounded in a mortar and sieved through 2 mm mesh and finally subjected to a microwave assisted acid digestion. In a Teflon vessel 0.1 g of compost were mixed with 5 mL of *aqua regia* and then digested in a Milestone MLS-1200 Mega (Milestone, Sorisole, Italy) digester following the heating program: *i)* 5 min at 250 W, *ii)* 5 min at 400 W, *iv)* 5 min at 600 W, *v)* 5 min at 250 W.

After cooling, the samples were filtered through Whatman n°5 filters previously washed with ultrapure water and then diluted up to 50 mL with ultra-pure water. The elements' content has been analysed with ICP-OES. For each compost sample the entire procedure has been done in triplicate.

3.4.2 Results and discussion

Burial test of HY-AC-SBP

Biodegradation of HY-AC-SBP was followed for 20 days (until the spheres were recognizable within the compost). Figure 3.20 shows the main qualitative outcome of the experiment.

Fig. 3.20 (A–C) show the macroscopic changes that occurred to hydrogels during 20 days of burial. It is noteworthy that the action of soil microorganisms and the formation of mould on the surface of the beads is clearly visible after only 4 days (Fig. 3.20-A). Other modifications can also be observed by handling the materials, which became less compact and broke easily when taken with tweezers. On the other hand, in sterilised soil, mould formation did not occur, and the hydrogels seem to keep their structure unchanged (Fig. 3.20-D). Fig. 3.20-E shows the surface morphology of HY-AC-SBP after 20 days of burial in compost, confirming the strong adhesion of the compost matter on the beads.

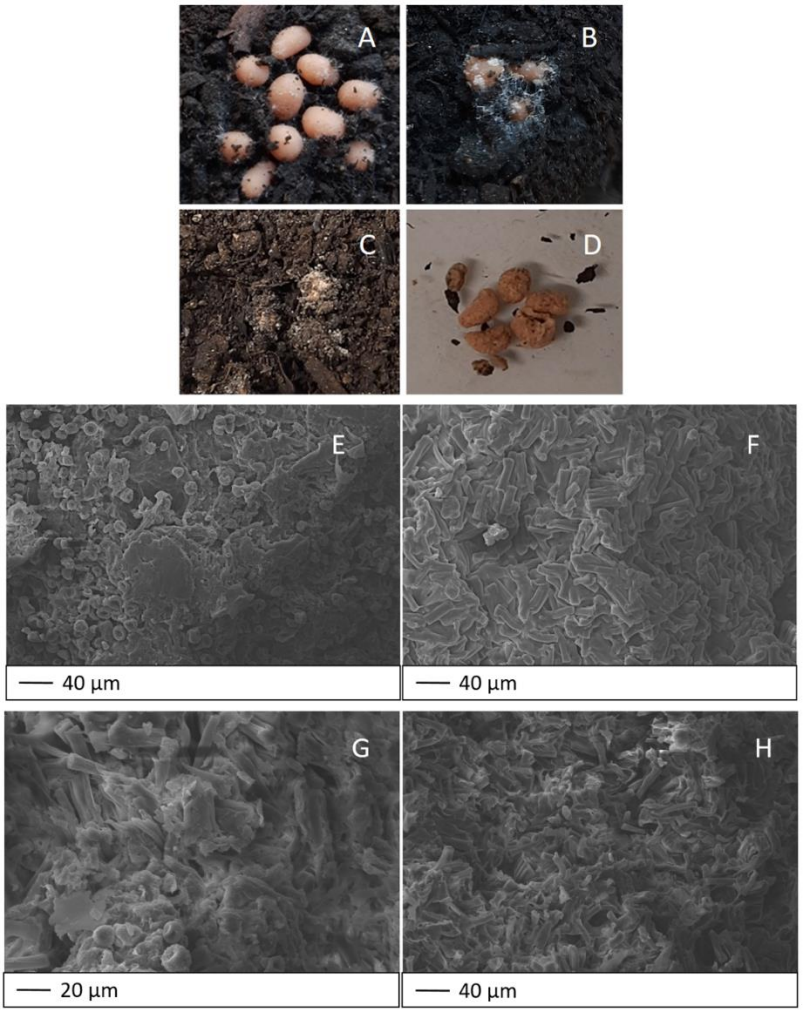

Figure 3.20 - (A) HY-AC-SBP after 4 days of burial; (B) HY-AC-SBP after 7 days of burial; (C) HY-AC-SBP after 20 days of burial; (D) HY-AC-SBP in sterilised soil after 20 days of burial; (E) SEM image of HY-AC-SBP surface after 20 days of burial in compost; (F) SEM image of HY-AC-SBP surface after 20 days of burial in sterilised soil; (G) SEM image of HY-AC-SBP bulk after 20 days of burial in compost; (H) SEM image of HY-AC-SBP bulk after 20 days of burial in sterilised soil.

On the contrary, in the case of the sterilised soil, the surface of the beads appears free of extraneous particles (Fig. 3.20-F).

Analysing the bead bulk, the cellulose fibres within the gel matrix, both in contact with compost (Fig. 3.20-G) and with sterilised soil (Fig. 3.20-H), maintain a pretty unvaried morphology after 20 days of burial. The foreign particles present in Fig.

3.20-G are probably due to residual compost transferred during the sample pre-processing for SEM analysis.

From these preliminary results, we can infer that these bio-based materials are clearly subjected to the action of soil microorganisms, but in this case the common visible effects of surface erosion and formation of holes and cracks in the internal structure reported in the literature (Durpekova et al., 2021; Mate et al., 2021) seem not to be applicable. Although the presence of a massive amount of cellulose fibres and stuck compost particles hinders the possibility of detecting those damages in the hydrogel matrix, SEM images show as the microorganism action initially affects the most superficial part of the hydrogels and only later their internal structure. However, further studies at longer burial times are needed to verify the mechanism of complete biodegradation of the hydrogels.

Burial test of HY-ACMC, HY-MGEL and HY-MCHI

The appearance of HY-ACMC, HY-MGEL and HY-MCHI was checked during the 58 days of burial in compost (Figure 3.21). As evidenced in the images related to the starting day of the biodegradation experiments (Fig. 3.21-A1, B1 and C1), the hydrogels were buried still wet after regeneration in Na_2EDTA and subsequent washing in ultrapure water.

The different behaviour during the burial period is clearly evidenced comparing the hydrogels' picture on the same day. Indeed, HY-MGEL is no longer distinguishable from the surrounding compost on day 34 (Fig. 3.21-B3), while for HY-ACMC it is necessary to wait until day 47 (figure not shown). In contrast, HY-MCHI is still visible at day 58 (Fig. 3.21-C4) even though signs of microbial activity are recognisable.

All compost samples have been digested and analysed to investigate the PTEs concentrations before and after biodegradation experiments. Four kind of samples have been considered: pristine compost (Compost t_0), blanks (compost after burial of hydrogels never put in contact with PTEs solution but regenerated), compost after

burial of regenerated hydrogels (identified by the name of the type of buried hydrogel) and sterilized compost.

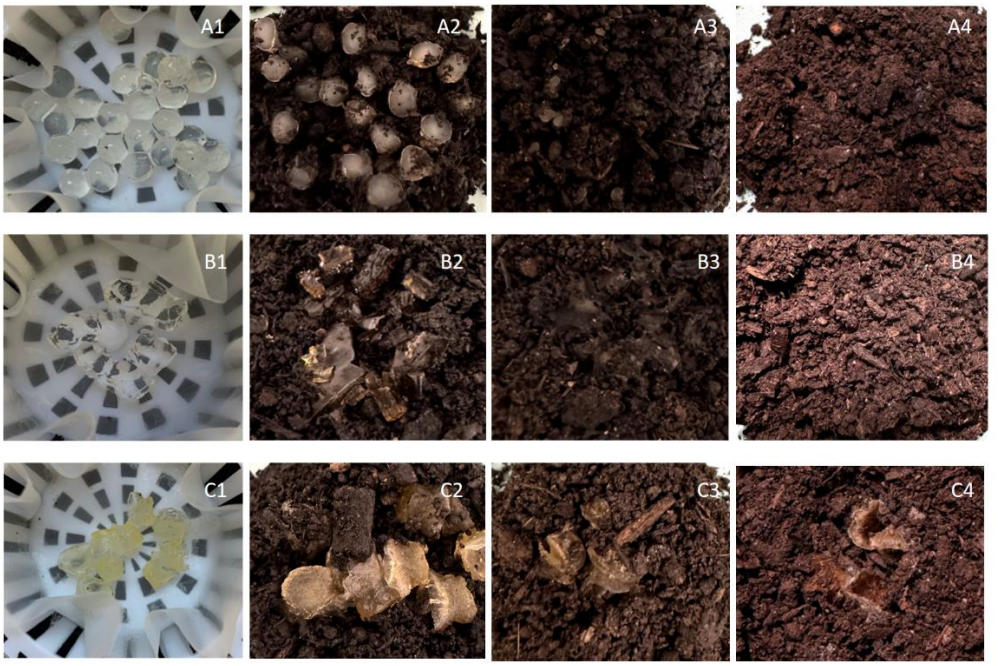

Figure 3.21 – Macroscopic changes of hydrogels during biodegradation experiments: A) HY-ACMC; B) HY-MGEL; C) HY-MCHI. The selected days are: 1) 0 days; 2) 6 days; 3) 34 days; 4) 58 days.

PTEs concentrations in each sample are summarized in Figure 3.22.

What clearly emerges is that the background concentrations are not significantly changed for all PTEs except for mercury in the compost samples after burial of the chitosan-based hydrogels. These results have been confirmed with the analysis of variance (ANOVA) performed with the statistical software XLSTAT and considering Dunnett's test results (Appendix IV, Tables AIV-4).

Indeed, the ANOVA did not highlight statistically significant differences between the average concentrations of PTEs present in the pre-biodegradation compost and those found in the samples containing HY-ACMC and HY-MGEL.

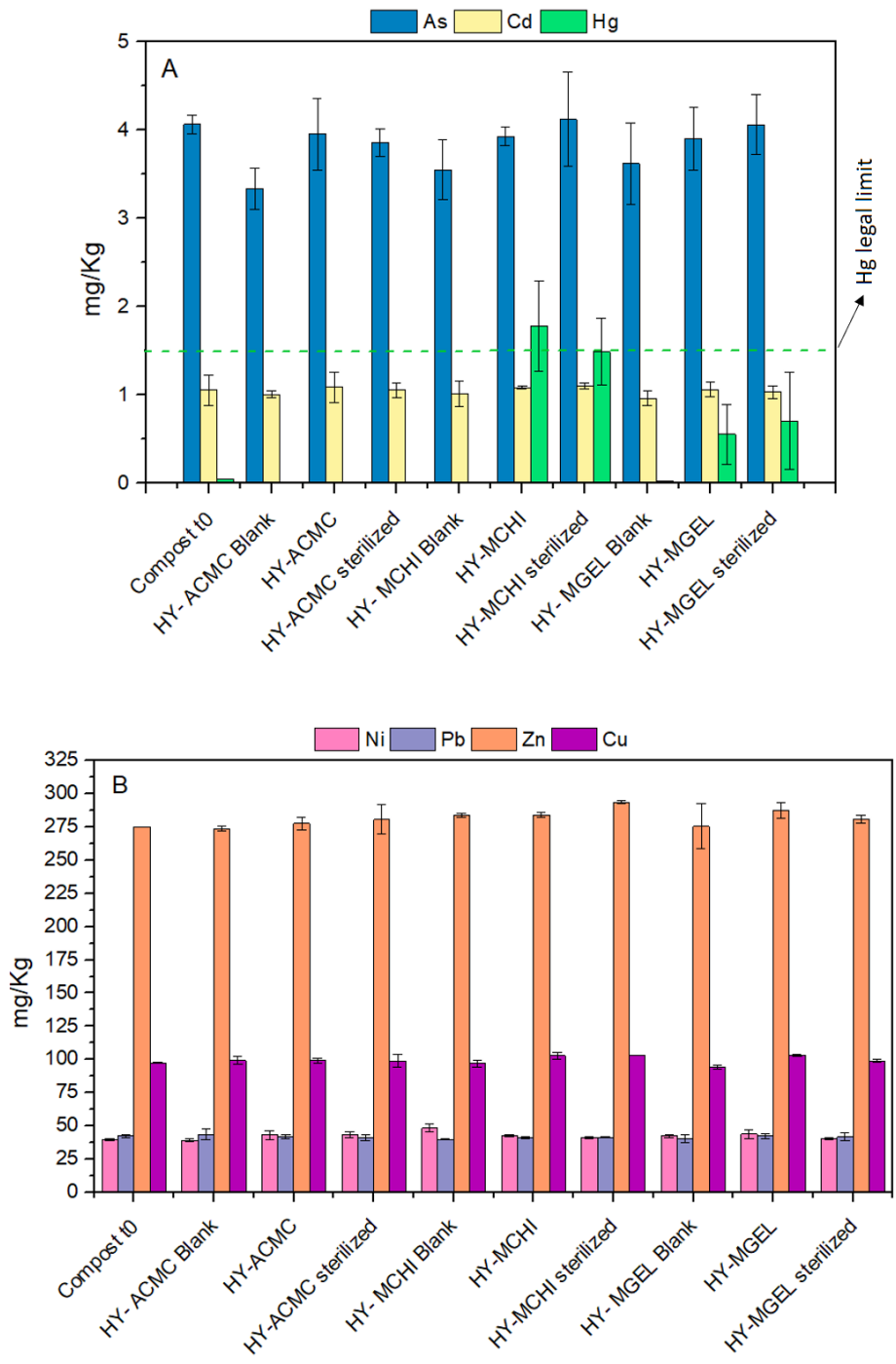

Figure 3.22 - PTEs concentration in compost before and after hydrogel biodegradation: A) As, Cd and Hg; B) Ni, Pb, Zn and Cu

This concentration increase may be related to the lower effectiveness of the regeneration treatment for HY-MCHI leading to a limited Hg desorption (Figure 3.11-C) and a consequent higher release during the biodegradation phase.

3.5 Final remarks

Biopolymers functionalized and characterized in Chapter 2 were used to prepare different types of hydrogels which were in turn characterized and tested for the remediation of aqueous matrices.

These studies were designed to investigate all factors that could influence the real applicability of the developed materials. Aspects such as the influence of the contaminants' concentration, the solutions pH value, the presence of organic matter and competitive inorganic species cannot be overlooked together with the efficiency of the tested hydrogels, the possibility of regenerating, reusing and disposing them in a safe and sustainable way.

Cellulose-based materials have been prepared employing water as a solvent and working at room temperature. The ease of preparation together with the absence of hazardous solvents constitute a strength for these materials which have proven to be effective for the removal of organic contaminants and in the adsorption of inorganic species not only from spiked ultra-pure water but also from aquaculture water samples.

The investigations about the pH-dependent PTEs removal have demonstrated that the adsorption phenomenon is generally influenced by the acidity of the systems due to the pH effect on the adsorbents' surface ionic state and on contaminants' speciation. However, HY-ACMC has been shown to maintain good adsorption capabilities at different pH conditions, initial PTEs concentrations and in real water samples, which makes it attractive for applications in a wide range of real-world conditions.

The coupling of cellulose with soybean peroxidase in HY-AC-SBP made it possible to treat aqueous solutions containing TCP, TCS and BPA, significantly reducing their toxicity in just 5 hours of reaction. The efficiency of the enzymatic catalysis was maintained for 8 treatment cycles, with a slowdown in the reaction kinetics but not

such as to affect the outcome at the end of the treatment. The possibility of reusing materials for multiple reaction cycles constitutes an important result because it makes the water treatment process less impactful by reducing the use of raw materials and solvents.

Unfortunately, regeneration is not always a viable option. HY-ACMC, as physically cross-linked hydrogels, are structurally unstable when treated with Na_2EDTA, an essential step to desorb the PTEs removed from the water and to be reused. On the contrary, permanent hydrogels containing covalent bonds and therefore characterized by a more stable network, can overcome this drawback. Indeed, HY-MCHI and HY-MGEL were effectively regenerated and used for three successive PTEs contaminated water treatment cycles.

End-of-life can also be a critical point in the materials' development process. The choice of biopolymers as raw materials is already aimed at trying to follow the path of biodegradation, however the different functionalisations that often have to be carried out can alter materials biodegradability. In this work qualitative evidence of microbial activity on hydrogels during experiments of burial in compost have been obtained as the formation of mold (for HY-AC-SBP and HY-MCHI) or even the disappearance of materials (for HY-MGEL and HY-ACMC). The analysis of contaminant concentrations in the compost following biodegradation tests confirmed that, except for chitosan-based hydrogels, regeneration is sufficient to guarantee an *end-of-life* through burial in soil safe and eco-sustainable.

3.6 References

Academic Software. Sourby Old Farm, Timble, Otley, Yorks, LS21 2PW. In SC-Database. The IUPAC Stability Constant Database,Version 5.84. (s.d.). [Dataset].

Adjuik, T. A., Nokes, S. E., & Montross, M. D. (2023). Biodegradability of bio-based and synthetic hydrogels as sustainable soil amendments: A review. Journal of Applied Polymer Science, 140(12), e53655. https://doi.org/10.1002/app.53655

Ahmad, A., Kurniawan, S. B., Abdullah, S. R. S., Othman, A. R., & Hasan, H. A. (2022). Contaminants of emerging concern (CECs) in aquaculture effluent: Insight into breeding and rearing activities, alarming impacts, regulations, performance of

wastewater treatment unit and future approaches. Chemosphere, 290, 133319. https://doi.org/10.1016/j.chemosphere.2021.133319

Ahmad, A. L., Chin, J. Y., Mohd Harun, M. H. Z., & Low, S. C. (2022). Environmental impacts and imperative technologies towards sustainable treatment of aquaculture wastewater: A review. Journal of Water Process Engineering, 46, 102553. https://doi.org/10.1016/j.jwpe.2021.102553

Ahmad, I., Fatima, N., Naz, E., Farooqi, Z. U. R., & Bulgariu, L. (2024). Treatment Methods for Mercury Removal From Soil and Wastewater. In N. Kumar (A c. Di), Mercury Toxicity Mitigation: Sustainable Nexus Approach (pp. 257–281). Springer Nature Switzerland. https://doi.org/10.1007/978-3-031-48817-7_12

Alakhras, F. A., Dari, K. A., & Mubarak, M. S. (2005). Synthesis and chelating properties of some poly(amidoxime-hydroxamic acid) resins toward some trivalent lanthanide metal ions. Journal of Applied Polymer Science, 97(2), 691–696. https://doi.org/10.1002/app.21825

Aleku, D. L., Lazareva, O., & Pichler, T. (2024). Mercury in groundwater – Source, transport and remediation. Applied Geochemistry, 170, 106060. https://doi.org/10.1016/j.apgeochem.2024.106060

Alemdar, A., & Sain, M. (2008). Isolation and characterization of nanofibers from agricultural residues – Wheat straw and soy hulls. Bioresource Technology, 99(6), 1664–1671. https://doi.org/10.1016/j.biortech.2007.04.029

Alemzadeh, I., & Nejati, S. (2009). Removal of Phenols with Encapsulated Horseradish Peroxidase in Calcium Alginate. Iranian Journal of Chemistry & Chemical Engineering, 28(2), 43–49.

Algieri, V., Tursi, A., Costanzo, P., Maiuolo, L., De Nino, A., Nucera, A., Castriota, M., De Luca, O., Papagno, M., Caruso, T., Ciurciù, S., Corrente, G. A., & Beneduci, A. (2024). Thiol-functionalized cellulose for mercury polluted water remediation: Synthesis and study of the adsorption properties. Chemosphere, 355, 141891. https://doi.org/10.1016/j.chemosphere.2024.141891

Awad, F. S., Bakry, A. M., Ibrahim, A. A., Lin, A., & El-Shall, M. S. (2021). Thiol- and Amine-Incorporated UIO-66-NH2 as an Efficient Adsorbent for the Removal of Mercury(II) and Phosphate Ions from Aqueous Solutions. Industrial & Engineering Chemistry Research, 60(34), 12675–12688. https://doi.org/10.1021/acs.iecr.1c01892

Awasthi, S. K., Kumar, M., Kumar, V., Sarsaiya, S., Anerao, P., Ghosh, P., Singh, L., Liu, H., Zhang, Z., & Awasthi, M. K. (2022). A comprehensive review on recent advancements in biodegradation and sustainable management of biopolymers. Environmental Pollution, 307, 119600. https://doi.org/10.1016/j.envpol.2022.119600

Badsha, M. A. H., Khan, M., Wu, B., Kumar, A., & Lo, I. M. C. (2021). Role of surface functional groups of hydrogels in metal adsorption: From performance to mechanism. Journal of Hazardous Materials, 408, 124463. https://doi.org/10.1016/j.jhazmat.2020.124463

Bahadar, H., Maqbool, F., Niaz, K., & Abdollahi, M. (2016). Toxicity of Nanoparticles and an Overview of Current Experimental Models. Iranian Biomedical Journal, 20(1), 1–11. https://doi.org/10.7508/ibj.2016.01.001

Bashir, S., Hina, M., Iqbal, J., Rajpar, A. H., Mujtaba, M. A., Alghamdi, N. A., Wageh, S., Ramesh, K., & Ramesh, S. (2020). Fundamental Concepts of Hydrogels: Synthesis, Properties, and Their Applications. Polymers, 12(11), 2702. https://doi.org/10.3390/polym12112702

Bastos, L. P. H., de Carvalho, C. W. P., & Garcia-Rojas, E. E. (2018). Formation and characterization of the complex coacervates obtained between lactoferrin and sodium alginate. International Journal of Biological Macromolecules, 120, 332–338. https://doi.org/10.1016/j.ijbiomac.2018.08.050

Basu, N., Bastiansz, A., Dórea, J. G., Fujimura, M., Horvat, M., Shroff, E., Weihe, P., & Zastenskaya, I. (2023). Our evolved understanding of the human health risks of mercury. Ambio, 52(5), 877–896. https://doi.org/10.1007/s13280-023-01831-6

Benbachir, H., Gaffour, H., & Mokhtari, M. (2017). Photodegradation of 2,4,6-trichlorophenol using natural hematite modified with chloride of zirconium oxide. Reaction Kinetics, Mechanisms and Catalysis, 122(1), 635–653. https://doi.org/10.1007/s11144-017-1248-1

Benbettaïeb, N., Mahfoudh, R., Moundanga, S., Brachais, C.-H., Chambin, O., & Debeaufort, F. (2020). Modeling of the release kinetics of phenolic acids embedded in gelatin/chitosan bioactive-packaging films: Influence of both water activity and viscosity of the food simulant on the film structure and antioxidant activity. International Journal of Biological Macromolecules, 160, 780–794. https://doi.org/10.1016/j.ijbiomac.2020.05.199

Besharati Vineh, M., Saboury, A. A., Poostchi, A. A., Rashidi, A. M., & Parivar, K. (2018). Stability and activity improvement of horseradish peroxidase by covalent immobilization on functionalized reduced graphene oxide and biodegradation of high phenol concentration. International Journal of Biological Macromolecules, 106, 1314–1322. https://doi.org/10.1016/j.ijbiomac.2017.08.133

Borges-Vilches, J., Figueroa, T., Guajardo, S., Meléndrez, M., & Fernández, K. (2020). Development of gelatin aerogels reinforced with graphene oxide by microwave-assisted synthesis: Influence of the synthesis conditions on their physicochemical properties. Polymer, 208, 122951. https://doi.org/10.1016/j.polymer.2020.122951

Bornscheuer, U. T., & Buchholz, K. (2005). Highlights in Biocatalysis – Historical Landmarks and Current Trends. Engineering in Life Sciences, 5(4), 309–323. https://doi.org/10.1002/elsc.200520089

Bousoumah, R., Leso, V., Iavicoli, I., Huuskonen, P., Viegas, S., Porras, S. P., Santonen, T., Frery, N., Robert, A., & Ndaw, S. (2021). Biomonitoring of occupational exposure to bisphenol A, bisphenol S and bisphenol F: A systematic review. Science of The Total Environment, 783, 146905. https://doi.org/10.1016/j.scitotenv.2021.146905

Bracco, L. F., Levin, G. J., Navarro del Ca?izo, A. A., Wolman, F. J., Miranda, M. V., & Cascone, O. (2017). Simultaneous purification and immobilization of soybean hull peroxidase with a dye attached to chitosan mini-spheres. Biocatalysis and Biotransformation, 1–9. https://doi.org/10.1080/10242422.2017.1334767

Cai, R., Zhou, Y., Hu, J., Lu, J., Fan, X., Chen, Y., Ding, M., Rong, J., Liu, W., & Chen, Y. (2022). A novel sodium alginate/cellulose nanofiber self-supported hydrogel membrane and its filtration performance. Journal of Water Process Engineering, 50, 103303. https://doi.org/10.1016/j.jwpe.2022.103303

Cai, T., Yang, Z., Li, H., Yang, H., Li, A., & Cheng, R. (2013). Effect of hydrolysis degree of hydrolyzed polyacrylamide grafted carboxymethyl cellulose on dye removal efficiency. Cellulose, 20(5), 2605–2614. https://doi.org/10.1007/s10570-013-9987-2

Calza, P., Zacchigna, D., & Laurenti, E. (2016). Degradation of orange dyes and carbamazepine by soybean peroxidase immobilized on silica monoliths and titanium dioxide. Environmental Science and Pollution Research, 23(23), 23742–23749. https://doi.org/10.1007/s11356-016-7399-1

Cassone, G., Chillé, D., Foti, C., Giuffré, O., Ponterio, R. C., Sponer, J., & Saija, F. (2018). Stability of hydrolytic arsenic species in aqueous solutions: As3+vs. As5+. Physical Chemistry Chemical Physics, 20(36), 23272–23280. https://doi.org/10.1039/C8CP04320E

Castellino, L., Alladio, E., Bertinetti, S., Lando, G., De Stefano, C., Blasco, S., García-España, E., Gama, S., Berto, S., & Milea, D. (2023). PyES – An open-source software for the computation of solution and precipitation equilibria. Chemometrics and Intelligent Laboratory Systems, 239, 104860. https://doi.org/10.1016/j.chemolab.2023.104860

Cerkvenik-Flajs, V., Fonda, I., & Gombač, M. (2018). Analysis and Occurrence of Bisphenol A in Mediterranean Mussels (Mytilus galloprovincialis) Sampled from the Slovenian Coastal Waters of the North Adriatic Sea. Bulletin of Environmental Contamination and Toxicology, 101(4), 439–445. https://doi.org/10.1007/s00128-018-2415-4

Chagas, P. M. B., Torres, J. A., Silva, M. C., & Correa, A. D. (2015). Immobilized soybean hull peroxidase for the oxidation of phenolic compounds in coffee processing wastewater. International Journal of Biological Macromolecules, 81, 568–575. https://doi.org/10.1016/j.ijbiomac.2015.08.061

Chandra, R., & Rustgi, R. (1998). Biodegradable polymers. Progress in Polymer Science, 23(7), 1273–1335. https://doi.org/10.1016/S0079-6700(97)00039-7

Charpentier, T. V. J., Neville, A., Lanigan, J. L., Barker, R., Smith, M. J., & Richardson, T. (2016). Preparation of Magnetic Carboxymethylchitosan Nanoparticles for Adsorption of Heavy Metal Ions. ACS Omega, 1(1), 77–83. https://doi.org/10.1021/acsomega.6b00035

Chen, C., Ting, Y., Ch'ng, B.-L., & Hsi, H.-C. (2020). Influence of sulfide, chloride and dissolved organic matter on mercury adsorption by activated carbon in aqueous system. Sustainable Environment Research, 30(1), 22. https://doi.org/10.1186/s42834-020-00065-5

Chen, P. H., Hsu, C.-F., Tsai, D. D.-W., Lu, Y.-M., & Huang, W.-J. (2014). Adsorption of mercury from water by modified multi-walled carbon nanotubes: Adsorption behaviour and interference resistance by coexisting anions. Environmental Technology, 35(15), 1935–1944. https://doi.org/10.1080/09593330.2014.886627

Chizitere Emenike, E., George Adeniyi, A., Iwuozor, K. O., Okorie, C. J., Egbemhenghe, A. U., Omuku, P. E., Chidiebere Okwu, K., & Saliu, O. D. (2023). A critical review on the removal of mercury (Hg2+) from aqueous solution using nanoadsorbents. Environmental Nanotechnology, Monitoring & Management, 20, 100816. https://doi.org/10.1016/j.enmm.2023.100816

Choi, H. Y., Bae, J. H., Hasegawa, Y., An, S., Kim, I. S., Lee, H., & Kim, M. (2020). Thiol-functionalized cellulose nanofiber membranes for the effective adsorption of heavy metal ions in water. Carbohydrate Polymers, 234, 115881. https://doi.org/10.1016/j.carbpol.2020.115881

Chowdhury, A., Das, S. K., Mondal, S., Ruidas, S., Chakraborty, D., Chatterjee, S., Bhunia, M. K., Chandra, D., Hara, M., & Bhaumik, A. (2021). Sulfur-containing nitrogen-rich robust hierarchically porous organic polymer for adsorptive removal of mercury: Experimental and theoretical insights. Environmental Science: Nano, 8(9), 2641–2649. https://doi.org/10.1039/D1EN00448D

Chung, C.-C., Chen, H.-W., & Wu, H.-T. (2022). Discussions on the Properties of Emulsion Prepared by Using an Amphoteric Chitosan as an Emulsifier. Applied Sciences, 12(10), Articolo 10. https://doi.org/10.3390/app12105249

COMMISSION REGULATION (EU) 2023/915 of 25 April 2023 on maximum levels for certain contaminants in food and repealing Regulation (EC) No

1881/2006. (s.d.). Recuperato 6 dicembre 2024, da https://eur-lex.europa.eu/eli/reg/2023/915/oj

COMMUNICATION FROM THE COMMISSION TO THE EUROPEAN PARLIAMENT, THE COUNCIL, THE EUROPEAN ECONOMIC AND SOCIAL COMMITTEE AND THE COMMITTEE OF THE REGIONS Strategic Guidelines for a More Sustainable and Competitive EU Aquaculture for the Period 2021 to 2030 (2021). https://eur-lex.europa.eu/legal-content/en/ALL/?uri=CELEX:52021DC0236

Contardo-Jara, V., Meinecke, S., Feibicke, M., Berghahn, R., Schmidt, R., & Mohr, S. (2021). Fate, bioaccumulation and toxic effects of triclosan on a freshwater community – A mesocosm study. Environmental Advances, 5, 100100. https://doi.org/10.1016/j.envadv.2021.100100

Council of the European Union. (2006). Council Directive 2006/88/EC on animal health requirements for aquaculture animals and products thereof, and on the prevention and control of certain diseases in aquatic animals. | FAOLEX. https://www.fao.org/faolex/results/details/en/c/LEX-FAOC067636/

Cui, H., Qian, Y., Li, Q., Wei, Z., & Zhai, J. (2013). Fast removal of Hg(II) ions from aqueous solution by amine-modified attapulgite. Applied Clay Science, 72, 84–90. https://doi.org/10.1016/j.clay.2013.01.003

D. Lgs 31/2001. (s.d.). Decreto Legislativo 2 febbraio 2001, n. 31 «Attuazione della direttiva 98/83/CE relativa alla qualita' delle acque destinate al consumo umano». Recuperato 6 dicembre 2024, da https://www.parlamento.it/parlam/leggi/deleghe/01031dl.htm

Dalev, P., Staromanova, E., Dalev, D., Patil, R. D., Mark, J. E., Vassileva, E., & Fakirov, S. (2014). Biodegradation of Chemically Modified Gelatin Films in a Simulated Natural Environment. Biotechnology & Biotechnological Equipment, 15(2), 116–123. https://doi.org/10.1080/13102818.2001.10819142

Deepa, B., Abraham, E., Pothan, L. A., Cordeiro, N., Faria, M., & Thomas, S. (2016). Biodegradable Nanocomposite Films Based on Sodium Alginate and Cellulose Nanofibrils. Materials, 9(1), 50. https://doi.org/10.3390/ma9010050

Dhillon, G., Kaur, S., Pulicharla, R., Brar, S., Cledón, M., Verma, M., & Surampalli, R. (2015). Triclosan: Current Status, Occurrence, Environmental Risks and Bioaccumulation Potential. International Journal of Environmental Research and Public Health, 12(5), 5657–5684. https://doi.org/10.3390/ijerph120505657

Díaz-Báez, M. C., & Valderrama-Rincon, J. D. (2017). Rapid restoration of methanogenesis in an acidified UASB reactor treating 2,4,6-trichlorophenol (TCP). Journal of Hazardous Materials, 324, 599–604. https://doi.org/10.1016/j.jhazmat.2016.11.031

Doh, H., Dunno, K. D., & Whiteside, W. S. (2020). Cellulose nanocrystal effects on the biodegradability with alginate and crude seaweed extract nanocomposite films. Food Bioscience, 38, 100795. https://doi.org/10.1016/j.fbio.2020.100795

Donadelli, J. A., García Einschlag, F. S., Laurenti, E., Magnacca, G., & Carlos, L. (2018). Soybean peroxidase immobilized onto silica-coated superparamagnetic iron oxide nanoparticles: Effect of silica layer on the enzymatic activity. Colloids and Surfaces B: Biointerfaces, 161, 654–661. https://doi.org/10.1016/j.colsurfb.2017.11.043

Dong, C., Chen, W., & Liu, C. (2014). Flocculation of algal cells by amphoteric chitosan-based flocculant. Bioresource Technology, 170, 239–247. https://doi.org/10.1016/j.biortech.2014.07.108

Du, J., Ye, Q., Dong, Z., Yang, X., & Zhao, L. (2021). Selective adsorption of mercury(II) ions from aqueous solution by two kinds of modified cellulose microsphere. DESALINATION AND WATER TREATMENT, 229, 302–313. https://doi.org/10.5004/dwt.2021.27372

Dubey, R., Bajpai, J., & Bajpai, A. K. (2016). Chitosan-alginate nanoparticles (CANPs) as potential nanosorbent for removal of Hg (II) ions. Environmental Nanotechnology, Monitoring & Management, 6, 32–44. https://doi.org/10.1016/j.enmm.2016.06.008

Durpekova, S., Di Martino, A., Dusankova, M., Drohsler, P., & Sedlarik, V. (2021). Biopolymer Hydrogel Based on Acid Whey and Cellulose Derivatives for Enhancement Water Retention Capacity of Soil and Slow Release of Fertilizers. Polymers, 13(19), Articolo 19. https://doi.org/10.3390/polym13193274

Emenike, E. C., Iwuozor, K. O., & Anidiobi, S. U. (2022). Heavy Metal Pollution in Aquaculture: Sources, Impacts and Mitigation Techniques. Biological Trace Element Research, 200(10), 4476–4492. https://doi.org/10.1007/s12011-021-03037-x

Esfandiar, N., Suri, R., & McKenzie, E. R. (2022). Competitive sorption of Cd, Cr, Cu, Ni, Pb and Zn from stormwater runoff by five low-cost sorbents; Effects of co-contaminants, humic acid, salinity and pH. Journal of Hazardous Materials, 423, 126938. https://doi.org/10.1016/j.jhazmat.2021.126938

EU Platform on Animal Welfare Own Initiative Group on Fish. (2022, luglio). GUIDELINES ON WATER QUALITY AND HANDLING FOR THE WELFARE OF FARMED VERTEBRATE FISH. https://food.ec.europa.eu/system/files/2022-07/aw_platform_plat-conc_guide_farmed-fish_en.pdf

Faheem, M., & Bhandari, R. K. (2021). Detrimental Effects of Bisphenol Compounds on Physiology and Reproduction in Fish: A Literature Review.

Environmental Toxicology and Pharmacology, 81, 103497. https://doi.org/10.1016/j.etap.2020.103497

Fan, H., Ma, X., Zhou, S., Huang, J., Liu, Y., & Liu, Y. (2019). Highly efficient removal of heavy metal ions by carboxymethyl cellulose-immobilized Fe3O4 nanoparticles prepared via high-gravity technology. Carbohydrate Polymers, 213, 39–49. https://doi.org/10.1016/j.carbpol.2019.02.067

FAO. (2022). The State of World Fisheries and Aquaculture 2022: Towards Blue Transformation. FAO. https://doi.org/10.4060/cc0461en

Farias, S., Mayer, D. A., de Oliveira, D., de Souza, S. M. A. G. U., & de Souza, A. A. U. (2017). Free and Ca-Alginate Beads Immobilized Horseradish Peroxidase for the Removal of Reactive Dyes: An Experimental and Modeling Study. Applied Biochemistry and Biotechnology, 182(4), 1290–1306. https://doi.org/10.1007/s12010-017-2399-2

Fei, Y., Li, Y., Han, S., & Ma, J. (2016). Adsorptive removal of ciprofloxacin by sodium alginate/graphene oxide composite beads from aqueous solution. Journal of Colloid and Interface Science, 484, 196–204. https://doi.org/10.1016/j.jcis.2016.08.068

Fernández, E., López, D., López-Cabarcos, E., & Mijangos, C. (2005). Viscoelastic and swelling properties of glucose oxidase loaded polyacrylamide hydrogels and the evaluation of their properties as glucose sensors. Polymer, 46(7), 2211–2217. https://doi.org/10.1016/j.polymer.2004.12.039

Ferrari, R. P., Laurenti, E., & Trotta, F. (1999). Oxidative 4-dechlorination of 2,4,6-trichlorophenol catalyzed by horseradish peroxidase. JBIC Journal of Biological Inorganic Chemistry, 4(2), 232–237. https://doi.org/10.1007/s007750050309

Freundlich, H. (1932). Of the adsorption of gases. Section II. Kinetics and energetics of gas adsorption. Introductory paper to section II. Transactions of the Faraday Society, 28(0), 195–201. https://doi.org/10.1039/TF9322800195

Georgin, J., Franco, D. S. P., Dehmani, Y., Nguyen-Tri, P., & El Messaoudi, N. (2024). Current status of advancement in remediation technologies for the toxic metal mercury in the environment: A critical review. Science of The Total Environment, 947, 174501. https://doi.org/10.1016/j.scitotenv.2024.174501

Giwa, A. S., Ndungutse, J. M., Li, Y., Mabi, A., Liu, X., Vakili, M., Memon, A. G., Ai, L., Chenfeng, Z., & Sheng, M. (2022). Modification of biochar with Fe3O4 and humic acid-salt for removal of mercury from aqueous solutions: A review. Environmental Pollutants and Bioavailability, 34(1), 352–364. https://doi.org/10.1080/26395940.2022.2115402

Gomez, J. L., Bódalo, A., Gomez, E., Bastida, J., Hidalgo, A. M., Gomez, M., Gómez, J. L., Bódalo, A., Gómez, E., Bastida, J., Hidalgo, A. M., & Gómez, M.

(2006). Immobilization of peroxidases on glass beads: An improved alternative for phenol removal. Enzyme and Microbial Technology, 39(5), 1016–1022. https://doi.org/10.1016/j.enzmictec.2006.02.008

Goudie, K. J., McCreath, S. J., Parkinson, J. A., Davidson, C. M., & Liggat, J. J. (2023). Investigation of the influence of pH on the properties and morphology of gelatin hydrogels. Journal of Polymer Science, 61(19), 2316–2332. https://doi.org/10.1002/pol.20230141

Gul, S., Memon, F. N., & Memon, S. (2022). Optimization of toxic metal adsorption on DEA-calix[4]arene appended silica resin using a central composite design. New Journal of Chemistry, 46(7), 3448–3463. https://doi.org/10.1039/D1NJ05669G

Hammel, K. E., & Tardone, P. J. (1988). The Oxidative 4-Dechlorination of Polychlorinated Phenols Is Catalyzed by Extracellular Fungal Lignin Peroxidases+. Biochemistry, 27, 6563–6568. https://doi.org/10.1021/bi00417a055

Harrison, J. P., Boardman, C., O'Callaghan, K., Delort, A.-M., & Song, J. (2018). Biodegradability standards for carrier bags and plastic films in aquatic environments: A critical review. Royal Society Open Science, 5(5), 171792. https://doi.org/10.1098/rsos.171792

Hautphenne, C., Penninckx, M., & Debaste, F. (2016). Product formation from phenolic compounds removal by laccases: A review. Environmental Technology & Innovation, 5, 250–266. https://doi.org/10.1016/j.eti.2016.04.001

Henriksen, A., Mirza, O., Indiani, C., Teilum, K., Smulevich, G., Welinder, K. G., & Gajhede, M. (2001). Structure of soybean seed coat peroxidase: A plant peroxidase with unusual stability and haem-apoprotein interactions. Protein Science, 10(1), 108–115. https://doi.org/10.1110/ps.37301

Horn, C., Pospiech, D., Allertz, P. J., Müller, M., Salchert, K., & Hommel, R. (2021). Chemical Design of Hydrogels with Immobilized Laccase for the Reduction of Persistent Trace Compounds in Wastewater. ACS Applied Polymer Materials, 3(5), 2823–2834. https://doi.org/10.1021/acsapm.1c00380

Hu, Y., Jiang, X., Ding, Y., Ge, H., Yuan, Y., & Yang, C. (2002). Synthesis and characterization of chitosan–poly(acrylic acid) nanoparticles. Biomaterials, 23(15), 3193–3201. https://doi.org/10.1016/S0142-9612(02)00071-6

Hu, Z.-H., Omer, A. M., Ouyang, X., & Yu, D. (2018). Fabrication of carboxylated cellulose nanocrystal/sodium alginate hydrogel beads for adsorption of Pb(II) from aqueous solution. International Journal of Biological Macromolecules, 108, 149–157. https://doi.org/10.1016/j.ijbiomac.2017.11.171

Huang, C.-L., Ma, H.-W., & Yu, C.-P. (2014). Substance flow analysis and assessment of environmental exposure potential for triclosan in mainland China.

Science of The Total Environment, 499, 265–275. https://doi.org/10.1016/j.scitotenv.2014.08.032

Huang, Q., & Weber, W. J. (2005). Transformation and Removal of Bisphenol A from Aqueous Phase via Peroxidase-Mediated Oxidative Coupling Reactions: Efficacy, Products, and Pathways. Environmental Science & Technology, 39(16), 6029–6036. https://doi.org/10.1021/es050036x

Jeong, S.-S., Park, B.-J., Yoon, J.-H., Kirkham, M. B., Yang, J.-E., & Kim, H.-S. (2024). Mechanistic Evidence for Hg Removal from Wastewater by Biologically Produced Sulfur. Toxics, 12(4), Articolo 4. https://doi.org/10.3390/toxics12040278

Johs, A., Eller, V. A., Mehlhorn, T. L., Brooks, S. C., Harper, D. P., Mayes, M. A., Pierce, E. M., & Peterson, M. J. (2019). Dissolved organic matter reduces the effectiveness of sorbents for mercury removal. Science of The Total Environment, 690, 410–416. https://doi.org/10.1016/j.scitotenv.2019.07.001

Kamal, J. K. A., & Behere, D. V. (2002). Thermal and conformational stability of seed coat soybean peroxidase. Biochemistry, 41(29), 9034–9042. https://doi.org/10.1021/bi025621e

Kanmani, P., Aravind, J., Kamaraj, M., Sureshbabu, P., & Karthikeyan, S. (2017). Environmental applications of chitosan and cellulosic biopolymers: A comprehensive outlook. Bioresource Technology, 242, 295–303. https://doi.org/10.1016/j.biortech.2017.03.119

Karci, A. (2014). Degradation of chlorophenols and alkylphenol ethoxylates, two representative textile chemicals, in water by advanced oxidation processes: The state of the art on transformation products and toxicity. Chemosphere, 99, 1–18. https://doi.org/10.1016/j.chemosphere.2013.10.034

Kaur, K., & Jindal, R. (2019). Comparative study on the behaviour of Chitosan-Gelatin based Hydrogel and nanocomposite ion exchanger synthesized under microwave conditions towards photocatalytic removal of cationic dyes. Carbohydrate Polymers, 207, 398–410. https://doi.org/10.1016/j.carbpol.2018.12.002

Kumah, E. A., Fopa, R. D., Harati, S., Boadu, P., Zohoori, F. V., & Pak, T. (2023). Human and environmental impacts of nanoparticles: A scoping review of the current literature. BMC Public Health, 23(1), 1059. https://doi.org/10.1186/s12889-023-15958-4

Kumar, S., Paul, T., Shukla, S. P., Kumar, K., Karmakar, S., Bera, K. K., & Bhushan kumar, C. (2021). Biomarkers-based assessment of triclosan toxicity in aquatic environment: A mechanistic review. Environmental Pollution, 286, 117569. https://doi.org/10.1016/j.envpol.2021.117569

Lai, W. W.-P., Lin, Y.-C., Wang, Y.-H., Guo, Y. L., & Lin, A. Y.-C. (2018). Occurrence of Emerging Contaminants in Aquaculture Waters: Cross-Contamination between Aquaculture Systems and Surrounding Waters. Water, Air, & Soil Pollution, 229(8), 249. https://doi.org/10.1007/s11270-018-3901-3

Lam, B., Déon, S., Morin-Crini, N., Crini, G., & Fievet, P. (2018). Polymer-enhanced ultrafiltration for heavy metal removal: Influence of chitosan and carboxymethyl cellulose on filtration performances. Journal of Cleaner Production, 171, 927–933. https://doi.org/10.1016/j.jclepro.2017.10.090

Langmuir, I. (1918). THE ADSORPTION OF GASES ON PLANE SURFACES OF GLASS, MICA AND PLATINUM. Journal of the American Chemical Society, 40(9), 1361–1403. https://doi.org/10.1021/ja02242a004

Lee, H.-R., Jung, S. M., Yoon, S., Yoon, W. H., Park, T. H., Kim, S., Shin, H. W., Hwang, D. S., & Jung, S. (2019). Immobilization of planktonic algal spores by inkjet printing. Scientific Reports, 9(1), 12357. https://doi.org/10.1038/s41598-019-48776-z

Lee, K. Y., & Mooney, D. J. (2012). Alginate: Properties and biomedical applications. Progress in Polymer Science, 37(1), 106–126. https://doi.org/10.1016/j.progpolymsci.2011.06.003

Li, D., Wang, Y., Deng, W., & Wang, D. (2024). Efficient and selective capture of various mercury species from water using an exfoliated thiocellulose. Science of The Total Environment, 920, 171063. https://doi.org/10.1016/j.scitotenv.2024.171063

Li, J., Peng, J., Zhang, Y., Ji, Y., Shi, H., Mao, L., & Gao, S. (2016). Removal of triclosan via peroxidases-mediated reactions in water: Reaction kinetics, products and detoxification. Journal of Hazardous Materials, 310, 152–160. https://doi.org/10.1016/j.jhazmat.2016.02.037

Li, J., Zhang, Y., Peng, J., Wu, X., Gao, S., & Mao, L. (2017). The effect of dissolved organic matter on soybean peroxidase-mediated removal of triclosan in water. Chemosphere, 172, 399–407. https://doi.org/10.1016/j.chemosphere.2017.01.013

Li, L. (2021). Toxicity evaluation and by-products identification of triclosan ozonation and chlorination. Chemosphere, 263, 128223. https://doi.org/10.1016/j.chemosphere.2020.128223

Li, N., & Bai, R. (2005). Copper adsorption on chitosan–cellulose hydrogel beads: Behaviors and mechanisms. Separation and Purification Technology, 42(3), 237–247. https://doi.org/10.1016/j.seppur.2004.08.002

Li, Y., Wang, C., Luan, Y., Liu, W., Chen, T., Liu, P., & Liu, Z. (2022). Preparation of pH-responsive cellulose nanofibril/sodium alginate based hydrogels for drug

release. Journal of Applied Polymer Science, 139(7), 51647. https://doi.org/10.1002/app.51647

Li, Z., Wu, L., Liu, H., Lan, H., & Qu, J. (2013). Improvement of aqueous mercury adsorption on activated coke by thiol-functionalization. Chemical Engineering Journal, 228, 925–934. https://doi.org/10.1016/j.cej.2013.05.063

Liu, C., Zhang, Z., Kong, Q., Zhang, R., & Yang, X. (2019). Enhancing the antitumor activity of tea polyphenols encapsulated in biodegradable nanogels by macromolecular self-assembly. RSC Advances, 9(18), 10004–10016. https://doi.org/10.1039/C8RA07783E

Liu, D.-M., Chen, J., & Shi, Y.-P. (2018). Advances on methods and easy separated support materials for enzymes immobilization. TrAC Trends in Analytical Chemistry, 102, 332–342. https://doi.org/10.1016/j.trac.2018.03.011

Liu, Y., & Chen, J. Y. (2016). Enzyme immobilization on cellulose matrixes. Journal of Bioactive and Compatible Polymers, 31(6), 553–567. https://doi.org/10.1177/0883911516637377

López-Muñoz, M. J., Aguado, J., Arencibia, A., & Pascual, R. (2011). Mercury removal from aqueous solutions of HgCl2 by heterogeneous photocatalysis with TiO2. Applied Catalysis B: Environmental, 104(3), 220–228. https://doi.org/10.1016/j.apcatb.2011.03.029

Lucas, N., Bienaime, C., Belloy, C., Queneudec, M., Silvestre, F., & Nava-Saucedo, J.-E. (2008). Polymer biodegradation: Mechanisms and estimation techniques – A review. Chemosphere, 73(4), 429–442. https://doi.org/10.1016/j.chemosphere.2008.06.064

Lv, J., Luo, L., Zhang, J., Christie, P., & Zhang, S. (2012). Adsorption of mercury on lignin: Combined surface complexation modeling and X-ray absorption spectroscopy studies. Environmental Pollution, 162, 255–261. https://doi.org/10.1016/j.envpol.2011.11.012

Ma, J., Liu, Y., Ali, O., Wei, Y., Zhang, S., Zhang, Y., Cai, T., Liu, C., & Luo, S. (2018). Fast adsorption of heavy metal ions by waste cotton fabrics based double network hydrogel and influencing factors insight. Journal of Hazardous Materials, 344, 1034–1042. https://doi.org/10.1016/j.jhazmat.2017.11.041

Maghraby, Y. R., El-Shabasy, R. M., Ibrahim, A. H., & Azzazy, H. M. E.-S. (2023). Enzyme Immobilization Technologies and Industrial Applications. ACS Omega, 8(6), 5184–5196. https://doi.org/10.1021/acsomega.2c07560

Magnacca, G., Laurenti, E., Vigna, E., Franzoso, F., Tomasso, L., Montoneri, E., & Boffa, V. (2012). Refuse derived bio-organics and immobilized soybean peroxidase for green chemical technology. Process Biochemistry, 47(12), 2025–2031. https://doi.org/10.1016/j.procbio.2012.07.021

Magri, M. L., Miranda, M. V., & Cascone, O. (2005). Immobilization of soybean seed coat peroxidase on polyaniline: Synthesis optimization and catalytic properties. Biocatalysis and Biotransformation, 23(5), 339–346. https://doi.org/10.1080/10242420500292302

Marchis, T., Cerrato, G., Magnacca, G., Crocellà, V., & Laurenti, E. (2012). Immobilization of soybean peroxidase on aminopropyl glass beads: Structural and kinetic studies. Biochemical Engineering Journal, 67, 28–34. https://doi.org/10.1016/j.bej.2012.05.002

Martucci, J. F., & Ruseckaite, R. A. (2009). Biodegradation of three-layer laminate films based on gelatin under indoor soil conditions. Polymer Degradation and Stability, 94(8), 1307–1313. https://doi.org/10.1016/j.polymdegradstab.2009.03.018

Mate, Ch. J., Mishra, S., & Srivastava, P. K. (2021). Design of pH sensitive low-cost adsorbent from the exudate of Lannea coromandelica (Houtt) for remediation of Malachite Green dye from aqueous solution. Polymer Bulletin, 78(7), 3459–3487. https://doi.org/10.1007/s00289-020-03263-8

Maulvault, A. L., Camacho, C., Barbosa, V., Alves, R., Anacleto, P., Cunha, S. C., Fernandes, J. O., Pousão-Ferreira, P., Paula, J. R., Rosa, R., Diniz, M., & Marques, A. (2019). Bioaccumulation and ecotoxicological responses of juvenile white seabream (Diplodus sargus) exposed to triclosan, warming and acidification. Environmental Pollution, 245, 427–442. https://doi.org/10.1016/j.envpol.2018.11.020

McNaught, A. D., & Wilkinson, A. (1997). IUPAC - Compendium of Chemical Terminology (The Gold Book) (Second Edition). Blackwell Science.

Medeiros Borsagli, F. G. L., Mansur, A. A. P., Chagas, P., Oliveira, L. C. A., & Mansur, H. S. (2015). O-carboxymethyl functionalization of chitosan: Complexation and adsorption of Cd (II) and Cr (VI) as heavy metal pollutant ions. Reactive and Functional Polymers, 97, 37–47. https://doi.org/10.1016/j.reactfunctpolym.2015.10.005

Mehta, P., Sharma, M., & Devi, M. (2023). Hydrogels: An overview of its classifications, properties, and applications. Journal of the Mechanical Behavior of Biomedical Materials, 147, 106145. https://doi.org/10.1016/j.jmbbm.2023.106145

Melo, C. F., & Dezotti, M. (2013). Evaluation of a horseradish peroxidase-catalyzed process for triclosan removal and antibacterial activity reduction. Journal of Chemical Technology and Biotechnology, 88(5), 930–936. https://doi.org/10.1002/jctb.3924

Merci, A., Urbano, A., Grossmann, M. V. E., Tischer, C. A., & Mali, S. (2015). Properties of microcrystalline cellulose extracted from soybean hulls by reactive

extrusion. Food Research International, 73, 38–43. https://doi.org/10.1016/j.foodres.2015.03.020

Mohsen, M., Lin, C., Tu, C., Zhang, C., Xu, S., & Yang, H. (2022). Association of heavy metals with plastics used in aquaculture. Marine Pollution Bulletin, 174, 113312. https://doi.org/10.1016/j.marpolbul.2021.113312

Monier, M., & Abdel-Latif, D. A. (2013). Synthesis and characterization of ion-imprinted chelating fibers based on PET for selective removal of Hg2+. Chemical Engineering Journal, 221, 452–460. https://doi.org/10.1016/j.cej.2013.02.003

Morsi, R., Al-Maqdi, K. A., Bilal, M., Iqbal, H. M. N., Khaleel, A., Shah, I., & Ashraf, S. S. (2021). Immobilized Soybean Peroxidase Hybrid Biocatalysts for Efficient Degradation of Various Emerging Pollutants. Biomolecules, 11(6), Articolo 6. https://doi.org/10.3390/biom11060904

Mukherjee, D., Ferreira, N. G. C., & Saha, N. C. (2022). Effects of 2,4,6-Trichlorophenol on Clarias batrachus: A biomarkers approach. Environmental Science and Pollution Research, 29(31), 47011–47024. https://doi.org/10.1007/s11356-022-19213-y

Nabais, J. M. V., Carrott, P. J. M., Carrott, M. R., Silvestre, S., & Durán-Valle, C. J. (2007). Adsorption of Aqueous Mercury(II) Species by Commercial Activated Carbon Fibres with and without Surface Modification. Adsorption Science & Technology, 25(3–4), 199–215. https://doi.org/10.1260/026361707782398236

Ngo, T. T., & Lenhoff, H. M. (1980). A sensitive and versatile chromogenic assay for peroxidase and peroxidase-coupled reactions. Analytical Biochemistry, 105(1), 389–397. https://doi.org/10.1016/0003-2697(80)90475-3

Nikolaivits, E., Pantelic, B., Azeem, M., Taxeidis, G., Babu, R., Topakas, E., Brennan Fournet, M., & Nikodinovic-Runic, J. (2021). Progressing Plastics Circularity: A Review of Mechano-Biocatalytic Approaches for Waste Plastic (Re)valorization. Frontiers in Bioengineering and Biotechnology, 9. https://doi.org/10.3389/fbioe.2021.696040

Noè, C., Cosola, A., Chiappone, A., Hakkarainen, M., Grützmacher, H., & Sangermano, M. (2021). From polysaccharides to UV-curable biorenewable organo/hydrogels for methylene blue removal. Polymer, 235, 124257. https://doi.org/10.1016/j.polymer.2021.124257

Noè, C., Zanon, M., Arencibia, A., López-Muñoz, M.-J., Fernández de Paz, N., Calza, P., & Sangermano, M. (2022). UV-Cured Chitosan and Gelatin Hydrogels for the Removal of As(V) and Pb(II) from Water. Polymers, 14(6), Articolo 6. https://doi.org/10.3390/polym14061268

Olaniran, A. O., & Igbinosa, E. O. (2011). Chlorophenols and other related derivatives of environmental concern: Properties, distribution and microbial

degradation processes. Chemosphere, 83(10), 1297–1306. https://doi.org/10.1016/j.chemosphere.2011.04.009

Oliveira, J., Belchior, A., da Silva, V. D., Rotter, A., Petrovski, Ž., Almeida, P. L., Lourenço, N. D., & Gaudêncio, S. P. (2020). Marine Environmental Plastic Pollution: Mitigation by Microorganism Degradation and Recycling Valorization. Frontiers in Marine Science, 7. https://doi.org/10.3389/fmars.2020.567126

Pavithra, K. G., SundarRajan, P., Kumar, P. S., & Rangasamy, G. (2023). Mercury sources, contaminations, mercury cycle, detection and treatment techniques: A review. Chemosphere, 312, 137314. https://doi.org/10.1016/j.chemosphere.2022.137314

Pearson, R. G. (1988). Absolute electronegativity and hardness: Application to inorganic chemistry. Inorganic Chemistry, 27(4), 734–740. https://doi.org/10.1021/ic00277a030

Peng, L., Peng, Y., Primo, A., & García, H. (2021). Porous Graphitic Carbons Containing Nitrogen by Structuration of Chitosan with Pluronic P123. ACS Applied Materials & Interfaces, 13(11), 13499–13507. https://doi.org/10.1021/acsami.0c19463

Pezzana, L., Melilli, G., Guigo, N., Sbirrazzuoli, N., & Sangermano, M. (2023). Cross-Linking of Biobased Monofunctional Furan Epoxy Monomer by Two Steps Process, UV Irradiation and Thermal Treatment. Macromolecular Chemistry and Physics, 224(1), 2200012. https://doi.org/10.1002/macp.202200012

Prokopijevic, M., Prodanovic, O., Spasojevic, D., Kovacevic, G., Polovic, N., Radotic, K., & Prodanovic, R. (2017). Tyramine-modified pectins via periodate oxidation for soybean hull peroxidase induced hydrogel formation and immobilization. Applied Microbiology and Biotechnology, 101(6), 2281–2290. https://doi.org/10.1007/s00253-016-8002-x

Prokopijevic, M., Prodanovic, O., Spasojevic, D., Stojanovic, Z., Radotic, K., & Prodanovic, R. (2014). Soybean hull peroxidase immobilization on macroporous glycidyl methacrylates with different surface characteristics. Bioprocess and Biosystems Engineering, 37(5), 799–804. https://doi.org/10.1007/s00449-013-1050-z

Ramírez-Malule, H., Quiñones-Murillo, D. H., & Manotas-Duque, D. (2020). Emerging contaminants as global environmental hazards. A bibliometric analysis. Emerging Contaminants, 6, 179–193. https://doi.org/10.1016/j.emcon.2020.05.001

Rana, A. K., Gupta, V. K., Hart, P., & Thakur, V. K. (2024). Cellulose-alginate hydrogels and their nanocomposites for water remediation and biomedical applications. Environmental Research, 243, 117889. https://doi.org/10.1016/j.envres.2023.117889

Rigoletto, M., Calza, P., Cunha, A. S. da, Sederino, V., Fabbri, D., Tummino, M. L., & Laurenti, E. (2023). Soybean peroxidase immobilised on cellulose-alginate hydrogels for removal of recalcitrant organic pollutants in water. Reaction Chemistry & Engineering, 8(7), 1629–1637. https://doi.org/10.1039/D3RE00009E

Rigoletto, M., Calza, P., Gaggero, E., & Laurenti, E. (2022). Hybrid materials for the removal of emerging pollutants in water: Classification, synthesis, and properties. Chemical Engineering Journal Advances, 10, 100252. https://doi.org/10.1016/j.ceja.2022.100252

Ruan, W., Liu, H., Qi, Y., Zhou, M., Wu, H., & Yang, H. (2022). Post-modification of Uio-66-NH2 based on Schiff-base reaction for removal of Hg2+ from aqueous solution: Synthesis, adsorption performance and mechanism. Fuel, 319, 123816. https://doi.org/10.1016/j.fuel.2022.123816

Russo, G., Barbato, F., Mita, D. G., & Grumetto, L. (2019). Occurrence of Bisphenol A and its analogues in some foodstuff marketed in Europe. Food and Chemical Toxicology, 131, 110575. https://doi.org/10.1016/j.fct.2019.110575

Sangermano, M., Razza, N., & Crivello, J. V. (2014). Cationic UV-Curing: Technology and Applications. Macromolecular Materials and Engineering, 299(7), 775–793. https://doi.org/10.1002/mame.201300349

Sarkar, D., Essington, M. E., & Misra, K. C. (2000). Adsorption of Mercury(II) by Kaolinite. Soil Science Society of America Journal, 64(6), 1968–1975. https://doi.org/10.2136/sssaj2000.6461968x

Sesia, R., Cardone, A. G., Ferraris, S., Spriano, S., & Sangermano, M. (2024). Exploitation of tannic acid as additive for the adhesion enhancement of UV-curable bio-based coating. Progress in Organic Coatings, 189, 108311. https://doi.org/10.1016/j.porgcoat.2024.108311

Sesia, R., Ferraris, S., Sangermano, M., & Spriano, S. (2022). UV-Cured Chitosan-Based Hydrogels Strengthened by Tannic Acid for the Removal of Copper Ions from Water. Polymers, 14(21), Articolo 21. https://doi.org/10.3390/polym14214645

Sharma, A., Vázquez, L. A. B., Hernández, E. O. M., Becerril, M. Y. M., Oza, G., Ahmed, S. S. S. J., Ramalingam, S., & Iqbal, H. M. N. (2022). Green remediation potential of immobilized oxidoreductases to treat halo-organic pollutants persist in wastewater and soil matrices—A way forward. Chemosphere, 290, 133305. https://doi.org/10.1016/j.chemosphere.2021.133305

Sheldon, R. A., & Pelt, S. van. (2013). Enzyme immobilisation in biocatalysis: Why, what and how. Chemical Society Reviews, 42(15), 6223–6235. https://doi.org/10.1039/C3CS60075K

Shih, F.-Y., Su, I.-J., Chu, L.-L., Lin, X., Kuo, S.-C., Hou, Y.-C., & Chiang, Y.-T. (2018). Development of Pectin-Type B Gelatin Polyelectrolyte Complex for

Curcumin Delivery in Anticancer Therapy. International Journal of Molecular Sciences, 19(11), Articolo 11. https://doi.org/10.3390/ijms19113625

Silva, R. R. A., Marques, C. S., Arruda, T. R., Teixeira, S. C., & de Oliveira, T. V. (2023). Biodegradation of Polymers: Stages, Measurement, Standards and Prospects. Macromol, 3(2), Articolo 2. https://doi.org/10.3390/macromol3020023

Singh, J., Srivastav, A. N., Singh, N., Singh, A., Singh, J., Srivastav, A. N., Singh, N., & Singh, A. (2019). Stability Constants of Metal Complexes in Solution. In Stability and Applications of Coordination Compounds. IntechOpen. https://doi.org/10.5772/intechopen.90183

Sizemore, S. R., Nichols, R., Tatum, R., Atanassov, P., Johnson, G. R., & Luckarift, H. R. (2013). Immobilization of Whole Cells by Chemical Vapor Deposition of Silica. In J. M. Guisan (A c. Di), Immobilization of Enzymes and Cells: Third Edition (pp. 301–312). Humana Press. https://doi.org/10.1007/978-1-62703-550-7_20

Song, L., Liu, F., Zhu, C., & Li, A. (2019). Facile one-step fabrication of carboxymethyl cellulose based hydrogel for highly efficient removal of Cr(VI) under mild acidic condition. Chemical Engineering Journal, 369, 641–651. https://doi.org/10.1016/j.cej.2019.03.126

Subash, A., Naebe, M., Wang, X., & Kandasubramanian, B. (2023). Biopolymer – A sustainable and efficacious material system for effluent removal. Journal of Hazardous Materials, 443, 130168. https://doi.org/10.1016/j.jhazmat.2022.130168

Sun, Z., Yin, Y., An, Y., Deng, C., Wei, Z., Jiang, Z., Duan, X., Xu, X., & Chen, J. (2022). A novel modified carboxymethyl cellulose hydrogel adsorbent for efficient removal of poisonous metals from wastewater: Performance and mechanism. Journal of Environmental Chemical Engineering, 10(4), 108179. https://doi.org/10.1016/j.jece.2022.108179

Tarafdar, A., Sirohi, R., Balakumaran, P. A., Reshmy, R., Madhavan, A., Sindhu, R., Binod, P., Kumar, Y., Kumar, D., & Sim, S. J. (2022). The hazardous threat of Bisphenol A: Toxicity, detection and remediation. Journal of Hazardous Materials, 423, 127097. https://doi.org/10.1016/j.jhazmat.2021.127097

Tavares, T. S., Torres, J. A., Silva, M. C., Nogueira, F. G. E., da Silva, A. C., & Ramalho, T. C. (2018). Soybean peroxidase immobilized on δ-FeOOH as new magnetically recyclable biocatalyst for removal of ferulic acid. Bioprocess and Biosystems Engineering, 41(1), 97–106. https://doi.org/10.1007/s00449-017-1848-1

Tokiwa, Y., Calabia, B. P., Ugwu, C. U., & Aiba, S. (2009). Biodegradability of Plastics. International Journal of Molecular Sciences, 10(9), Articolo 9. https://doi.org/10.3390/ijms10093722

Tolardo, V., García-Ballesteros, S., Santos-Juanes, L., Vercher, R., Amat, A. M., Arques, A., & Laurenti, E. (2019). Pentachlorophenol Removal from Water by Soybean Peroxidase and Iron(II) Salts Concerted Action. Water, Air, & Soil Pollution, 230(6), 140. https://doi.org/10.1007/s11270-019-4189-7

Tran, L., Wu, P., Zhu, Y., Yang, L., & Zhu, N. (2015). Highly enhanced adsorption for the removal of Hg(II) from aqueous solution by Mercaptoethylamine/Mercaptopropyltrimethoxysilane functionalized vermiculites. Journal of Colloid and Interface Science, 445, 348–356. https://doi.org/10.1016/j.jcis.2015.01.006

Ugwu, E. I., Tursunov, O., Kodirov, D., Shaker, L. M., Al-Amiery, A. A., Yangibaeva, I., & Shavkarov, F. (2020). Adsorption mechanisms for heavy metal removal using low cost adsorbents: A review. IOP Conference Series: Earth and Environmental Science, 614(1), 012166. https://doi.org/10.1088/1755-1315/614/1/012166

US EPA, O. (2015, agosto 12). Treatment Technologies for Mercury in Soil, Waste, and Water [Reports and Assessments]. https://www.epa.gov/remedytech/treatment-technologies-mercury-soil-waste-and-water

Vigata, M., Meinert, C., Pahoff, S., Bock, N., & Hutmacher, D. W. (2020). Gelatin Methacryloyl Hydrogels Control the Localized Delivery of Albumin-Bound Paclitaxel. Polymers, 12(2), Articolo 2. https://doi.org/10.3390/polym12020501

Wang, B., Yang, X., Ma, L., Zhai, L., Xuan, J., Liu, C., & Bai, Z. (2020). Ultra-high efficient pH induced selective removal of cationic and anionic dyes from complex coexisted solution by novel amphoteric biocomposite microspheres. Separation and Purification Technology, 231, 115922. https://doi.org/10.1016/j.seppur.2019.115922

Wang, H., Wang, Z., Yue, R., Gao, F., Ren, R., Wei, J., Wang, X., & Kong, Z. (2020). Rapid preparation of adsorbent based on mussel inspired chemistry and simultaneous removal of heavy metal ions in water. Chemical Engineering Journal, 383, 123107. https://doi.org/10.1016/j.cej.2019.123107

Wang, M., Han, Q., Shu, Y., Wang, K., Wang, L., Liu, B., Zucker, I., & Wang, Z. (2022). Matrix effects on the performance and mechanism of Hg removal from groundwater by MoS2 nanosheets. Environmental Science: Advances, 1(1), 59–69. https://doi.org/10.1039/D1VA00035G

Wang, W.-B., Huang, D.-J., Kang, Y.-R., & Wang, A.-Q. (2013). One-step in situ fabrication of a granular semi-IPN hydrogel based on chitosan and gelatin for fast and efficient adsorption of Cu2+ ion. Colloids and Surfaces B: Biointerfaces, 106, 51–59. https://doi.org/10.1016/j.colsurfb.2013.01.030

Wang, Z., Zhang, A., Hua, T., Chen, X., Zhu, M., Guo, Z., Song, Y., Yang, G., Li, S., Feng, J., Li, M., & Yan, W. (2024). Revealing the interaction forms between Hg(II) and group types (–Cl, –CN, –NH2, –OH, –COOH) in functionalized Poly(pyrrole methane)s for efficient mercury removal. Environmental Pollution, 351, 124049. https://doi.org/10.1016/j.envpol.2024.124049

World Health Organization. (2021). The public health impact of chemicals: Knowns and unknowns. https://www.who.int/publications-detail-redirect/WHO-FWC-PHE-EPE-16-01

Wu, N. C., & Seebacher, F. (2020). Effect of the plastic pollutant bisphenol A on the biology of aquatic organisms: A meta-analysis. Global Change Biology, 26(7), 3821–3833. https://doi.org/10.1111/gcb.15127

Yang, Y., Li, J., Shi, H., Zhai, L., Wang, X., & Gao, S. (2018). Influence of natural organic matter on horseradish peroxidase-mediated removal of 17α-ethinylestradiol: Role of molecular weight. Journal of Hazardous Materials, 356, 9–16. https://doi.org/10.1016/j.jhazmat.2018.05.032

Zanon, M., Montalvillo-Jiménez, L., Bosch, P., Cue-López, R., Martínez-Campos, E., Sangermano, M., & Chiappone, A. (2022). Photocurable Thiol–yne Alginate Hydrogels for Regenerative Medicine Purposes. Polymers, 14(21), Articolo 21. https://doi.org/10.3390/polym14214709

Zhan, W., Xu, C., Qian, G., Huang, G., Tang, X., & Lin, B. (2018). Adsorption of Cu(II), Zn(II), and Pb(II) from aqueous single and binary metal solutions by regenerated cellulose and sodium alginate chemically modified with polyethyleneimine. RSC Advances, 8(33), 18723–18733. https://doi.org/10.1039/C8RA02055H

Zhang, D., Yin, Y., & Liu, J. (2017). Removal of Hg2+ and methylmercury in waters by functionalized multi-walled carbon nanotubes: Adsorption behavior and the impacts of some environmentally relevant factors. Chemical Speciation & Bioavailability, 29(1), 161–169. https://doi.org/10.1080/09542299.2017.1378596

Zhang, G., Liu, H., Liu, R., & Qu, J. (2009). Removal of phosphate from water by a Fe–Mn binary oxide adsorbent. Journal of Colloid and Interface Science, 335(2), 168–174. https://doi.org/10.1016/j.jcis.2009.03.019

Zhang, L., Zeng, Y., & Cheng, Z. (2016). Removal of heavy metal ions using chitosan and modified chitosan: A review. Journal of Molecular Liquids, 214, 175–191. https://doi.org/10.1016/j.molliq.2015.12.013

Zhang, M., Yin, Q., Ji, X., Wang, F., Gao, X., & Zhao, M. (2020). High and fast adsorption of Cd(II) and Pb(II) ions from aqueous solutions by a waste biomass based hydrogel. Scientific Reports, 10(1), 3285. https://doi.org/10.1038/s41598-020-60160-w

Zhao, S., Zhou, F., Li, L., Cao, M., Zuo, D., & Liu, H. (2012). Removal of anionic dyes from aqueous solutions by adsorption of chitosan-based semi-IPN hydrogel composites. Composites Part B: Engineering, 43(3), 1570–1578. https://doi.org/10.1016/j.compositesb.2012.01.015

Zhou, G., Luo, J., Liu, C., Chu, L., Ma, J., Tang, Y., Zeng, Z., & Luo, S. (2016). A highly efficient polyampholyte hydrogel sorbent based fixed-bed process for heavy metal removal in actual industrial effluent. Water Research, 89, 151–160. https://doi.org/10.1016/j.watres.2015.11.053

Zhou, W., Zhang, W., & Cai, Y. (2021). Laccase immobilization for water purification: A comprehensive review. Chemical Engineering Journal, 403, 126272. https://doi.org/10.1016/j.cej.2020.126272

Zhu, F., Chen, L., & Feng, Q. (2022). Waste gelatin based layer by layer assembly for sustainable solution to cotton fabrics flame retardancy. Progress in Organic Coatings, 163, 106688. https://doi.org/10.1016/j.porgcoat.2021.106688

Zhu, J., Deng, B., Yang, J., & Gang, D. (2009). Modifying activated carbon with hybrid ligands for enhancing aqueous mercury removal. Carbon, 47(8), 2014–2025. https://doi.org/10.1016/j.carbon.2009.03.047

Zhu, Y., Bhandari, B., & Prakash, S. (2018). Tribo-rheometry behaviour and gel strength of κ-carrageenan and gelatin solutions at concentrations, pH and ionic conditions used in dairy products. Food Hydrocolloids, 84, 292–302. https://doi.org/10.1016/j.foodhyd.2018.06.016

4 Photocatalysts for self-sustaining systems and contaminant degradation

4.1 Synthesis and characterization of C_3N_4 –based materials for H_2O_2 production exploiting visible light

All the systems that use enzymes belonging to the peroxidase class must include a source of hydrogen peroxide to activate the catalytic cycle (Figure 1.6, Chapter 1). Usually H_2O_2 is obtained through the reaction between anthraquinone and oxygen but more safe and environmentally friendly production method have been also developed (Moon et al., 2017). Heterogeneous catalyst-based methods are considered greener to permit both easier recycling of active materials and a decrease in costs and pollution (Testa & Tummino, 2021). According to the literature (Rigoletto et al., 2024), the two most common methods to produce hydrogen peroxide in heterogeneous systems are electrocatalysis and photocatalysis.

Among the catalysts developed to this purpose, polymeric carbon nitrides are widely studied. They are semiconductor compounds that contain nitrogen and carbon atoms organized in triazine or tri-s-triazine (also known as heptazine) units cross-linked by N-bridges forming an extended layered network (Figure 4.1).

These materials show different advantages such as moderate bang gap, facile synthesis, thermal and physical-chemical stability, and visible light response (bandgap around 2.7 eV corresponding to and optical wavelength of ~ 460 nm) (Gómez-Velázquez et al., 2023; Lin et al., 2023).

The possibility to employ carbon nitrides for hydrogen peroxide photogeneration is attributable to their conjugated structure that can provide sites for $2e^-$ oxygen reduction reaction (ORR, equation 4.1) (Shiraishi et al., 2014).

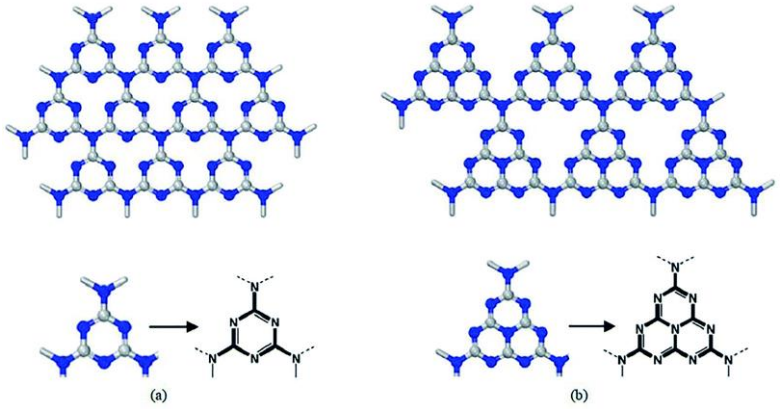

Figure 4.1 – Carbon nitrides structure based on (a) s-triazine and (b) tri-s-triazine (Ma et al., 2021)

$$O_2 + 2H^+ + 2e^- \rightarrow H_2O_2 \text{ (0.695 V versus NHE)} \quad (4.1)$$

$$2H_2O + 4h^+ \rightarrow O_2 + 4H^+ \text{ (1.23 V vs. NHE)} \quad (4.2)$$

In addition, the water oxidation reaction (WOR, equation 4.2) is also required to achieve H_2O_2 photogeneration.

However, the efficiency of carbon nitrides is limited because of: (i) high charge recombination, partially attributable to the presence of defects introduced during the thermal synthesis that led to the formation of hydrogen bonds in the layer structure in addition to the covalent ones between melons precursor; (ii) the small visible light absorption, and (iii) the difficult prevention of the $1e^-$ oxygen reduction reaction (reaction (4.3) and (4.4)):

$$H^+ + O_2 + e^- \rightarrow \bullet OOH \text{ (-0.046 V vs. NHE)} \quad (4.3)$$

$$O_2 + e^- \rightarrow \bullet O_2^- \text{ (-0.284 V vs. NHE)} \quad (4.4)$$

$$O_2 + 4H^+ + 4e^- \rightarrow 2H_2O \text{ (1.23V vs. NHE)} \quad (4.5)$$

To overcome these drawbacks, different strategies have been developed, such as suppressing charge recombination, narrowing the bandgap to promote light

absorption in visible wavelength region and introducing active site for selective $2e^-$ ORR reaction (Teng et al., 2023).

A possible strategy to narrowing the bandgap and to shift the light absorption toward higher wavelengths is the copolymerization of nitrogen-rich carbon nitrides precursors, with light absorption unit containing C=O groups, such as barbituric acid (Figure 4.2).

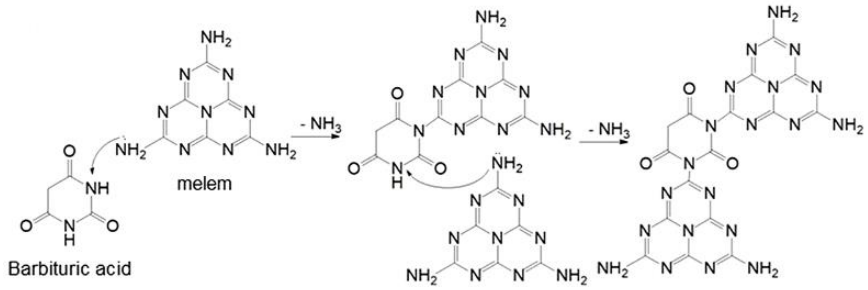

Figure 4.2 - Process for polymerization of PCNBA with barbituric acid and melem as precursors (Teng et al., 2023)

The C_3N_4 precursor plays a crucial role. Indeed, with low steric hindrance precursors a S_N2 nucleophilic substitution can occur leading to the removal of oxygen groups (Teng et al., 2020; Zhang et al., 2010). This nucleophilic reaction would be suppressed if the molecular weights of nucleophilic regents are increased. Hence, precursor like melem are preferable rather than cyanamide, dicyandiamide or melamine (Teng et al., 2020).

The introduction of C=O groups into the carbon nitrides matrix leads to an improved photocatalytic water oxidation activity and an enhanced light usage of the C_3N_4-based photocatalyst.

On the other hand, to promote the $2e^-$ ORR reaction, it is possible to introduce specific atomically isolated metallic site in the carbon nitrides network for the end-on O_2 adsorption (also known as Pauling-type) (Figure 4.3). This configuration can minimize O-O bond breaking suppressing the $4e^-$ ORR (reaction (4.5)) and enhancing the $2e^-$ one.

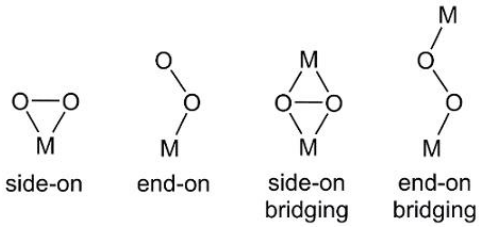

Figura 4.3 - O_2 interaction with metallic sites

It is important to note that on metal particles surface both end-on and side-on O_2 adsorption can occur, while on single atom catalysts (SAC) the oxygen adsorption is usually end-on (Montemore et al., 2018; Teng et al., 2023; Wang et al., 2018).
Furthermore, the introduction of atomically dispersed elements with d^{10} electronic configuration in the materials network avoid the formation of intermediate band in the band structure, leading to an efficient charge separation and a consequent formation of sites with high density of electrons/holes. Teng et al. (Teng et al., 2021) successfully introduced atomically dispersed Sb^{+3}, with a $4d^{10}5s^2$ electronic configuration, in carbon nitride network obtaining a very good non sacrificial photocatalytic H_2O_2 generator.
In this research work we decide to synthesize polymeric carbon nitrides through the copolymerization of melem and barbituric acid and adding different amount of antimony to enhance H_2O_2 photogeneration under visible light and LED irradiation. Four different photocatalytic materials have been prepared, characterised and tested for hydrogen peroxide production under different conditions.

4.1.1 Materials and methods

Materials

All chemical reagents are in analytical grade and used without purification.
Melamine was purchased by Wako Pure Chemical Industries, Ltd.); barbituric acid, 5,5-dimethyl-1-pyrroline-N-oxide DMPO; Phenol; 4-aminoantipyrine and

Horseradish peroxidase HRP were purchased by Sigma Aldrich. NaSbF6 was purchased by HuNan HuaJing Powdery Material.

Photocatalysts preparation

All the photocatalysts were prepared starting from Melem. Melem was obtained by calcination of Melamine at 420°C in N_2 for 4h with an increasing temperature rate of 2.2°C/min. A tubular furnace AS ONE was used.

Five kind of materials have been synthesised: polymeric carbon nitride co-polymerized with barbituric acid (PCNBA0.2) and four variants of this one obtained by introducing different amount of antimony namely Sb0.5-PCNBA0.2, Sb3-PCNBA0.2, Sb5-PCNBA0.2 and Sb15-PCNBA0.2.

PCNBA0.2 was prepared following the method proposed by Teng et al. (Teng et. al 2020). In brief, 3g of melem and 0.2 g of barbituric acid were ball-milled in presence of 30 ml of ethanol for 2 hours at 400 rpm using a Fritsch polverisette 7. The so obtained mixture was dried using a rotary evaporator. The resulting white powder was left for 4h in a vacuum oven at 60°C and then calcinated at 560°C in N_2 for 8h with an increasing temperature rate of 2.2°C/min.

For the preparation of Sb0.5-PCNBA0.2, Sb3-PCNBA0.2, Sb5-PCNBA0.2 and Sb15-PCNBA0.2, 0.2g of barbituric acid were dissolved in 120 ml of ethanol under sonication for 60 min at 60°C in the presence of 0.5, 3, 5, and 15 mmol of $NaSbF_6$ respectively; then 3g of melem were added and suspended under sonication for 60 min at 60°C. Ethanol was removed by combination of rotatory evaporator and vacuum oven. The obtained white powder was transferred into a tube furnace and calcinated at 560°C in N_2 for 4h with an increasing temperature rate of 2.2°C/min. Gas flow was maintained for 30 min before heat treatment (Teng et al., 2021).

Photocatalyst physicochemical characterization

Physicochemical properties of the prepared photocatalysts have been studied with different techniques.

The crystallinity of the samples was evaluated by a powder X–ray diffraction (XRD) instrument (MiniFlex II, Rigaku Co.) with CuKα (λ=1.5418 Å) radiation (cathode voltage: 30 kV, current: 15 mA) with the 2ɵ scan ranged from 5° to 60°.

Point microanalysis and element distribution maps were obtained with FESEM Tescan S9000G instrument with a Schottky emission source equipped with the Ultim Max detector (Oxford, UK).

Fourier transform infrared spectra were recorded with an FT-IR spectrometer (IR Shimadzu Prestige-21).

X–ray photoelectron spectroscopy (XPS) measurements were performed using a Kratos AXIS Supra spectrometer (Shimadzu Co.) with a monochromatic Al Kα X-ray source.

Brunauer-Emmett-Teller (BET) surface area measurements were performed by a full analysis of nitrogen adsorption-desorption tests at liquid nitrogen temperature of 77 K after a degasification step of 8 h at 100 ◦C using an ASAP2020 (Micromeritics, Norcross, GA, USA). The pore size and volume were evaluated with BJH Adsorption Cumulative Pore Volume analysis.

UV–vis diffuse reflectance spectroscopy (UV-DRS) was executed using a UV/VIS/NIR spectrometer UV-2600 (Shimadzu Co.). Photoluminescence (PL) spectroscopy was acquired using a FP-8500 spectrofluorometer (JASCO Corporation, Japan) with an excitation wavelength of 320 nm. An electrochemical workstation CHI760E (Chenhua corporation) was used to test the Mott-Schottky plots.

Photocatalytic activities for H_2O_2 production

All the synthetized photocatalysts were tested for the hydrogen peroxide production under four different conditions, using a concentration equal to 2 g/L.

Firstly, ideal conditions with sacrificial reagent have been employed. Each photocatalyst was suspended into a 10% solution of ethanol by 15 minutes of sonication, followed 15 min of oxygen bubbling. The samples suspensions were

irradiated at $420 < \lambda < 800$ nm using a Xe lamp (60 mW/cm^2) under continuous magnetic stirring for different time (60, 90, 120 min).

Secondly, no sacrificial reagent was used, so Milli-Q water was used as reaction medium.

To reach more realistic H_2O_2 production condition, the third set of measurement was performed without oxygen bubbling in a Solarbox (CO.FO.MEGRA Milan, Italy) equipped with a 420 nm cut-off filter.

Finally, the photocatalysts performances have been testes under different LED irradiation. Each suspension has been irradiated in a cylindrical setup containing an RGB LED strip and equipped with mechanical stirring (LED emission graph are reported in Appendix V, Figure AV-1). A natural exchange of oxygen with the atmosphere has been ensure removing the caps.

At the end of all the experiments, the production of H_2O_2 have been evaluated both with the PACKTEST kit (WAK- H_2O_2, KYORITSU CHEMI-CAL-CHECK Lab., Corp.) equipped with a digital PACKTEST spectrometer (ED723, GL Sciences Inc.) and with the colorimetric method proposed by Frew et al. (Frew et al., 1983) based on the reaction between phenol and 4-aminoantipyrine catalysed by the HRP in presence of hydrogen peroxide.

Radical species evaluation

Electron paramagnetic resonance (EPR) analysis was performed with a X-band Bruker EMX spectrometer equipped with a cylindrical cavity operating at 100 kHz field modulation. Measurements were carried out in quartz capillary tubes under the following conditions: 9.42 GHz (77 K) or 9.86 GHz (room temperature) microwave frequency, 5 mW microwave power, 2 Gauss modulation amplitude and 40 msec time constant.

Paramagnetic defects present in the solid material were investigated in the dark and after different irradiation time. To determine the radical species formed in aqueous suspensions after irradiation, 2 g/L samples suspensions were irradiated for 30 min, and then 0.017 M of HO• radicals' scavenger, 5,5-dimethyl-1-pirroline-N-oxide

(DMPO) was added. To observe the DMPO-O_2^- adduct, the same experiments were also performed in methanol to avoid the rapid interconversion of this species in DMPO-OH.

4.1.2 Results and discussion

Morphology and structural information

XRD measurements were used to initially explore the crystalline structures of synthetized materials (Figure 4.4-A)

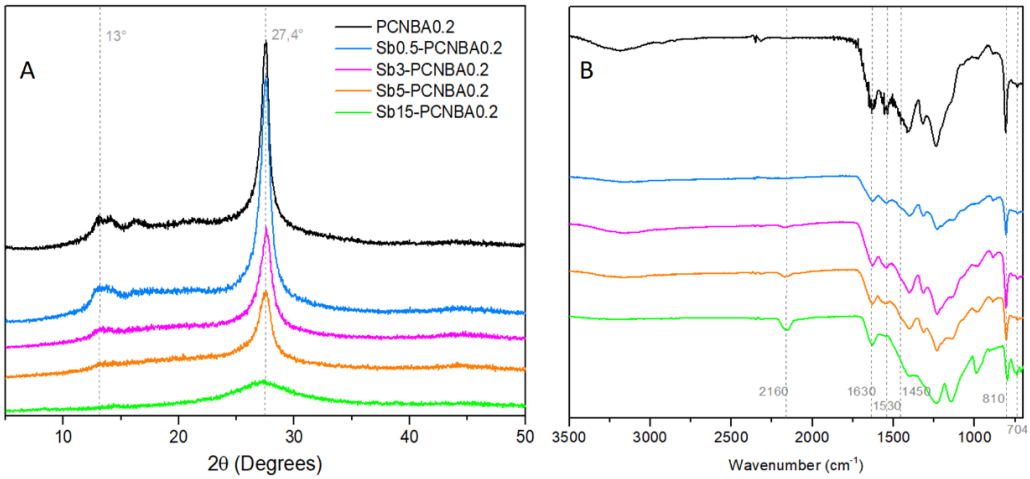

Figure 4.4 – A) XRD diffraction pattern and B) FTIR spectra of the synthesized materials

XRD diffraction patterns show the characteristic peaks associated with graphitic carbon nitrides, 27.4° and 13°, related to the interlayer stacking (002) and the inner planar structure packing (100) of tri-s-triazine units (Dong et al., 2011; Gaggero et al., 2024). The intensity of the diffraction maxima decrease as the antimony amount increases. The lowering of the 13° peak indicates a lower crystallinity degree, while the little shift of the position of 27.4° can be attributable to the electrostatic repulsion between interlayer matrix caused by the positive ions incorporated (Gaggero et al., 2024).

PCNBA0.2 and Sb0.5-PCNBA0.2 present also two less intense peaks around 2ϴ values of 22°, ascribable to the (100) plane and that seems to be observable only in high crystallinity samples (Inagaki et al., 2019), and 17° that could be assigned to the in-plane diffraction from the (310) plane in melon-type structure (Gómez-Velázquez et al., 2023).

The disappearance of 17° and 22° peaks with the increasing amount of Sb, together with the less intensity and the broadening of peaks at 27.4° and 13°, suggest a progressive transition toward amorphous samples.

The FTIR spectra of prepared photocatalysts are displayed in Figure 4.4-B. All samples show the carbon nitride characteristic pattern suggesting that the introduction of the antimony does not change PCNBA0.2 skeleton (Gómez-Velázquez et al., 2023; Teng et al., 2020).

The broad groups of peaks extending from 3500 to 2700 cm^{-1} are attributed to O-H and N-H stretching bands because of the presence of adsorbed water and uncondensed amino groups on the surface. The signals in the 1700-1200 cm^{-1} correspond to C−N stretching modes of aromatic heterocycles (Gómez-Velázquez et al., 2023) and overlap the signal related to the presence of C=O introduced in the structure with the copolymerization with barbituric acid (Teng et al., 2020). The sharp peak at 810 cm^{-1} could be assigned to the out-of-plane bending of the 1,3,5-s-triazine ring, while those at 1530 and 1450 cm^{-1} are assigned to 1,3,5-s-triazine stretching mode. The 1630 cm^{-1} peak, according to cited literature, is attributable to in-plane shear vibration of N−H bonds, while the small peak at 704 cm^{-1} is due to the out-of-plane N−H bend (Gómez-Velázquez et al., 2023). The 2160 cm^{-1} peak, which is not present in PCNBA0.2 sample and that increase with the increasing amount of antimony, is connected to the presence of -C≡N groups. The formation of these groups is in accordance with the results obtained by Teng et al. (Teng et al., 2021) and Gaggero et al. (Gaggero et al., 2024). They attributed this phenomenon to the incorporation of metal ions, as already observed for the incorporation of alkaline metal cation (Qiu et al., 2019), and to the synthesis method. Indeed, in literature is reported that this kind of defects are common in polymerisation of nitrogen-rich

precursors in furnace under N_2 atmosphere (Chang et al., 2023). These groups are recognised as electron-withdrawing groups that may significantly enhance the charge separation and promote a better visible light absorption.

From a morphological point of view, as evidenced in Figure 4.5, all samples present a granular structure. Low amount of incorporated antimony does not seem to influence the morphology as demonstrated by the images relating to Sb0.5-PCNBA0.2 (Fig. 4.5-B1, B2 and B3) and Sb3-PCNBA0.2 (Fig. 4.5-C1 and C2).

On the contrary, Sb5-PCNBA0.2 presents a different particles aggregate shape (Fig. 4.5-D3) which could be ascribable to Sb-induced modification occurred during the synthesis. These modifications are more evident in Sb15-PCNBA0.2 (Fig. 4.5-E3) for which, at high magnifications, it is possible to see a compact structure containing some porosity.

As evidenced by nitrogen adsorption isotherms (Appendix V, Figure AV-2) and by BET results (Table 4.1), the addition of antimony leads to an alteration in the samples structure reducing their surface area and the porosity (Table 4.1).

The total pore volume values (Table 4.1), are also in agreement with those reported in the literature for similar samples (Teng et al., 2021).

Energy Dispersive Spectroscopy (EDS) and Element Mapping Analyses were utilized to provide additional confirmation of the compositions and the spatial distribution of elements in the materials.

As shown in Figure 4.6 and Figure AV-3 (Appendix V), the EDS results indicate that the main components of the sample are C, N, O, Sb and Na, the latter deriving from the precursor used for the synthesis of antimony-containing materials, namely $NaSbF_6$. Elemental mapping reveal that N and C elements are the most contained elements and evidence a homogeneous distribution of Sb throughout the sample, indicating its successful incorporation in the PCNBA0.2 structure.

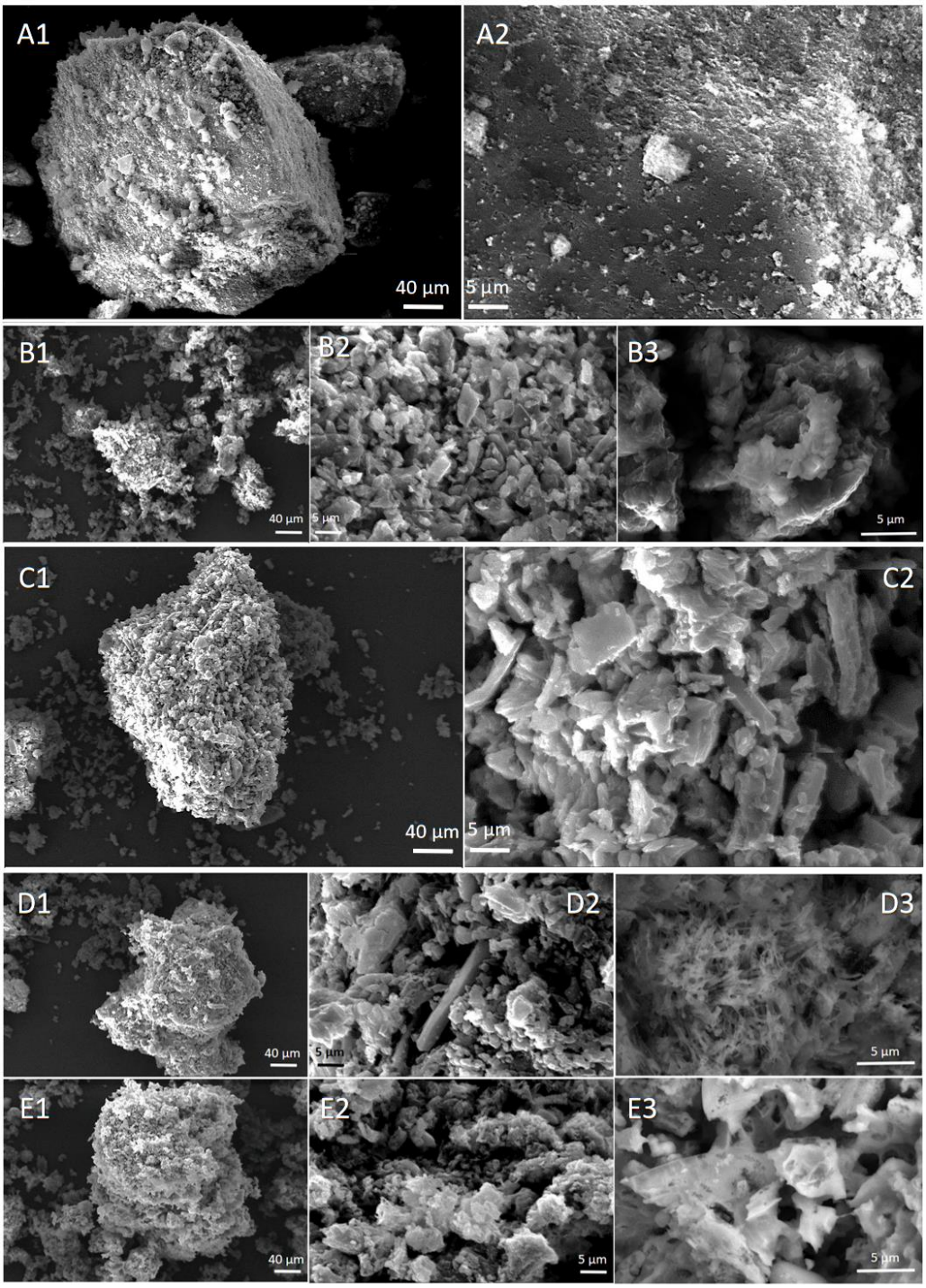

Figure 4.5 – SEM images of A) PCNBA0.2; B) Sb0.5-PCNBA0.2; C) Sb3-PCNBA0.2; D) Sb5-PCNBA0.2 and E) Sb15-PCNBA0.2

Table 4.1- Specific surface area obtained from N_2 adsorption/desorption isotherms and total pore volume

Sample name	SSA (m^2/g)	V_{tot} (cm^3/g)
PCNBA0.2	29	0.04
Sb0.5-PCNBA0.2	3	0.003
Sb3-PCNBA0.2	4	0.004
Sb5-PCNBA0.2	4	0.004
Sb15-PCNBA0.2	4	0.004

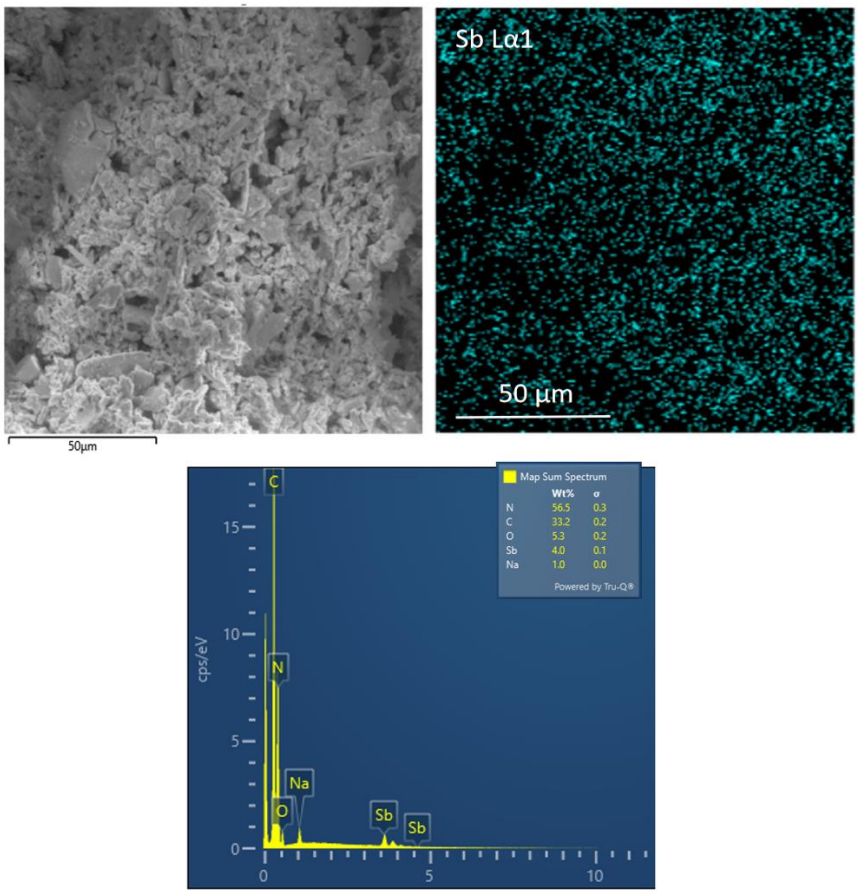

Figure 4.6 - Example of FESEM-images (secondary electrons); map of the antimony dispersion and FESEM-EDS results for the sample Sb0.5-PCNBA0.2

To further reveal the surface chemical compositions of the obtained materials, X-ray photoelectron spectra (XPS) were recorded (Figure 4.7 and Figure AV-4, Appendix V).

The incorporation of C=O functionalities in carbon nitrides structure is confirmed by the peak centred at 532 eV of high resolution O 1s XPS spectra of PCNBA0.2 (Fig. 4.7-A) (Teng et al., 2017). This peak is present also after antimony addition in Sb0.5-PCNBA 0.2 (Fig. AV-4b), Sb3-PCNBA0.2 (Fig. 4.7-B) and Sb5-PCNBA0.2 (Fig. AV-4c).

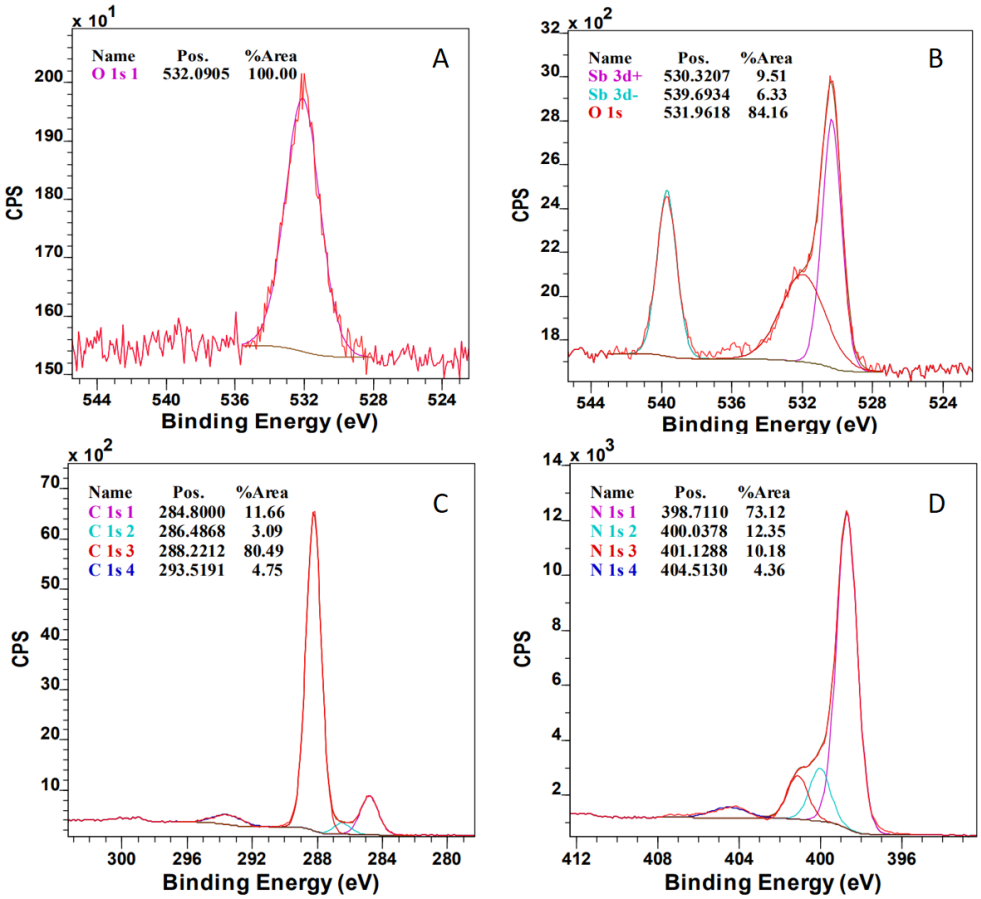

Figure 4.7 – A) High resolution O 1s XPS spectra of PCNBA0.2. High resolution O 1s-Sb 3d (B); C 1s (C) and N1s XPS spectra of Sb3-PCNBA0.2.

On the contrary, in O 1s-Sb 3d XPS spectra of Sb15-PCNBA0.2 this peak shifts at lower values of binding energy reaching 530.6 eV which is usually ascribable to metal oxides. This evidence suggests that at higher Sb concentration the C_3N_4-like structure change and the incorporation of the metal can be mainly in the form of Sb_2O_3 (He et al., 2022). This is also in accordance with the Sb $3d_{3/2}$ and Sb $3d_{5/2}$ values, 539.68 eV and 530.32 eV respectively (Fig. 4.7-B), which are those observed for antimony oxide (He et al., 2022). However, in the other Sb-containing samples (Fig. AV-4) the Sb 3d peaks, together with the O1s peak of C=O functional groups, suggest that the antimony has been incorporated with an oxidation state of +3 in form of cation (Gaggero et al., 2024; Teng et al., 2021).

In the C 1s XPS spectra of all Sb-containing samples there are 3 peaks at around 288.2 eV, 286.5 eV and 284.8 eV. The latter can be attributed to carbon impurity signals (Gaggero et al., 2024), while the more intense peak with a binding energy of 288.2 eV can be identified as sp^2 hybridized carbon in an aromatic ring containing nitrogen (N-C=N). The less intense 286.6 eV peak can be related to the presence of C≡N groups (Teng et al., 2021) which had already been identified in the FTIR spectra. As already highlighted in the latter (Fig. 4.7-B), these XPS signals increase in intensity as the amount of antimony incorporated increases (2.03% in Sb0.5; 3.09% in Sb3; 5.40% in Sb5 and 18.5% in Sb15 – Fig. AV- 4 Appendix V).

All the N 1s spectra can be deconvoluted into three peaks with binding energies around 398.6 eV, 400.1 eV, and 401.1 eV, respectively. The main peak at 398.6 eV is assigned to sp^2 hybridized nitrogen in triazine rings containing C triazine (C-N=C), while the peak at 400.1 eV is typically attributed to tertiary nitrogen groups $N-(C)_3$. The peak at 401.1 eV indicates the presence of amino groups (N-H) (Gaggero et al., 2024; Teng et al., 2019; Zhou et al., 2015).

Charge transfer properties

Photoluminescence analyses were employed to investigate charge recombination in synthesized photocatalysts.

As shown in Figure 4.8, the influence of the amount of antimony on charge recombination is marked. Indeed, the intensity of photo luminescence significantly decreases when increasing the Sb millimoles, so indicating that electron-hole recombination is suppressed. This was already reported in literature for similar studies (Gaggero et al., 2024; Teng et al., 2021) and seems to be related to the elimination of the intermediate band in the band structure by incorporation of atomically dispersed antimony with the d^{10} electronic configuration. Additionally, a slight bathochromic effect is observed with a shift of the maximum of the emission wavelength from 462 nm to 466 nm. This behaviour could be also ascribable to the band gap narrowing or to a presence of defects, as -C≡N groups, that could capture electrons or holes resulting in a decrease of PL intensity (Dong et al., 2015).

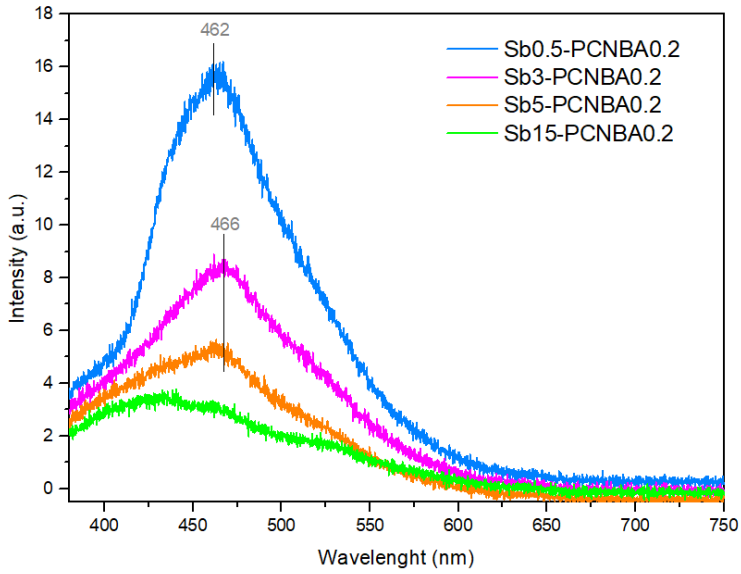

Figure 4.8 - Photoluminescence spectra of prepared materials

Furthermore, the appearance of a less intense additional emission peak at 430 nm, which increases with the amount of antimony contained into the materials, could be related to the n→π* transition of the defects (Y. Chen et al., 2014).

Optical properties

The absorption spectra of the synthesized materials are shown in Figure 4.9-A. PCNBA0.2 shows an absorption of visible radiation at wavelengths between 400 and 500 nm as a consequence of the introduction of C=O into the C_3N_4 structure. The Sb incorporation leads to a red shift of the ~450 nm absorption edge, which is related to the π→π* transition, with the following trend PCNBA0.2 < Sb3-PCNBA0.2 < Sb15-PCNBA0.2 ~ Sb0.5-PCNBA0.2 < Sb5-PCNBA0.2. This can be ascribe to an extension of the electron delocalisation (Chang et al., 2023; Y. Chen et al., 2014). An additional absorption band appears around 500 nm for Sb-containing materials and it could be attributable to n→π* transition related to lone-pair electrons on defect sites as -C≡N groups (Chang et al., 2023; Y. Chen et al., 2014).

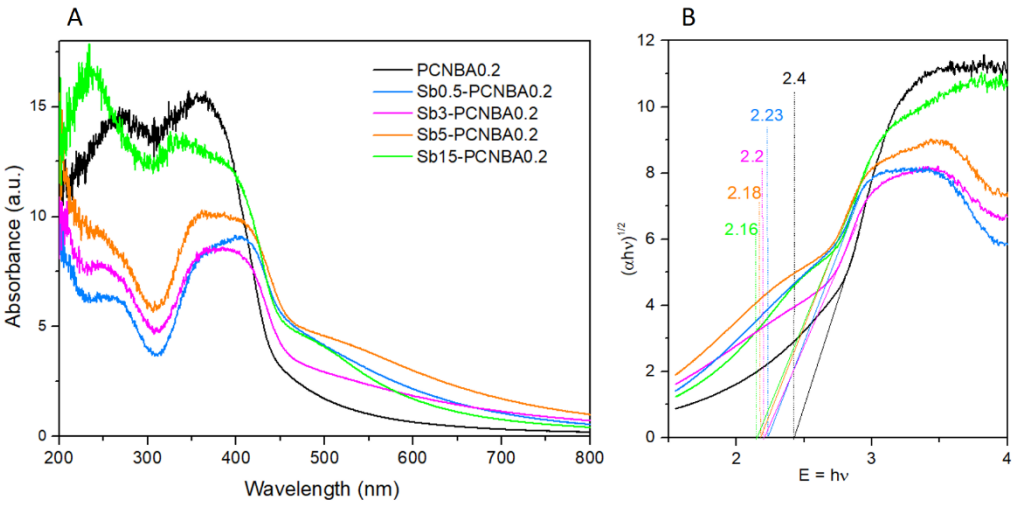

Figure 4.9 - (A) DR-UV-Vis absorption spectra and (B) related Tauc-plot of the synthesized materials

The absorbances seem not proportional to the amount of antimony introduced and the Sb5-PCNBA0.2 sample is the one that shows the highest absorption values. However, the optical properties reflect the materials colours (Appendix V, Figure AV-5).

Indeed, Sb5-PCNBA0.2, which shows the higher absorbance values, is also the darker sample.

From the study in diffuse reflectance, processing the Kubelka-Munk function of the spectra, through the Tauc plot method (Makuła et al., 2018) it is possible to determine the optical band gaps of the materials (Figure 4.9-B, Table 4.2). The obtained values confirm a band gap narrowing as function of Sb amount from 2.4 eV to 2.16 eV.

The Mott-Schottky plots (Figure AV-6, Table 4.2) indicate a progressive slight increase in the conduction band minimum of the prepared samples, transitioning from -1 eV to -0.94 eV.

Using this information, together with the energy band gaps obtained by Tauc plots, the band position diagram was assessed for all samples, as depicted in Figure 4.10.

Table 4.2 - Bandgap, conductive and valence band values

Sample	Eg*	Ecb(Ag/AgCl)‡	Ecb (NHE)ɣ	Evb calc	Evb (XPS)
PCNBA0.2	2.4	-1	-0.343	2.06	2.1
Sb0.5-PCNBA0.2	2.23	-1.04	-0.383	1.847	2.04
Sb3-PCNBA0.2	2.2	-1.03	-0.373	1.827	1.96
Sb5-PCNBA0.2	2.18	-1.06	-0.403	1.777	1.96
Sb15-PCNBA0.2	2.16	-0.94	-0.283	1.877	1.97

* obtained with Tauc-Plot measurements; ‡ obtained from elaboration of Mott-Schottky values; ɣ obtained from Ecb(Ag/AgCl) through the relation $E_{NHE} = E_{Ag/AgCl} + 0.059\ pH + 0.197$ (pH=7.8)

Hydrogen peroxide production

Figure 4.11 summarise the amount of photogenerated H_2O_2 as function of irradiation time under different experimental conditions.

In presence of the sacrificial reagent for holes' suppression, oxygen blowing and under Xenon lamp visible light irradiation, all materials show a H_2O_2 production linearly increasing over time. The higher amount was observed after 120 minutes for Sb5-PCNBA0.2 (3.4 mg/L) followed by Sb0.5-PCNBA0.2, Sb3-PCNBA0.2 and Sb15-PCNBA0.2 (3, 2.6 and 1.11 mg/L respectively) (Figure 4.11-A).

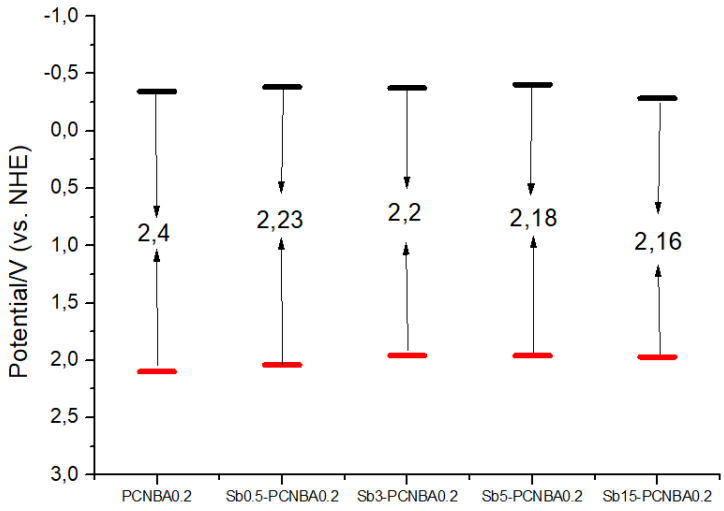

Figure 4.10 – Band position diagram obtained from experimental measurements

Removing the contribution of the sacrificial reagent (Figure 4.11-B), Sb5-PCNBA0.2 is confirmed as the most promising material with a H_2O_2 photoproduction of 2.5 mg/L after 120 minutes of irradiation while Sb0.5-PCNBA0.2 appears to be the most sensitive to ethanol removal with a production of only 0.5 mg/L (less than 17% of the value obtained in the presence of the sacrificial reagent). Sb3-PCNBA0.2 and Sb15-PCNBA0.2 seems to be less affected maintaining a quite similar production (1.5 and 0.92 mg/L respectively) after 120 minutes of irradiation.

On the contrary, Figure 4.11-C evidence that in a close system, without oxygen saturation of the solutions, the production of H_2O_2 does not follow a linear increasing over time but after reaching a maximum it decreases.

According to the literature (Gaggero et al., 2024), this phenomenon could be explained considering the recombination with the holes resulting in the decomposition to water or it can be due to the release of Na^+ ions in solution. Indeed, EDS analyses evidenced the presence of sodium in the prepared materials containing antimony (Figure AV-3, Appendix V), which is introduced during the synthesis using $NaSbF_6$ as reagent. Furthermore, not having blown in oxygen before irradiation and being in a closed system which does not allow its exchange with the atmosphere, the O_2 concentration decreases over time and this could limit the production of H_2O_2

In an open system and under white LED irradiation the materials produce less amount of hydrogen peroxide but following an approximately linear trend over time, probably due to the oxygen equilibrium reached between the solution and the environment. The best material is confirmed to be Sb5-PCNBA0.2 with a H_2O_2 production of 0.82 mg/L after 120 minutes of irradiation, followed by Sb15-PCNBA0.2, Sb3-PCNBA0.2 and Sb0.5-PCNBA0.2 with a production of 0.58, 0.52 and 0.5 mg/L respectively.

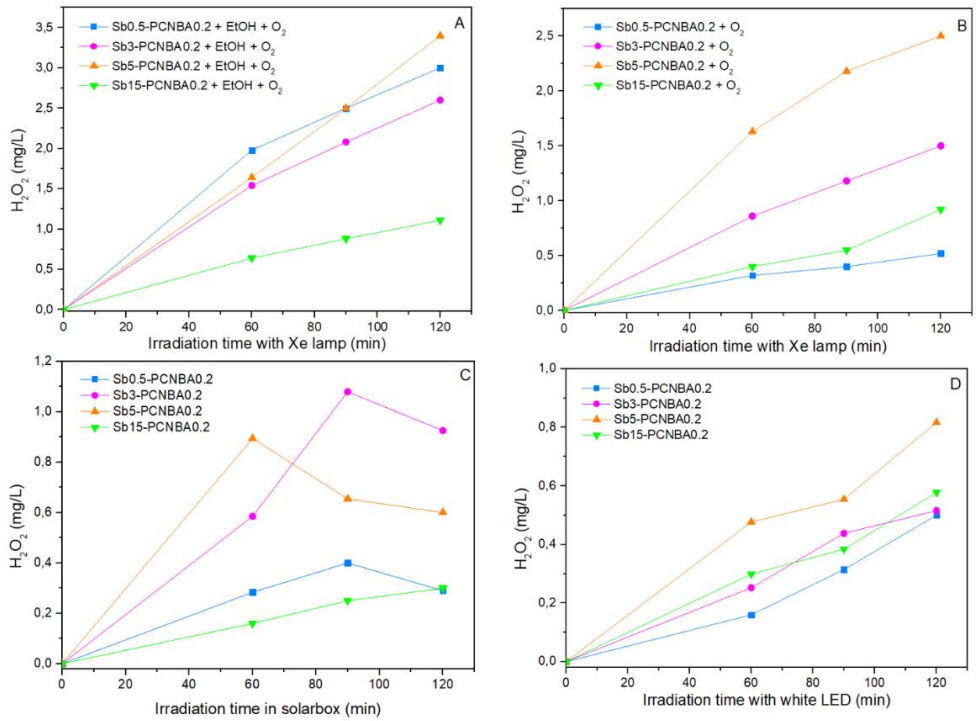

Figure 4.11 - hydrogen peroxide production photogenerated under different condition: (A) Xe lamp visible light irradiation of suspended samples in EtOH 10% solution and after oxygen bubbling; (B) Xe lamp visible light irradiation of suspended samples in ultra-pure water and after oxygen bubbling; (C) irradiation in solarbox of suspended sample in ultra-pure water; (D) white LED irradiation of samples suspended in ultra-pure water

Radical species

The materials' structure, composition and the presence of defects or distortions could affect their response under light irradiation (Actis et al., 2022; Gómez-Velázquez et

al., 2023). EPR spectra obtained on solid materials in the dark at room temperature evidence the presence of a C-centred persistent radical (example for Sb5-PCNBA0.2 shown in Figure 4.12-A *inset*) whose area, normalized for 1 mg of material, changes as the antimony content increases with a bell-shaped trend (Figure 4.12-A).

According to the literature, this radical is due to the presence of unpaired electrons on the carbon atoms of the heptazine rings (Dvoranová et al., 2018; Liu et al., 2018) and could be enhanced from the presence of defects, like nitrogen vacancies (Lu et al., 2024).

Since all the samples are similar in the percentage composition of C, N and O (Fig. AV-8 and Table AV-1, Appendix V), with the exception of Sb15-PCNBA0.2, differences in radical intensities could be influenced by Sb amount. Figure 4.12-A highlights that, for low quantities of incorporated antimony, the intensity of the radical increases (Sb3-PCNBA0.2 > Sb0.5-PCNBA0.2 > PCNBA0.2) and then decreases for higher Sb concentrations (Sb5-PCNBA0.2 > Sb15-PCNBA0.2). This suggests good electron delocalization properties, which are reduced when a high amount of Sb is introduced in the system, possibly due to an excessive distortion of the C_3N_4 structure. Figure 4.12-B shows the variation of the radical area as function of irradiation time with white LED.

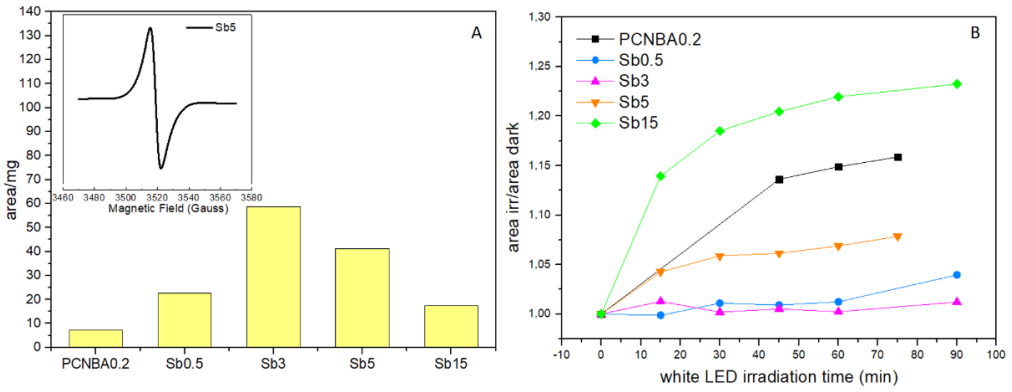

Figure 4.12 - A) normalized area of C-centered radicals of prepared samples obtained in the dark at room temperature (inset: example of Sb5-PCNBA0.2 EPR-spectrum); B) C-centered radicals areas increments over time of irradiation with white LED

All samples increase the radical intensity, highlighting the photoinduced electron trapping by empty and single occupied defective sites (Actis et al., 2022; Gómez-Velázquez et al., 2023). Indeed, C defects may act both as acceptors of photogenerated electrons, thus inhibiting charge carrier recombination, and as providers of preferential adsorption sites of activatable O_2 molecules (Tan et al., 2021; Zhang et al., 2020).

The sample showing the greatest percentage increase in the area of radical signal is Sb15-PCNBA0.2 (about 23% after 90 minutes of irradiation), followed by Sb5-PCNBA0.2 (showing an increase of 8% after 90 minutes), while for Sb3-PCNBA0.2 and Sb0.5-PCNBA0.2 the growth of the area is not significant. PCNBA0.2 shows an intermediate behaviour between Sb15-PCNBA0.2 and Sb5-PCNBA0.2. The different response to light excitation supports a different redistribution of photoinduced charge carriers between the conduction band and empty and/or doubly occupied intragap states (Gomez-Velazquez, 2023).

EPR experiments in suspension were successively carried out to evaluate the reactive species generated under LED irradiation (Figure 4.13).

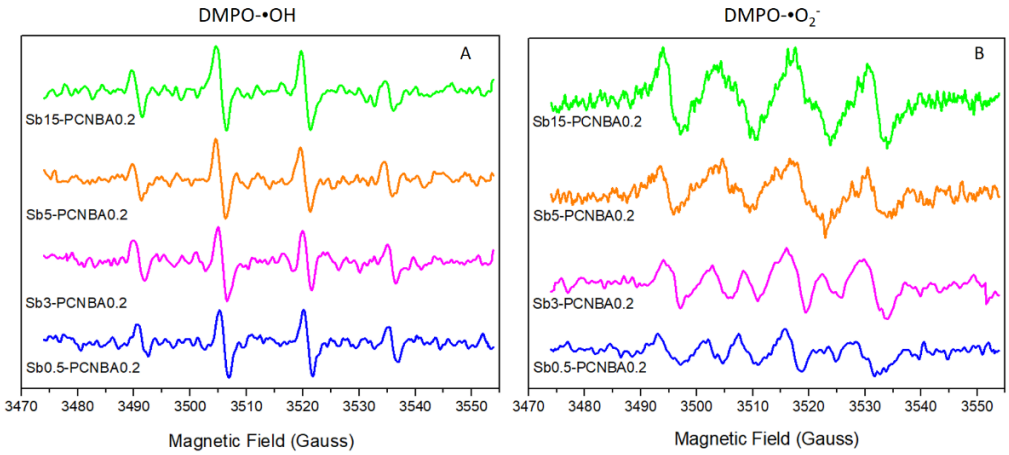

Figure 4.13 - EPR spectra of (A) DMPO-OH radical in water and (B) DMPO-O_2 anion radical in methanol of different samples

All samples are able to generate both hydroxyl (Fig. 4.13-A) and superoxide radicals (Fig. 4.13-B) and Sb15-PCNBA0.2 shows the higher production of both species.

Analysing EPR spectra of DMPO-$^{\bullet-}O_2$ some changes in spectral shape have been evidenced as the amount of incorporated Sb increases. Simulating the spectrum by the software Spinfit (Bruker) a change in the hyperfine separation constants a_H is observed (Table 4.3).

Table 4.3 - Hyperfine constants calculated with simulated spectra of DMPO-O_2 radicals (expressed in Gauss)

Sample name	a_N	a_H
Sb0.5-PCNBA0.2	13.58	7.36
Sb3-PCNBA0.2	13.64	8.29
Sb5-PCNBA0.2	13.31	10.34
Sb15-PCNBA0.2	13.38	10.24

Parameters obtained for Sb15-PCNBA0.2 and Sb5-PCNBA0.2 are consistent with those reported in the literature for the DMPO-$^{\bullet-}O_2$ adduct (Harbour & Hair, 1978). Whereas, for Sb0.5-PCNBA0.2 and Sb3-PCNBA0.2 a_H value is smaller. This could suggest the presence of a second radical species formed during the irradiation and competing with superoxide radical for DMPO-adduct formation. These hypotheses will have to be confirmed with *ad hoc* experiments in the presence of selective quenchers for the different radical species.

4.2 Structural and Physicochemical Properties of Carbon Nitride Nanoparticles via Precursor Thermal Treatment: Effect on Methyl Orange Photocatalytic Discoloration

Since C_3N_4-based materials under irradiation generates reactive species as hydroxyl or superoxide radicals, they cannot be only used in the production of hydrogen peroxide but also be employed as photocatalyst for the degradation of organic contaminants and dyes.

Through a collaboration with an Argentine research group from the University of La Plata, the correlation between the structure and degradation of methyl orange of carbon nitrides obtained from different precursors was studied.

Melamine, urea, cyanamide, dicyandiamide, and cyanuric chloride are among the most frequently used precursors used for C_3N_4 synthesis, whereas the polycondensation of these precursors can be done either via annealing in a typical laboratory furnace, solvothermal treatment, or combustion synthesis (Bojdys et al., 2008).

Different synthesis methods using different precursors lead to C_3N_4 powders with different degrees of condensation, physical-chemical properties, and photocatalytic efficiencies. C_3N_4 synthesis by thermal polymerization of either melamine, guanidine carbonate, or dicyandiamide showed different band gap energies and photocatalytic performance toward methyl orange (MO) degradation under visible light (>400 nm) (Zhao et al., 2018).

Crystallinity and disorder have also been proven to significantly influence the activity of C_3N_4 photocatalysts and crystalline C_3N_4 powders show the best performance in the photocatalytic tests (Zheng et al., 2021). According to many authors, disordered C_3N_4 structures showed an increased specific surface area but a decline in the photocatalytic activity compared to crystalline samples.

In this study, various CN photocatalysts obtained by the condensation pyrolysis of different nitrogen rich molecules such as urea (CNu), melamine (CNm), dicyandiamide (CNd), and dicyandiamide/barbituric acid (CNdac) were synthetized and thoroughly characterized. Moreover, their photocatalytic efficiency toward MO degradation was investigated under λ=350 nm and simulated solar light (SSL). Also, CNm samples were exfoliated (eCNm) to evaluate the effect of tuning a given 3D structure into a 2D structure, and CNd samples were subjected to amorphization (aCNd) to evaluate the effect of the loss of crystallinity.

MO was selected as a model compound due to its extensive use in the textile and paper industry, its potential in causing serious effects in the environment and living beings, and because MO degradation mechanisms are well reported in the literature, as will be discussed further in the text. Therefore, the design of efficient and sustainable MO degradation photocatalysts is of actual importance. From an analysis of the obtained results, a correlation between characteristic structure parameters (%

crystallinity, area, band gap, visible absorption capacity, and C defects) and the photocatalytic efficiency was analysed for the C_3N_4 nanoparticles synthesized from the different precursors.

4.2.1 Material and methods

The aspects relating to the synthesis (summarized in Figure 4.14) and the characterization of the materials are not reported here but can be consulted in the research article of Gómez-Velázquez and co-workers (Gómez-Velázquez et al., 2023). In this thesis a focus is made on the study of the relationship between precursor- methyl orange degradation.

EPR measurements

Electron paramagnetic resonance (EPR) analysis was performed with a X-band Bruker EMX spectrometer equipped with a cylindrical cavity operating at 100 kHz field modulation. Measurements were carried out in quartz capillary tubes under the following conditions: 9.42 GHz (77 K) or 9.86 GHz (room temperature) microwave frequency, 5 mW microwave power, 2 Gauss modulation amplitude, and 40 msec time constant.

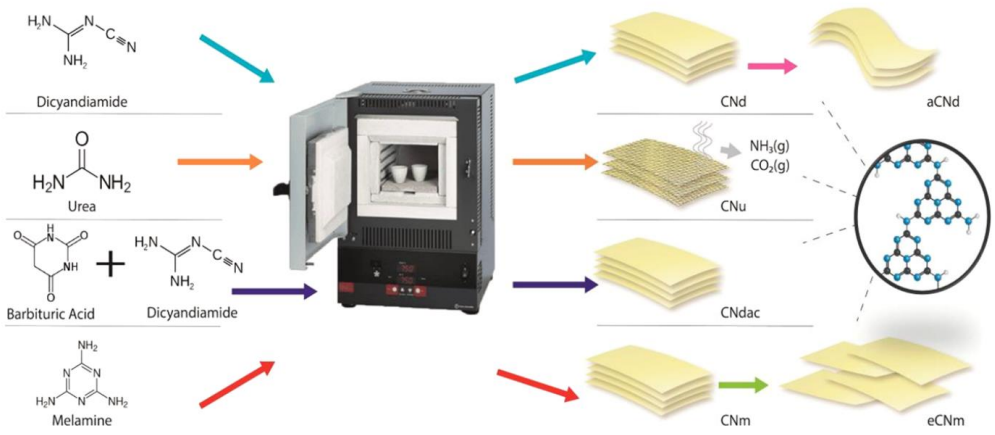

Figure 4.14 - Illustration of the Synthesis Procedure and Particular Structural Characteristics of the Obtained CN Nanoparticles Depending on the Precursors

Paramagnetic defects present in the solid material were investigated at low temperature in the dark and after 30 min irradiation with a SSL lamp. To determine the radical species formed in aqueous suspensions after SSL irradiation, 1 g L^{-1} C_3N_4 suspensions were irradiated for 30 min, and then either 0.017 M HO• and O_2•− radicals' scavenger, 5,5-dimethyl-1-pirroline-N-oxide (DMPO), or 0.017 M singlet oxygen ($^1O_2$) spin-trap, 2,2,6,6-tetramethyl-4-piperidone hydrochloride (TMP), was added. The reaction mixture was irradiated for 10 min, and the EPR spectrum was immediately acquired. Experiments to reveal the formation of the DMPO-O_2^- radical adduct were also performed in methanol (to avoid the rapid interconversion of this species in DMPO-OH). Experimental parameters were the same as reported above but with 1 Gauss of modulation amplitude.

Photocatalytic measurements

Visible irradiation experiments were achieved in an Oriel 96,000 solar simulator; the irradiance was 360 W/m^2 and the lamp power was 150 W. In both cases, 100 mL of 20 mg/L aqueous suspensions of the photocatalyst samples and 1×10^{-5} M MO were placed in a quartz cylindrical tube and submitted to continuous magnetic stirring. Before illumination, the samples were kept in the dark for 30 min. At different time intervals, 2 mL of the samples were taken and filtered with 0.22 μm pore size acetate membranes. The UV−vis absorption spectra of the filtrates were obtained, and the absorption at 465 nm was compared with the initial values to calculate the discoloration as

$$discoloration\ \% = (1 - \frac{A_{(t)}}{A_0}) \times 100 \quad \text{(eq. 4.6)}$$

where $A_{(t)}$ is the 465 nm absorbance at time t and A_0 is the initial absorbance at 465 nm. The original pH of the samples was around 6.5. Considering that the pH criteria for water to be considered a "fresh water" is in the range from 6.5 to 9,16 further

investigation of CN photocatalytic efficiency was performed at the samples' original pH. Thus, extra addition of pH buffers to the reaction mixture was avoided.

4.2.2 Results and discussion

Formation of HO• and $O_2^{\bullet-}$ radicals is observed for all of the obtained C_3N_4 powders, as expected from the reactions of photogenerated holes with water and photogenerated electrons with adsorbed molecular oxygen, respectively (Figure 4.15-A). On the other hand, formation of $^1O_2$ could not be observed under these experimental conditions for any of the C_3N_4 samples. Figure 4.15-B shows the characteristic signals of DMPO-OH and DMPO-O_2^- radical species for CNu photocatalyst, while Figure AV-10 (Appendix V) shows those obtained for the other C_3N_4 nanoparticles.

It is well reported in the literature that the concentration and nature of the defective states present in the photocatalyst may strongly affect its response under light excitation (Actis et al., 2022). To observe possible defective states in C_3N_4 nanoparticles, EPR spectroscopic studies were performed on solid samples at 77 K, both in the dark and under illumination, to correlate the amount and nature of defects with the synthesis precursors. The EPR signals of the different C_3N_4 powders (normalized to 1 mg of sample) in the dark (Figure 4.15-C and Figure AV-11 in Appendix V) reveal the presence of C-centred radical defects (g = 2.0034) which are probably adjacent to oxygen atoms (Dellinger et al., 2007). The relative area of dark C radical signals (S_{dark}) is similar for most C_3N_4 nanoparticles, except for CNu and aCNd (Figure 4.15-B).

Upon 30 min irradiation of the solid samples with SSL, a strong increase in the signal intensity was observed for all samples (Figure 4.15-C + *inset* and Figure AV-11 in Appendix V).

Such an increase in the signals upon irradiation is suggested in the literature to be due to the trapping of the photoinduced electron by empty and single occupied defective sites (Actis et al., 2022).

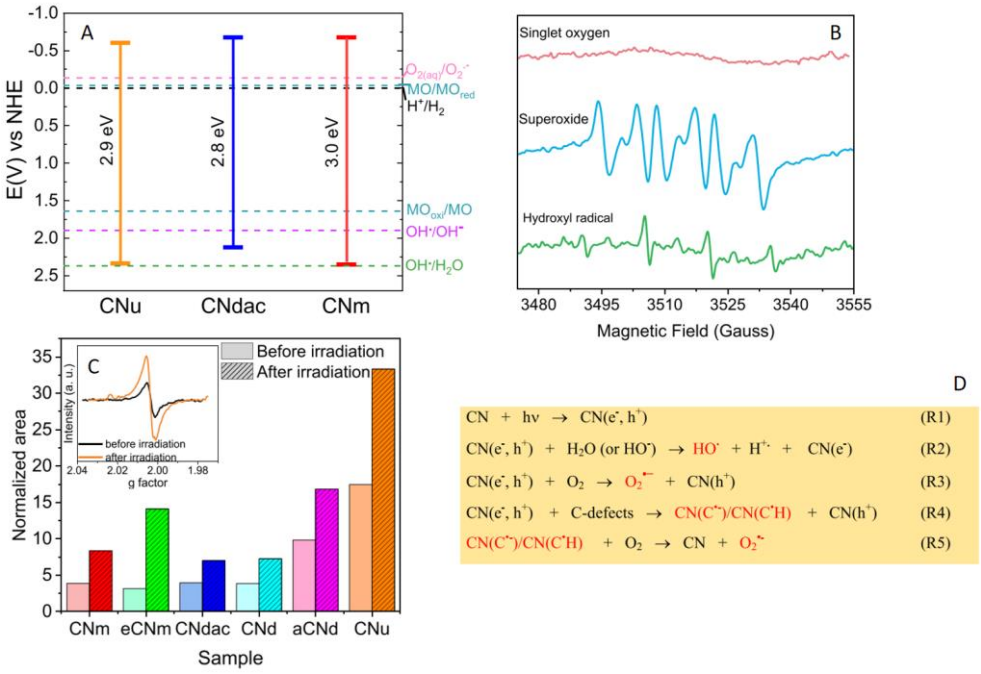

Figure 4.15 – A) ECB and EVB obtained for CNu, CNdac, and CNm and MO reduction and oxidation potentials and comparison with the standard reduction potential of reaction intermediates of interest; B) EPR results obtained for CNu suspensions irradiated with SSL at room temperature in the presence of DMPO (in water and in methanol) or TMP (in water) revealing the formation of DMPO-OH (green) and DMPO-O_2− (blue) radicals: C) Relative signal area (normalized to 1 mg) of solid samples in the dark (S_{dark}) and after 30 min irradiation in SSL (S_{irr}). Inset: Solid CNu EPR spectra at 77 K in the dark and after 30 min SSL irradiation; D) Reactions of Primary and Secondary Reactive Species Formed after Light Absorption (Those highlighted in red were detected in EPR experiments).

The different response to SSL excitation observed for each material supports a different redistribution of photoinduced charge carriers between the conduction band and empty and/or doubly occupied intragap states.

The increase in intensity of the C-centred radical shows a linear correlation with the surface area of the samples that strongly suggest that the number of defects produced upon irradiation principally originated on the particle surface (Figure AV-12, Appendix V).

It is suggested in the literature (Tan et al., 2021; Zhang et al., 2020) that C defects may act as acceptors of photogenerated electrons, thus inhibiting charge carrier recombination, and as providers of preferential adsorption sites of activatable O_2 molecules.

On the basis of these results, a series of equation related to the reactive species formation have been proposed (Figure 4.15-D). Reaction (R1) depicts the formation of photoinduced charge carriers C_3N_4 (e^-, h^+) upon light absorption. Further reactions (R2) and (R3) between photogenerated electron−holes with water (or HO^-) and O_2 inhibit charge carrier recombination and lead to the formation of hydroxyl radicals, $HO^{\bullet}$, and superoxide radical anions, $O_2^{\bullet-}$, respectively. It should be recalled that these radicals were observed here in EPR experiments. Reaction (R4) shows the trapping of photogenerated electrons by C-defects, leading to the formation of surface carbon radicals, that are CN(C•−)/CN(C•H). The latter radicals are prone to readily react with O_2 to generate $O_2^{\bullet-}$ (reaction (R5)).

Methyl orange (MO) was used as a model contaminant to probe the photocatalytic performance of the different materials. As shown in Figure 4.16-A, it is observed that though with quite different efficiencies, all C_3N_4 samples were able to remove MO. Less than 7% discoloration was observed after 210 min irradiation in the absence of catalyst. CNdac was the least efficient of all nanoparticles CNu the most efficient ones reaching removal efficiency of 99% after 210 min irradiation.

Despite the absorption spectrum of C_3N_4 samples playing a definite role on the efficiency of the photocatalysts, it is not the only factor influencing their performance. Among several other aspects of the nanoparticles influencing their catalytic efficiency, the specific surface area (A_{sp}) seems a major one, as depicted in Figure 4.16-C. CNdac, CNm, and CNu photocatalytic performances are clearly strongly dependent on A_{sp}. An increase in the surface area is expected to ensure greater availability of active surface sites for MO and $O_{2(g)}$ uptake; however, this may not be the only cause leading to an improved photocatalytic performance. In fact, Figure AV-12 (Appendix V) *inset* shows a clear correlation between the amount of C-defects generated upon SSL irradiation of CN nanoparticles and the photocatalyst efficiency (MO RE%). According to the previous discussion, surface carbon defects readily scavenge photoinduced electrons, thus further inhibiting charge carrier recombination.

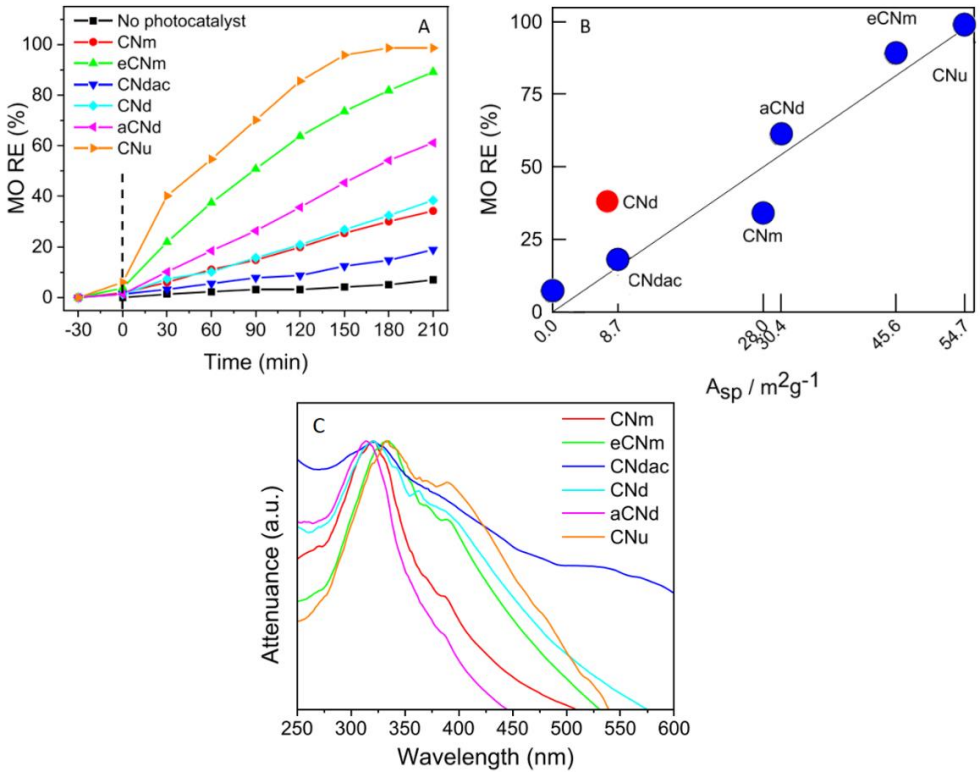

Figure 4.16 – A) MO removal efficiency vs SSL irradiation time of 10^{-5} M MO initial concentration in the presence and absence of 20 mg/L of different samples; B) MO removal efficiency vs Asp for samples irradiated SSL. Red symbols stand for CNd samples deviating from a linear dependence with the specific area; C) Attenuance obtained from total reflectance spectra of the synthesized samples

It is well reported in the literature that HO• radicals and h^+ reactions with MO are the main causes of MO degradation (Nguyen et al., 2018). Primary reactions between MO and oxidizing radicals lead to the formation of monohydroxylated products, while further reactions of the latter lead to the rupture of the azo group to smaller molecules as benzene-substituted rings (T. Chen et al., 2008). It is important to consider that even if discoloration may be taken as the degradation of MO molecule and its chromophore group, though it does not assure complete mineralization to CO_2, H_2SO_4, H_2O, and HNO_3. It is therefore essential to always characterize the degradation products and determine their toxicity compared to the parent molecules to evaluate the real effectiveness of the decontamination process.

4.3 Final remarks

Carbon nitrides based photocatalysts have been prepared *via* facile syntheses and comprehensive characterization techniques were employed to assess materials features. The relationship between the structure and the photocatalytic performance emerged from both the studies carried out highlighting the fundamental role of light absorption, band gap, electrons/holes recombination, crystallinity of the samples, their morphology and surface area in define their properties.

All the described materials show absorptions in the typical wavelength range of visible light, even if with different efficiencies, an essential property to develop photocatalytic systems capable of effectively exploiting natural solar radiation as source of light.

Among the antimony-containing materials, Sb5-PCNBA0.2 has proven to be the most promising for the production of hydrogen peroxide under different conditions (3.4 mg/L, 2.5 mg/L, 0.82 mg/L after 120 min of irradiation with Xenon lamp with and without sacrificial reagent and in presence of oxygen bubbling or under LED irradiation in an open system respectively). Indeed, it is the material with a more intense absorption band in the visible region. Additionally, it contains such a quantity of antimony as to guarantee reduced charge recombination without excessively distorting the structure. All these features seem determine its better performance compared to its analogues containing different quantities of Sb. To improve its effctiveness under LED irradiation, a lamp with higher irradiance can be employed, while to test performances in real condition direct solar irradiation can be used.

For the development of self-sustaining systems for water purification, photocatalysts able to photogenerate H_2O_2 can be coupled with the peroxidases to activate their catalytic cycle for organic contaminants' oxidation. As already underlined in the previous chapter, enzymes immobilization, despite reducing their activity, increases their stability and guarantees their reuse. The synthesis of materials containing both the enzyme and the photocatalyst simultaneously immobilized could be an interesting future perspective for this research.

The use of different precursors for C_3N_4 synthesis can affect the final materials' structure and related methyl orange photodegradation efficiency. The specific surface area (Asp) appears as one of the major factor affecting the photocatalytic performance of C_3N_4 nanoparticles, while low crystallinity seems a second, less important, requirement. The importance of the specific surface area in C_3N_4 photocatalytic performance is dual. On the one hand, it ensures greater availability of active surface sites for MO and O_2(g) uptake. On the other hand, higher amounts of surface C-defects are observed, which readily scavenge photoinduced electrons, thus inhibiting charge carrier recombination. Therefore, rational strategies improving photogenerated charge carrier separation as coupling with other semiconductors forming heterojunctions are essential for competitive technological uses of C_3N_4 nanomaterials.

4.4 References

Actis, A., Melchionna, M., Filippini, G., Fornasiero, P., Prato, M., Salvadori, E., & Chiesa, M. (2022). Morphology and Light-Dependent Spatial Distribution of Spin Defects in Carbon Nitride. *Angewandte Chemie International Edition*, *61*(43), e202210640. https://doi.org/10.1002/anie.202210640

Bojdys, M. J., Müller, J.-O., Antonietti, M., & Thomas, A. (2008). Ionothermal Synthesis of Crystalline, Condensed, Graphitic Carbon Nitride. *Chemistry – A European Journal*, *14*(27), 8177–8182. https://doi.org/10.1002/chem.200800190

Chang, X., Fan, H., Lei, L., Wu, X., Wang, W., & Ma, L. (2023). Generation Mechanism of the Defects in g-C3N4 Synthesized in N2 Atmosphere and the Method for Improving Photocatalysis Activity. *Catalysts*, *13*(2), Articolo 2. https://doi.org/10.3390/catal13020269

Chen, T., Zheng, Y., Lin, J.-M., & Chen, G. (2008). Study on the photocatalytic degradation of methyl orange in water using Ag/ZnO as catalyst by liquid chromatography electrospray ionization ion-trap mass spectrometry. *Journal of the American Society for Mass Spectrometry*, *19*(7), 997–1003. https://doi.org/10.1016/j.jasms.2008.03.008

Chen, Y., Wang, B., Lin, S., Zhang, Y., & Wang, X. (2014). Activation of n → π* Transitions in Two-Dimensional Conjugated Polymers for Visible Light

Photocatalysis. *The Journal of Physical Chemistry C*, *118*(51), 29981–29989. https://doi.org/10.1021/jp510187c

Dellinger, B., Lomnicki, S., Khachatryan, L., Maskos, Z., Hall, R. W., Adounkpe, J., McFerrin, C., & Truong, H. (2007). Formation and stabilization of persistent free radicals. *Proceedings of the Combustion Institute*, *31*(1), 521–528. https://doi.org/10.1016/j.proci.2006.07.172

Dong, F., Li, Y., Wang, Z., & Ho, W.-K. (2015). Enhanced visible light photocatalytic activity and oxidation ability of porous graphene-like g-C3N4 nanosheets via thermal exfoliation. *Applied Surface Science*, *358*, 393–403. https://doi.org/10.1016/j.apsusc.2015.04.034

Dong, F., Wu, L., Sun, Y., Fu, M., Wu, Z., & Lee, S. C. (2011). Efficient synthesis of polymeric g-C3N4 layered materials as novel efficient visible light driven photocatalysts. *Journal of Materials Chemistry*, *21*(39), 15171–15174. https://doi.org/10.1039/C1JM12844B

Dvoranová, D., Mazúr, M., Papailias, I., Giannakopoulou, T., Trapalis, C., & Brezová, V. (2018). EPR Investigations of G-C3N4/TiO2 Nanocomposites. *Catalysts*, *8*(2), Articolo 2. https://doi.org/10.3390/catal8020047

Gaggero, E., Cai, W., Calza, P., & Ohno, T. (2024). Enhanced hydrogen peroxide production and organic substrates degradation using atomically dispersed antimony P-doped carbon nitride photocatalysts. *Surfaces and Interfaces*, *48*, 104143. https://doi.org/10.1016/j.surfin.2024.104143

Gómez-Velázquez, L. S., Madriz, L., Rigoletto, M., Laurenti, E., Bizarro, M., Dell'Arciprete, M. L., & González, M. C. (2023). Structural and Physicochemical Properties of Carbon Nitride Nanoparticles via Precursor Thermal Treatment: Effect on Methyl Orange Photocatalytic Discoloration. *ACS Applied Nano Materials*, *6*(15), 14049–14062. https://doi.org/10.1021/acsanm.3c01935

Harbour, J. R., & Hair, M. L. (1978). Detection of superoxide ions in nonaqueous media. Generation by photolysis of pigment dispersions. *The Journal of Physical Chemistry*, *82*(12), 1397–1399. https://doi.org/10.1021/j100501a015

He, N., Cao, S., Gu, J., Uddin, A., Zhang, C., Yu, Y., Chen, H., & Jiang, F. (2022). Well-designed oxidized Sb/g-C3N4 2D/2D nanosheets heterojunction with enhanced visible-light photocatalytic disinfection activity. *Journal of Colloid and Interface Science*, *606*, 1284–1298. https://doi.org/10.1016/j.jcis.2021.08.122

Inagaki, M., Tsumura, T., Kinumoto, T., & Toyoda, M. (2019). Graphitic carbon nitrides (*g*-C3N4) with comparative discussion to carbon materials. *Carbon*, *141*, 580–607. https://doi.org/10.1016/j.carbon.2018.09.082

Lin, H., Wu, J., Zhou, F., Zhao, X., Lu, P., Sun, G., Song, Y., Li, Y., Liu, X., & Dai, H. (2023). Graphitic carbon nitride-based photocatalysts in the applications of

environmental catalysis. *Journal of Environmental Sciences*, *124*, 570–590. https://doi.org/10.1016/j.jes.2021.11.017

Liu, P., Sun, N., Liang, Y., & Chen, F. (2018). Modified graphitic carbon nitride prepared via a copolymerization route for superior photocatalytic activity. *Research on Chemical Intermediates*, *44*(2), 843–857. https://doi.org/10.1007/s11164-017-3139-5

Lu, Y., Guo, Y., Zhang, S., Li, L., Jiang, R., Zhang, D., Yu, J. C., & Wang, J. (2024). Promoting Proton Donation through Hydrogen Bond Breaking on Carbon Nitride for Enhanced H2O2 Photosynthesis. *ACS Nano*, *18*(31), 20435–20448. https://doi.org/10.1021/acsnano.4c04797

Ma, D., Li, X., Wang, X., & Luo, Y. (2021). Research development on graphitic carbon nitride and enhanced catalytic activity on ammonium perchlorate. *RSC Advances*, *11*(10), 5729–5740. https://doi.org/10.1039/D0RA09079D

Makuła, P., Pacia, M., & Macyk, W. (2018). How To Correctly Determine the Band Gap Energy of Modified Semiconductor Photocatalysts Based on UV–Vis Spectra. *The Journal of Physical Chemistry Letters*, *9*(23), 6814–6817. https://doi.org/10.1021/acs.jpclett.8b02892

Montemore, M. M., van Spronsen, M. A., Madix, R. J., & Friend, C. M. (2018). O2 Activation by Metal Surfaces: Implications for Bonding and Reactivity on Heterogeneous Catalysts. *Chemical Reviews*, *118*(5), 2816–2862. https://doi.org/10.1021/acs.chemrev.7b00217

Moon, G., Fujitsuka, M., Kim, S., Majima, T., Wang, X., & Choi, W. (2017). Eco-Friendly Photochemical Production of H2O2 through O2 Reduction over Carbon Nitride Frameworks Incorporated with Multiple Heteroelements. *ACS Catalysis*, *7*(4), 2886–2895. https://doi.org/10.1021/acscatal.6b03334

Nguyen, C. H., Fu, C.-C., & Juang, R.-S. (2018). Degradation of methylene blue and methyl orange by palladium-doped TiO2 photocatalysis for water reuse: Efficiency and degradation pathways. *Journal of Cleaner Production*, *202*, 413–427. https://doi.org/10.1016/j.jclepro.2018.08.110

Qiu, C., Xu, Y., Fan, X., Xu, D., Tandiana, R., Ling, X., Jiang, Y., Liu, C., Yu, L., Chen, W., & Su, C. (2019). Highly Crystalline K-Intercalated Polymeric Carbon Nitride for Visible-Light Photocatalytic Alkenes and Alkynes Deuterations. *Advanced Science*, *6*(1), 1801403. https://doi.org/10.1002/advs.201801403

Rigoletto, M., Laurenti, E., & Tummino, M. L. (2024). An Overview of Environmental Catalysis Mediated by Hydrogen Peroxide. *Catalysts*, *14*(4), 267. https://doi.org/10.3390/catal14040267

Shiraishi, Y., Kanazawa, S., Sugano, Y., Tsukamoto, D., Sakamoto, H., Ichikawa, S., & Hirai, T. (2014). Highly Selective Production of Hydrogen Peroxide on

Graphitic Carbon Nitride (g-C3N4) Photocatalyst Activated by Visible Light. *ACS Catalysis*, *4*(3), 774–780. https://doi.org/10.1021/cs401208c

Tan, J., Tian, N., Li, Z., Li, J., Yao, X., Vakili, M., Lu, Y., & Zhang, T. (2021). Intrinsic defect engineering in graphitic carbon nitride for photocatalytic environmental purification: A review to fill existing knowledge gaps. *Chemical Engineering Journal*, *421*, 127729. https://doi.org/10.1016/j.cej.2020.127729

Teng, Z., Cai, W., Liu, S., Wang, C., Zhang, Q., Chenliang, S., & Ohno, T. (2020). Bandgap engineering of polymetric carbon nitride copolymerized by 2,5,8-triamino-tri-s-triazine (melem) and barbituric acid for efficient nonsacrificial photocatalytic H2O2 production. *Applied Catalysis B: Environmental*, *271*, 118917. https://doi.org/10.1016/j.apcatb.2020.118917

Teng, Z., Cai, W., & Ohno, T. (2023). Functionalized Graphitic Carbon Nitrides for Photocatalytic H2O2 Production: Desired Properties Leading to Rational Catalyst Design. *KONA Powder and Particle Journal*, *40*, 124–148. https://doi.org/10.14356/kona.2023004

Teng, Z., Lv, H., Wang, C., Xue, H., Pang, H., & Wang, G. (2017). Bandgap engineering of ultrathin graphene-like carbon nitride nanosheets with controllable oxygenous functionalization. *Carbon*, *113*, 63–75. https://doi.org/10.1016/j.carbon.2016.11.030

Teng, Z., Yang, N., Lv, H., Wang, S., Hu, M., Wang, C., Wang, D., & Wang, G. (2019). Edge-Functionalized g-C3N4 Nanosheets as a Highly Efficient Metal-free Photocatalyst for Safe Drinking Water. *Chem*, *5*(3), 664–680. https://doi.org/10.1016/j.chempr.2018.12.009

Teng, Z., Zhang, Q., Yang, H., Kato, K., Yang, W., Lu, Y. R., Liu, S., Wang, C., Yamakata, A., Su, C., Liu, B., & Ohno, T. (2021). Atomically dispersed antimony on carbon nitride for the artificial photosynthesis of hydrogen peroxide. *Nature Catalysis*, *4*(5), 374–384. https://doi.org/10.1038/s41929-021-00605-1

Testa, M. L., & Tummino, M. L. (2021). Lignocellulose Biomass as a Multifunctional Tool for Sustainable Catalysis and Chemicals: An Overview. *Catalysts*, *11*(1), 125. https://doi.org/10.3390/catal11010125

Wang, A., Li, J., & Zhang, T. (2018). Heterogeneous single-atom catalysis. *Nature Reviews Chemistry*, *2*(6), 65–81. https://doi.org/10.1038/s41570-018-0010-1

Zhang, J., Chen, J., Wan, Y., Liu, H., Chen, W., Wang, G., & Wang, R. (2020). Defect Engineering in Atomic-Layered Graphitic Carbon Nitride for Greatly Extended Visible-Light Photocatalytic Hydrogen Evolution. *ACS Applied Materials & Interfaces*, *12*(12), 13805–13812. https://doi.org/10.1021/acsami.9b21115

Zhang, J., Chen, X., Takanabe, K., Maeda, K., Domen, K., Epping, J. D., Fu, X., Antonietti, M., & Wang, X. (2010). Synthesis of a Carbon Nitride Structure for

Visible-Light Catalysis by Copolymerization. *Angewandte Chemie International Edition*, *49*(2), 441–444. https://doi.org/10.1002/anie.200903886

Zhao, Z., Ma, Y., Fan, J., Xue, Y., Chang, H., Masubuchi, Y., & Yin, S. (2018). Synthesis of graphitic carbon nitride from different precursors by fractional thermal polymerization method and their visible light induced photocatalytic activities. *Journal of Alloys and Compounds*, *735*, 1297–1305. https://doi.org/10.1016/j.jallcom.2017.11.033

Zheng, Y., Ren, J., Zhang, N., & Li, J. (2021). Preparation of carbon nitride from different precursors through pyrolysis: Correlating the photocatalytic activity to the crystallinity and disorder. *Journal of Environmental Chemical Engineering*, *9*(6), 106410. https://doi.org/10.1016/j.jece.2021.106410

Zhou, Y., Zhang, L., Liu, J., Fan, X., Wang, B., Wang, M., Ren, W., Wang, J., Li, M., & Shi, J. (2015). Brand new P-doped g-C3N4: Enhanced photocatalytic activity for H2 evolution and Rhodamine B degradation under visible light. *Journal of Materials Chemistry A*, *3*(7), 3862–3867. https://doi.org/10.1039/C4TA05292G

5 Conclusions

This PhD project aimed to maximize the valorisation of soybean hulls, a residue from soy industrial processing, through the recovery of soybean peroxidase (SBP) and cellulose. These two components have been employed for the development of new materials for environmental applications. The research was inserted within the framework of the circular economy and tried to maintain the objective of circularity in the development, use and *end-of-life* of the prepared materials. At the same time, attention was also paid to the impacts reduction, focusing particularly on the initial biomass tratment. Indeed, alongside the multi-hydrolysis cellulose extraction, an alternative two-step hulls fractionation method assisted by microwaves has also been optimised. Subcritical water and diluted NaOH solution were employed as extraction solvents. Both strategies led to final samples enriched in cellulose (up to 88% with multi-hydrolysis and 91.5% with microwaves) and with comparable features, but the microwave-assisted process reduced cellulose isolation steps from three to two and completely avoided the use of hydrochloric acid. It is important to underline that, although the first evidences suggest an impacts reduction, to compare the two methods exhaustively it will be necessary to carry out a life cycle assessment study and to consider the whole processes in all their aspects.

Cellulose has been used for the synthesis of materials developed to treat water samples contaminated by both organic and inorganic pollutants. For this purpose, several chemical modifications have been carried out to introduce functional groups within the structure of the biopolymer in order to enhance its affinity towards specific contaminants.

Hydrogels prepared with amine and thiol-functionalised cellulose or carboxymethyl cellulose showed good removal capabilities of potentially toxic elements from aqueous matrices not only in mono-elemental solutions but also in mixture. Moreover, the primary amino groups in the cellulose structure made it suitable also for enzyme immobilization allowing the development of SBP-containing bio-based systems for efficient organic contaminants' oxidation.

Preliminary studies on photocatalysts for hydrogen peroxide photoproduction have been carried out with the aim of developing self-sustaining systems coupled with SBP that ensure organic compounds degradation avoiding an external H_2O_2 addition.
Considerable attention was paid to evaluating the actual applicability of our strategies outside the controlled laboratory conditions. Therefore, the performances of all the prepared materials have been tested also employing real aquaculture water as solvent for contaminants' solutions preparation in order to evaluate the influence of pH, inorganic ions and dissolved organic matter on water treatments outcomes.
However, this is only the first of a series of aspects that need to be considered when applying a strategy in a real context (Figure 5.1).

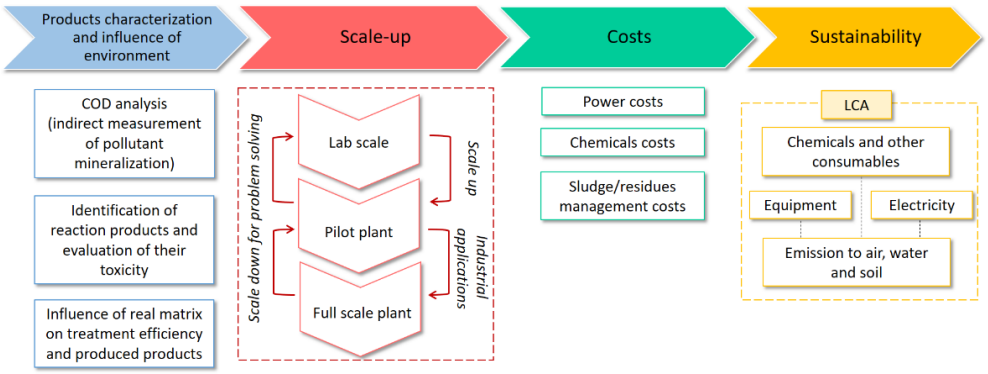

Figure 5.1 - aspects to take into consideration for evaluating the applicability of the processes in real contexts (modified from (Rigoletto et al., 2024))

For instance, the evaluation of the efficiency of a water remediation strategy should also include the analysis of the toxicity of any contaminants' degradation products (Yoon & Cho, 2024). Although the optimum should be to achieve organic contaminants complete mineralization, often the degradation is uncomplete. Furthermore, some treatments, like those exploiting biocatalysis, occur through radicalic reaction mechanisms which do not lead to a real mineralisation of organic substrates. Therefore, the positive effect of removing substances that are difficult to break down must not be rendered useless by the formation of new substances with

equal or greater toxicity of the starting ones (Carvalho Neves et al., 2020; Priyadarshini et al., 2022).

In our work, this critical issue has been consider studying the efficiency of the oxidation of (chlorinated) phenolic compounds mediated by the developed SBP-containing hydrogels. Toxicity tests results demonstrated that the reaction products with higher molecular weight were less toxic than the parent molecules, confirming an effective water decontamination.

Many other challenges are related to real applications. First of all, the scalability of the processes moving from laboratory scale to pilot plants and full-scale plants. At the basis of the process scalability, there are several critical points that have to be considered as the efficiency of materials' synthesis (yield, quality, *etc.*) or change in catalyst/adsorbent effectiveness, degradation kinetic parameters and pathways (Rigoletto et al., 2024). Secondly, the assessment of the feasibility of purification procedures must involve techno-economic aspects together with the environmental impact through LCA analyses (Tummino et al., 2023).

In the case of the strategies developed in this doctoral project it was not possible to make any of these evaluations as they are still limited to the laboratory scale and therefore have a low Technology Readiness Level.

However, we have always developed materials that are not only derived from waste but also reusable and biodegradable to increase their lifespan as much as possible and reduce their impacts to a minimum.

We tried to respond to the enormous challenge of the contamination of water resources, which represent an asset that we cannot deprive ourselves of, through strategies that are circular and characterized by minimal impact and low costs. Research must certainly move towards the industrial feasibility of the most promising technologies in order to provide society with new effective strategies, but basic research is undoubtedly the first step towards a greener and more sustainable future.

5.1 References

Carvalho Neves, L., Beber de Souza, J., de Souza Vidal, C. M., Herbert, L. T., de Souza, K. V., Geronazzo Martins, K., & Young, B. J. (2020). Phytotoxicity indexes and removal of color, COD, phenols and ISA from pulp and paper mill wastewater post-treated by UV/H2O2 and photo-Fenton. *Ecotoxicology and Environmental Safety*, *202*, 110939. https://doi.org/10.1016/j.ecoenv.2020.110939

Priyadarshini, M., Das, I., Ghangrekar, M. M., & Blaney, L. (2022). Advanced oxidation processes: Performance, advantages, and scale-up of emerging technologies. *Journal of Environmental Management*, *316*, 115295. https://doi.org/10.1016/j.jenvman.2022.115295

Rigoletto, M., Laurenti, E., & Tummino, M. L. (2024). An Overview of Environmental Catalysis Mediated by Hydrogen Peroxide. *Catalysts*, *14*(4), 267. https://doi.org/10.3390/catal14040267

Tummino, M. L., Varesano, A., Copani, G., & Vineis, C. (2023). A Glance at Novel Materials, from the Textile World to Environmental Remediation. *Journal of Polymers and the Environment*, *31*(7), 2826–2854. https://doi.org/10.1007/s10924-023-02810-4

Yoon, Y., & Cho, M. (2024). Understanding atrazine elimination via treatment of the enzyme-based Fenton reaction: Kinetics, mechanism, reaction pathway, and metabolites toxicity. *Chemosphere*, *349*, 140982. https://doi.org/10.1016/j.chemosphere.2023.140982

6 Research products

6.1 Publications

6.1.1 Papers directly concerning the PhD project

Rigoletto, M., Calza, P., Gaggero, E., & Laurenti, E. (2022).
Hybrid materials for the removal of emerging pollutants in water: Classification, synthesis, and properties.
Chemical Engineering Journal Advances, 10, 100252.
https://doi.org/10.1016/j.ceja.2022.100252
Bibliographic research reported in this review have been used to write the Chapter 1 and the introduction of Chapter 3

Rigoletto, M., Calza, P., Cunha, A. S. da, Sederino, V., Fabbri, D., Tummino, M. L., & Laurenti, E. (2023).
Soybean peroxidase immobilised on cellulose-alginate hydrogels for removal of recalcitrant organic pollutants in water.
Reaction Chemistry & Engineering, 8(7), 1629–1637.
https://doi.org/10.1039/D3RE00009E
Result reported in this paper are discussed in Chapter 3

Gómez-Velázquez, L. S., Madriz, L., **Rigoletto, M**., Laurenti, E., Bizarro, M., Dell'Arciprete, M. L., & González, M. C. (2023).
Structural and Physicochemical Properties of Carbon Nitride Nanoparticles via Precursor Thermal Treatment: Effect on Methyl Orange Photocatalytic Discoloration. ACS Applied Nano Materials, 6(15), 14049–14062.
https://doi.org/10.1021/acsanm.3c01935
Result reported in this paper are discussed in Chapter 4

Rigoletto, M., Laurenti, E., & Tummino, M. L. (2024).
An Overview of Environmental Catalysis Mediated by Hydrogen Peroxide.
Catalysts, 14(4), 267.
https://doi.org/10.3390/catal14040267
Bibliographic research reported in this review have been used to write the introduction of Chapter 4 and conclusions

Rigoletto M., Rapp M., Arencibia A., López-Muñoz M.J., Tummino M.L., Laurenti E.
Adsorption of mercury in aqueous solutions by functionalized cellulose extracted from soybean hulls
ChemPlusChem - under review
Result reported in this paper are discussed in Chapter 3

Rigoletto M., Sesia R., Malandrino M., Berto S., Calza P., Laurenti E., Sangermano M.
Chitosan, gelatine and cellulose based hydrogels for the removal of potentially toxic elements from aquaculture water: a comparative study
Advanced Sustainable Systems – under review
Result reported in this paper are discussed in Chapter 3

Santuchi da Cunha A., **Rigoletto M.,** dos Santos Vianna Jr. A., Laurenti E.
Single and multi-substrate degradation kinetics of chlorinated phenolic compounds catalyzed by soybean peroxidase
Chemical Engineering Journal – under review

Rigoletto M., Grillo G., Natali E., Tummino M.L., Laurenti E., Tabasso S.
Optimization of microwave-assisted cellulose isolation from soybean hulls
Article in preparation
Results that will be reported in this paper are discussed in Chapter 2

6.1.2 Other published papers

Gomes B.R., Lopes J.L., Cohelo L., Ligonzo M., **Rigoletto M.**, Magnacca G., Deganello F (2023).
Development and Upscaling of SiO2@TiO2 Core-Shell Nanoparticles for Methylene Blue Removal
Nanomaterials 2023, 13(16), 2276
https://doi.org/10.3390/nano13162276

Tummino M.L., Vineis C., Varesano A., Liotta L.F., **Rigoletto M.**, Laurenti E., Deganello F. (2023)
$Sr_{0.85}Ce_{0.15}Fe_{0.67}Co_{0.33-x}Cu_xO_3$ perovskite oxides: effect of B-site copper codoping on the physicochemical, catalytic and antibacterial properties upon UV or thermal activation
Frontiers in Environmental Engineering 2:1249931
https://doi.org/10.3389/fenve.2023.1249931

Tummino M.L., Magnacca G., **Rigoletto M**., Malandrino M., Vineis C., Laurenti E. (2024)
Insights into performances of magnetic and bio-based doped-nanohydroxyapatites as water decontamination agents
Reaction Chemistry & Engineering 9, 2321-2332
https://doi.org/10.1039/D4RE00160E

6.2 Contributes in Conferences and Congresses

EMEC2024 - 2024 European Meeting on Environmental Chemistry
Oral contribution: *Chitosan, gelatine and cellulose based hydrogels for the removal of potentially toxic elements from aquaculture water: a comparative study*
Poster: *Functionalized cellulose from deproteinized soybean hulls as an environmental decontamination and disinfection tool*
26th -29th November 2024, Alicante, Spain

XI Workshop Nazionale Green Chemistry – Chimica Sostenibile (Società Chimica Italiana, gruppo interdivisionale di Green Chemistry)
Oral contribution: *Cellulose fibres from soybean hulls: efficiency and sustainability of different isolation methods*
24th-25th October 2024, Turin, Italy

IconBM2024 - International Conference on Biomass
Oral contribution: *Optimization of microwave-assisted cellulose isolation from soybean hulls*
19th-22nd May 2024, Palermo, Italy

XIth Edition of Italian-French Chemistry Days
Poster: *Study of influence of organic matter and inorganic ions on soybean peroxidase activity: from the lab to real applications*
4th – 5th April 2024, Turin, Italy

16th International Symposium on Applied Bioinorganic Chemistry (16-ISABC)
Poster + Flash presentation: *Removal of recalcitrant organic pollutants by soybean peroxidase immobilized on cellulose-alginate hydrogels*
11th- 14th June 2023, Ioannina, Greece)

Xth Franco-Italian Days of Chemistry

Oral contribution: *Valorization of an agro-industrial waste: synthesis of soybean hulls derivatives based hybrid materials for water purification*
26th – 27th April 2022, Tolone, France

Merck Young Chemists' Symposium (MYCS) 2021
Poster: *Synthesis of new bio-based hybrid materials for water purification*
22nd – 24th November 2021, Rimini, Italy

7 Appendix

7.1 Appendix I: NREL protocol

Table AI-1: summary of biomass compositional analysis (NREL phases + calcination)

Step	1	2	3	4
Solvent	Ethanol:Benzene (50:50 v/v)	Sulfuric acid 0.94M	Sulfuric acid 13.5 M	-
Biomass : solvent	1 : 50	1 : 50	1 : 50	-
Time (h)	2	2 (reflux)	24 (4°C)	4 (650°C)
Estimated fraction	Lipids	Hemicellulose and possible soluble ashes	Cellulose (+ Lignin by difference)	Insoluble inorganic components

The amount of each fraction is evaluated through gravimetric analysis. The mass of the final residue after filtration of step 1, 2 and 3 (Table AI-1) and the related losses are obtained using the equation s1 and s2

$$\text{Residual mass (g)} = m_{Sf} = m_{F+Sf} - m_F \quad \text{(s1)}$$

$$\text{Loss (g)} = m_{Si} - m_{Sf} \quad \text{(s2)}$$

Where m_{F+Sf} is the mass (g) of the filter containing the dried biomass after the NREL step, m_F is the tare weight of the filter, m_{Si} is the mass (g) of the biomass before the NREL step and m_{Sf} is the dried biomass after NREL step.

The loss at the end of the steps 2 and 3 has to be corrected considering the mass of the residual of the previous step (equation s3)

$$\text{Correct loss (g)} = \frac{m_{Sf-(n-1)}}{100} \times Loss_n \quad \text{(s3)}$$

Where $m_{Sf-(n-1)}$ is the mass of the residual biomass of the step(n-1) and $loss_n$ is the mass of the loss calculated for the step(n).

The amounts of the fractions of interest are the correct losses of each NREL step. In particular:

- Correct loss of NREL step 1: lipid's fraction
- Correct loss of NREL step 2: hemicellulose + possible soluble ashes
- Correct loss of NREL step 3: cellulose

Each loss mass is converted into percentage considering 100% the mass of the biomass subjected to the NREL protocol. The lignin percentages could be calculated by difference (equation s4)

$$\text{Lignin (\%)} = 100 - (\text{Cellulose\%} + \text{Hemicellulose\%} + \text{Lipids\%}) \quad \text{(s4)}$$

Step 4, which involves the calcination of the residue of step 3, returns the value of the insoluble inorganic component which should be subtracted from the value of the lignin resulting from the NREL analysis

7.2 Appendix II: Supplementary data on hydrogels' PTEs adsorption

Figure AII-1: Removal percentages at different contact time with 1g/L of adsorbent; PTEs concentration 10^{-4}, 10^{-5}, 10^{-6} M, pH 5

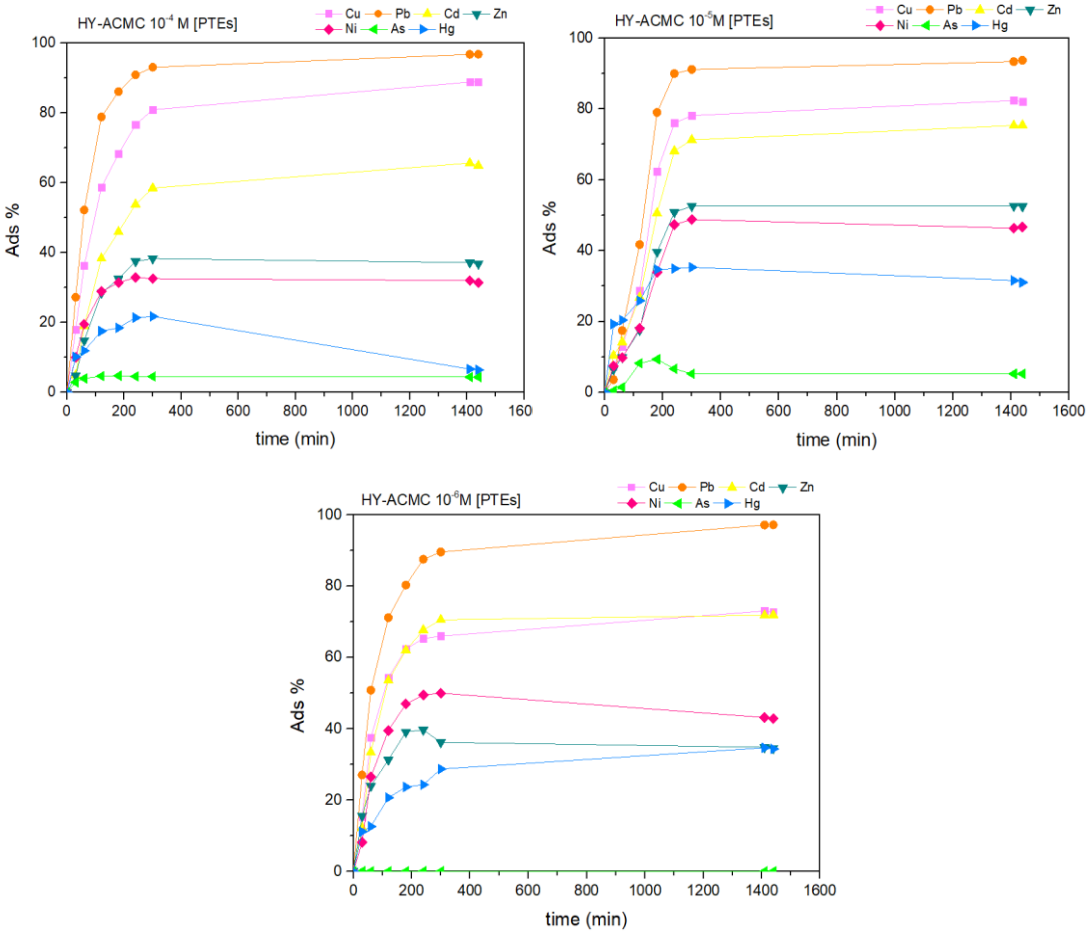

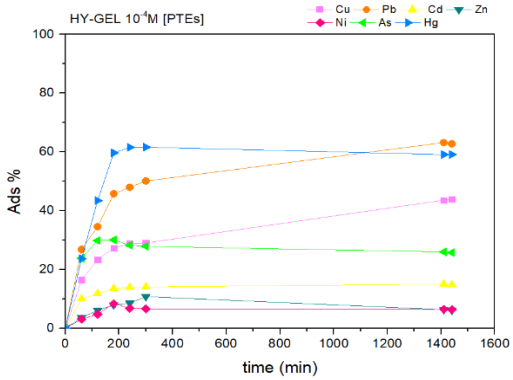
HY-GEL 10-4M [PTEs]
Cu Pb Cd Zn
Ni As Hg
Ads %
time (min)

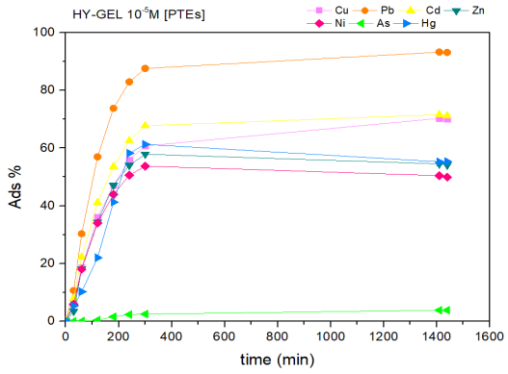
HY-GEL 10-5M [PTEs]
Cu Pb Cd Zn
Ni As Hg
Ads %
time (min)

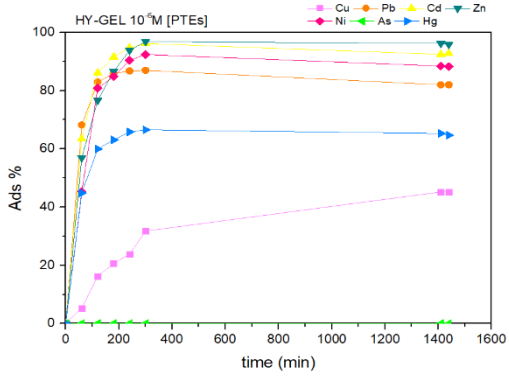
HY-GEL 10-6M [PTEs]
Cu Pb Cd Zn
Ni As Hg
Ads %
time (min)

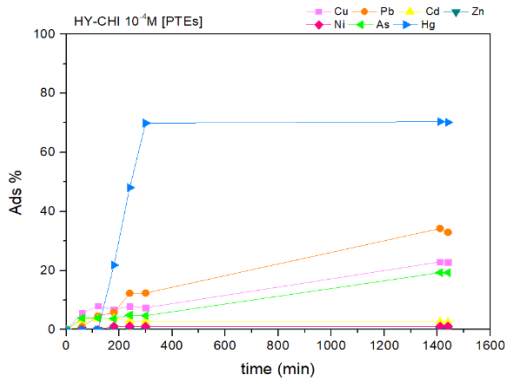
HY-CHI 10-4M [PTEs]
Cu Pb Cd Zn
Ni As Hg
Ads %
time (min)

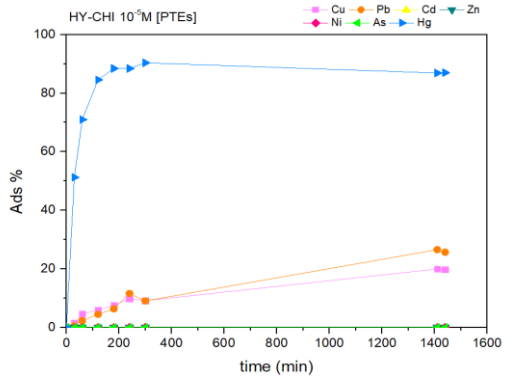
HY-CHI 10-5M [PTEs]
Cu Pb Cd Zn
Ni As Hg
Ads %
time (min)

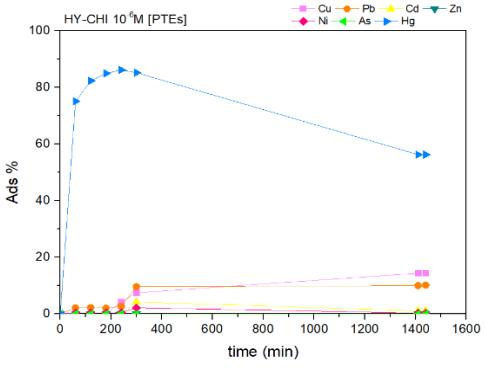
HY-CHI 10-6M [PTEs]
Cu Pb Cd Zn
Ni As Hg
Ads %
time (min)

Figure AII-2: Removal percentages at different contact time with 1g/L of adsorbent; PTEs concentration 10^{-5}M, pH 3.5 and 7

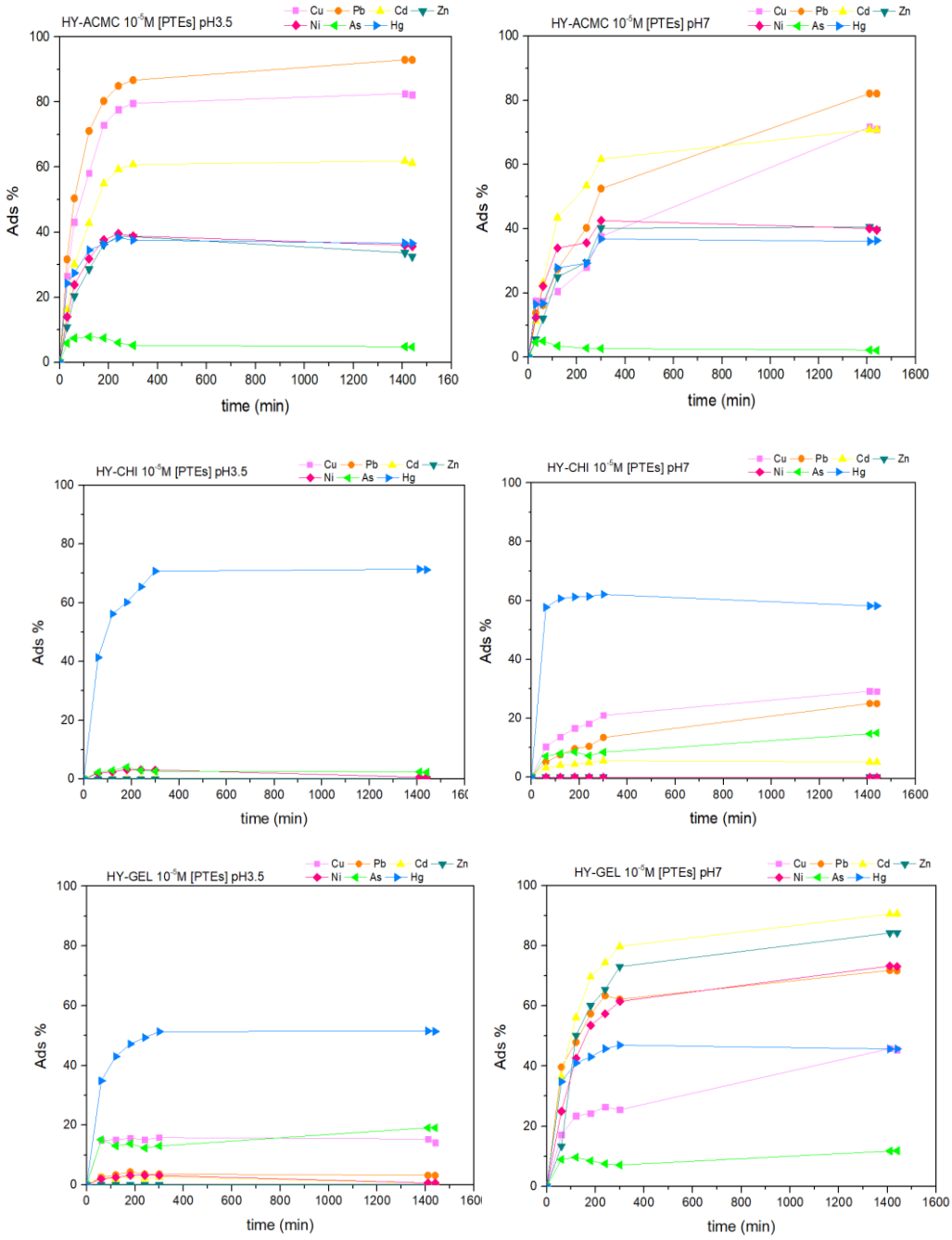

Figure AII-3: PTEs speciation and comments

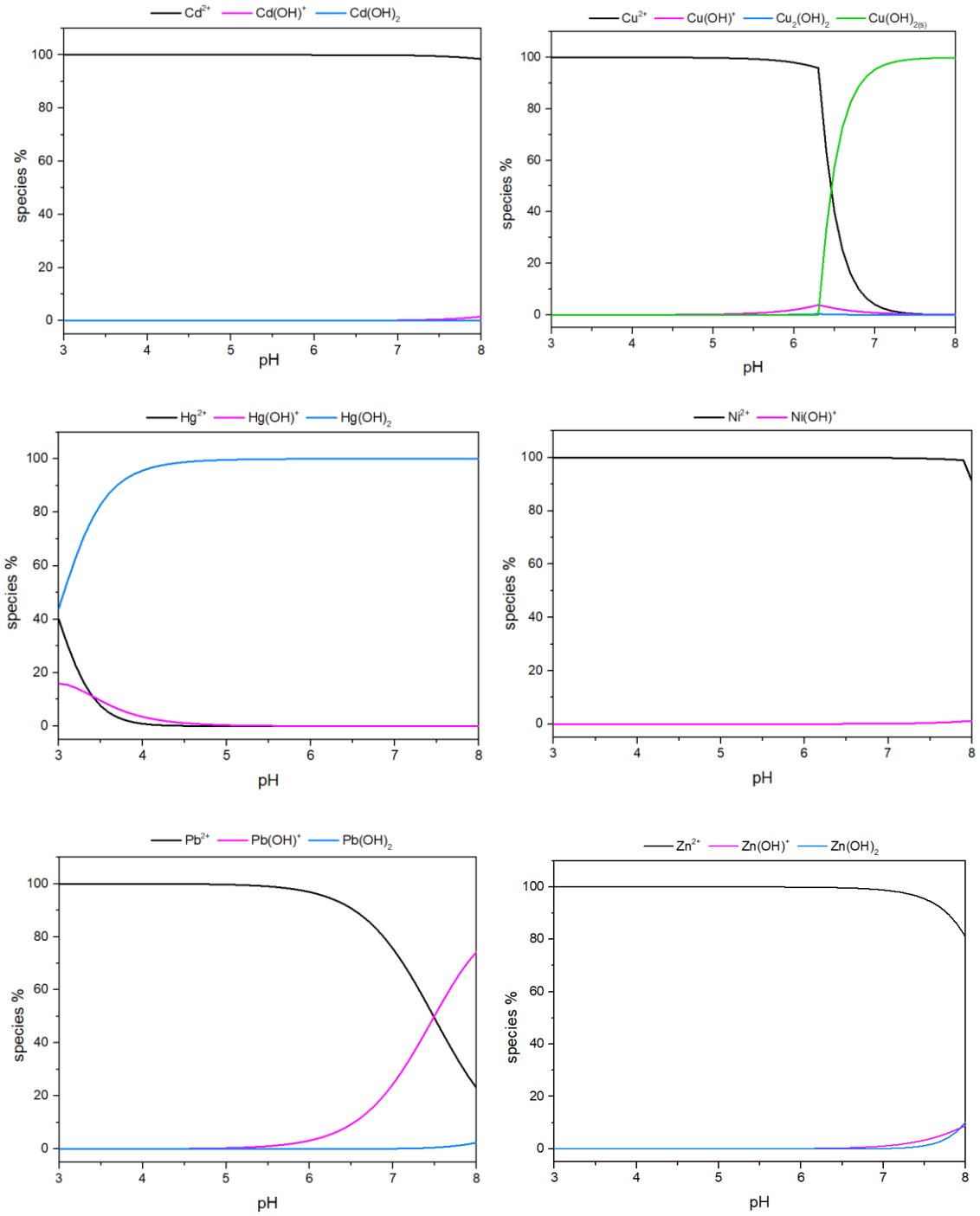

Speciation of all studied element has been modelled in the pH range between 3 and 8 assuming that only hydrolysis equilibria occur as expected on the basis of the composition of solutions used during the test. Speciation diagrams for each metal cation were obtained by PyES software (Castellino et al., 2023) taking into consideration: (i) thermodynamic formation constants (infinite dilution condition) (*Academic Software. Sourby Old Farm, Timble, Otley, Yorks, LS21 2PW. In SC-Database. The IUPAC Stability Constant Database,Version 5.84*, s.d.) (iii) temperature of 25°C; (iv) metal concentration 10^{-5} M.

Cd an Ni are present as aquaions throughout the pH range studied. At pH values higher than 7 both cadmium and nickel could be present in a few percentage as the charged hydrolytic species $Cd(OH)^+$ and $Ni(OH)^+$.

Up to pH 7 Zn is present in 100% solution as aquaions. Increasing the pH value, there is a small percentage (<10%) of formation of the hydrolytic species $Zn(OH)^+$ and $Zn(OH)_2$.

Between pH 3 and 6 Cu and Pb are mainly present in solution as aquaions species. Increasing the pH values (5.5-7.5) a small percentage of the charged hydrolytic species $Cu(OH)^+$ is formed and then, for values higher than 6, the solid $Cu(OH)_{2(s)}$ is formed and precipitates. On the other hand, at pH higher than 6, lead forms the hydrolytic species $Pb(OH)^+$ which reaches 80% at pH 8.

Unlike the elements previously described, Hg is mostly present as a neutral hydrolytic species $Hg(OH)_2$ with percentages ranging from 40% to 100% going from pH 3 to pH 4.5, a value beyond which it remains the only species present. At pH lower then 4, mercury could be present at lower percentages as aquaions species and as $Hg(OH)^+$.

According to literature, As(III) is present as H_3AsO_3 up to pH 7 while it coexists with the $H_2AsO_3^-$ species for values between 7 and 11 (Cassone et al., 2018).

Table AII-1: PTEs properties

	Pb^{2+}	Cu^{2+}	Cd^{2+}	Zn^{2+}	Ni^{2+}
charge (q)	2	2	2	2	2
ionic radius Shannon (Å)	1.32	0.73 o 0.87	0.95	0.74	0.69
N° coordination**	6	4 or 6	4	4	4
charge density (with ionic radius) (ρ)	0.207	0.73	0.557	1.18	1.45
idrate radius (Å)	4.01	4.19	4.26	4.3	4.04
charge density x 10^{-3} (with idrate radius) (ρ)	7.41	6.49	6.18	6.01	7.24
electronegativity	2.33	1.9	1.69	1.65	1.91
LogK_{ML} M^{2+}-acetate*	2.58	2.21	1.92	1.57	1.44

* NIST SDR 96 Database (t = 25 °C, I = 0)
**(Huheey et al., s.d.)

Charge densities have been calculated with the following equation (s5):

$$\rho = \frac{q}{\frac{4}{3}\pi r^3} \quad \text{(s5)}$$

where ρ is the charge density, q is the charge of the ions, r is the ionic radius

Table AII-2: Real aquaculture water characterization and law concentration limits

	Italian koi carps water	**Danish aquaculture water**	**Concentration limit law for human usage***	**Concentration limit law for salmon health (hardness between 50 and 100) ‡**	**Concentration limit law for salmon health (hardness between 150 and 199) ‡**
Hardness (mg/L $CaCO_3$)	96.08	194.71	-	-	-
pH	8.03	7.76	-	-	-
Al (µg/L)	1.145 ± 0.115	0.31	-	-	-
As (µg/L)	1.485 ± 0.149	18.84	10	50	50
Ba (µg/L)	22.795 ± 2.280	24.13	-	-	-
Ca (mg/L)	19.54 ± 0.98	60.29	-	-	-
Cd (µg/L)	0.025 ± 0.003	0.04	5	2.5	2.5
Co (µg/L)	0.330 ± 0.033	0.14	-	-	-
Cr (µg/L)	< LOD	0.12	50	10	20
Cu (µg/L)	0.925 ± 0.093	5.34	1000	40	40
Fe (µg/L)	6.465 ± 0.647	119.57	-	-	
Hg (µg/L)	< LOD	0.06	1	0.5	0.5
K (mg/L)	2.84 ± 0.14	46.37	-	-	-
Mg (mg/L)	12.05 ± 0.6	10.73	-	-	-
Mn (µg/L)	0.615 ± 0.062	< LOD	-	-	-
Na (mg/L)	5.31 ± 0.27	842.59	-	-	-
Ni (µg/L)	7.95 ± 0.791	0.02	20	50	75
Pb (µg/L)	1.565 ± 0.157	< LOD	10	10	20
Sn (µg/L)	0.155 ± 0.016	0.04	-	-	-
Sb (µg/L)	1.560 ± 0.156	1.04	5	-	-
V (µg/L)	0.615 ± 0.062	2.38	50	-	-
Zn (µg/L)	39.505 ± 3.951	20.41	-	200	300

*Decreto Legislativo 2 febbraio 2001, n. 31, Attuazione della direttiva 98/83/CE relativa alla qualità delle acque destinate al consumo umano.

‡ D.Lgs. Governo 3 aprile 2006, n. 152 [Allegati 2 alla parte III], Sezione B: Criteri generali e metodologie per il rilevamento delle caratteristiche qualitative, per la classificazione ed il calcolo della conformità delle acque dolci superficiali idonee alla vita dei pesci salmonicoli e ciprinicoli.

Figure AII-4: Removal percentages at different contact time in real water samples (PTEs concentration near Italian legal limits) with 1g/L of adsorbent.

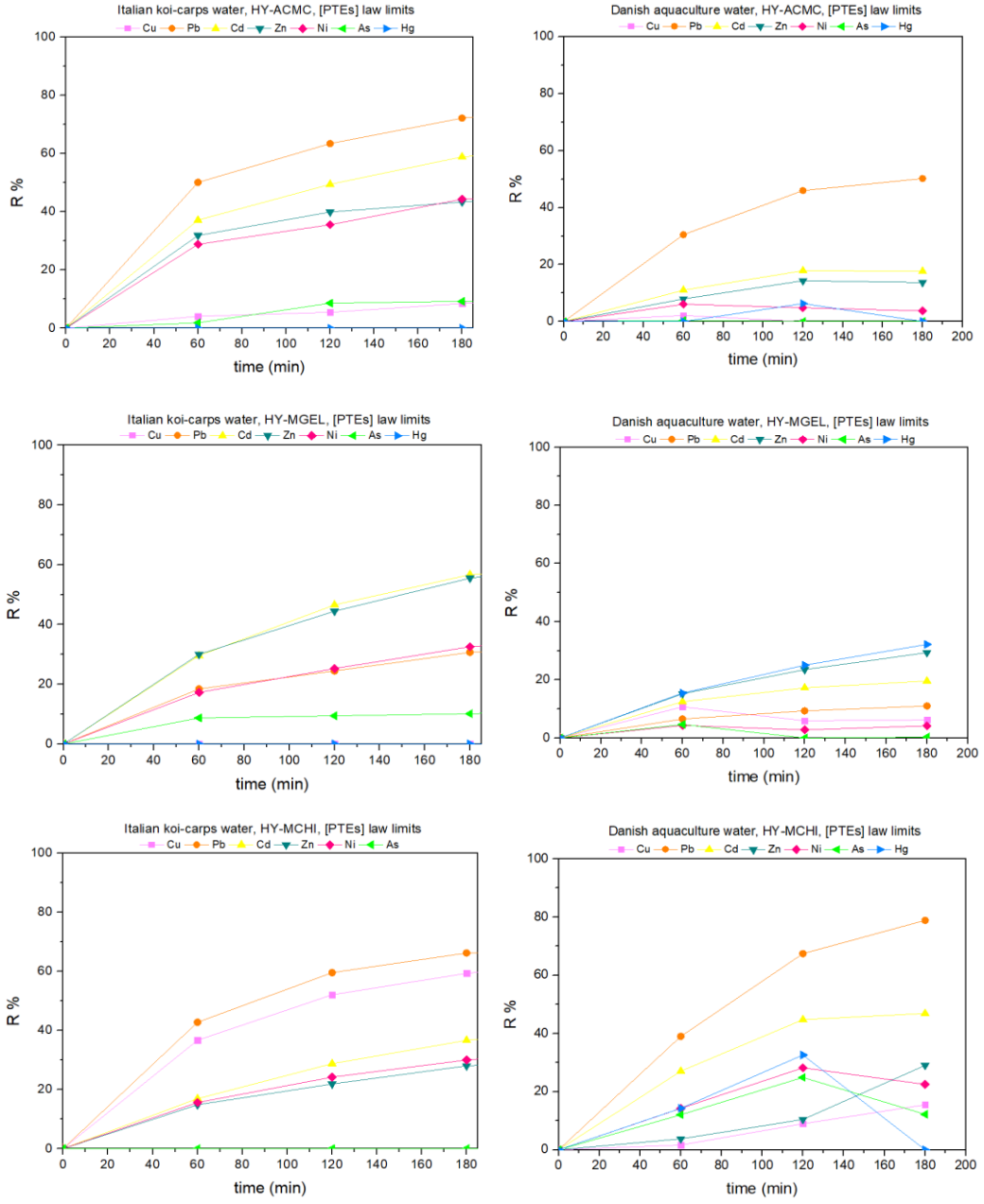

Table AII-3: Complexation constants of H_4EDTA with PTEs (t = 25°C; ionic strength 0.1 $molL^{-1}$)*

	As^{3+}	Cd^{2+}	Cu^{2+}	Hg^{2+}	Ni^{2+}	Pb^{2+}	Zn^{2+}
logβ(ML)	unknown	16.5	18.8	21.5	18.4	18	16.5
logβ(MHL)	unknown	19.4	21.88	24.7	21.5		19.5
logβ(MH_2L)		-	23.88	-	-		-

* NIST SDR 96 Database

Table AII-4: Reusability of different materials for PTEs removal from water regenerated with EDTA-based reagents (RIFERIMENTI)

Adsorbent	PTE	Regeneration reagent concentration	Number of adsorption cycle	Residual efficiency compared to the first cycle	Reference
HY-ACMC	Pb(II) Cu(II) Cd(II) Zn(II) Ni(II) Hg(II) **TOT**	0.01M	2	Pb(II) -23% Cu(II) – 19% Cd(II) -20% Zn(II) – 25.6% Ni(II) – 35.2% Hg(II) – 142% **30%**	This work
HY-MGEL	Pb(II) Cu(II) Cd(II) Zn(II) Ni(II) Hg(II) **TOT**	0.01M	3	Pb(II) -48.8% Cu(II) – 23.3% Cd(II) – 14.7% Zn(II) – 8.8% Ni(II) – 7% Hg(II) – 51.5% **34%**	This work
HY-MCHI	Pb(II) Cu(II) Cd(II) Zn(II) Ni(II) Hg(II) **TOT**	0.01M	3	Pb(II) -130% Hg(II)-188% PTEs not removed in the first cycle (R%): Cu(II)-27% Cd(II) -23% Ni(II)-21% Zn(II) – 24.6% **232,28%**	This work
Magnetic chitosan beads/cystein glutaraldehyde's Schiff	Cu(II)	0.01M	3	91%	(Abou El-Reash, 2016)
Magnetic chitosan/rectorite composite microspheres	Cu(II) Cd(II)	0.01M	4	>55%	(Xie et al., 2015)
Chitosan/maleic anhydride/titania	Pb(II)	0.01M	3	92%	(Shaker & Yakout, 2016)
chitosan-tripolyphosphate beads	Pb(II) Cu(II)	0.01M	3	Pb(II)-94%[(a)] Cu(II)-90%[(a)]	(Ngah & Fatinathan, 2010)

chitosan/poly(ethylene glycol)/poly(acrylic acid) adsorbent	Pb(II) Cd(II)	0.015M	4	constant	(Yu et al., 2016)
Fe_3O_4/ chitosan/Serratia marcescens ion imprinted polymer, Pb-IMB	Pb(II)	0.1M	5	>85%	(He et al., 2019)
regenerated cellulose and sodium alginate chemically modified with polyethyleneimine	Cu(II) Zn(II) Pb(II)	0.1M	4	Cu(II) - 92% [(a)] Zn(II) - 71.3% [(a)] Pb(II) – 95.2% [(a)]	(Zhan et al., 2018)
EDTA-Modified Chitosan-Carboxymethyl Cellulose	Cu(II)	0.01M	5	constant	(Manzoor et al., 2019)
Carboxymethyl cellulose-based cryogels	Pb(II) Ni(II) Co(II)	0.1M	4	Pb(II) – 56% [(a)] Ni(II) – 78% [(a)] Co(II) - 91% [(a)]	(S.-S. Li et al., 2020)
nanocellulose/sodium alginate/carboxymethyl-chitosan gel beads	Cu(II) Pb(II)	0.1M	5	Cu(II)-33% [(a)] Pb(II) -52% [(a)]	(W. Li et al., 2021)
Carboxymethyl cellulose/polyacrylamide composite hydrogel	Cu(II) Pb(II) Cd(II)	0.1M	3	Cu(II)-91% [(a)] Pb(II) – 91.6%[(a)] Cd(II) – 90.2% [(a)]	(Godiya et al., 2019)
gelatin/TiO_2/ethylene imine polymer composite aerogels	Cu(II)	0.05M	5	76.58%	(Jiang et al., 2019)

(a) Calculated value

7.3 Appendix III: Supplementary data on organic contaminants removal

Figure AIII-1: (A) Single contaminant solutions abatement related to H_2O_2 10^{-4}M in ultrapure water; (B) contaminants mixture solution abatement related to H_2O_2 10^{-4}M in ultrapure water

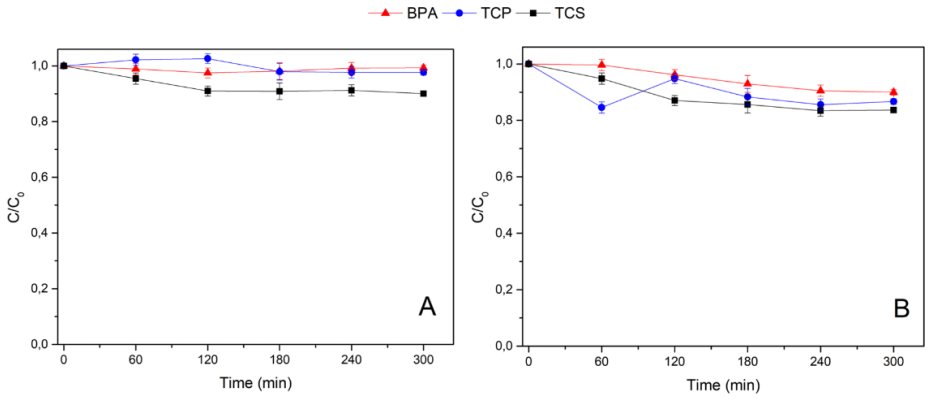

Figure AIII-2: Adsorption of (A) single contaminant solutions in ultrapure water; (B) contaminants mixture in ultrapure water; (C) contaminants mixture in real water (pond water)

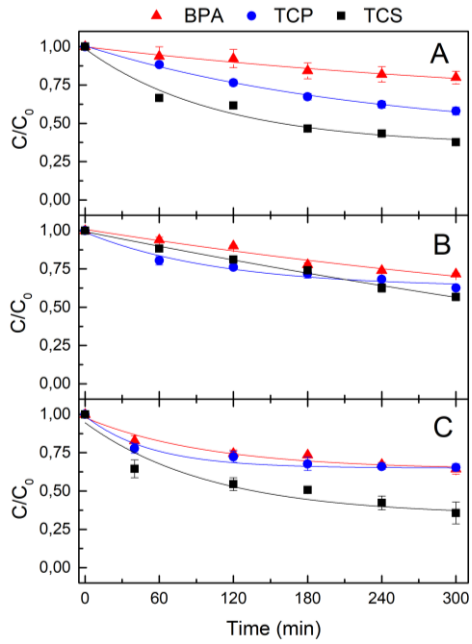

Figure AIII-3: Diagram summarizing the radical intermediates generated during the SBP reaction cycle and the main reaction products.

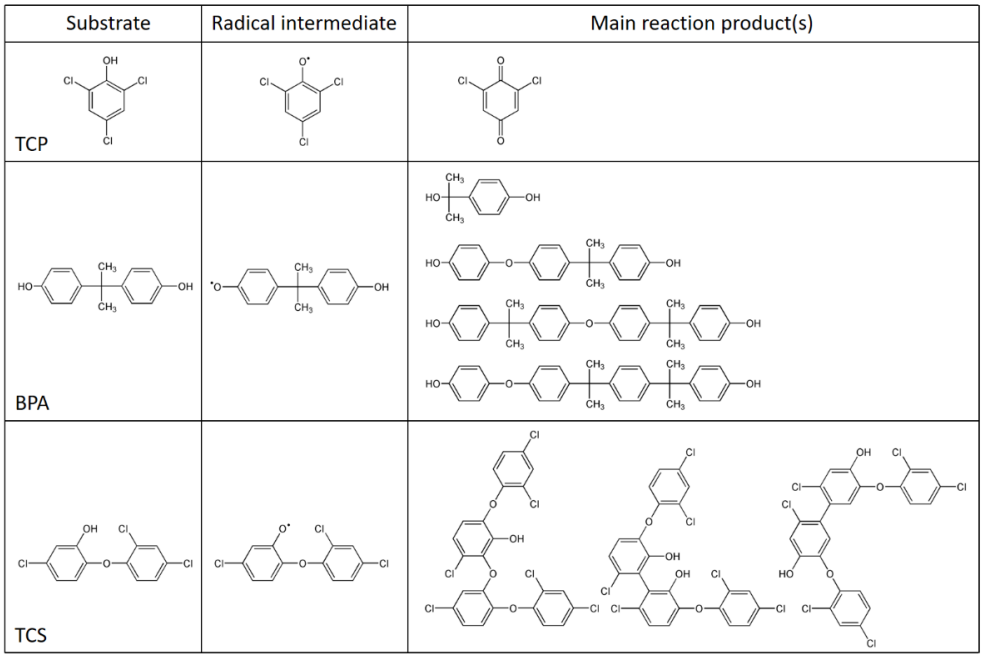

(Ferrari et al., 1999; Hammel & Tardone, 1988; Huang & Weber, 2005; J. Li et al., 2016)

Figure AIII-4: (A) Enzymatic removal results of single contaminant ultrapure water solutions with free SBP; (B) Enzymatic removal results of contaminants mixture ultrapure water solution.

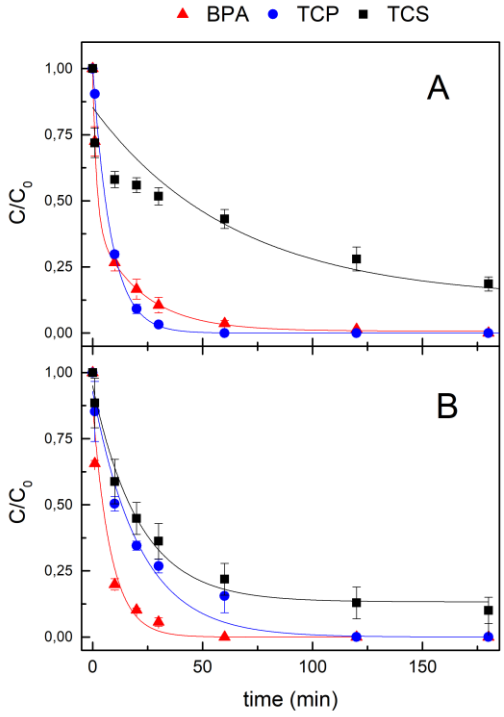

Figure AIII-5: (A) comparison between enzymatic removal of TCP in ultrapure water and pond water with HY-AC-SBP hydrogels; (B) comparison between enzymatic removal of TCP in ultrapure water at natural pH and pH 8 with HY-AC-SBP hydrogels; (C) comparison between enzymatic removal of TCP in pond water with HY-AC-SBP hydrogels using a normal (10^{-4} M) and double ($2x10^{-4}$M) concentration of H_2O_2.

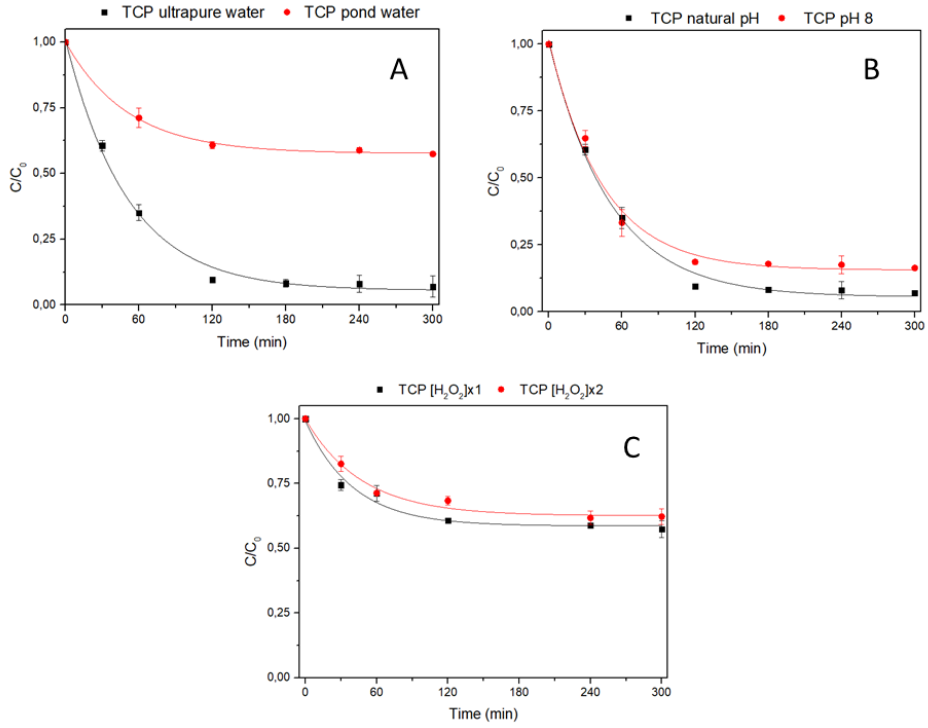

7.4 Appendix IV: Hydrogels biodegradation experiments

Table AIV-1: Compost Florawiva® characteristics

parameter	value*
origin	degradation and maturation of green and organic waste from separate waste collection
pH	7-8.8
Organic nitrogen	20% (w/w)
C/N ratio	25
Humic carbon (humic acids + fulvic acids)	7%
electrical conductivity	1.8 mS/cm

*values declared by the producer - https://ambiente.aceapinerolese.it/

Table AIV-2: Compost Folrawiva® characterization (concentration expressed in mg/kg)

Element	Legal Limits	Compost Florawiva®
Al	-	19177 ± 963
Ca	-	56365 ± 2537
Fe	-	16031 ± 358
K	-	11915 ± 311
Mg	-	9613 ± 351
P	-	11664 ± 304
Ba	-	155 ± 7
Ce	-	21 ± 2
Co	-	6 ± 0.2
Cr	-	69 ± 5
Cu	230	100 ± 5
La	-	8 ± 2
Mn	-	410 ± 8
Na	-	1736 ± 61
Ni	100	40 ± 1
Pb	140	42 ± 1
Sr	-	177 ± 6
Ti	-	653 ± 50
V	-	17 ± 2
Zn	500	280 ± 9
As	-	4.1 ± 0.1
Cd	1.5	1.1 ± 0.2
Hg	1.5	0.05

Table AIV-3: database for ANOVA analysis. Values represent PTEs concentration in compost samples and are expressed in mg/kg.

	As	Cd	Cu	Hg	Ni	Pb	Zn
HY-ACMC Blank 1	3.069	0.984	97.460	0.376	38.384	39.786	272.319
HY-ACMC Blank 2	3.439	1.056	102.660	2.207	40.536	42.951	293.717
HY-ACMC Blank 3	3.501	0.982	97.416	-0.662	38.583	47.694	274.944
HY-ACMC 1	4.073	1.276	99.404	-0.066	61.471	43.281	287.291
HY-ACMC 2	3.992	0.970	96.360	-0.065	42.266	40.448	278.419
HY-ACMC 3	4.305	1.013	101.758	-0.143	48.315	42.196	282.983
HY-ACMC Sterile 1	3.751	1.112	105.779	-0.041	44.783	42.361	290.865
HY-ACMC Sterile 2	3.967	0.959	95.639	-0.171	41.738	39.524	270.931
HY-MCHI Blank 1	3.444	1.136	102.714	0.120	45.212	40.399	285.129
HY-MCHI Blank 2	3.278	0.853	95.017	-0.472	48.224	39.664	284.220
HY-MCHI Blank 3	3.936	1.054	98.741	-0.095	51.058	39.506	282.052
HY-MCHI 1	3.819	1.098	105.772	2.287	43.714	40.771	279.234
HY-MCHI 2	3.950	1.071	101.768	1.262	42.319	41.966	286.506
HY-MCHI 3	4.025	1.082	100.735	1.802	42.364	41.325	285.722
HY-MCHI Sterile 1	3.590	1.127	103.122	1.220	40.340	41.789	294.287
HY-MCHI Sterile 2	4.045	1.079	103.086	1.757	41.659	40.975	293.213
HY-MGEL Blank 1	3.115	1.001	92.920	-0.249	42.905	37.273	254.687
HY-MGEL Blank 2	3.747	0.938	108.960	0.669	41.069	42.903	287.474
HY-MGEL Blank 3	4.013	1.010	95.082	-0.339	43.296	40.176	263.603
HY-MGEL 1	3.581	1.144	104.016	0.940	44.536	41.208	292.522
HY-MGEL 2	4.280	1.064	102.695	0.334	46.703	44.686	302.654
HY-MGEL 3	3.849	0.983	103.416	0.386	40.464	40.826	273.360
HY-MGEL Sterile 1	3.821	1.083	99.712	0.321	40.009	43.772	282.837
HY-MGEL Sterile 2	4.301	0.982	98.433	1.094	40.651	39.441	278.700
Compost T.Q. 1	4.035	1.146	97.052	0.130	40.561	42.663	274.891
Compost T.Q. 2	3.984	1.162	105.536	0.301	39.565	41.095	290.662
Compost T.Q. 3	4.184	0.853	97.936	-0.281	38.914	43.228	275.082

Tables AIV-4: results of ANOVA for mercury concentration in compost samples obtained with the statistical software XLSTAT, Dunnett's test

AIV-4-I: Dunnett (bilateral) / Analysis of differences between Q1-TQ control mode and other modalities with a 95% confidence interval

Mode	Difference	Standardized difference	Critic value	Critic difference	Pr > Diff	significant
TQ vs HY-MCHI Blank	0,199	0,402	2,946	1,459	1,000	No
TQ vs HY-ACMC	0,141	0,285	2,946	1,459	1,000	No
TQ vs HY-MGEL Blank	0,023	0,046	2,946	1,459	1,000	No
TQ vs HY-MCHI	-1,734	-3,500	2,946	1,459	0,015	Si
TQ vs HY-MCHI Sterile	-1,098	-2,217	2,946	1,459	0,203	No
TQ vs HY-ACMC Blank	-0,590	-1,192	2,946	1,459	0,795	No
TQ vs HY-MGEL Sterile	-0,577	-1,166	2,946	1,459	0,811	No
TQ vs HY-MGEL	-0,503	-1,016	2,946	1,459	0,892	No
TQ vs HY-ACMC Sterile	-0,035	-0,071	2,946	1,459	1,000	No

AIV-4-II: Dunnett (one-sided left) / Analysis of differences between Q1-TQ control mode and other modalities with a 95% confidence interval

Mode	Difference	Standardized difference	Critic value	Critic difference	Pr > Diff	significant
TQ vs HY-MCHI Blank	0,199	0,402	-2,601	-1,288	0,215	No
TQ vs HY-ACMC	0,141	0,285	-2,601	-1,288	0,176	No
TQ vs HY-MGEL Blank	0,023	0,046	-2,601	-1,288	0,110	No
TQ vs HY-MCHI	-1,734	-3,500	-2,601	-1,288	0,000	Si
TQ vs HY-MCHI Sterile	-1,098	-2,217	-2,601	-1,288	0,000	No
TQ vs HY-ACMC Blank	-0,590	-1,192	-2,601	-1,288	0,004	No
TQ vs HY-MGEL Sterile	-0,577	-1,166	-2,601	-1,288	0,004	No
TQ vs HY-MGEL	-0,503	-1,016	-2,601	-1,288	0,006	No
TQ vs HY-ACMC Sterile	-0,035	-0,071	-2,601	-1,288	0,086	No

AIV-4-III: Dunnett (one-sided right) / Analysis of differences between Q1-TQ control mode and other modalities with a 95% confidence interval

Mode	Difference	Standardized difference	Critic value	Critic difference	Pr > Diff	significant
TQ vs HY-MCHI Blank	0,199	0,402	2,601	1,288	0,785	No
TQ vs HY-ACMC	0,141	0,285	2,601	1,288	0,824	No
TQ vs HY-MGEL Blank	0,023	0,046	2,601	1,288	0,890	No
TQ vs HY-MCHI	-1,734	-3,500	2,601	1,288	1,000	No
TQ vs HY-MCHI Sterile	-1,098	-2,217	2,601	1,288	1,000	No
TQ vs HY-ACMC Blank	-0,590	-1,192	2,601	1,288	0,996	No
TQ vs HY-MGEL Sterile	-0,577	-1,166	2,601	1,288	0,996	No
TQ vs HY-MGEL	-0,503	-1,016	2,601	1,288	0,994	No
TQ vs HY-ACMC Sterile	-0,035	-0,071	2,601	1,288	0,914	No

7.5 Appendix V: Supplementary data regarding photocatalysts for self-sustaining systems and contaminant degradation

Figure AV-1: LED-RGB emission graph (Irradiance in W/m^2)

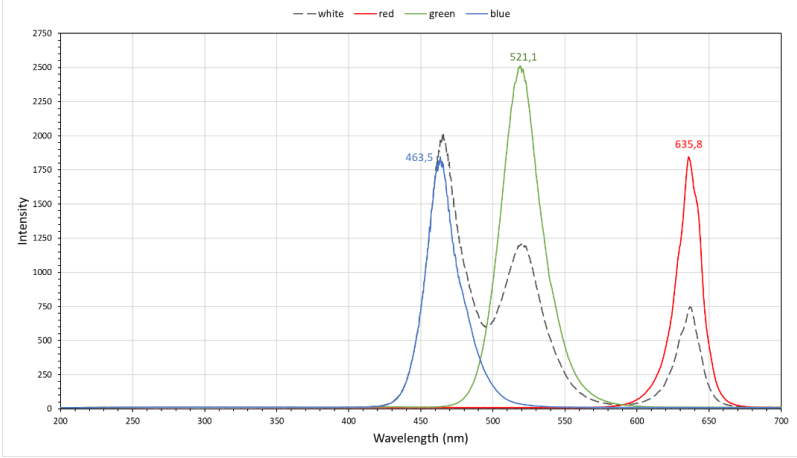

Figure AV-2: Adsorption isotherms of N_2 of synthesized samples (BET analysis)

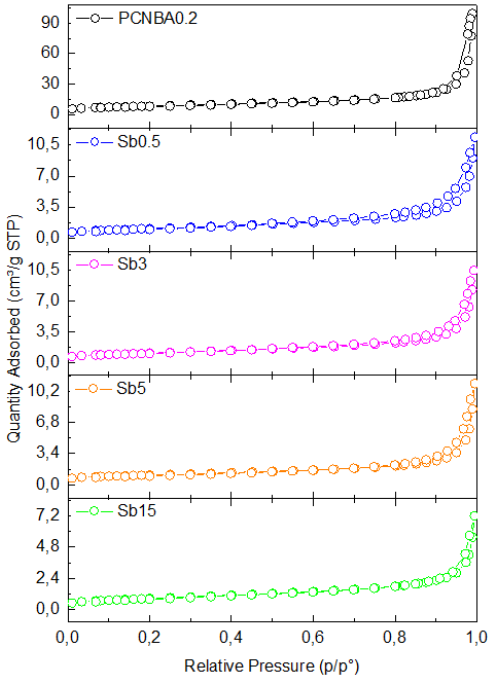

Figure AV-3: Element Mapping Analyses of the prepared photocatalysts

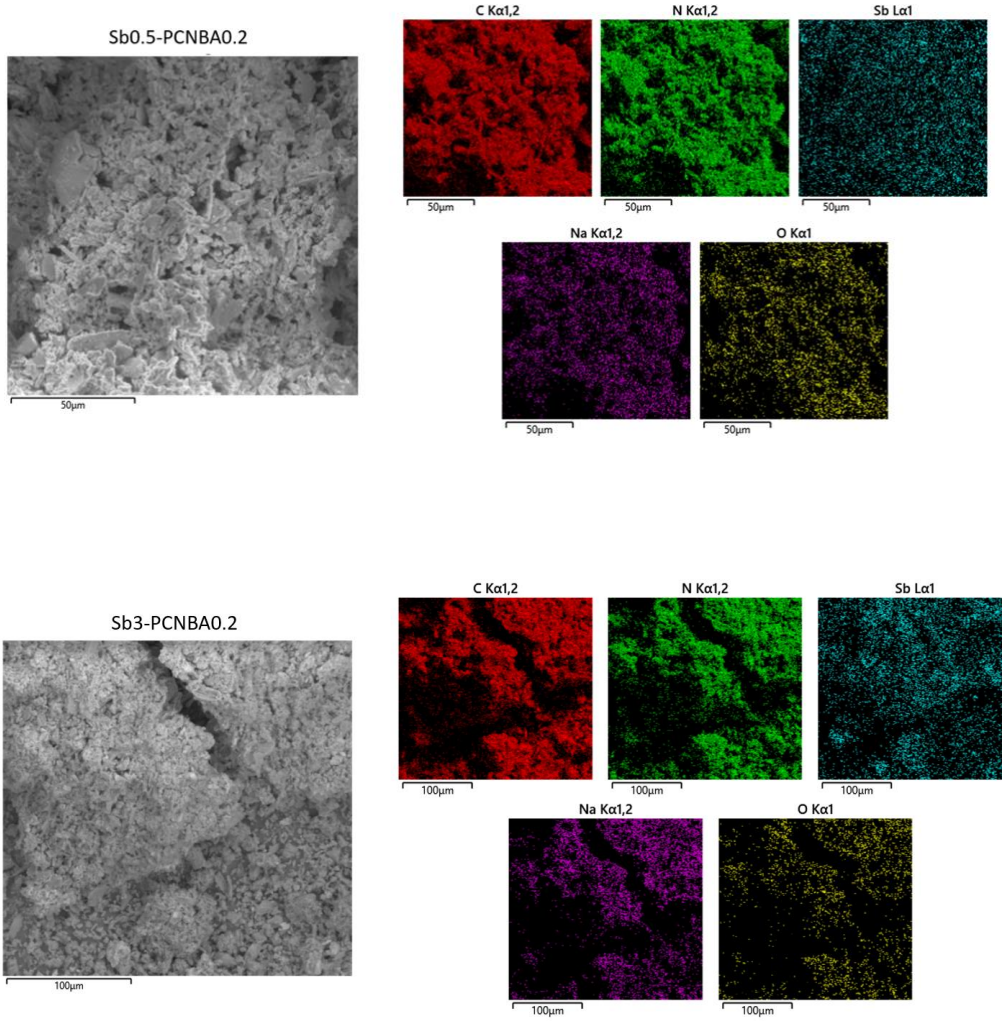

Sb5-PCNBA0.2

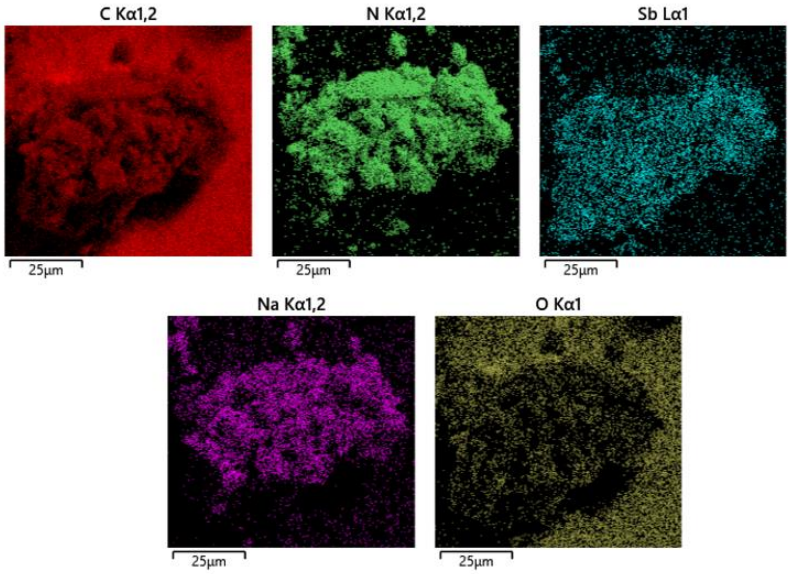
C Kα1,2
N Kα1,2
Sb Lα1
25μm
25μm
25μm
Na Kα1,2
O Kα1
25μm
25μm

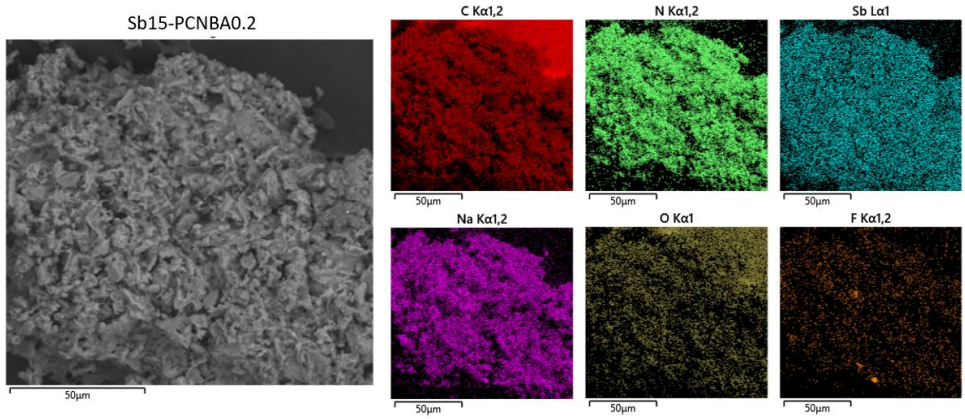
Sb15-PCNBA0.2
50μm
C Kα1,2
N Kα1,2
Sb Lα1
50μm
50μm
50μm
Na Kα1,2
O Kα1
F Kα1,2
50μm
50μm
50μm

Figure AV-4: High resolution O 1s, Sb 3d, C 1s, N 1s XPS spectra of prepared samples

a) PCNBA0.2

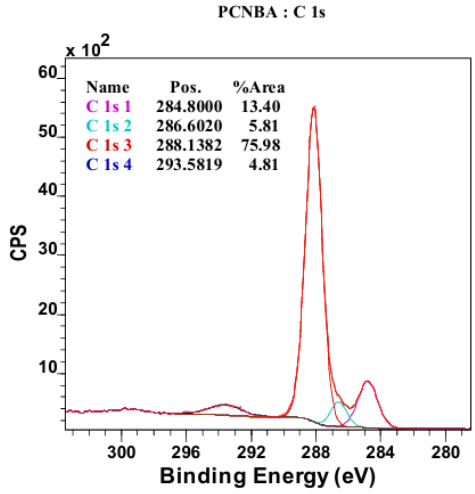

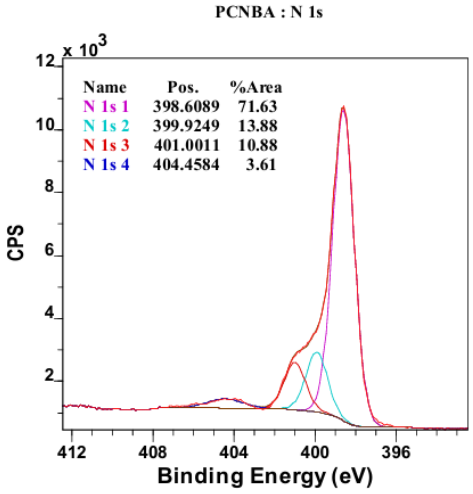

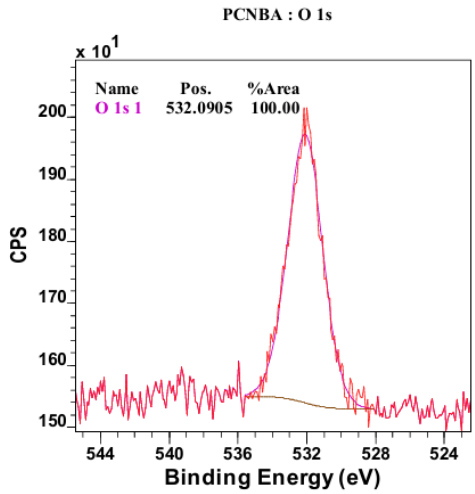

b) Sb0.5-PCNBA0.2

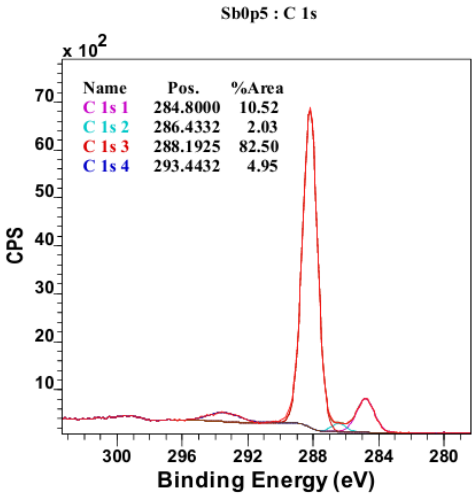

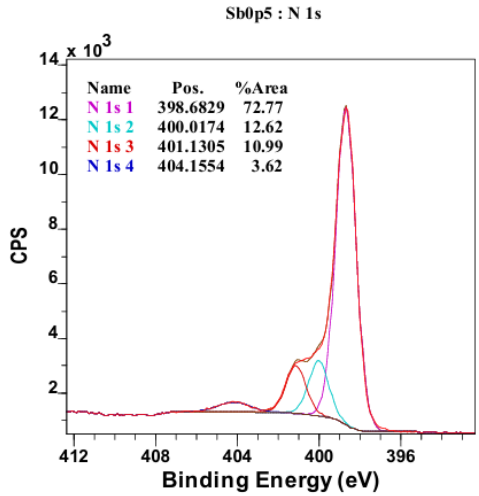

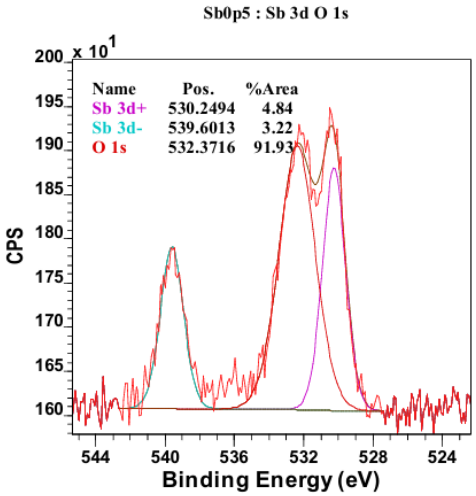

c) Sb3-PCNBA0.2

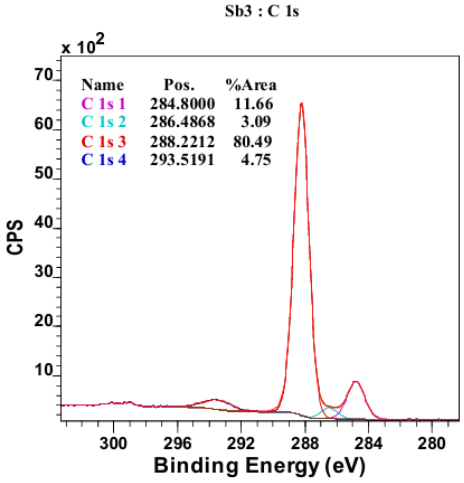

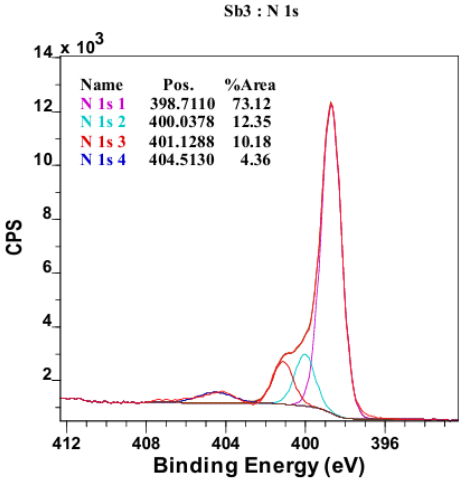

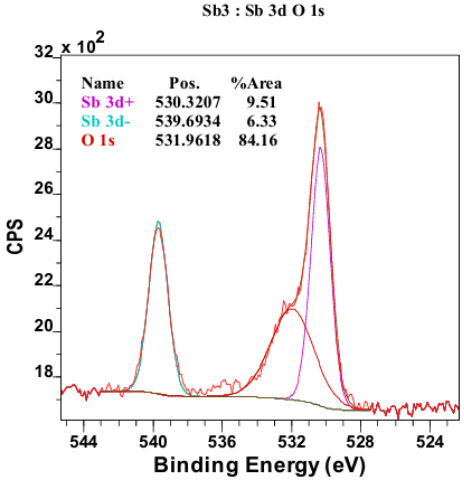

d) Sb5-PCNBA0.2

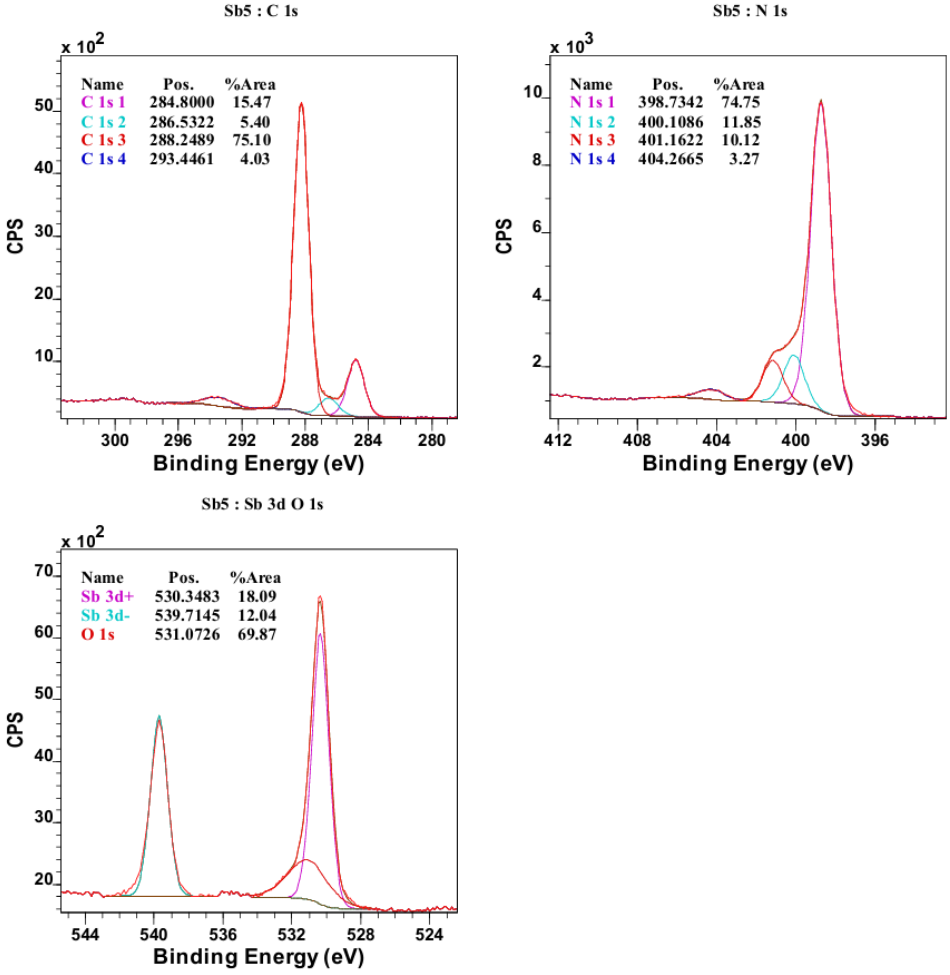

e) Sb15-PCNBA0.2

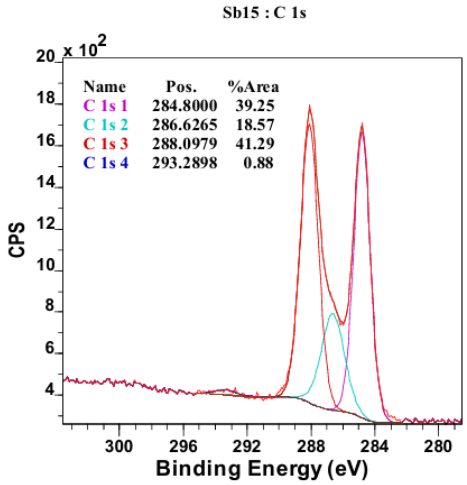

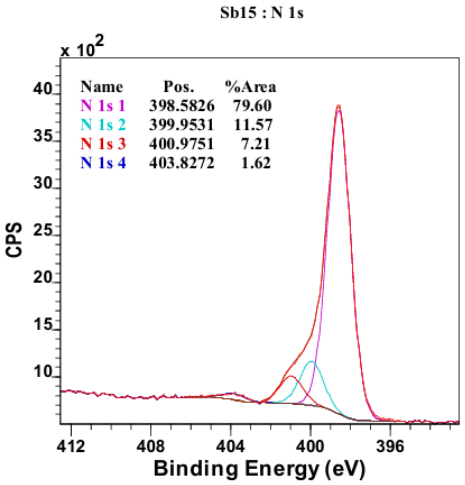

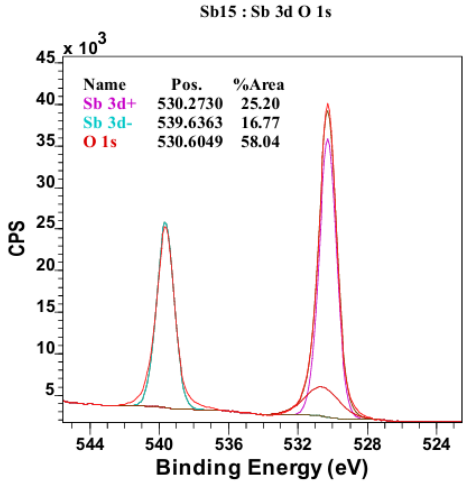

Figure AV-5: Pictures of obtained Sbx-PCNBA0.2 samples

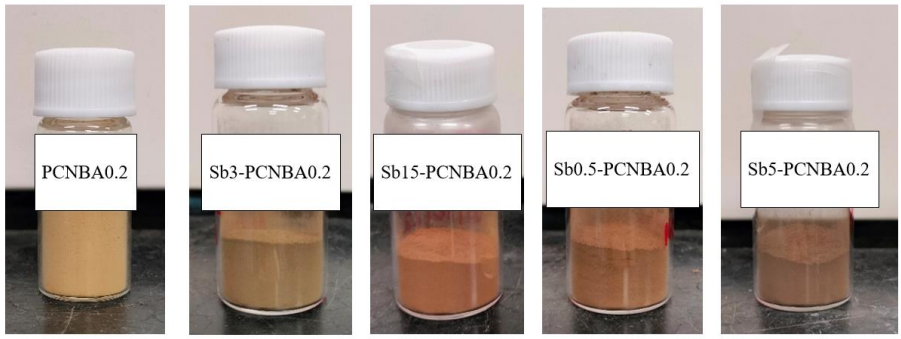

Figure AV-6: Mott-Schottky curves of the synthesised materials

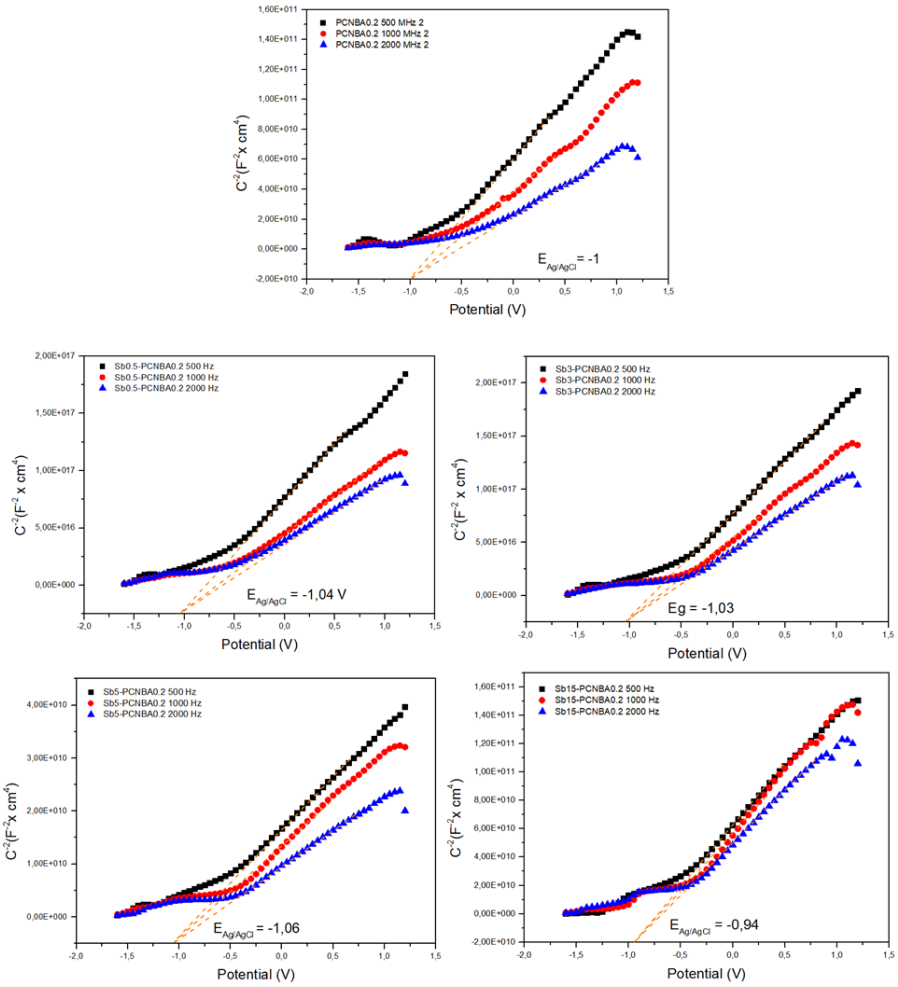

Figure AV-7: XPS valence band of prepared samples

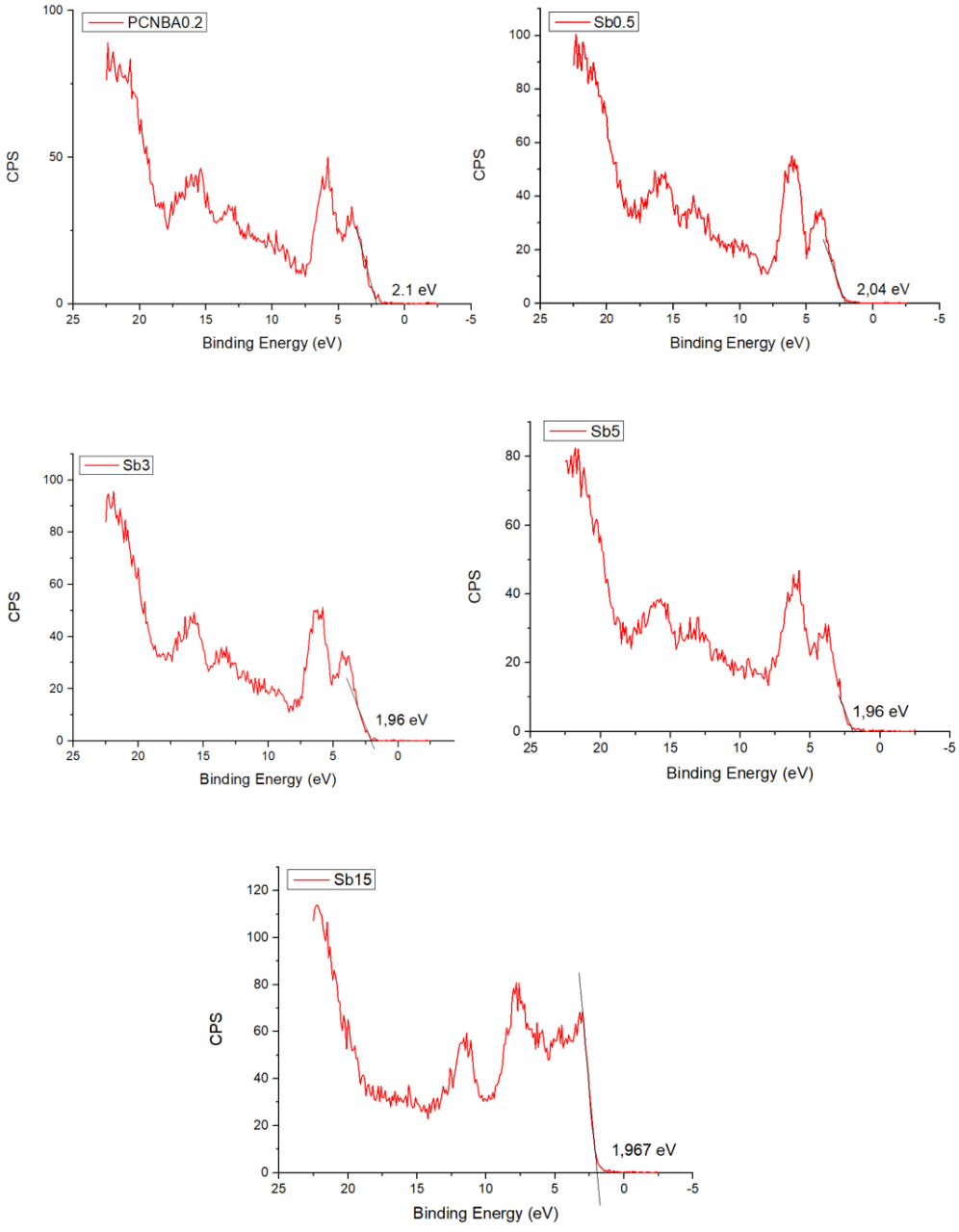

Figure AV-8: The following pictures show a general survey spectrum for each sample including the results of the quantification of detected elements. It must be taken into account that the values obtained for Sb are overestimated due to the signal of Sb 3d is overlapped with O 1s signal

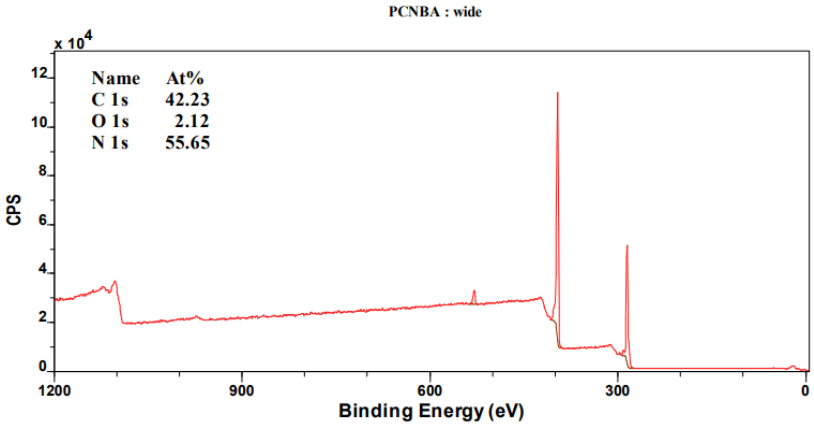

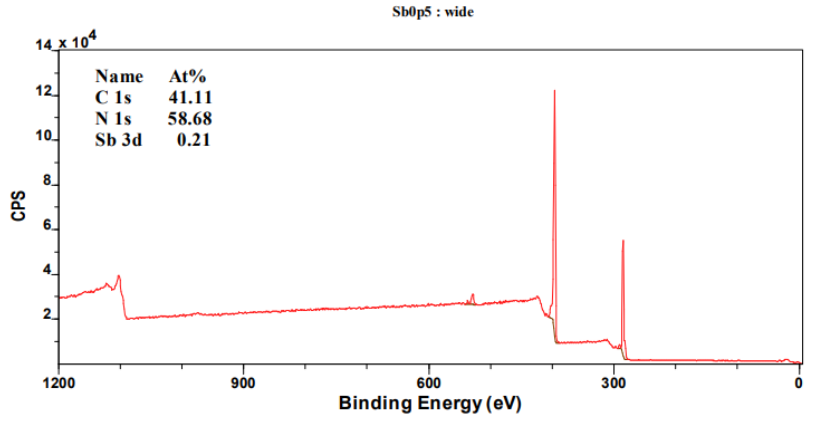

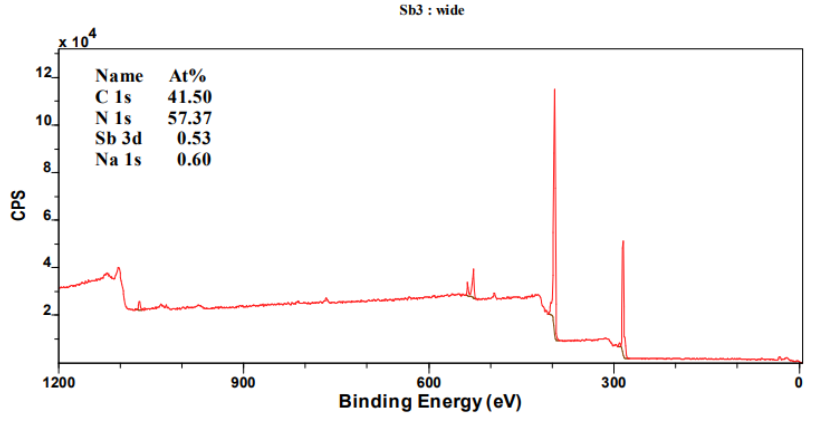

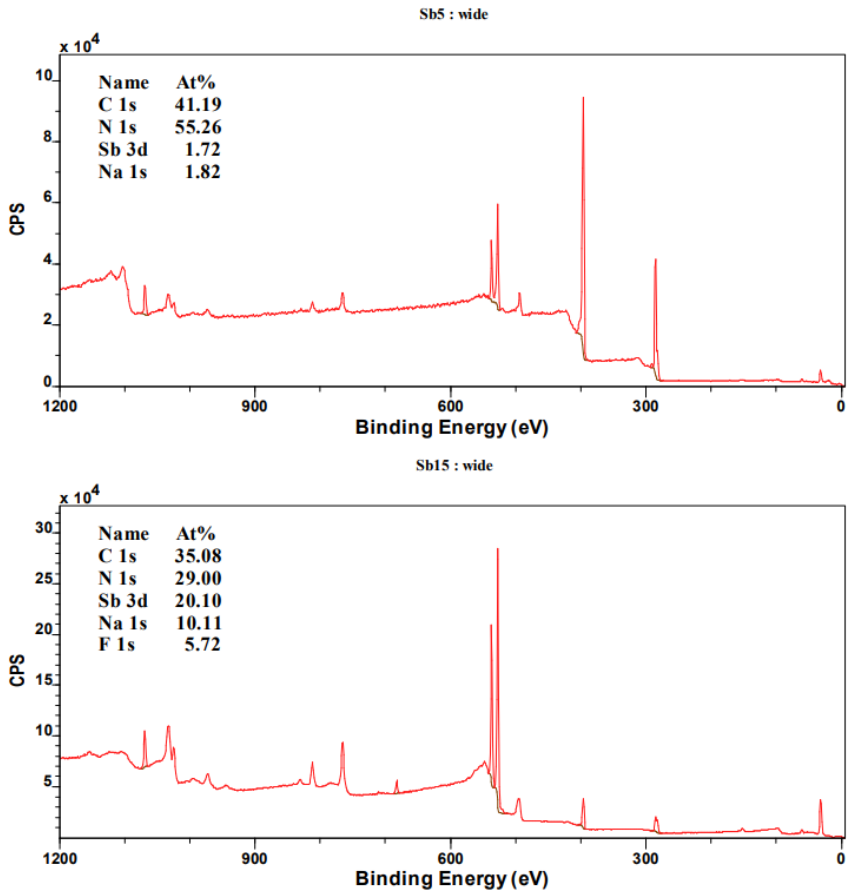

Table AV-1: The following tables show the results of the relative quantification (atomic %) resultant from high resolution spectra of selected elements.

Sample / At. %	C 1s	N 1s	O 1s	Sb 3d
PCNBA	46.55	51.57	1.89	---
Sb0.5	45.66	52.93	1.30	0.11
Sb3	44.83	52.78	2.01	0.38
Sb5	44.84	50.06	3.56	1.54
Sb15	35.93	25.33	22.48	16.25
i-PCNBA	44.90	53.25	1.85	---
i-Sb0.5	46.57	51.93	1.36	0.14
i-Sb3	45.98	51.28	2.23	0.51
i-Sb5	45.11	50.40	3.42	1.07
i-Sb15	33.14	21.52	26.51	18.83

Figure AV-10: EPR signals of DMPO-OH (green), DMPO-O2-(blue), and TEMP-singlet oxygen (red). Signals were obtained for eCNm, CNm, CNd, CNdac, and aCNd aqueous suspensions under Simulated Solar Light irradiation at room temperature

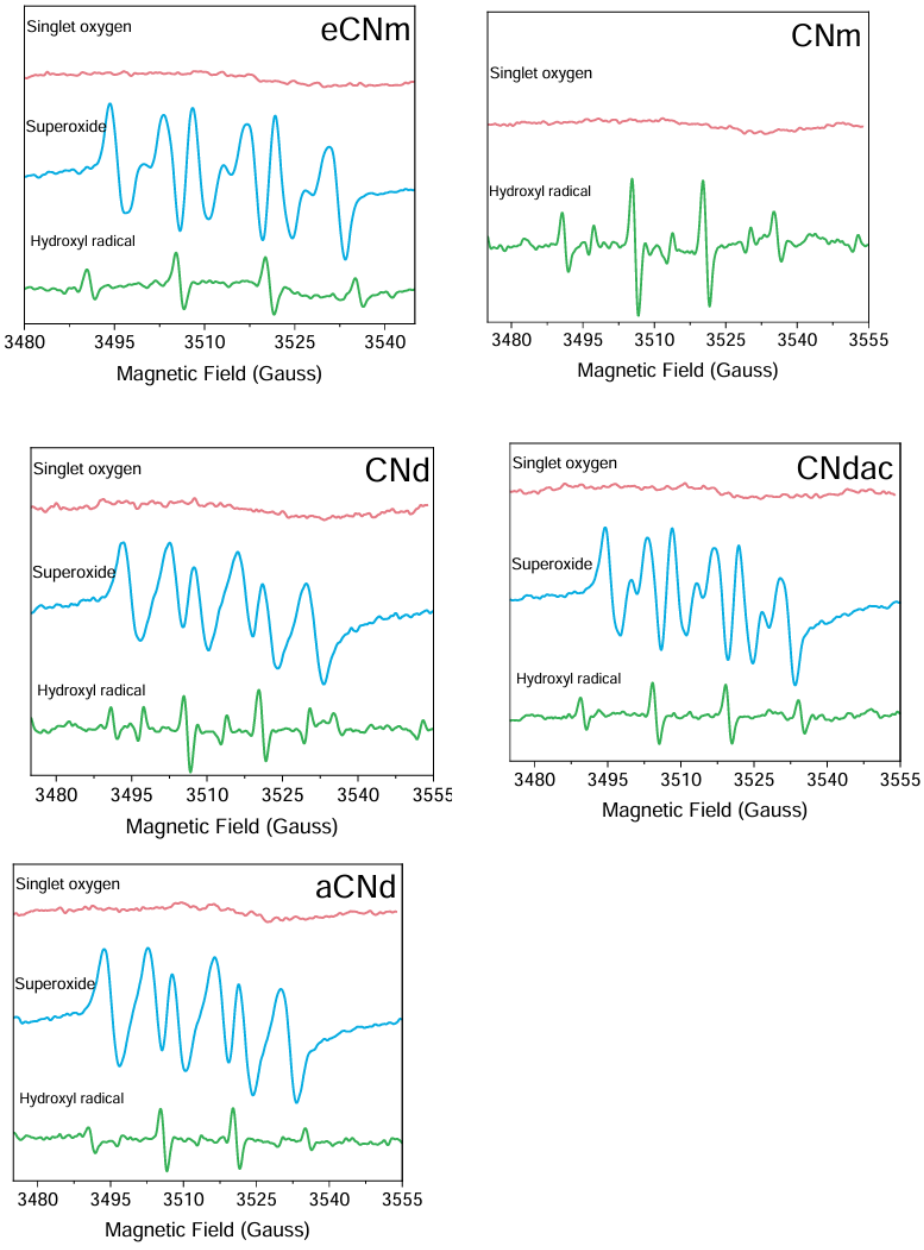

Figure AV-11: Solid EPR spectra at 77 K in the dark and after 30 min irradiation with Simulated Solar Light. Intensities are normalized for 1 mg of sample. Experimental conditions: microwave frequency 9.42 GHz; microwave power 5 mW; modulation amplitude 2 Gauss.

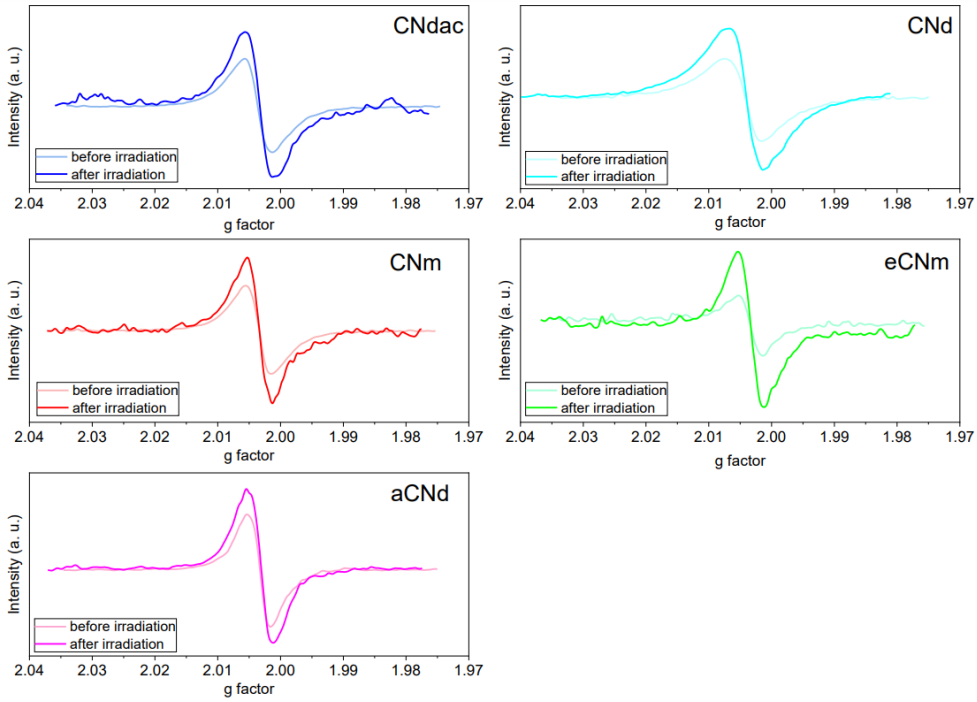

Figure AV-12: EPR signal area difference between irradiated and dark samples (S_{irr} − S_{dark}) vs the specific surface area (Asp) of the corresponding sample. Inset: Correlation plot of (S_{irr} − S_{dark}) vs methyl orange removal [MO RE (%)]. The specific surface areas measured for the samples are 8.7±0.1, 7.27±0.08, 30.4±0.1, 28.0±0.2, 45.6 and 54.7±0.5 for CNdac, CNd, aCNd, CNm, eCNm and CNu respectively.

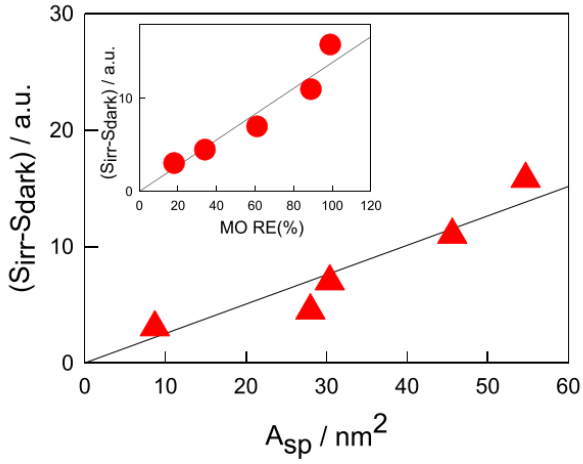

7.6 References

Abou El-Reash, Y. G. (2016). Magnetic chitosan modified with cysteine-glutaraldehyde as adsorbent for removal of heavy metals from water. *Journal of Environmental Chemical Engineering*, *4*(4, Part A), 3835–3847. https://doi.org/10.1016/j.jece.2016.08.014

Academic Software. Sourby Old Farm, Timble, Otley, Yorks, LS21 2PW. In SC-Database. The IUPAC Stability Constant Database,Version 5.84. (s.d.). [Dataset].

Cassone, G., Chillé, D., Foti, C., Giuffré, O., Ponterio, R. C., Sponer, J., & Saija, F. (2018). Stability of hydrolytic arsenic species in aqueous solutions: As3+vs. As5+. *Physical Chemistry Chemical Physics*, *20*(36), 23272–23280. https://doi.org/10.1039/C8CP04320E

Castellino, L., Alladio, E., Bertinetti, S., Lando, G., De Stefano, C., Blasco, S., García-España, E., Gama, S., Berto, S., & Milea, D. (2023). PyES – An open-source software for the computation of solution and precipitation equilibria. *Chemometrics and Intelligent Laboratory Systems*, *239*, 104860. https://doi.org/10.1016/j.chemolab.2023.104860

Ferrari, R. P., Laurenti, E., & Trotta, F. (1999). Oxidative 4-dechlorination of 2,4,6-trichlorophenol catalyzed by horseradish peroxidase. *JBIC Journal of Biological Inorganic Chemistry*, *4*(2), 232–237. https://doi.org/10.1007/s007750050309

Godiya, C. B., Cheng, X., Li, D., Chen, Z., & Lu, X. (2019). Carboxymethyl cellulose/polyacrylamide composite hydrogel for cascaded treatment/reuse of heavy metal ions in wastewater. *Journal of Hazardous Materials*, *364*, 28–38. https://doi.org/10.1016/j.jhazmat.2018.09.076

Hammel, K. E., & Tardone, P. J. (1988). The Oxidative 4-Dechlorination of Polychlorinated Phenols Is Catalyzed by Extracellular Fungal Lignin Peroxidases+. *Biochemistry*, *27*, 6563–6568. https://doi.org/10.1021/bi00417a055

He, Y., Wu, P., Xiao, W., Li, G., Yi, J., He, Y., Chen, C., Ding, P., & Duan, Y. (2019). Efficient removal of Pb(II) from aqueous solution by a novel ion imprinted magnetic biosorbent: Adsorption kinetics and mechanisms. *PLOS ONE*, *14*(3), e0213377. https://doi.org/10.1371/journal.pone.0213377

Huang, Q., & Weber, W. J. (2005). Transformation and Removal of Bisphenol A from Aqueous Phase via Peroxidase-Mediated Oxidative Coupling Reactions: Efficacy, Products, and Pathways. *Environmental Science & Technology*, *39*(16), 6029–6036. https://doi.org/10.1021/es050036x

Huheey, J. E., Keiter, E. A., & Keiter, R. L. (s.d.). *Inorganic Chemistry. Principles of Structures and Reactivity* (Fourth Edition). HarperCollins College Publishers.

Jiang, J., Zhang, Q., Zhan, X., & Chen, F. (2019). A multifunctional gelatin-based aerogel with superior pollutants adsorption, oil/water separation and photocatalytic properties. *Chemical Engineering Journal*, *358*, 1539–1551. https://doi.org/10.1016/j.cej.2018.10.144

Li, J., Peng, J., Zhang, Y., Ji, Y., Shi, H., Mao, L., & Gao, S. (2016). Removal of triclosan via peroxidases-mediated reactions in water: Reaction kinetics, products and detoxification. *Journal of Hazardous Materials*, *310*, 152–160. https://doi.org/10.1016/j.jhazmat.2016.02.037

Li, S.-S., Song, Y.-L., Yang, H.-R., An, Q.-D., Xiao, Z.-Y., & Zhai, S.-R. (2020). Carboxymethyl cellulose-based cryogels for efficient heavy metal capture: Aluminum-mediated assembly process and sorption mechanism. *International Journal of Biological Macromolecules*, *164*, 3275–3286. https://doi.org/10.1016/j.ijbiomac.2020.08.186

Li, W., Zhang, L., Hu, D., Yang, R., Zhang, J., Guan, Y., Lv, F., & Gao, H. (2021). A mesoporous nanocellulose/sodium alginate/carboxymethyl-chitosan gel beads for efficient adsorption of Cu2+ and Pb2+. *International Journal of Biological Macromolecules*, *187*, 922–930. https://doi.org/10.1016/j.ijbiomac.2021.07.181

Manzoor, K., Ahmad, M., Ahmad, S., & Ikram, S. (2019). Synthesis, Characterization, Kinetics, and Thermodynamics of EDTA-Modified Chitosan-Carboxymethyl Cellulose as Cu(II) Ion Adsorbent. *ACS Omega*, *4*(17), 17425–17437. https://doi.org/10.1021/acsomega.9b02214

Ngah, W. S. W., & Fatinathan, S. (2010). Adsorption characterization of Pb(II) and Cu(II) ions onto chitosan-tripolyphosphate beads: Kinetic, equilibrium and thermodynamic studies. *Journal of Environmental Management*, *91*(4), 958–969. https://doi.org/10.1016/j.jenvman.2009.12.003

Shaker, M. A., & Yakout, A. A. (2016). Optimization, isotherm, kinetic and thermodynamic studies of Pb(II) ions adsorption onto N-maleated chitosan-immobilized TiO2 nanoparticles from aqueous media. *Spectrochimica Acta Part A: Molecular and Biomolecular Spectroscopy*, *154*, 145–156. https://doi.org/10.1016/j.saa.2015.10.027

Xie, M., Zeng, L., Zhang, Q., Kang, Y., Xiao, H., Peng, Y., Chen, X., & Luo, J. (2015). Synthesis and adsorption behavior of magnetic microspheres based on chitosan/organic rectorite for low-concentration heavy metal removal. *Journal of Alloys and Compounds*, *647*, 892–905. https://doi.org/10.1016/j.jallcom.2015.06.065

Yu, J., Zheng, J., Lu, Q., Yang, S., Zhang, X., Wang, X., & Yang, W. (2016). Selective adsorption and reusability behavior for Pb2+ and Cd2+ on chitosan/poly(ethylene glycol)/poly(acrylic acid) adsorbent prepared by glow-

discharge electrolysis plasma. *Colloid and Polymer Science*, *294*(10), 1585–1598. https://doi.org/10.1007/s00396-016-3920-9

Zhan, W., Xu, C., Qian, G., Huang, G., Tang, X., & Lin, B. (2018). Adsorption of Cu(II), Zn(II), and Pb(II) from aqueous single and binary metal solutions by regenerated cellulose and sodium alginate chemically modified with polyethyleneimine. *RSC Advances*, *8*(33), 18723–18733. https://doi.org/10.1039/C8RA02055H